Optically Reconfigurable Microwave and Millimetre Wave Switches

Alexander Weiran Pang

Department of Electrical and Electronic Engineering

University of Bristol

Thesis submitted in support of the degree of Doctor of Philosophy in the Faculty of Engineering, University of Bristol

September 2018

DECLARATION AND DISCLAIMER

I declare that the work in this dissertation was carried out in accordance with the requirements of the University's Regulations and Code of Practice for Doctoral Postgraduate Programmes and that it has not been submitted for any other academic award.

Except where indicated by specific reference in the text, this work is my own work. Work done in collaboration with, or with the assistance of others, is indicated as such. I have identified all material in this dissertation which is not my own work through appropriate referencing and acknowledgement. Where I have quoted from the work of others, I have included the source in the references/bibliography.

Any views expressed in the dissertation are those of the author.

The author confirms that the printed copy and the electronic version of this thesis are identical.

Signed:

Date:

Abstract

Reconfigurability has become a desirable and essential feature of modern Radio-Frequency (RF) systems for wireless communications due to the unprecedented challenge to accommodate multiple bands in communication standards. Reconfigurable circuitry makes it possible to reduce the size and cost of the system by providing RF tuning instead of duplicating the same circuits for every desired band. Optical reconfiguration is distinguished by its elimination of an electrical bias system and ElectroMagnetic Interference (EMI), while potentially providing fast switching compared with other conventional RF tunable approaches.

This project is primarily interested in the new designs and characterisations of optically-tunable switches which remove the need of a diode junction and thus, inherently demonstrate high linearity and power-handling ability. In addition, the recent development of a semiconductor laser and Light Emitting Diode (LED)/Infra-Red Emitting Diode (IRED) techniques has enabled the achievement of high-intensity and spatial illumination in a pulsed tuning operation. These facts are the motivation for a new investigation of optically reconfigurable microwave and millimetre wave switches. Initial work focuses on generating an ElectroMagnetic (EM) simulation model and investigating the high insertion loss in the photoconductive switches presented in previous work. It then involves the use of improved designs for optically-controlled switches at microwave and millimetre wave frequencies. The RF characterisation of these proposed devices is performed in terms of insertion loss, isolation, nonlinearity, power-handling and switching speed.

A novel, high-power optically controlled microwave microstrip switch is presented with superstrate structure through a low-loss glass substrate which reduces insertion loss to $1.11dB$ and simultaneously maintains good isolation of $20dB$ at $2GHz$. 3rd-order Input-referenced Intercept Point (IIP3) is measured up to $+78.5dBm$ in a two-tone nonlinearity test with maximum power handled at over $60W$, which is reported for the first time. An optically reconfigurable Grounded-CoPlanar Waveguide (GCPW) microwave and millimetre-wave (mmW) switch has been designed and measured with good results showing an insertion loss of less than $3dB$ and isolation over $30dB$ in millimetre wave frequencies.

Remembered with Love

Always in our Hearts

In memory of my grandmothers,

Rulan Yue (16/01/1934-21/11/2017)

Shukai Sun (31/12/1929-29/03/2018)

Acknowledgements

I would like to express my sincere appreciation to Professor Martin Cryan, Dr. Souheil Bensmida and Dr. Chris Gamlath for their invaluable and constructive support. This research could not have been completed without their kindness, patience and guidance from the very beginning to the final stage.

I would also like to acknowledge the Department of Electrical and Electronic Engineering, Faculty of Engineering and University of Bristol for providing various funding opportunities and conference grants to complete my studies. I am particularly grateful to my colleagues in the Photonics group and the Communication Systems and Networks group for their help with equipment and devices. Thanks are also given to my colleague, Yutian Zhang, and the BEng, MEng, MSc and intern students who participated in this project.

I would like to especially thank Dr. Andrew Murray for his tremendous help with the circuit fabrication in the clean room, to Michael Penny for his skills in testing the fixture fabrication, to Rob Davies for his skills in the PCB circuit fabrication and to Peter Crook for his help in the CSN laboratory. Their vast experience and invaluable patience were extremely helpful throughout this project.

My greatest gratitude must be reserved for my parents, my wife and my family, whose financial and spiritual support has sustained me through all the challenges and troubles in the UK and enabled me to complete this degree.

Finally, my blessings and special thanks to one who has and always will support me in all circumstances through the best and most challenging years of our lives.

Publications

Journals

- A. W. Pang, C. D. Gamlath, M. J. Cryan, “An Optically Controlled Coplanar Waveguide Millimeter-Wave Switch”, IEEE Microwave and Wireless Components Letters, vol. 28, no. 8, pp. 669-71, Aug. 2018

- A. W. Pang, S. Bensmida, C. D. Gamlath, M. J. Cryan, “Non-linear characteristics of an optically reconfigurable microwave switch”, IET Microwaves, Antennas & Propagation, vol. 12, no. 7, pp. 1060-1063, Jan. 2018

- Y. Zhang, A. W. Pang, M. J. Cryan, “Optically Controlled Millimeter-wave Attenuator with Stepped-Impedance Lines”, to be submitted, Oct. 2018

- C. D. Gamlath, A. W. Pang, M. J. Cryan, “Investigation of an optically induced superstrate plasma for tuning microstrip antennas”, IET Optoelectronics, vol. 11, no. 6, pp. 230-236, Sep. 2017

Conferences

- A. W. Pang, S. Bensmida, M. J. Cryan, “Nonlinearity and Power Handling Characterization of an Optically Reconfigurable Microwave Switch”, IEEE/MTT-S International Microwave Symposium (IMS 2018), Philadelphia, Pennsylvania, U.S.A., pp. 420-422, Jun. 2018

- A. W. Pang, C. D. Gamlath, M. J. Cryan, “An Optically Controlled Co-Planar Waveguide Microwave Switch”, UK-Europe-China Workshop on Millimetre-Waves and Terahertz Technologies (UCMMT 2017), Liverpool, U.K., Sep. 2017

- A. W. Pang, C. D. Gamlath, M. J. Cryan, “An Optically Controlled Co-Planar Waveguide Microwave Switch”, International Symposium on Photonics and Optoelectronics (SOPO 2017), Guilin, China, Aug. 2017

- A. W. Pang, S. Bensmida, M. J. Cryan, “Non-linear Characteristics of an Optically Reconfigurable Microwave Switch”, Union Radio-Scientifique Internationale (U.R.S.I. 2016), York, U.K., December 2016

- A. W. Pang, C. D. Gamlath, M. J. Cryan, “Superstrate Based Optically Reconfigurable Microwave Circuits”, Semiconductor and Integrated OptoElectronics (SIOE 2016), Cardiff. U.K., Apr. 2016

Table of Contents

List of Figures

List of Tables

List of Acronyms

CST	Computer Simulation Technology
CW	Continuous Wave
DC	Direct Current
DUT	Device Under Test
EMI	ElectroMagnetic Interference
FDTD	Finite-Difference Time-Domain
GCPW	Grounded CoPlanar Waveguide
HCL	Hydrochloric acid
IC	Integrated Circuit
IIP	Input-power-referenced Intercept Point
IMD	Intermodulation Distortion
IRED	InfraRed Emitting Diode
LED	Light Emitting Diode
LT-GaAs	Low-Temperature grown Gallium Arsenide
MEMS	MicroElectroMechanical Systems
mmW	Millimetre Wave
MWO	Microwave Office
NIR	Near InfraRed
PCB	Printed Circuit Board
RF	Radio Frequency
SI-GaAs	Semi-Insulating Gallium Arsenide
SRH	Shockley–Read–Hall
TEM	Transverse Electromagnetic
TFA	Trifluoracetic acid
TPA	Two-photo absorption
UV	Ultra-Violet
VCSEL	Vertical-Cavity Surface Emitting Laser
VNA	Vector Network Analyser

CHAPTER 1

1. Introduction

1.1 Introduction

The coexistence of several wireless communication standards, combined with the use of several frequency bands, has become an important challenge in the design of radiofrequency (RF) circuits [1.1]. In response to this problem, there has been a growing interest in the design of tunable RF switches, which allow multi-task reconfiguring from one single compact circuit. Therefore, this chapter will begin with an introduction to RF tuning technologies, a number of which will then be compared as motivation to develop a switch using an optical reconfiguring method. This will be followed by a review of literature related to optically-controlled switches with a focus on state-of-the-art design, while the disadvantages of these switches, which need to be improved, will be also discussed. The subsequent chapters will contain more detailed reviews and comparisons in order to highlight the aspects of potential improvement that correspond with the proposed work in each chapter. A full parametric comparison of commercial and designed RF switches will be listed in a table as a preview. Finally, the primary contributions of this study and outlines of the following chapters will also be discussed.

1.2 RF Switching Technology

Reconfigurability has become a desired and essential feature of modern RF systems for wireless communication and telecommunications due to the unprecedented challenge to accommodate multiple frequency bands and communication standards. Reconfigurable circuitry provides the possibility of incorporating RF devices that can communicate simultaneously in a congested environment. It can also reduce the system size and cost by providing frequency tuning instead of duplicating the same circuits for every desired band. Early RF switching methods from the 1960s were mainly achieved through mechanical and material change. However, there has been a growing demand for more compact, faster tuning methods in today's wireless systems, particularly when frequency bands in microwave region are almost fully occupied and some of the existing reconfigurable technologies have begun to show their limit of performance in wider bandwidths and higher frequencies.

Contemporary commercial and mature reconfiguration techniques are mainly based on varactor diodes, PIN diodes and Radio-Frequency MicroElectroMechanical Systems (RF MEMS) [2-10]. A varactor diode, also called varicap diode, is a diode that exploits the voltage to control the capacitance across the p-n junction in a reverse-bias condition. Since it is operated in a reserve-bias condition, there is only a very small reverse leakage current flowing through the junction and the capacitance is inversely proportional to the square root of the applied voltage. Varactor diodes have generally demonstrated the advantages of low cost and a wide tuning range [1.2, 1.3]. Their main drawback is the existence of a diode junction, which can generate nonlinear behaviour. In addition, the breakdown voltage rate of the p-n junction also limits its ability to handle power [1.4]. This can be improved by incorporating more varactor diodes in stacks, although the system design can be complex. Furthermore, the crosstalk from these introduced additional electric paths will result in intermodulation distortion and hence linearity deterioration.

PIN diodes are similarly p-n-junction-based devices. The advance of this technique has been demonstrated in its ability to handle high-power signals due to the existence of an additional undoped intrinsic semiconductor region with a high-level injection of carriers [1.5, 1.6]. In forward-bias conditions, this high-level injection in the intrinsic region makes PIN diodes

behave like a perfect resistor and significantly helps to accelerate the transport of charge carriers, which makes PIN diodes suitable devices for high-frequency operations. However, the inherently nonlinear behaviour of the diodes remains. In addition, the PIN diode's electrical isolation suffers when no bias voltage is applied in the switch-OFF state, especially at high frequencies [1.7].

MEMS switching is realised through electrical bias and a metal cantilever movement. When a large bias voltage is applied, it exerts an electrostatic force on the cantilever, which forms a mechanical contact between two metals and thus, generates an open or closed circuit. RF MEMS switches have demonstrated excellent isolation values and linear behaviour. However, in addition to their high cost, there are issues related to reliability and high-power performance, particularly with "hot-switching" [1.8, 1.9]. Long relaxation and settling time need to be considered when different switching modes are used. Another shortcoming of this mechanical switching mechanism is the switching speed, which is limited to the order of microseconds [1.10].

One overriding issue with all these approaches is the requirement for DC bias lines as the actuation mechanism for the tuning. This is not a major issue for simple switching/tuning networks at low microwave frequencies, but it will demand extremely complex circuits with many tens and hundreds of elements and produce electromagnetic interference (EMI), thereby deteriorating the quality of the signal during transmission. The requirement of complex DC biased networks can severely limit the system's performance at millimetre wave frequencies and beyond. The method proposed here uses optical tuning, which entirely isolates the microwave and millimetre wave from optical control terminals. Optically-tunable devices remove the need for bias circuits and a very linear performance [1.11] and faster switching speed [1.12] can be expected, since no diode junction or Schottky barrier is required within the structure. One drawback of this optical reconfiguring method is the loss incurred from the optically-induced plasma region. Another aspect to be improved is the additional optical control elements in terms of both power supply and optical arrangement. This optical tuning will be further discussed in the literature review.

1.3 Optically-Controlled Switches

The mechanism of optical reconfiguration is based on the interaction between light and a semiconductor. When an area of the semiconductor is illuminated, it becomes electrically-conductive, provided that the photon energy is greater than the semiconductor band gap, so that pairs of electrons and holes are generated, and a plasma region is formed by the excess carriers [1.13]. The reconfigurability of optical illumination simply depends on the intensity and pattern or shape of the created plasma region. The drawback of this optical tuning approach was previously considered to be insufficient optical power and intensity. However, this problem has been resolved with the recent development of high power, micro-scale optical sources. Micro Vertical-Cavity Surface-Emitting Laser (VCSEL) arrays [1.14] and Pixelated LEDs [1.15] have provided the possibility of high spatial resolution illumination and digital tuning from dynamically-pulsed operations. There are strong motivations to study the development of a miniaturised, low-loss, fast, optically-reconfigurable RF switch. The following text focuses on the reviews of previous investigations related to optically-controlled switches.

The first known photoconductive switch was demonstrated by Auston *et al.* [1.12] in 1975. It was achieved by powerful laser illumination interleaved at $530nm$ and $1060nm$ wavelengths using picosecond excitation to switch circuit ON and OFF respectively. $530nm$ illumination was used to create an electron-hole plasma which substantially increased the conductivity and allowed the propagation of an RF signal, while $1060nm$ illumination was used due to its long wavelength and deep diffusion, which resulted in a conductive path to ground, leading to a short circuit and switching to the OFF state. This novel technique utilised the different properties of optical illuminations at two wavelengths, which opened an era of RF tuning in a novel way. A year later, Lee [1.16] repeated Auston's measurement with a similar setup but changed the substrate to GaAs after finding that, although the photoconductive approach produced remarkably fast switching, the repetition rate was slow due to the slow recombination in silicon. Hence, he employed a GaAs-based substrate in photoconductive high-speed switching. Nevertheless, both experiments demanded significant power from bulky lasers, which seems not to be a practical solution for modern communication systems.

Many studies have been conducted on photoconductive switches since the initial work of Auston and Lee. Lee published another research paper in 1980 [1.17] in which he focused on the investigation of electron-hole plasma physics and created a theoretical model to evaluate permittivity and phase change. This concluded the fundamental control theories and offered the potential to precisely determine phase shifting, switching, and modulating mechanisms. Later, Platte [1.18] and Gevorgian [1.19] provided a further analysis of plasma diffusion and proposed a plan to optimise efficiency, which was based on a semiconductor microstrip gap structure. The analysis was also confirmed by experiments. The microstrip gap structure was chosen based on its simple optical illumination application and direct alteration from an impedance-matched transmission line. Several examples of this gapline structure are discussed below.

A microstrip gapline-based optically-controlled switch, which was originally designed for antenna tuning, was demonstrated in [1.20]. As shown in Figure 1.1, a piece of silicon was placed over a gap in a transmission line and silver epoxy was used to hold it in place. The optical feeding approach was through an optical fibre cable, which illuminated the top of the silicon. The performance of the device was only slightly degraded compared with [1.12] when the excitation signal was delivered through the optical fibre and the operating wavelength of the optical source was at the range of 800 to 1000 nanometres.

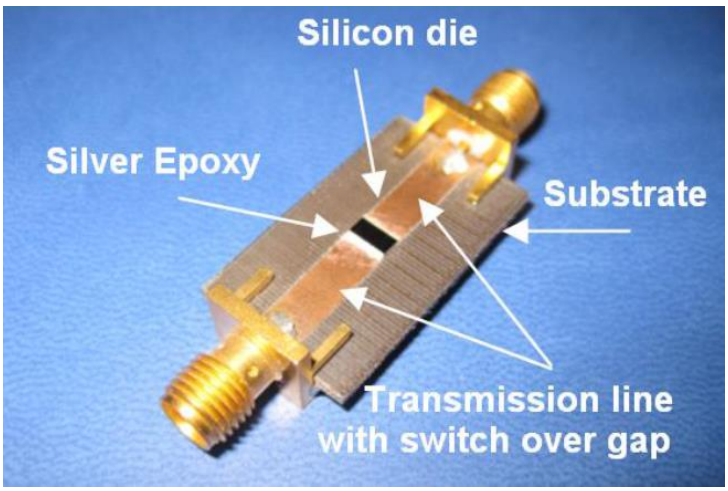

Figure 1.1 Example of an optically-controlled microwave switch with silicon die [1.20] (optical illumination of 200mW at 980nm on n-type silicon)

This switch was applied to create a short path for antenna parts and it demonstrated very good transmission under $3GHz$, which dynamically changed the characteristics of the microwave antenna. However, since the illumination came from the top and the highest conductivity region at the bottom of the silicon was not fully utilised, this device could be further improved in terms of optical power efficiency with a geometric redesign. Another aspect is the tested frequency limit up to $3GHz$, while an optically switch is envisaged to have a broadband tuning range. Another similar example of this optically-controlled switch used for antenna tuning [1.21] is demonstrated in Figure 1.2.

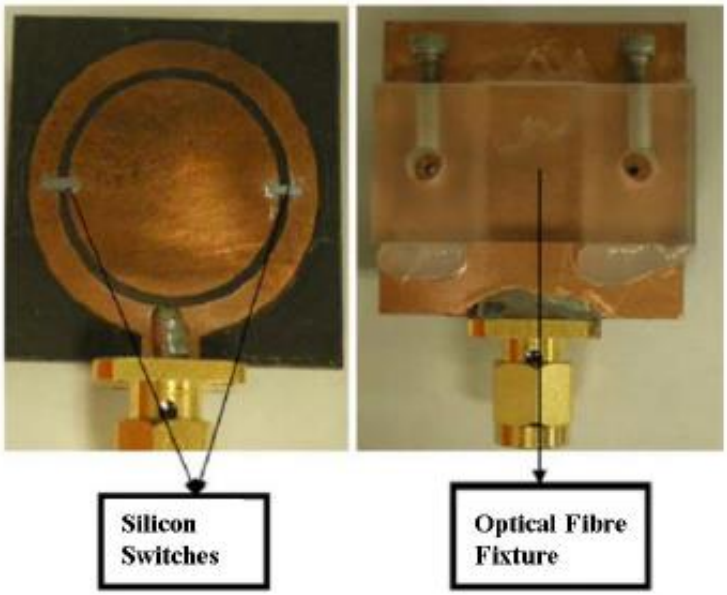

Figure 1.2 Example of a patch antenna based on optically-reconfigurable switch [1.21] (optically-induced plasma silicon switches creating conductive path for resonance)

As can be seen from Figure 1.2, this circular patch antenna uses two silicon switches to create dual resonance. A resonance at around $18GHz$ is dominated by the outer ring when no optical illumination is provided. The silicon switch needs to be illuminated to activate the frequency tunability of this antenna; hence, a radiating mode can be created at lower frequency since the inner disc is now coupled. Therefore, the extent of frequency shift to around $12GHz$ depends on which switch has been illuminated.

The advantage of these optical tuning methods in microwave antennas is flexibility, since the switch can be employed with low illumination power under $200mW$ in contrast with [1.12][1.16]. However, as [1.21] indicated, the insertion loss directly influences the efficiency and gain of the antenna. Material loss has been found in the silicon switch, which reduces the radiation efficiency of the antenna. Hence, the switch performance is considered to be an important factor in antenna design.

It is also interesting to introduce a different photoconductive switch, which is mainly used as an attenuator [1.22]. This attenuator switch is shown in Figure 1.3, is based on a slow-wave structure. This design has improved the signal attenuation more than other optically-controlled attenuators that have been reported. More than $30dB$ attenuation has been achieved by illumination from underneath by an Infra-Red Emitting Diode (IRED). Although this device was fabricated within a coplanar waveguide structure, which normally gives a good performance at high frequency, the slow-wave meandered structure limits the frequency response beyond $7GHz$ so that a sharp increase in insertion loss can be observed. This shows that a trade-off has been found between the conflicting aims of a low insertion loss and a high attenuation range.

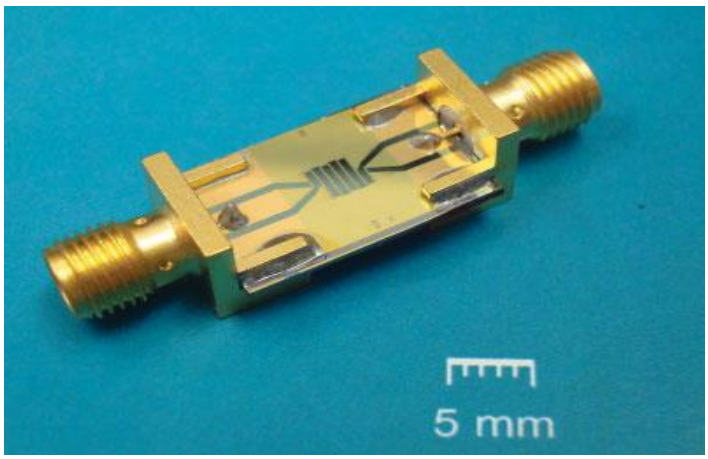

Figure 1.3 Optically-controlled attenuator based on silicon substrate [1.22] (bottom illumination by an Infra-Red Emitting Diode (IRED) at 870nm)

State-of-the-art RF switching devices implemented through various optical tuning approaches and circuit designs have been presented in this review section. Further detailed discussions and comparisons with the proposed designs in this research will be continued in the following section and Chapters 4 and 5 according to their relevance.

1.4 Primary Contributions

The significant contributions in this dissertation can be summarised as follows;

- A novel design of superstrate microstrip gapline with bottom illumination has been proposed and tested, which has effectively reduced the insertion loss [1.23].

- A two-tone nonlinearity characterisation measurement on a photoconductive switch with the highest third-order Input-referenced Intercept Point ($IIP_{3)}$ achieving $+77dBm$ [1.23] has been reported for the first time.

- The RF power-handling ability has been enhanced beyond $40W$ [1.24].

- A Grounded-CPW microwave and millimetre wave switch has been designed and measured with good results showing an insertion loss of less than $3dB$ and isolation over $30dB$ in millimetre wave frequencies [1.25].

A full parametric comparison of commercial and designed RF switches has been listed in a table shown in the Appendix I.

1.5 Chapter Summaries

An overview of the contents of each following chapter is outlined below.

Chapter 2 contains an explanation of the fundamental physics involved in the interaction between optical illumination and semiconductors. This interaction is studied from both a classical physics and quantum perspective. The absorption and attenuation of electromagnetic waves are elaborated in detail. The band transition theory is employed to explain the mechanism of the generation, recombination and diffusion of electron-hole excess carriers. Importantly, the recombination mechanism is introduced, and the significant plasma diffusion of high concentrations electron-hole plasma is analysed. As a result, the total carrier

concentration and photoconductivity are quantified in equations for a subsequent analysis. Along with dielectric permittivity studies, critical electrical properties are eventually obtained through the derived physics equations and this provides a solution for simulation, which is later employed to predict the performance of the circuit. Finally, the comparison and selection of the materials are discussed.

Chapter 3 contains a description of the simulation, measurement and fabrication involved in this research work. The distributed element modelling and full-wave electromagnetic analysis are firstly compared in the simulation part. A further comparison and selection is made within the scope of full-wave modelling methodologies. The Finite-Integration-Technique method evolved from Finite-Difference Time-Domain is clearly superior based on its characteristics of higher computational efficiency and broadband analysis adaptability. A free-space VCSEL laser with solid optics, fibre-coupled laser and LEDs/IREDs are shown in the measurement part, which provide a number of optical tuning choices, depending on the circuit implementation. Other measurement setups, such as fixtures for silicon and connectors with the flexibility for optical and RF engineering to interact with each other are also presented. A standard photolithography procedure is described for circuit fabrication in a clean room in the fabrication part. An alternative circuit fabrication technique of PCB laser-cutting is also shown for different designs to improve integration.

A superstrate-structure microwave gapline switch is presented in Chapter 4 with a standard characterisation test on this novel device. This is followed by optimisation with the aim of achieving a better linearity performance and higher power-handling ability. This chapter begins with a further detailed review of the features of an optically-controlled microwave switch, followed by a list of the possible aspects of improvement targeted in this work. A microstrip gap switch from previous work is then analysed with the aid of CST simulation, which helps to identify the large transmission loss around the plasma region and substrate. A superstrate microstrip gapline switch model is proposed in view of other work on antennae. This circuit is fabricated and measured based on a sensitivity analysis in simulation and the simulated and measured results show good agreement. A two-tone non-linearity test with power-handling ability observation is designed and conducted to present a full characterisation of the designed switch. Since the initial results fail to demonstrate significant improvement from other

microwave switches, these aspects are optimised and several fixtures are redesigned and tested to avoid damaging the device. Finally, a new structure design is proposed and measured with improved non-linearity and power-handling ability.

Chapter 5 is focused on the design of devices at higher frequencies in the millimetre wave region. It begins with a literature review of current millimetre wave switches and a proposal of several aspects for improvement. The chapter is then divided into two parts. The first part contains the design of an optically-controlled Grounded CoPlanar Waveguide (GCPW) switch operating in the millimetre wave region, which is based on a transmission line model. A full-wave analysis with a multi-layer plasma model is employed to find the optimum circuit dimension. The circuit fabrication and use of V connectors for high frequency are also described in detail. A millimetre-wave GCPW switch illuminated by a single IRED is presented in the second part. This device is designed to better integrate on-board circuits and a compact optical source. Insertion loss and surface modes are found to have been reduced compared with the device proposed in the first part.

Chapter 6 is concentrated on two superstrate materials, silicon and GaAs, for switching implementation on the superstrate microwave gapline switch developed in Chapter 4. An arbitrary programmable signal generation system with laser modification is specifically designed for pulsed operations. The excess carrier recombination time in silicon is measured and found to be less than ideal for fast switching. Hence, the study of GaAs with a shorter carrier lifetime is performed. Due to the insufficient photon energy provided from the laser configured in the system designed for silicon, LED/IREDs with more choices of wavelengths are selected as new candidates. However, the power requirement is also found to be significant in the subsequent investigation. The laboratory measurement with DC bias assistance toward photoconductive GaAs later proves the theoretical assumption that large intensity is needed for a semi-insulating GaAs (SI-GaAs).

1.6 References

[1.1] R. Berezdivin, R. Breinig, and R. Topp, "Next-Generation Wireless Communications Concepts and Technologies," IEEE Commun. Mag., vol. 40, no. 3, pp. 108-116, Mar. 2002.

[1.2] C. Huang, K. Buisman, L.K. Nanver, L.C. De Vreede, "The state-ofthe-art of RF capacitive tunable components", 10th IEEE International Conference on Solid-State and Integrated Circuit Technology, Nov. 2010

[1.3] P. Monajemi, F. Ayazi, "A high-g low-voltage HARPSS tunable capacitor", Microwave Symposium Digest, IEEE MTT-S International, 2005

[1.4] R. L. Haupt, M. Lanagan, "Reconfigurable antennas", *IEEE Antennas Propagat. Mag.*, 2013, **55**, (1), pp. 49–61

[1.5] W. E. Doherty Jr, R. Joos, "The PIN Diode Circuit Designers Handbook", Microsemi Corporation, 1998

[1.6] C.G. Christodoulou, T. Youssef, A.L. T. Steven, *et al.* "Reconfigurable antennas for wireless and space applications", *Proc. IEEE*, vol. 100, no. 7, pp. 2250-2261, 2012

[1.7] C. Rauscher, "Reconfigurable bandpass filter with a three-to-one switchable passband width", *IEEE Trans. Microw. Theory Tech.*, vol. 51, no. 2, pp. 573-577, 2003

[1.8] C. D. Patel, G. M. Rebeiz, "A high-reliability high-linearity high-power RF MEMS metal-contact switch for DC–40-GHz applications", IEEE Trans. Microw. Theory Tech, vol. 60, no. 10, pp. 3096-3112, 2012

[1.9] L. L. W. Chow, J. L. Volakis, K. Saitou, *et. al*, "Lifetime Extension of RF MEMS Direct Contact Switches in Hot Switching Operations by Ball Grid Array Dimple Design", IEEE Electron. Device Lett., vol. 28, no. 6, pp. 479-481, 2007

[1.10] Z. J. Yao, S. Chen, S. Eshelman, D. Denniston, C. Goldsmith, "Micromachined low-loss microwave switches", Microelectromechanical Systems, Journal of, vol. 8, no. 2, pp. 129-134, 1999

[1.11] T. Kaneko, T. Takenaka, T. S. Low, *et al.*, "Microwave switch: LAMPS (light activated microwave photoconductive switch)", IEEE Electronics Letters, vol. 39, no. 12, pp. 917-919, 2003

[1.12] D. H. Auston, K. P. Cheung, P. R. Smith, "Picosecond photoconducting Hertzian dipoles", Applied physics letters, vol. 45, no. 3, pp.284-286,1984

[1.13] C. D. Gamlath, D. M. Benton, M. J. Cryan, "Microwave Properties of an Inhomogeneous Optically Illuminated Plasma in a Microstrip Gap", IEEE Trans. Microw. Theory Tech., vol. 63, no. 2, pp. 374-383, 2015

[1.14] M. Grabherr, M. Miller, R. Jäger, R. Michalzik, U. Martin, H. J. Unold, K. J. Ebeling, "High-power VCSELs: single devices and densely packed 2-D-arrays", Selected Topics in Quantum Electronics, IEEE, vol. 5, no. 3, pp. 495-502, 1999

[1.15] A. E. Kelly, J. J. D. McKendry, S. Zhang, D. Massoubre, B. R. Rae, R. P. Green, M. D. Dawson, "High-speed GaN micro-LED arrays for data communications", Transparent Optical Networks (ICTON), IEEE, 14th International Conference, pp. 1-5, Jul. 2012

[1.16] C. H. Lee, "Picosecond optoelectronic switching in GaAs", Applied Physics Letters, vol. 30, no. 2, pp.84-86, 1977

[1.17] C. H. Lee, P. Mak, A. DeFonzo, "Optical control of millimeter-wave propagation in dielectric waveguides", IEEE Journal of Quantum Electronics, vol. 16, no.3, pp. 277-288, 1980

[1.18] W. Platte, B. E. Sauerer, "Optically CW-induced losses in semiconductor coplanar waveguides", IEEE Transactions on microwave theory and techniques, vol. 37, no. 1, pp.139-149, 1989

[1.19] S. S. Gevorgian, "Design considerations for an optically excited semiconductor microstrip gap at microwave frequencies", IEE Proceedings J-Optoelectronics, vol. 139, no. 2, pp.153-157, 1992

[1.20] C. J. Panagamuwa, A. Chauraya, J. C. Vardaxoglou, "Frequency and beam reconfigurable antenna using photoconducting switches", IEEE Trans. Antennas Propagat., vol. 54, no.2, pp. 449-454, 2006

[1.21] Y. Tawk, A. R. Albrecht, S. Hemmady, G. Balakrishnan, C. G. Christodoulou, "Optically pumped frequency reconfigurable antenna design", IEEE antennas and wireless propagation letters, vol. 9, pp. 280-283, 2010

[1.22] J. R. Flemish,, H. W. Kwan, R. L. Haupt, M. Lanagan, "A new silicon-based photoconductive microwave switch", Microwave and Optical Technology Letters, vol. 51, no. 1, pp. 248-52, 2009

[1.23] A.W. Pang, S. Bensmida, C. D. Gamlath, M. J. Cryan, "Non-linear characteristics of an optically reconfigurable microwave switch", IET Microwaves, Antennas & Propagation, vol. 12, no. 7, pp. 1060-1063, 2018

[1.24] A. W. Pang, S. Bensmida, M. J. Cryan, "Nonlinearity and Power Handling Characterization of an Optically Reconfigurable Microwave Switch", IEEE/MTT-S International Microwave Symposium-IMS, pp. 420-422, 2018

[1.25] A. W. Pang, C. D. Gamlath, M. J. Cryan, "An Optically Controlled Coplanar Waveguide Millimeter-Wave Switch", IEEE Microwave and Wireless Components Letters, vol. 28, no.8, pp. 669-71, 2018

CHAPTER 2

2. Semiconductor Physics and Photoconductance

2.1 Introduction

This chapter contains an introduction to semiconductor physics with a focus on electron-hole pair generation by means of optical illumination on semiconductors, which forms the photoconductance involved in the research of optically-reconfigurable microwave and millimetre wave switches. The diffusion of the excess carriers or the plasma within the silicon will be discussed in detail, since this can have a significant influence on microwave and millimetre wave electromagnetic propagation. The corresponding theory is used to provide a solution for electromagnetic simulation in terms of photoconductivity within the semiconductor. This simulation then provides good accuracy for the subsequent circuit design and comparison with measurements.

2.2 Semiconductor Physics

Compared to amorphous and polycrystalline solids, single-crystal materials have a high degree of ordered regions of regular atomic or molecular geometric distribution over the entire material. On the other hand, amorphous material only has order within a very limited area and polycrystalline material has various irregular single-crystal regions throughout the material. Single-crystal regions are called grains and grain boundaries usually cause the electrical characteristics to deteriorate. Single-crystal materials with fewer boundaries and uniform geometric periodicity have much more superior electrical properties. [2.1]

Since semiconductors are generically single-crystal materials with conductivity between that of metals and insulators, they are extremely widely used. There are two main semiconductor groups, one of which consists of materials from group IV of the periodic table, while the other is composed of a combination of compound semiconductor materials from groups III and V. Silicon and germanium are the fundamental materials which are composed of single atoms in group IV. Silicon is currently the most typical and widely-used material in the semiconductor industry [2.2] and this will be discussed in detail in the following text. Gallium Arsenide, a binary compound of groups III and V, will also be emphasised due to its superior optical properties, which can especially be observed in high speed applications.

As discussed, the aim of this research is to explore the interaction between semiconductors and light which can be considered to be a propagating wave of electromagnetic radiation and due to wave-particle duality, also as particles, known as photons at a range of frequencies. It is necessary to use both of these definitions of light in the subsequent discussion, especially in calculating the external and internal quantum efficiency, which is essential for the quantitative analysis and modelling in later parts of the study.

2.2.1 Reflection

Reflection, absorption and transmission can occur when light falls on a dielectric boundary. Reflection will firstly be discussed from the perspective of light as an electromagnetic wave in this section, and the absorption and transmission based on the interaction between light and a

semiconductor from both a "wave" and "particle" perspective will be emphasised in the next section.

Maxwell was the first to propose the electromagnetic phenomenon of light in the 1860s and the following set of equations are named after him [2.3];

$$\nabla \times \boldsymbol{E} = -\frac{\partial \boldsymbol{B}}{\partial t} \qquad \nabla \cdot \boldsymbol{D} = \rho$$
$$\nabla \cdot \boldsymbol{B} = 0 \qquad \nabla \times \boldsymbol{H} = \boldsymbol{J} + \frac{\partial \boldsymbol{D}}{\partial t} \tag{2.1}$$

where $\nabla \cdot$ denotes the divergence operator, the $\nabla \times$ symbol denotes the curl operator, $\boldsymbol{E}$ is the electric field, $\boldsymbol{B}$ is the magnetic field, $\boldsymbol{D}$ is the displacement field, $\boldsymbol{\rho}$ is the electric charge density, $\boldsymbol{J}$ is the electric current density, and $\boldsymbol{H}$ is the magnetising field.

D and **B** are related as follows;

$$\boldsymbol{D} = \varepsilon \boldsymbol{E} \qquad \boldsymbol{B} = \mu \boldsymbol{H} \tag{2.2}$$

where ε denotes the electrical permittivity and μ is the electrical permeability.

In homogeneous isotropic media,

$$\boldsymbol{J} = \sigma \boldsymbol{E} \tag{2.3}$$

where σ is the conductivity.

Using mathematical identity,

$$\nabla \times \nabla \times A = \nabla(\nabla A) - \nabla^2 A \qquad 2.4$$

to combine,

$$\nabla \times \boldsymbol{E} = -\frac{\partial \boldsymbol{B}}{\partial t} \qquad \nabla \times \boldsymbol{H} = \boldsymbol{J} + \frac{\partial \boldsymbol{D}}{\partial t} \qquad 2.5$$

in a lossy semiconductor medium, it yields,

$$\nabla^2 \boldsymbol{E} - \sigma\mu\frac{\partial \boldsymbol{E}}{\partial t} - \mu\varepsilon\frac{\partial^2 \boldsymbol{E}}{\partial t^2} = 0 \qquad 2.6$$

One possible solution to this differential equation could be,

$$\boldsymbol{E_x} = \boldsymbol{E_0} exp\,[j\omega\left(t - \frac{\gamma z}{c}\right)] \qquad 2.7$$

where the electromagnetic wave is polarised in *x*, provided that,

$$\gamma^2 = c^2\varepsilon_0\mu_0(\varepsilon_r - \frac{\sigma}{\omega\varepsilon_0}j) \qquad 2.8$$

where γ is the propagation constant travelling in *z*-direction, ω is the angular frequency, c is the speed of light, ε_0 is the permittivity in free space, and μ_0 is the permeability in free space, and ε_r is the relative permittivity.

If γ is written in terms of n, the refractive index of the medium, and k, the absorption index,

$$\gamma = n - jk \tag{2.9}$$

The possible solution becomes,

$$\boldsymbol{E_x} = \boldsymbol{E_0} exp(-\omega kz/c) exp[j\omega(t - nz/c)] \tag{2.10}$$

which represents a wave of frequency $\omega/2\pi$, travelling with a velocity of c/n and the rate of attenuation or absorption is determined by the absorption index, k.

As shown above, the absorption and reflection phenomena are closely related. Reflectivity describes the ratio of the radiation flux reflected by a different medium surface to the incident radiation flux. Further to 2.9, reflectivity, $\mathcal{R}$, can be written as [2.4],

$$\mathcal{R} = \left|\frac{n - jk - 1}{n - jk + 1}\right|^2 = \frac{(n-1)^2 + k^2}{(n+1)^2 + k^2} \tag{2.11}$$

where, moreover, the real part n indicates the phase velocity and k denotes the deterioration of the electromagnetic wave propagation. Reflectivity is as low as other dielectric materials with a low absorption when k is small, but when k becomes large, the material behaves like a metal

and the reflectivity will approach unity. [2.4] The absorption characteristic will be analysed further in the next subsections.

2.2.2 Absorption

Optical absorption will firstly be discussed in "wave" terms in this section and then quantum physics will be used to explain the interaction between light and semiconductors from a "particle" perspective.

Further to the previous subsection, the absorption index, k, in the complex refractive index form, could be used to describe the absorption coefficient, α. The relationship is written as follows;

$$\alpha = \frac{2\omega k}{c} = \frac{4\pi k}{\lambda} \qquad 2.12$$

where λ is the wavelength and the absorption coefficient, α, for the medium is defined by the condition that the power in the wave falls to $1/e$ at a distance of $1/\alpha$, where e is the exponential constant. This distance is known as the absorption depth. [2.3]

Before providing further details of the effect of absorbed energy on semiconductors, some fundamental quantum mechanics need to be explained. In 1900, Planck proposed that discrete bundles of energy could be emitted from a heated body through thermal radiation [2.5]. Not long after, the reverse effect was demonstrated in a photoelectric experiment and, in 1905, Einstein suggested that the light radiation absorbed by a medium is also of a discrete nature [2.6]. These packets of energy are called *quanta* and the minimum amount of this discrete energy is a *quantum*, known as a *photon* for light. The energy of a quanta or the photon energy in case of light is as follows;

$$E = hf \qquad 2.13$$

where h is Planck's constant, $6.625 \times 10^{-34}\ J.s$, and f is the frequency of the radiation. Later, in 1924, de Broglie postulated that electromagnetic waves show particle-like behaviour and particles should also be expected to behave as waves. This hypothesis was subsequently proved by tests on electrons and it became the *wave-particle duality* principle, by which the wavelength of matter can be determined from its momentum. This principle can be applied to small particles, like electrons, neutrons, and protons, while the equations can be reduced to those of classical mechanics for very large ones. It was this approach that enabled the switch to the wave perspective to study the motion of electrons in semiconductor crystals. In 1929, Schrodinger combined the *Heisenberg Uncertainty Principle* with the *wave equation* and statistically described the behaviour of the electron, especially predicting its absolute position at a particular time. Although this can doubtlessly be considered to have been an improvement on the classical mechanics theory, it was mainly based on statistical probability. [2.1]

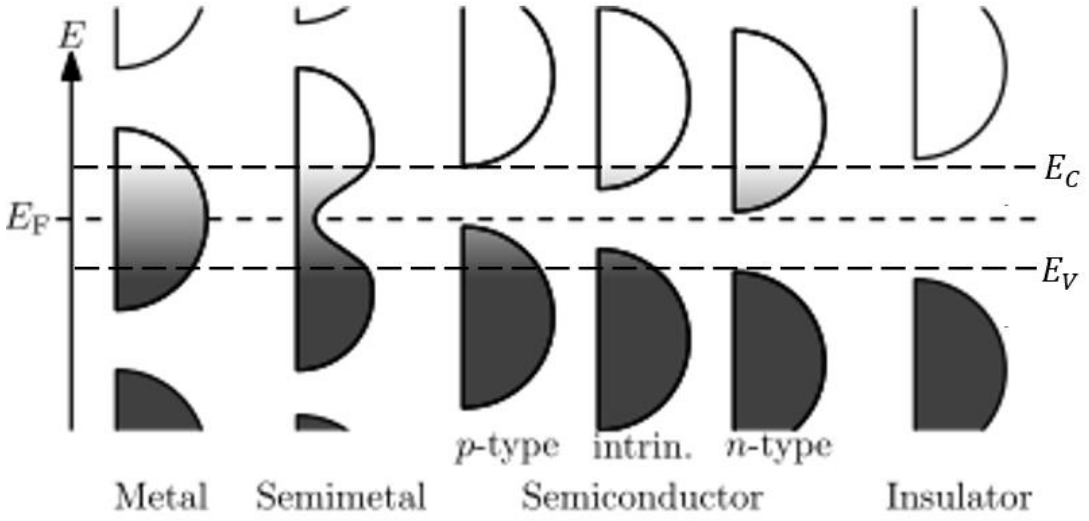

Figure 2.1 Various types of materials at different energy states with bands shifted [2.7]

A possible sample solution to the 1-dimensional (1D) Schrodinger equation with electrons' behaviour shown in a thermal equilibrium condition can be seen in Figure 2.1 [2.7]. The magnitude in the horizontal direction indicates the density of possible states where electrons

can reside at a certain energy, which is indicated in the vertical direction. The shaded areas for the listed materials follow the *Fermi-Dirac* energy distribution whereby the darker the colour is, the more electrons or the higher the probability of electrons are at those energy states. Therefore, solids can also be categorised as metal, semiconductor or insulator from the distribution of electron energy demonstrated in the band structure. Furthermore, an understanding of band theory is required for electrical conduction in solids. At a temperature of zero degree Kelvin ($T = 0K$), a single-crystal semiconductor behaves like an insulator. For example, in the case of silicon, its atoms are held in a regular tetrahedral structure by covalent bonds, as shown in Figure 2.2. Each silicon atom and its four neighbours share four electrons so that each bond can be regarded as having two electrons. This means that all electrons are held firmly by covalent bonds. No free electrons can be used to conduct electricity and the crystal acts as an insulator at this low temperature.

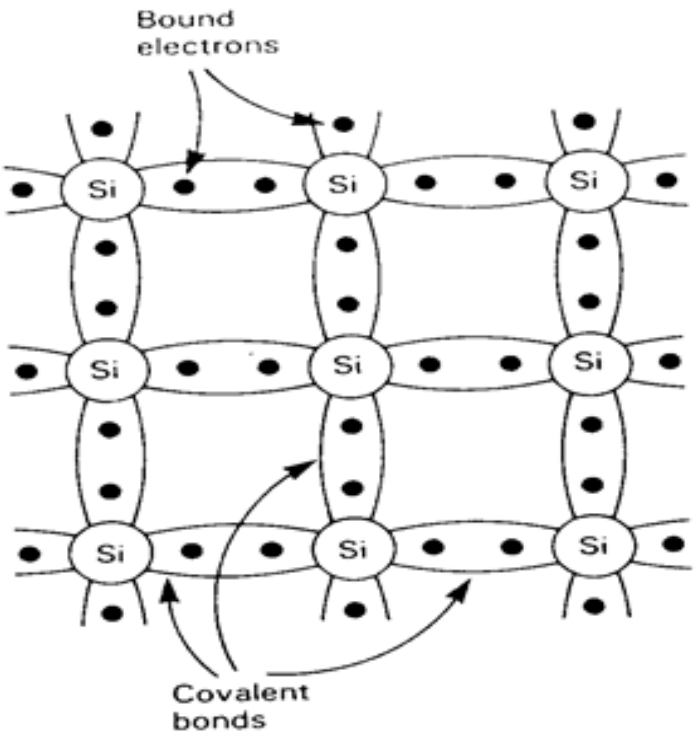

Figure 2.2 Covalent bonding in a single-crystal silicon lattice [2.8]

Based on the band theory, these covalent-bonded electrons will fully occupy the valence band, E_V, at their lowest energy state, while the upper band, the conduction band, E_C, will be empty at $T = 0K$. In this condition, semiconductors act like insulators with electron distributions in

Figure 2.1. As the temperature gradually increases, both the atoms and the electrons will absorb it due to energy being distributed in a random manner. When some energetic electrons have obtained sufficient thermal energy, they can escape the bonding forces, thereby breaking the covalent bonds. As shown in Figure 2.3, electrons at low energy states in the valence band may jump into the conduction band and be free to conduct electricity. These electrons cannot exist in any other energy region or state. This forbidden energy band is found where no electrons can exist between the conduction band and the valence band. In other words, this forbidden bandgap energy, E_g, shown in Figure 2.3, is the minimum energy an electron in the valence band must acquire to jump into the conduction band and be free to conduct electricity.

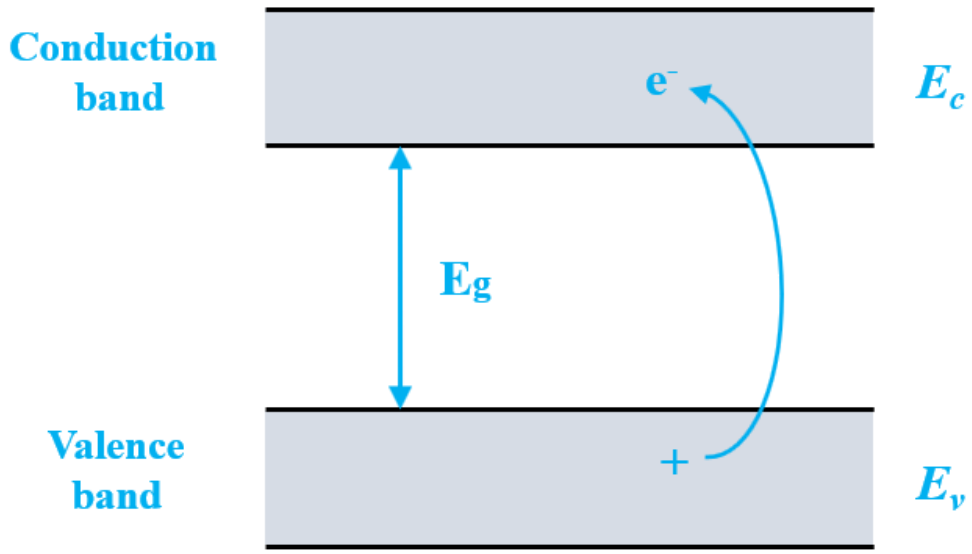

Figure 2.3 Representation of the energy bands and band gap in band diagram

There are several different conditions of energy bands associated with the classification of solids shown in Figure 2.1. For semiconductors, as explained above, electrons in the valence band need to obtain sufficient energy to be excited into the conduction band and the *Fermi level*, E_F, is inside the band gap in Figure 2.1. The *Fermi level* defines the energy level below which electrons can only exist but cannot acquire sufficient energy to rise above at absolute zero. These doped semiconductors, either p-type or n-type, will change the position of the Fermi level. Doping could further vary the band gap and the resistance, as will be discussed in later sections. When considering the semi-metals and metals shown in Figure 2.1, both the high

probability of electrons (indicated by the dark colour) and the large density distribution of energy states (indicated by the magnitude in the horizontal direction) indicate that the conduction band can be filled with a large number of electrons that can move freely to conduct electricity. Another possible energy band diagram for metals could be that E_F lies within at least one band, which indicates the existence of a superposition region between the valence band and the conduction band. In this case, many electrons can be excited into higher states as they become more active and this will result in a rise in conductivity, but they do not need to acquire relatively large bandgap energy for a band transition. As for insulators, as indicated by the black semi-circular shade below the conduction band in Figure 2.1, most available energy states and electrons are highly likely to be distributed under the region of the conduction band. The valence band could be completely filled with electrons, while the conduction band remains empty. There will be hardly any charged particles that can contribute to conduct electricity, even if an electric field is applied and observed at room temperature, due to the very high bandgap energy.

There are also two types of band gaps associated with semiconductors, namely direct and indirect. A semiconductor is characterised as having a direct band gap if the electrons and holes in both the conduction band and the valence band are in the same momentum, which is represented by a k-vector. Direct band semiconductors, such as Gallium Arsenide (GaAs), Indium Phosphide (InP), etc., can be directly triggered by a photon for the transition of energy bands. However, as the name indicates, indirect band semiconductors, such as Silicon (Si), Germanium (Ge), etc., cannot directly absorb a photon's energy to elevate the band due to the fact that an electron's momentum is several orders of magnitude larger than that of a photon in a crystal. As clearly shown in Figure 2.4, the lowest energy level of the conduction band is not aligned with the highest level of the valence band at the same k-vector. By momentum conservation, the band transition of an electron in an indirect band semiconductor requires a phonon to compensate for the momentum difference where the phonon is the quanta of an elementary thermal vibration motion in lattice. This will be discussed further in later sections regarding quantum efficiency and other mechanisms.

When the energy mentioned above that excites electrons to jump into the conduction band is provided by a photon, it is possible for several light-semiconductor interaction mechanisms to

occur. For example, heat can be converted and defects can be introduced to impure atoms from photon energy and its interaction. However, the acquisition of sufficient electron energy for band elevation when photons collide with valence bands is of the greatest interest to this study.

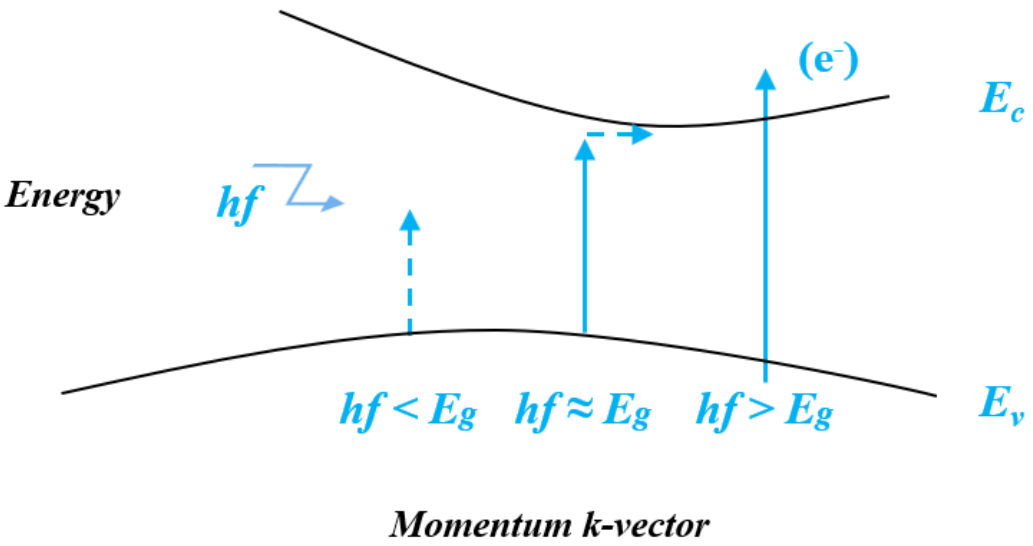

Figure 2.4 Phonon assisted transition for indirect bandgap material

When light falls on a semiconductor surface, the photons can be absorbed or transmitted through it in addition to a reflection. The extent of the absorption and transmission largely depends on the band gap energy, E_g, and the photon energy, $E = hf$ in 2.13. If $E = hf < E_g$, the light will be reflected and transmitted through the material without the absorption of many photons. When $hf > E_g$, there is a greater chance of photons interacting with electrons in the valence band and providing them with sufficient energy to be elevated to the conduction band. As seen from Figure 2.5, these active electrons in the conduction band first escape from the covalent bonds and then become free to move, leaving gaps to be filled with neighbouring or other electrons. These gaps are called holes and electrons and holes can both conduct electricity, but separately and independently. Hence, another explanation for the conduction band could be the energy domain within which electric currents can flow where the conduction band is for free electrons and the valence band is for the holes.

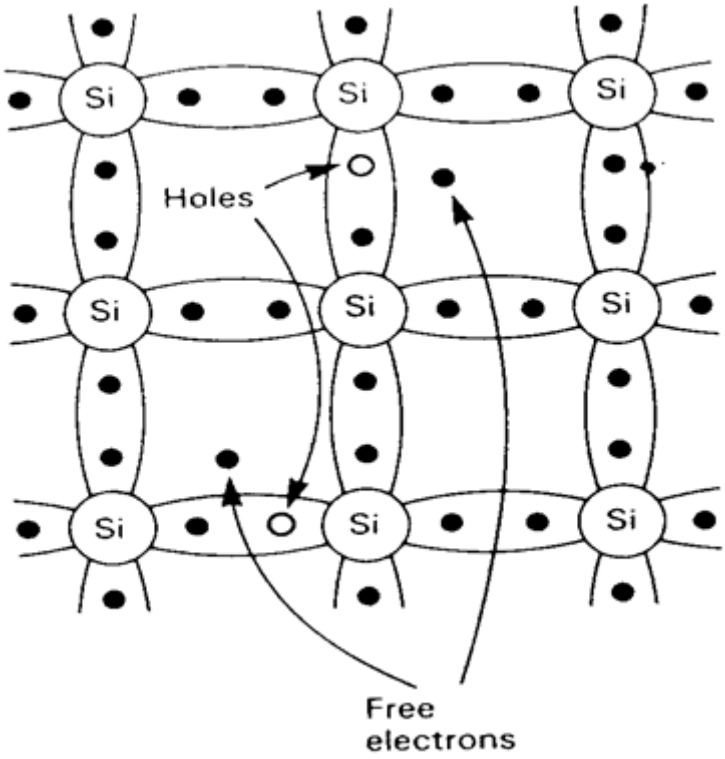

Figure 2.5 Schematic diagram of electron-hole pair generation [2.8]

The process by which an electron escapes from a covalent bond and leaves a hole behind is generally known as electron-hole pair generation. The carriers created from this process are called excess carriers, the density of which is denoted by n_{ex}, in the unit of the number of carriers per unit volume generated.

Having discussed the basic interaction mechanism between light and semiconductors from different perspectives, it will now be further explained with a quantitative analysis to obtain a good modelling method for simulation purposes and a comparative measurement.

2.2.3 Quantum Efficiency and Optimum Wavelength

The general term of quantum efficiency used in the fundamental modelling equations in this project will be discussed in this section, along with other associated parameters that need to be considered to determine the optimum wavelength of optical illumination for silicon. This optimum point occurs when the highest overall quantum efficiency has been achieved while maintaining a high level of photoconductivity. The direct answer of the optimum wavelength

cannot be derived from a quantitative calculation, but the range of choices may be narrowed down. This is because it largely depends on various materials and samples, which suggests that all the data used for the analysis should be based on experimental results.

The general quantum efficiency in this study may be defined as the ratio of the number of excess carriers generated by optical absorption to the number of photons of optical energy that fall on a silicon surface. If the photons are entirely absorbed and all photon energy is used to create excess carriers, a quantum efficiency of one can be achieved at that particular wavelength. This general quantum efficiency is a combination of the concepts of external and internal quantum efficiency. The external quantum efficiency here refers to the optical losses due to reflection and transmission, while the internal quantum efficiency is based on absorbed photons. The conversion of these photons to electron-hole pair plasma depends on other factors, such as electron-hole recombination and the diffusion of carriers within the silicon, which will be discussed in the following sections.

External quantum efficiency is mainly quoted in the literature, since it does not consider electron-hole pair generation and hence, depends less on sample variations. Besides, a standard measurement of the reflectivity and transmission ability of silicon can be used to easily determine the amount of absorbed energy. Before plotting a reflectivity graph in a range of wavelengths, it is necessary to check the cut-off boundary beyond which the photon energy is insufficient to excite electrons to elevate energy bands. Since the bandgap of silicon also depends on the temperature [2.4], it tends to decrease as the temperature increases. Hence,

$$E_g(T) = E_g(0) - \frac{AT^2}{T + B} \qquad 2.14$$

where $E_g(0)$, A and B are material constants, namely 1.166eV, 0.473meV/K and 636K respectively for silicon obtained from [2.4]. Under thermal equilibrium conditions at 300K,

$$E_G = 1.166 - 0.473E \times 10^{-3} \times \frac{300^2}{300 + 636} = 1.121eV \qquad 2.15$$

Therefore, substituting the E_G in 2.13, the cut-off wavelength is calculated as follows;

$$\lambda = \frac{hc}{E_G} = \frac{6.63 \times 10^{-34} \times 3 \times 10^8}{1.121 \times 1.6 \times 10^{-19}} = 1110nm \qquad 2.16$$

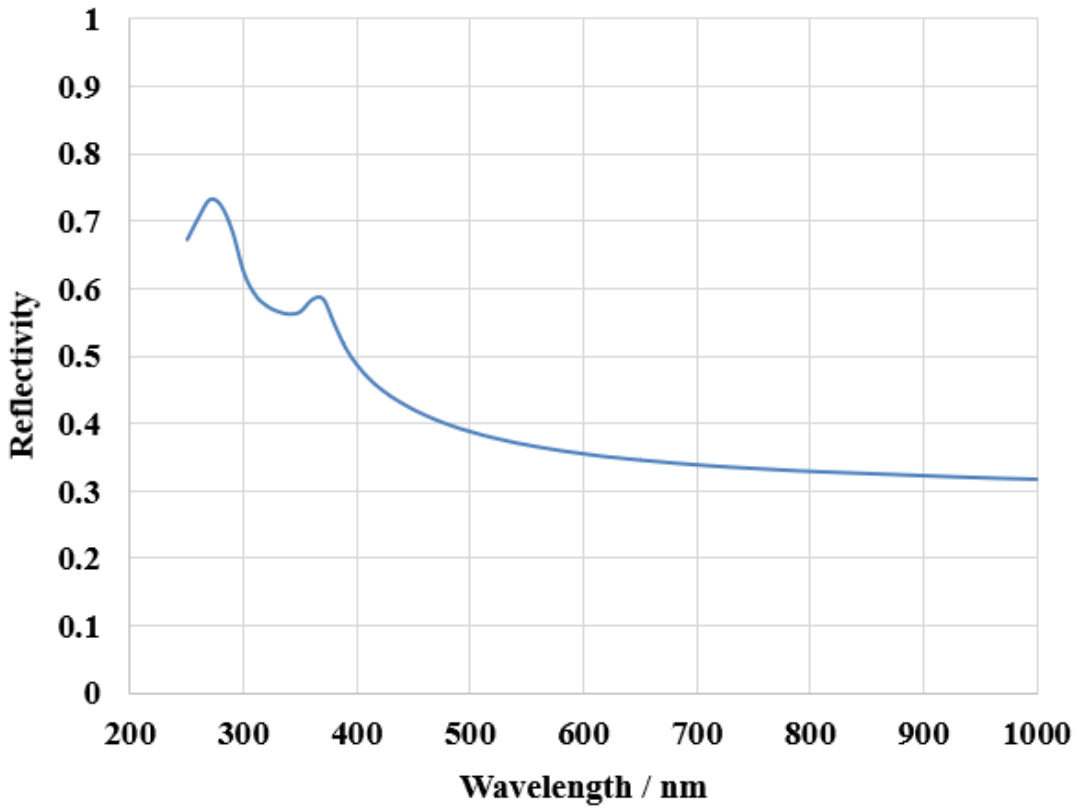

Figure 2.6 Reflectivity vs. Wavelength for intrinsic silicon (n_0=1.45×10^{10}cm^{-3}) [2.9]

Figure 2.6 contains a graph of reflectivity against wavelength for a polished silicon wafer at 300K, which is calculated by 2.11 and data from [2.9]. It depicts a declining trend of reflectivity from ~0.75 at a wavelength of around 250nm to ~0.31 at 1000nm. Hence, in terms of reflectivity, a range of wavelengths greater than 800nm can be good candidates for optical illumination.

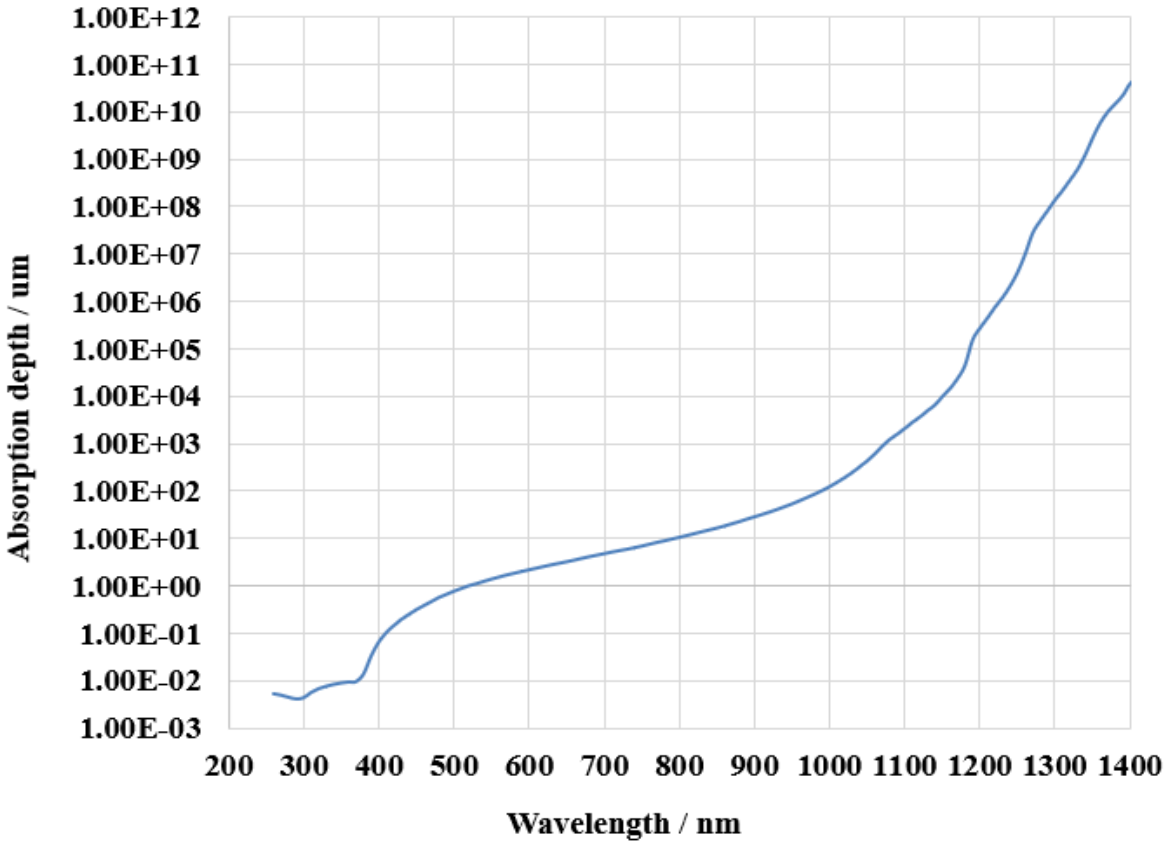

Figure 2.7 Absorption depth vs. Wavelength for intrinsic silicon (n_0=1.45×$10^{10}$$cm^{-3}$) [2.9]

In terms of internal quantum efficiency, several parameters need to be considered. When all unreflected photons enter the silicon, they are absorbed during their propagation through the medium. The absorption coefficient, α, introduced in the last section, can be used here to describe the relative number of photons absorbed per unit distance, in units of μm^{-1}. The absorption depth against wavelengths of light for silicon is shown in Figure 2.7. The absorption depth is the reciprocal of the absorption coefficient which describes the length at which the absorbed energy significantly drops to its $1/e$. As can be seen in Figure 2.7, photons from the 200nm to 500nm wavelength range show the strongest absorption compared to the absorption depth of between $10\mu m\ to\ 100\mu m$ in the wavelength range of $800nm\ to\ 1\mu m$, since more than 36.8% of power is absorbed within 100nm beneath the silicon surface. However, since this is a very small thickness that can be seen to be close to the surface, another mechanism needs to be considered, which is the velocity of the surface recombination. The surface recombination is caused by the severe disruption of the single-crystal lattice where there are defects and impurities and a gradient of carrier concentrations exists around the surface area.

This recombination is generally accelerated when the carrier concentrations between any two regions becomes large. For most semiconductors, the maximum velocity can be up to $1 \times 10^7 cm/s$. As a result, despite the high absorption of photons within a small depth, little contribution can be made to the generation of electron-hole pairs due to the high velocity of the surface recombination. Hence, the photoconductance cannot be increased very much and the internal quantum efficiency can be low [2.10]. This has also been proven using other measurements [2.11-2.13]. Figure 2.8 contains a simulation graph of photonconductance against depth for various surface recombination velocities. This simulation also includes the diffusion effect for accuracy, which will be explained in detail in the following sections. As shown, the surface recombination becomes less significant when the depth is larger than $20\mu m$.

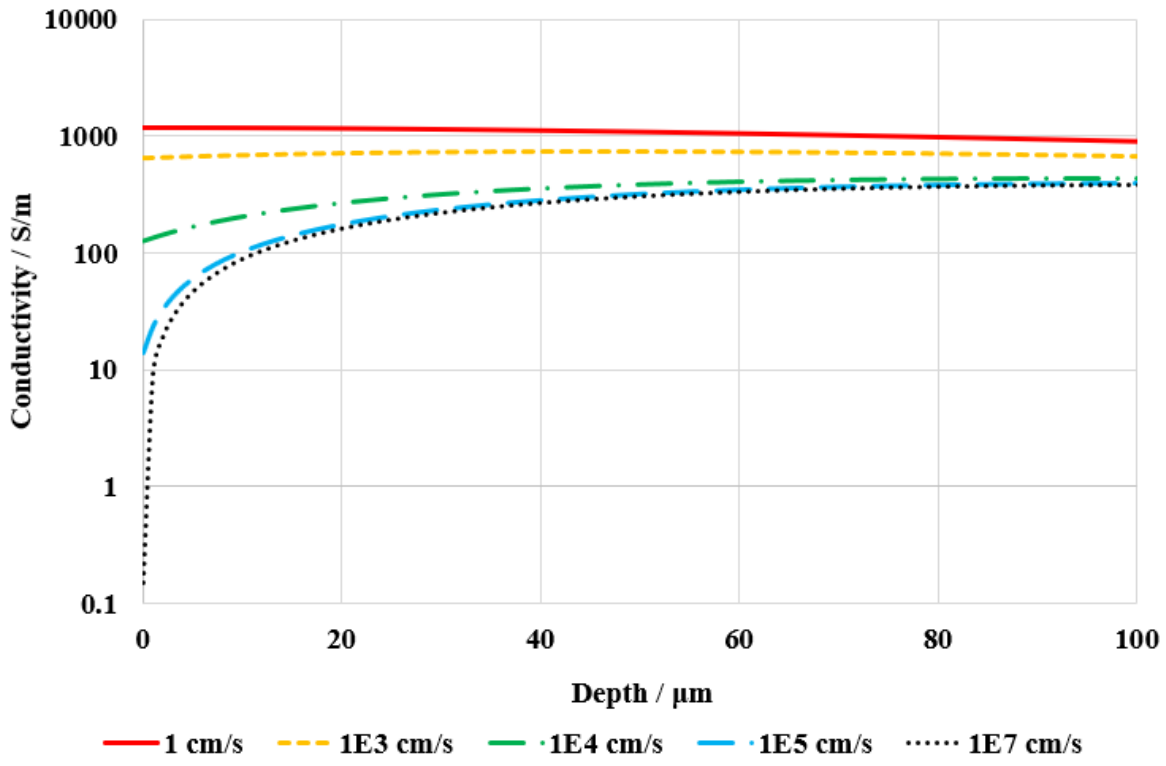

Figure 2.8 Conductivity vs. Depth below the surface of intrinsic silicon for various surface recombination velocities

It can be concluded that illumination in a wavelength range of $800nm\ to\ 1\mu m$ is the optimum because of its superior external quantum efficiency based on low reflectance and the maintenance of a good absorption, which contributes to internal quantum efficiency. Last, but not least, as mentioned earlier, phonons are critical in providing the momentum for energy

states and band transitions in indirect band semiconductors, where part of the energy for the light in this wavelength range can be easily and directly emitted as phonons to thermally promote the activity. The results of the study of [2.14, 2.15] also prove the effectiveness of this wavelength range and demonstrate that a light-semiconductor interaction at 980nm could be the most efficient for an optically-controlled microwave switch. It could be further said that, when choosing a wavelength range with an absorption depth of $10\mu m\ to\ 100\mu m$, the wafer thickness or substrate thickness selected should be a few times larger than the absorption depth. A silicon thickness of $500\mu m$ is used in this research as the standard value. Therefore, a higher utilisation of the interaction within the material or a larger number of electron-hole pairs are expected to be generated from the larger absorption space, but little will be wasted from the transmission.

2.3 Photoconductivity

The focus of this section will be the mechanisms that take place under the medium interface and the process that follows the optical absorption, which was explained above. These mainly involve excess carrier generation, recombination, and diffusion. Lastly, the characterisation results of semiconductor photoconductivity modelling will be formed, which are crucial to this research, especially for comparing simulations and measurements in later chapters.

2.3.1 Excess Carrier Generation

According to the above description, a flux of photons with sufficient photon energy that falls on a silicon surface will be absorbed and the excess carriers created will contribute to the generation of electron-hole pairs. The intensity of the photon flux can be expressed as I_z in units of W/cm^2 and the absorption coefficient, α, describes how intensity is absorbed and attenuated per unit distance in units of cm^{-1}, while z shows the distance beneath the surface. Based on the *Beer-Lambert law*, mainly derived from 2.10, the intensity of the light at a certain depth at which the direction is normal to the surface and pointing inwards to the silicon can be written as follows;

$$I_z = I_0 e^{-\alpha z} \tag{2.17}$$

where I_0 is the initial condition of the light intensity on the surface. The light intensity drops exponentially as it deepens, as can be seen from Equation 2.17. The significant attenuation of the photon flux can occur at very short distance if the absorption coefficient is large. Since I_z is in units of W/cm^2, αI_z would be the rate of absorbed photon energy per unit volume. The excess carrier generation rate can be determined if quantum efficiency is combined with this equation. As explained in the last section, the general quantum efficiency, η, consists of internal quantum efficiency and external quantum efficiency, mainly due to the reflection. Therefore, the electron-hole pair generation rate, G, will be the total energy available divided by single photon energy at an efficiency of η.

$$G = \frac{\eta \lambda q \alpha I_0 e^{-\alpha z}}{hc} \tag{2.18}$$

where h is Planck's constant, $6.625 \times 10^{-34}\ J.s$, c is the speed of light, $3 \times 10^8\ m/s$, λ is the wavelength of light.

2.3.2 Carrier Recombination

Electron-hole pair generation takes place as a result of external force, such as interaction with photons or the thermal vibration of the crystal lattice itself. Electrons can also spontaneously fall from the conduction band into the valence band in a process called recombination, while always maintaining the conservation of energy and momentum, both optically and thermally. These two processes of hole-electron pair generation and recombination occur simultaneously and competitively. All electrons and holes in a pure semiconductor that contains a negligible density of other kinds of atoms are in equilibrium, $n_0 = p_0$, and their production equals the intrinsic carrier density, n_i, namely $n_0 p_0 = {n_i}^2$ [2.8]. When the photon absorption suddenly raises the density of carriers, $np > {n_i}^2$, the rate of recombination becomes larger than the

generation rate, bringing the system toward an equilibrium and vice versa for $np < {n_i}^2$. This also suggests that the recombination rate, R, determines the number of electrons or carriers that are available at a steady state so that the conductivity corresponds to the change of the equilibrium levels. A high rate of recombination is important for fast switching applications and steady state plasma needs to be extinguished in a very short time. In contrast, the recombination rate for the application toward steady plasma conductivity should be minimised to preserve more excess carriers for a relatively longer period of time to save optical power.

The conductivity that corresponds to the equilibrium level mentioned above can generally be increased by semiconductor doping due to the higher concentration of carriers. An extrinsic semiconductor is produced by introducing impurities into an intrinsic semiconductor and can be categorised into two types, n-type and p-type, based on the dopants. The n-type refers to a semiconductor with a higher concentration of electrons, which are the main carriers. The common n-type dopants are Phosphorus (P) and Arsenic (As), which have 5 electrons in the outer shell of their atomic structure. In the case of silicon, which has 4 electrons in covalent bonds, an extra electron will be promoted from the donor to the conduction band to contribute to the electrical conduction. Similarly, the p-type refers to a semiconductor with a higher concentration of holes that act as positive charges. The common p-type dopants as electron acceptors are Boron (B) and Gallium (Ga), which have 3 electrons in their outer cell. Donor atoms have more valence electrons, while impure acceptors have more holes. The increase in conductivity by doping can also be explained by the band structure in terms of more energy states being able to be introduced within the band gap which used to be a forbidden energy region. Electron donors may create states close to the conduction band and the gap between those created states and the nearest energy band is relatively small, while this energy gap also depends on dopant impurities. This means that doping effectively reduces the band gap and makes band transitions easier for electrons. Furthermore, the intermediate energy states introduced by those impurities play an important role in both the generation of excess carriers and recombination, as will be discussed below.

The process of direct band-to-band recombination is spontaneous and the probability should be constant with time. Since the rate of recombination is proportional to the electron and hole concentrations, the rate of change in carrier concentration may be written as follows;

$$\frac{dn}{dt} = r[n_i^2 - np] \qquad 2.19$$

where r is generation constant [2.1],

$$n = n_0 + \delta n \qquad p = p_0 + \delta p \qquad 2.20$$

In thermal equilibrium, the product of rn_i^2 describes the generation rate, and the parameters of n_0 and p_0 are independent of time. Since excess electrons and holes are always generated and recombine in pairs, $\delta n = \delta p$, it leads to the following equation;

$$\frac{d(\delta n)}{dt} = -r\delta n[(n_0 + p_0) + \delta n] \qquad 2.21$$

This equation can be solved, for example, with an assumption made under low-level injection ($\delta n(t) \ll (n_0$ or $p_0)$) for *n*-type material ($n_0 \gg p_0$), so that the recombination rate, R, becomes

$$R = \frac{d(\delta n)}{dt} = rn_0\delta n = \frac{\delta n}{\tau} \qquad 2.22$$

where τ is a constant ($= 1/(rn_0)$), which, in this case, is called the excess carrier lifetime. This suggests that the recombination rate is inversely proportional to the carrier lifetime. However, this may be true for an ideal direct band-to-band recombination where there is no energy state within the forbidden region, but the existence of impurities and defects within the crystal can make a huge difference because energy states will be allowed to be created within the bandgap, especially when the density of impurities is high after doping. Therefore, this requires further

consideration; hence, three typical recombination theories and mechanisms are introduced below.

As discussed earlier, the impurities introduced by doping can enable the formation of energy states in the bandgap, which may predominantly determine the mean carrier lifetime based on the theory of Shockley–Read–Hall (SRH) [2.1]. These introduced energy states are also called traps, which act as a recombination centre, which has almost the same probability to capture electrons and holes to assist the band transitions. As mentioned earlier, indirect band transition may require the support of a phonon to offer and adjust the momentum for band elevation. This central state can absorb the difference in momentum and provide it to carriers and this is crucial for indirect bandgap materials, especially the generation and recombination of silicon's excess carrier. This SRH recombination can also be important for direct band transition under low-level injection.

The second important recombination mechanism is Auger recombination, which is a non-radiative process, since it may not result in emitting a photon from a direct band transition. Auger recombination involves an interaction with a third particle and this particle carrier obtains energy that is transferred from the recombination of an electron and hole. This third carrier could be either an electron or hole, depending on the concentration of the material. This process normally involves two electrons and one hole in a heavily doped n-type material or an electron and two holes in a p-type one. The energy obtained can excite the third carrier to a higher state of energy, but it may not move to the adjacent energy band. Eventually, the third carrier will lose the excess energy through thermal vibrations to the lattice via phonons. This recombination process is significant for direct bandgap materials at high concentrations from doping or the generation of optically-excited carriers, but it may not be produced easily due to the third carrier's instability at high energy.

As for a radiative recombination, this mainly occurs in direct bandgap materials, such as GaAs. Photons are emitted at a wavelength related to the energy released during a radiative recombination, which implies that the recombination can radiate a range of energies in a bandwidth, but not necessarily at a single and discrete spectrum. The emitted photons present within the material can be further absorbed to generate excess carriers or further stimulate

another recombination event that emits a photon with similar properties. Nevertheless, it is extremely unlikely that this direct band radiative recombination can occur in an indirect bandgap material, such as silicon. It is also worth pointing out that a radiative recombination, a form of spontaneous emission, is the basic working mechanism of the Light Emitting Diode (LED), and the stimulated emission is responsible for the action of laser diodes, while the word "laser" originated as an acronym for Light Amplification by Stimulated Emission of Radiation. Both LEDs and laser diodes are the optical sources used in this research.

2.3.3 Carrier Drift, Diffusion and Photoconduction

The important parameters of the generation of excess carriers and recombination rates have been discussed above, but, with the presence of an electric field and a rise in density due to optical excitation, the behaviour and characteristics of excess carriers are equally important. Therefore, this section will begin with a brief introduction of other relevant photoconduction mechanisms of carrier drift and diffusion, which will then be used in conjunction with excess carrier generation and recombination for a derivation of the photoconduction equation, as explained above. This will form the fundamental basis of the plasma physics simulation model used in this study.

When an electric field is applied to a semiconductor, the movement of electrons and holes is accelerated on condition that they are available in the conduction and valence bands. This movement of charge particles is called drift and the current drift velocity increases linearly with time if the electric field is constant. However, collisions or scattering may occur when the charged particles hit impure or thermally-vibrating lattice atoms in the crystal, when they will accelerate again until they are involved in another collision. The average velocity, the drift velocity, v_d, can be defined by the following equation [2.1];

$$v_d = \mu_c E \qquad 2.23$$

where *E* is the electric field strength and μ_c is the mobility of the carrier. Thus, the total drift current density, J_{dri}, the sum of all electron and hole drift current densities will be as follows;

$$J_{dri} = q(\mu_n n + \mu_p p)E \qquad 2.24$$

where q is the electron charge, μ_n and n are the mobility and carrier concentration of the electron, respectively, μ_p and p are the hole mobility and hole carrier concentration respectively.

In addition to drift, the second mechanism is carrier diffusion, which involves the movement of particles from a region of high concentration to that of a low concentration in a random manner. Assuming that the carrier concentration varies in one dimension at a uniform temperature, the diffusion movement at thermal velocity, v_{th}, in average distance of l before collision can be written as $v_{th} l \frac{dn}{dz}$, which is proportional to the density gradient of carrier concentration, $\frac{\delta n}{\delta z}$. Hence, the diffusion current density, J_{dif}, will be as follows;

$$J_{dif} = q v_{th} l \frac{\delta n}{\delta z} = q D_c \frac{\delta n}{\delta z} \qquad 2.25$$

where D_c is the parameter called carrier diffusion coefficient in units of cm^2/s and by Einstein relation in kinetic theory,

$$D_c = \mu_c kT \qquad 2.26$$

where k is Boltzmann's constant and T is the absolute temperature. Therefore, the total current density due to the carrier drift and diffusion will be as follows;

$$J = J_{dri} + J_{dif} = q(\mu_n n + \mu_p p)E + qD_n \frac{\delta n}{\delta z} - qD_p \frac{\delta P}{\delta z} \qquad 2.27$$

As excess electrons and holes drift at the same effective mobility and diffuse with the same effective diffusion coefficient [2.1]. This phenomenon is called ambipolar transport and can be further quantified by continuity equations. When a one-dimensional flux of photons enters a semiconductor medium space, absorption takes place and electron and hole pair excess carriers are generated. This flux of particles is then subject to recombination and diffusion, where drift can also occur with the application of an external electric field. Once they reach a dynamic steady state, a one-dimensional continuity equation can be written, as follows;

$$\frac{\partial n}{\partial t} = G - \frac{\delta n}{\tau} + \frac{\partial(\frac{J}{q})}{\partial z} \qquad 2.28$$

where G is the generation rate in 2.18, $\frac{\delta n(t)}{\tau}$ is the mean recombination rate in 2.22, $\frac{\partial(\frac{J}{q})}{\partial z}$ is the drift and diffusion flow of particles. Then, an ambipolar transport equation can be derived from the continuity equations in charge neutrality condition, $\delta n \approx \delta p$,

$$\frac{\partial(\delta n)}{\partial t} = G - \frac{\delta n}{\tau} + D_c \frac{\partial^2(\delta n)}{\partial z^2} + \mu_c E \frac{\partial(\delta n)}{\partial z} \qquad 2.29$$

The parameter L_c, the diffusion length, which defines the average distance the carriers diffuse before recombination can also be used here for an easier calculation, along with the electron-hole plasma depth in the z-direction,

$$L_c{}^2 = D_c\tau \tag{2.30}$$

Now, assuming that there is no external electric field and no change in carrier concentration in equilibrium, $\frac{\partial(\delta n)}{\partial t} = 0$, by substituting 2.18 and 2.22 into 2.29, it becomes,

$$\frac{\eta\lambda q\alpha I_0 e^{-\alpha z}}{hc} - \frac{\delta n}{\tau} + \frac{L_c{}^2}{\tau}\frac{\partial^2(\delta n)}{\partial z^2} = 0 \tag{2.31}$$

Two boundary conditions need to be specified to solve this partial differential equation;

$$\frac{d(\delta n_{z=0})}{dz} = \tau S\frac{\delta n_{z=0}}{L_c{}^2} \tag{2.32}$$

$$\delta n_{z=\infty} = 0 \tag{2.33}$$

where the first represents the surface condition expressed with S, the surface recombination velocity, as introduced earlier. The second explains the condition at an infinite distance from the surface, which only holds true if the thickness of the substrate is a few times larger than the absorption depth and the diffusion length, when a negligible excess carrier concentration needs to be considered. Therefore, the solved equation can be written as follows;

$$\delta n = \frac{-\tau\eta\lambda q\alpha I_0}{hc(\alpha^2 L_c{}^2 - 1)}\left(e^{-\alpha z} - \frac{\alpha L_c + \tau S/L_c}{1 + \tau S/L_c}e^{-z/L_c}\right) \tag{2.34}$$

As can be seen, the distribution of excess carriers is of exponential profile deep into the semiconductor and is largely determined by both the absorption depth, α, and the carrier

diffusion coefficient, L_c. Practical values of these coefficients and constants can be found in [2.16].

Since both electron and hole carriers contribute to the ambipolar transport, with excess carrier concentration now known as a function of the depth, the conductivity of the plasma can be calculated as follows;

$$\sigma = q(\delta n + n_0)(\mu_e + \mu_h) \qquad 2.35$$

where σ is the conductivity (S/m). Henceforth, the relationship between the illumination intensity and electrical conductivity can be derived. Figure 2.9 shows conductivity against substrate depth for various illumination intensities. As can be seen, the conductivity of every illumination intensity condition follows the exponential decaying profile.

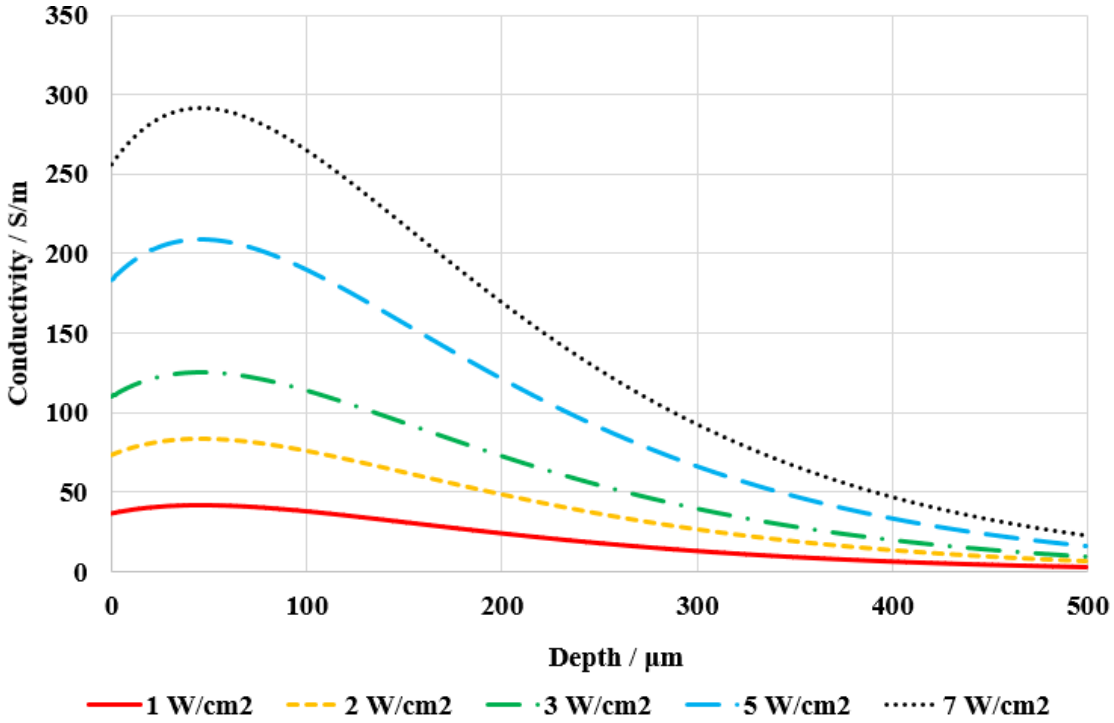

Figure 2.9 Simulated result of Conductivity vs. Substrate depth for intrinsic silicon (n_0=1.45×10^{10}cm^{-3}) under various illumination intensities (empirical and experimental values obtained from [2.16])

2.3.4 Dielectric Permittivity

Having quantified the photoconductivity change due to excess carrier generation by optical illumination in the last section, it is also essential to consider the change in the dielectric permittivity of a semiconductor when the concentration of carriers is altered. The electric permittivity, which describes the material's ability to resist an electric field, can be defined in a complex form as follows [2.3];

$$\varepsilon = \varepsilon' - j\varepsilon'' \tag{2.36}$$

Then, by substituting 2.36 into the 2.1 of Maxwell equations, it can be written as,

$$\nabla \times \boldsymbol{H} = (\sigma + j\omega\varepsilon)\boldsymbol{E} = j\omega\{\varepsilon' - j(\varepsilon'' + \frac{\sigma}{\omega})\}\boldsymbol{E} \tag{2.37}$$

where $\varepsilon_{total} = \{\varepsilon' - j(\varepsilon'' + \frac{\sigma}{\omega})\}$ gives the complex form of total permittivity integrated with conductivity, ε' is for the lossless real part of permittivity given by the product of the permittivity of free space and the real part of relative permittivity, $\varepsilon_0\varepsilon_r{}'$. $\varepsilon'' + \frac{\sigma}{\omega}$ is the imaginary part of permittivity, which gives the energy loss that cannot be distinguished from the loss due to the free charge conduction quantified by σ and ω is the angular frequency, $\omega = 2\pi f$. Then, the loss tangent is defined as the tangent of angle ratio between the phase differences in this complex plane,

$$tan\,\delta = \frac{\omega\varepsilon'' + \sigma}{\omega\varepsilon'} \tag{2.38}$$

The effect of the change in permittivity characterises the propagation of microwaves within the semiconductor. Hence, it is necessary to recall the propagation constant, γ, defined in the wave equation in 2.7, which can be written in the form of refractive index, n, and absorption index, k, but can also be represented as follows;

$$\gamma = \alpha + j\beta \qquad 2.39$$

where α is the attenuation coefficient and β is the phase coefficient. If no light falls on the silicon, the propagation constant can be calculated based on the real part of permittivity, since the dielectric loss is negligible [2.17]. When light is provided, the rise of conductivity due to an increase of carrier concentration will result in a decrease in the real part of permittivity, but an increase in the imaginary part [2.18]. As shown in Figure 2.9, the exponential decaying profile of conductivity suggests a non-uniform distribution of carriers, as well as electric field. This is the region where most of the loss of microwave or millimetre wave signal propagation occurs. This loss is mainly due to the charged particles motion and heat dissipation which is represented by the imaginary component of the permittivity as a function of frequency. The acceleration, deceleration and friction of particles originate from the relaxation and rotation of the polarised dipoles. If this lossy region is electrically small, typically smaller than 1/16th of the wavelength, it can be modelled by a lumped element circuit. (Some studies and simulated models will be shown later in Chapter 4) When this illuminated region is enlarged, LCR circuits may not accurately capture the response; therefore, the propagation constant will be employed for the analysis. With regard to the design of the phase shift application, the imaginary part of the propagation constant needs to be enlarged while reducing the attenuation coefficient, the real part of the propagation constant. On the contrary, to design a switch, which is the main concern of this project, the aim is to maximise the real part at switch-off condition, while minimising it at switch-on condition to provide a large ON/OFF ratio between insertion loss and isolation. In-depth investigations and deductions from dielectric permittivity to propagation constant were studied in [2.19, 2.20] and the key findings are shown below.

$$\varepsilon_p = (\varepsilon_r - \frac{{\omega_p}^2}{\omega^2{\tau_c}^2 + 1}) - j\frac{{\omega_p}^2}{\omega{\tau_c}^2(\omega^2{\tau_c}^2 + 1)} \quad 2.40$$

$${\omega_p}^2 = \frac{(\delta n + n_0)q^2}{\varepsilon_0 m^*} \quad 2.41$$

$$\tau_c = \frac{\mu_c m^*}{q} \quad 2.42$$

where ε_p is the relative permittivity of the plasma, ω_p is the angular speed of the plasma, τ_c is the carrier collision time, m^* is the effective mass of the charge carrier. As shown, the real and imaginary parts of the relative permittivity in the plasma region are given as functions of carrier concentration. By implementing 2.34 and 2.35, a graph of the real part of the relative permittivity in the plasma region against substrate depth along the photon absorbed direction can be plotted in Figure 2.10. Figure 2.9 and Figure 2.10 together provide good solutions for creating and modelling plasma layers in simulation software with theoretically-calculated electrical properties and parameters.

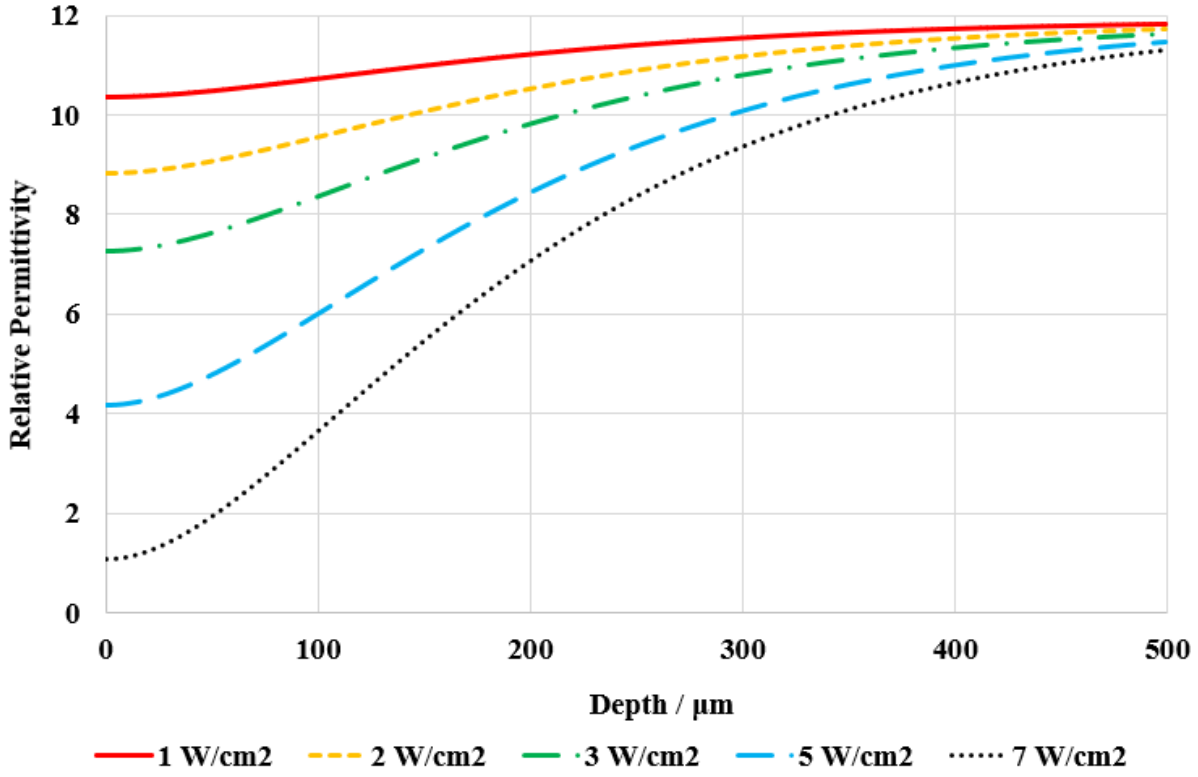

Figure 2.10 Relative permittivity (real part) vs. Substrate depth for intrinsic silicon (n_0=1.45×$10^{10}$$cm^{-3}$) under various illumination intensities

2.3.5 Selection of Material

The selection of the photoconductive material is extremely important. Elemental semiconductors (Silicon and Germanium), III-V compounds (GaAs, InP, etc.), other II or II-VI compounds, and some other materials (composite polymers) all have various optical and microwave properties, but there are many factors that limit their use in practice, such as low carrier mobility [2.21], the need of large photon energy [2.22, 2.23], and limited conductivity in the ON state [2.24]. It could already have been assumed from the detailed discussion in the last section that the best choice could be a direct bandgap semiconductor material, for example GaAs. However, silicon has also been proved to be an extremely good photoconductive material. A comparison of Silicon and GaAs is shown in Table 2-1 below.

Semiconductor		Silicon	GaAs
Characteristic	**Unit**		
Bandgap	eV	1.12	1.42
Electron mobility at $\mathbf{300}\boldsymbol{K}$	cm^2/Vs	1500	8500
Saturated (peak) electron velocity	$\times 10^7 cm/s$	1	1.3
Critical breakdown field	MV/cm	0.3	0.4
Thermal conductivity	$W/cm.K$	1.5	0.5
Relative dielectric constant	ε_r	11.9	12.8

Table 2.1 Comparison of electrical properties of Silicon and GaAs materials [2.25]

It can be seen from Table 2-1 that GaAs has a wider bandgap than silicon. This means that intrinsic GaAs is highly resistive and has a higher dielectric constant, which produces better isolation than silicon, which makes it a very good material for the substrate of Integrated Circuits (IC). Additionally, it is more resistive to radiation damage than silicon, which makes it a good candidate for space applications and high-power fields. The wider bandgap also suggests a lower cut-off wavelength. As explained in 2.2.3, high quantum efficiency occurs in the wavelength region close to the bandgap boundary so that visible light sources can be used, especially in the deep red and near infrared (NIR) regions, which increases the number of available sources to produce a photoconductive switch. Higher saturated electron velocity and less noise could be the other benefits of GaAs when used at high frequencies in the order of hundreds of GHz or THz. With regard to the use of GaAs as a compound direct-band semiconductor material, as explained earlier, no additional momentum in k-space is required from, for example, phonon's assistance for the transition of bands between conduction and valence bands. Hence, it could be highly efficient for the absorption and emission of photons. The transport of the generated excess carriers in terms of drift and diffusion depends strongly on the carriers' mobility. As shown in Table 2-1, GaAs's electrons respond much quicker and move more actively than those of silicon when an electric field is applied, and this electric field could be created by the different concentration of carriers across a region. This high mobility may effectively shorten the response time for the generation of electron-hole plasma, which will result in a short rise time. More importantly, the effects of SRH, Radiative and Auger

discussed previously will be all responsible for the provision of the shorter fall time by GaAs's recombination mechanisms. Therefore, these factors together could contribute to the possibility of faster switching than with silicon.

However, silicon also has many advantages over GaAs. Firstly, it is abundant and very cheap to acquire and process, while GaAs is relatively expensive. The current economies and markets in the silicon and semiconductor industry hinder the adoption of GaAs. Furthermore, from a manufacturing perspective, silicon is more stable and the crystal can be processed to such a large scale and volume to make the wafer easy to handle and preserve. Silicon's longer absorption depth of sunlight facilitates a larger planar device, especially in the solar cell industry, unlike GaAs's, which requires a substrate material and hence increases the cost and complexity of the system. In addition, the techniques in the silicon industry are more advanced in that a passivated layer can be easily engineered on the surface to obtain good electrical properties, while GaAs does not have a native oxide. It is also worth noting that toxicity could be another inferior factor of GaAs compared to neutral silicon. Significantly, GaAs requires a much higher intensity of optical illumination for a photoconductive switch design than silicon on account of its faster carrier mobility and response, as explained earlier. A detailed comparison for the implementation of a photoconductive switch will be made and analysed in the penultimate chapter of this research.

2.4 Conclusion

The basic semiconductor and quantum physics involved in this study of light-semiconductor interaction have been discussed in this chapter. This interaction with semiconductors mainly involved the reflection, absorption and transmission of light. Reflection was firstly discussed from the angle of light as an electromagnetic wave. Maxwell's equations were introduced to derive the wave equation and complex refractive index, which inspired the subsequent study of absorption and attenuation. Then, particle-wave duality was introduced in the absorption section and the chapter continued with a discussion of the band structure. The band transitions of the generation of electron-hole excess carriers were then described before defining quantum efficiency as a combination of external and internal quantum efficiency. Several examples of calculations were provided to reinforce the assumptions and conclude that silicon light at near

infrared wavelength region could be an optimum selection. This part of the discussion also included absorption depth, surface recombination and basic thermal problems.

Particle behaviour was explained in detail in the photoconductivity sections with a focus on the generation of electron-hole pairs to create absorbed photon energy, the recombination of excess carriers and the drift and diffusion of carriers' transport due to the application of an electric field and the gradient of carrier concentrations, respectively. Most importantly, the three recombination mechanisms of Shockley-Read-Hall, Radiative and Auger effects were introduced. Furthermore, this plasma region of a created high concentration of electron-hole pairs was analysed with physics equations so that the total carrier concentration, as well as the photoconductivity, could be calculated. Together with dielectric permittivity studies, the necessary electrical properties were quantified with physics equations to provide a solution for simulating photoconductivity within a semiconductor. Lastly, the choice of material was discussed with a comparison of GaAs and silicon.

In conclusion, the fundamental physics and theoretical part of this research is introduced in this chapter. The simulation methodology developed here will ensure the accuracy of the circuit design and measurement comparison in the remainder of the study.

2.5 References

[2.1] D. A. Neamen, “Semiconductor physics and devices: basic principles”, McGraw-Hill Inc., 4th edition, 2003

[2.2] M. Ohring, “Reliability and failure of electronic materials and devices”, Academic Press, pp. 310, 1998

[2.3] D. M. Pozar, “Microwave engineering”, John Wiley & Sons, 3th edition, 2009

[2.4] T. S. Moss, et al., “Semiconductor Opto-Electronics”, Chapter 5, London Butterworth, London, UK, pp. 135 – 137, 1973

[2.5] M. Planck, “The theory of heat radiation”, Courier Corporation, 2013

[2.6] A. Einstein, “On a heuristic point of view about the creation and conversion of light”, in “The Foundation of the Generalised Theory of Relativity”, vol. 22, no. 1

[2.7] C. Kittel, Introduction to solid state physics, New York: Wiley; 1976

[2.8] J. J. Sparkes, “Semiconductor Devices”, Chapman & Hall, 2-6 Boundary Row, London, UK, Chapter 1, pp. 2-16, 1994

[2.9] M. A. Green and M. J. Keevers, “Optical properties of intrinsic silicon at 300 K”, Progress in Photovoltaics: Research and Applications, vol. 3, pp. 189 - 192, 1995

[2.10] D. Baek, S. Rouvimov, B. Kim, T. C. Jo, D. K. Schroder, “Surface recombination velocity of silicon wafers by photoluminescence”, Applied Physics Letters, vol. 86, no. 11, pp. 110-112, 2005

[2.11] R. Brendel, M. Hirsch, M. Stemmer, U. Rau, J. H. Werner, “Internal quantum efficiency of thin epitaxial silicon solar cells”, Applied physics letters, vol. 66, no. 10, pp. 1261-1263, 1995

[2.12] B. K. Nayak, V. V. Iyengar, M. C. Gupta, “Efficient light trapping in silicon solar cells by ultrafast-laser-induced self-assembled micro/nano structures”, Progress in Photovoltaics: Research and Applications, vol. 19, no. 6, pp. 631-639, 2011

[2.13] T. R. Gentile, S. W. Brown, K. R. Lykke, P. S. Shaw, J. T. Woodward, “Internal quantum efficiency modeling of silicon photodiodes”, Applied optics, vol. 49, no. 10, pp. 1859-1864, 2010

[2.14] L. Lan, D. Zhao, F. Liang, Q. Zhang, B. Z. Wang, “Influence of laser wavelength on insertion loss of silicon-based optically controlled microwave switch”, Microwave and Optical Technology Letters, vol. 55, no. 1, pp. 187-190, 2013

[2.15] D. Zhao, Y. Han, Q. Zhang, B.Z. Wang, “Experimental study of silicon-based microwave switches optically driven by LEDs”, Microwave and Optical Technology Letters, vol. 57, no. 12, pp. 2768-2774, 2015

[2.16] D. K. Schroder, “Carrier lifetimes in silicon”, IEEE transactions on Electron Devices, vol. 44, no. 1, pp. 160-170, 1997

[2.17] R. E. Collin, “Foundations for microwave engineering”, John Wiley & Sons, 2007

[2.18] M. Dressel, G. Grüner, “Electrodynamics of Solids: Optical Properties of Electrons in Matter”, Cambridge University Press, 2002

[2.19] C. H. Lee, P. S. Mak, A. P. DeFonzo, “Optical control of millimeter-wave propagation in dielectric waveguides. Quantum Electronics”, IEEE Journal of, vol. 16, no. 3, pp. 277-288, 1980

[2.20] J. K. Butler, T. F. Wu, M. W. Scott, “Nonuniform layer model of a millimeterwave phase shifter”, IEEE Transactions Microwave Theory and Techniques, vol. 34, no. 1, pp. 147-155, 1986

[2.21] R. P. Tuffin, I. C. Sage, B. J. Hughes, G. J. Ball, “Electronically controlled metamorphic antenna”, Proc. 4th EMRS DTC, 2007

[2.22] K. S. Kelkar, N. E. Islam, C. M. Fessler, W. C. Nunnally, “Design and characterization of silicon carbide photoconductive switches for high field applications”, Journal of applied physics, vol. 100, no. 12, pp. 1249, 2006.

[2.23] M. Bhatnagar, B. J. Baliga, “Comparison of 6H-SiC, 3C-SiC, and Si for power devices”, IEEE Transactions on electron devices, vol. 40, no. 3, pp. 645-655, 1993

[2.24] R. L. Haupt, J. R. Flemish, “Reconfigurable and adaptive antennas using materials with variable conductivity”, IEEE Adaptive Hardware and Systems, 2007, Second NASA/ESA Conference, pp. 20-26, 2007

[2.25] California State University Northridge, Gallium Arsenide Semiconductors, [accessible: http://www.csun.edu/~rdconner/630/slides/GaAs.ppt]

CHAPTER 3

3. Simulation, Measurement and Fabrication

3.1 Introduction

The methods used to simulate, measure and fabricate the switches being studied are introduced in this chapter. The simulation part begins with a description of the model of the distributed element and this is followed by an overview of the full electromagnetic wave in-structure simulation methodology. As explained in the last chapter, lumped circuits may not be suitable for use, depending on the working frequency band when the electrical length is considerably large. Secondly, the fundamental optical and RF (Radio Frequency) measurement mechanisms will be introduced and finally, fabrication techniques, including photo-lithography and PCB (Printed Circuit Board) laser cutting, are described in detail.

3.2 Simulation Methods

3.2.1 Distributed Element Model

The lumped element model mentioned in the last chapter simplifies the circuit by assuming that perfect electrical components, namely resistors, capacitors and inductors, are connected by lossless wires. However, this is only valid when the electrical length of the circuit is much smaller than the operating wavelength. If they are in the same order of magnitude, the time the signal is propagated will not be negligible compared to its operating period. This means that the actual signal amplitude will vary with time as the signal is propagated in the circuit, but it cannot be assumed as a constant value anymore. Since more errors occur when the signal propagation time increases, a larger phase difference has an impact on the actual signal amplitude. The more generic method discussed here is the distributed element model, which corresponds with Maxwell's equations in dynamic manners. In this modelling method, the individual circuit element is assumed to be infinitesimally small and the conducting wires are assumed to be somewhat impeded. A transmission line can be employed as a fundamental explanation. Transmission lines are composed of two or more conductors and are used to transfer power or information from one point to another. Unlike the ordinary electric circuits described in lumped elements, transmission lines can radiate power and generate standing waves described by distributed parameters. An example of a transmission line equivalent circuit in a distributed element model is shown in Figure 3.1. [3.1]

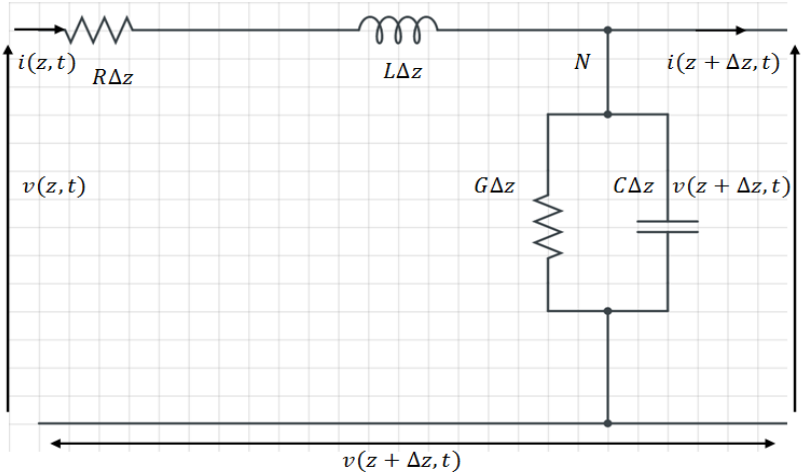

Figure 3.1 Example of transmission line circuit [3.1] represented by distributed elements

The instantaneous voltages and currents are denoted by $v(z,t)$ and $i(z,t)$ respectively and the distributed parameters are as follows;

Series resistance per unit length R(Ω/m)

Series inductance per unit length L(H/m)

Shunt conductance per unit length G(S/m)

Shunt capacitance per unit length C(F/m)

Since the Δz is assumed to be infinitesimally small, the distributed element model can be more accurate than the lumped element one. Linear algebra provides an easy solution for a lumped element analysis whereas a more complex calculus is needed to analyse a distributed element model. The distributed element model is preferred when accuracy is required, since the circuit component dimensions are comparable to the wavelengths of the operating signal. A rule of thumb is the significance of a distributed element analysis in electrical and electronic engineering when a 10th of a signal wavelength is smaller than the circuit's physical dimension [3.1]. Again, this suggests that distributed element modelling will only be valid within a limited range of frequency. However, this issue could be resolved by the use of distributed circuits in a series or cascaded, particularly at high frequency. Moreover, the distributed model has the potential benefit of a reduction in simulation time compared to full electromagnetic wave simulation, which will be discussed below. However, the need to repeat the manual work of cascaded electric circuit components and simulation software are drawbacks for the wideband analysis in electronic component design proposed in this research. Additionally, the full electromagnetic wave in-structure simulation facilitates a more comprehensive analysis and the fact that the results are based on the direct input of microwave engineering parameters and material properties makes it easy to calculate the characteristics of individual components. The results will be compared in detail in the following chapters.

3.2.2 Full-Wave Simulation

Full-wave electromagnetic field simulation methodology is based on resolving Maxwell's equations by using one of two classes of methods with discretion within boundaries, both of which rely on analytical geometry. Then, these equations are subjected to iterative algorithms through convergence to obtain a certain desired accuracy. The difference between these two classes of methods is that one of them resolves Maxwell's equations in an integral form, while the other solves them in differential form, which only requires the discretisation of the source of the electromagnetic field for a coaxial transmission line, which is usually called an electromagnetic port. The Boundary Element Method (BEM) is a typical solution to the source of a surface in a three-dimensional problem [3.2]. Only a small region of the port needs to be considered in an open boundary condition rather than involving the whole electromagnetic field and this has been proved to be a faster and less costly method than those in the second class derived from different forms of Maxwell's equations. However, this is only true when the problem region to be analysed is small or open, since this method generates a high density of linear system equations, which require a large volume of memory for storage and Gaussian elimination. Hence, the analysis of complex interconnecting factors increases the number of computations required to resolve problems of growing sizes, especially with increased circuit speeds and highly dense components. Therefore, different forms of method solving could be more competitive in these scenarios.

In terms of the second class of full-wave simulation methods, the two most common approaches are the Finite Element Method (FEM) and Finite Difference (FD) methods and other variations and techniques normally fall into these two subcategories. FEM and FD methods can both be used to resolve equations in different forms within a discretised meshing system. The FEM method was originally applied to mechanical and civil engineering problems based on its advanced ability to deal with different boundary equations related to the distribution of static linear stress on bridges [3.3, 3.4]. It was later adopted as a solution to other physical problems and became one of the most popular methods for resolving different non-linear equations to tackle complex boundary problems. As the name suggests, the FEM method involves dividing the interested volume into many finite elements in any dimension. Every element can be represented by nodes and edges. In a nodal analysis, each element can be

expressed in a matrix and element boundary coordinates can be easily stored. In an edge analysis, vectors are used to represent nodes and geometric information is saved. Importantly, these partitioned spaces can be of any arbitrary finite element, which could be considered as an advantage, since higher discretisation density can be applied to certain regions with rapid variation. This flexibility to implement a meshing grid reduces the computational demand for non-boundary spaces, since it reduces the number of fragments based on the number of nodes being determined from an interpolation function. Meanwhile, accuracy can be maintained for complex structures with many curved elements. In addition, FEM modelling is also useful for resolving problems related to various boundaries and different non-linear equations [3.5]. As for its disadvantages, FEM may need a large memory for storing matrix information, which suggests that its use will be limited by computer hardware. Furthermore, most simulation software packages for FEM are based on frequency domain solvers, which are useful for resonant structures, but could be very time-consuming when studying a broadband switch. This is because the result of every single move during a frequency band region needs to be calculated if it is considered using a frequency domain solver.

The Finite Difference method discussed here refers to the Finite-Difference Time-Domain (FDTD) algorithm. Since the 1960s, when it was first proposed by Yee to resolve Maxwell's equations, the FDTD method has played a leading role as one of the fastest techniques in modern full-wave electromagnetic solvers [3.6] [3.7]. The major difference between the FDTD method and the FEM method is that FDTD method resolves Maxwell's equations in a different form and time domain. This difference is based on a grid or mesh system with partial derivatives, while the time-dependent characteristic facilitates the coverage of wide frequency bands, since a single-pulse triggered at the source port can be continuously calculated in a leapfrog manner, even for non-linear materials, which can be treated in a natural way. The best way to explain the algorithm in detail is to start by introducing Yee's mesh.

The Chinese-American applied mathematician, Kane S. Yee, originally proposed the Finite-Difference Time-Domain method to resolve Maxwell's equations in a different form and time domain. It is also called Yee's method and it involves the implementation of Yee's cube, as shown in Figure 3.2 in which the standard Cartesian Yee cell employed in the FDTD method is illustrated and the distribution of the electric and magnetic field components in 3-

dimensional vectors around the cube is demonstrated. Each element of the cell is given an appropriate electric permittivity value and assigned magnetic permeability data. The aforementioned leapfrog implementation refers to the process whereby the first electric field vector is solved at a time interval and is immediately followed by the next time instance, where the magnetic field vector is calculated in the same spatial volume. This process is repeated until a desired transient response or steady state condition is obtained. It can be seen that this also follows Maxwell's curl equations in a different form stated in 2.1 where the change in the E-field is dependent on that in the H-field in time and space. Therefore, in the next time step, an updated value in the E-field vector component is recalculated based on the data value stored in the adjacent E-field component in the previous step, which also depends on the numerical curl of the local H-field distribution. Similarly, the H-field component vector values depend on the registered values and the numerical curl of the local E-field distribution in time and space. This process is constantly conducted and continuously repeated with memory-stored data updated on the E-field and H-field vector components along the wave propagation. As can be imagined, calculating the curl of an element of multiple dimensions superimposed with the E-field and H-field would be extremely complex and Yee proposed a staggering spatial technique in a rectangular unit cell where the grid is set in the middle of an E-field and H-field pair [3.6]. This is still regarded as the most robust modern FDTD software solver, since it provides numerical solutions to different equations explicitly in a stepwise or leapfrog manner. This explicit scheme avoids the need to resolve simultaneous equations by setting the threshold to complete a large number of time steps to ensure numerical stability [3.8].

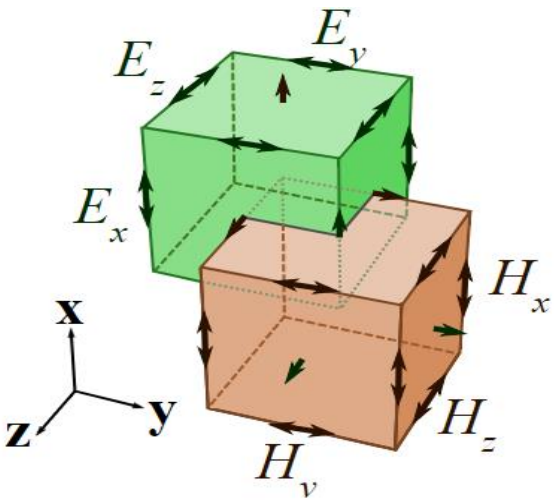

Figure 3.2 Yee Cube [3.9]

The greatest benefits of the FDTD method is its simplicity, which enable users to resolve difficult practical problems due to its ease of understanding and ability to give them an idea of what to expect by its convenient implementation. Another important advantage is that a broadband analysis can be obtained based on its time-domain attribute, especially since the port source is a Gaussian type, and it also enables previously unknown resonance to be predicted. Moreover, the memory requirement is already explicitly registered since the grid or meshing system is predefined and the solution matrix will not be increased proportionally during the processing. Besides, the FDTD method is able to naturally accommodate a variety of linear or nonlinear, homogeneous or heterogeneous materials so that no additional algorithms are needed for a complex dispersive lossy anisotropic dielectric material. Lastly, the restrictions of the FDTD method as opposed to the previously-discussed advantage of the FEM method related to open boundary problems, have now broken by many recent studies [3.10, 3.11], which has increased its popularity for antennas and other RF circuits.

On the other hand, the greatest disadvantage of the FDTD method is the drawback of the meshing system. Since the FDTD method requires complete spatial discretisation in grids in the form of Yee's cubes, it is inadequate for calculating complex geometrical structures. This is essential for the FDTD method, since the smallest mesh size needs to be 10 times lower than the smallest electromagnetic wavelength to maintain the accuracy of the solution and the cells of the FDTD method are less flexible than the arbitrary element in the FEM. If there are many dielectric layers or numerous variations or curves around the surface of the material, large numbers of FDTD meshes will need to be employed to compensate, which means that an increased simulation time will be expected to complete the increasing number of steps. Although other dynamic meshing and sub-meshing systems [3.12] have been developed, their implementation may not be straightforward and they also demand more computational power or memory at the beginning. Another disadvantage is that the simulation time of the FDTD method could increase considerably for resonant structures or multi-port systems due to the slowly deteriorating transient response. Fortunately, this is not the case in this research which is based on studying aspects of a broadband switch.

The Finite Integration Technique (FIT) method, which is a variation and subcategory of the FDTD technique, was proposed by Thomas Weiland in 1977 [3.13]. This is an integral form of

a spatial discretisation scheme for Maxwell's equations, which provides computers with suitable reformulations and facilitates explicit calculations in the same way as the FDTD method. This technique contributes to the enhancement of many commercial simulation software programmes since it covers a wide range of electromagnetic analyses, from static to high frequency, and even optic implementation. Most simulations were performed in this work using the FIT solver in Computer Simulation Technology (CST) Microwave Studio of CST Studio Suite. The main reason for this is the requirement of a wide bandwidth simulation and analysis and the fact that the frequency solver in CST, which uses the FEM technique, can be employed for a complementary analysis in terms of resonance.

3.3 Measurement Setup

Some generic measurement techniques that include the setup of optical sources, fibre optics, circuit fixtures, RF connector mounting and switching electronics are introduced in this section and detailed descriptions for specific individual studies will be provided in each of the following chapters.

3.3.1 Laser and Optical Setups

The first optical source is a 1W continuous wave (CW) laser manufactured by Roithner Laser Technik (RLCO-830-1000-TO3) [3.14]. This is a standard transverse-mode Vertical-Cavity Surface-Emitting Laser (VCSEL) diode whose field pattern is perpendicular to its propagation beam direction. Its beam follows Gaussian profile and has a facet size of $50\mu m \times 5\mu m$ at a wavelength of $830nm$. This laser is mainly used for an initial microstrip gapline test and the switching measurement of GaAs, which benefit from its implementation of collimation and focus on optic techniques. A standard VCSEL facet laser is shown in Figure 3.3.

Figure 3.3 Image of a standard VCSEL facet laser

The large inherent beam profile and rectangular shape of this laser is initially problematic for collimation, but it can also be considered as beneficial for illuminating a wide area. The photograph in the Figure 3.4 shows an example of the basic setup for the optical illumination of a device under test (DUT). Micrometre stages were used to provide good alignment between the laser and lenses. The collimating lens used here is the Thorlabs C390TME-B aspheric collimating lens [3.15] with low loss. The laser light is emitted from the VCSEL and is then passed through the collimating lens and a spherical lens of [3.16] so that it can finally focus on the DUT fixed on a brass block where the optical illumination interacts with the semiconductor-based microwave or millimetre wave circuits. The RF connectors mounted on the brass block connect the circuit to the Vector Network Analyser (VNA) on both sides. Parameter results can be obtained from the VNA for further analysis.

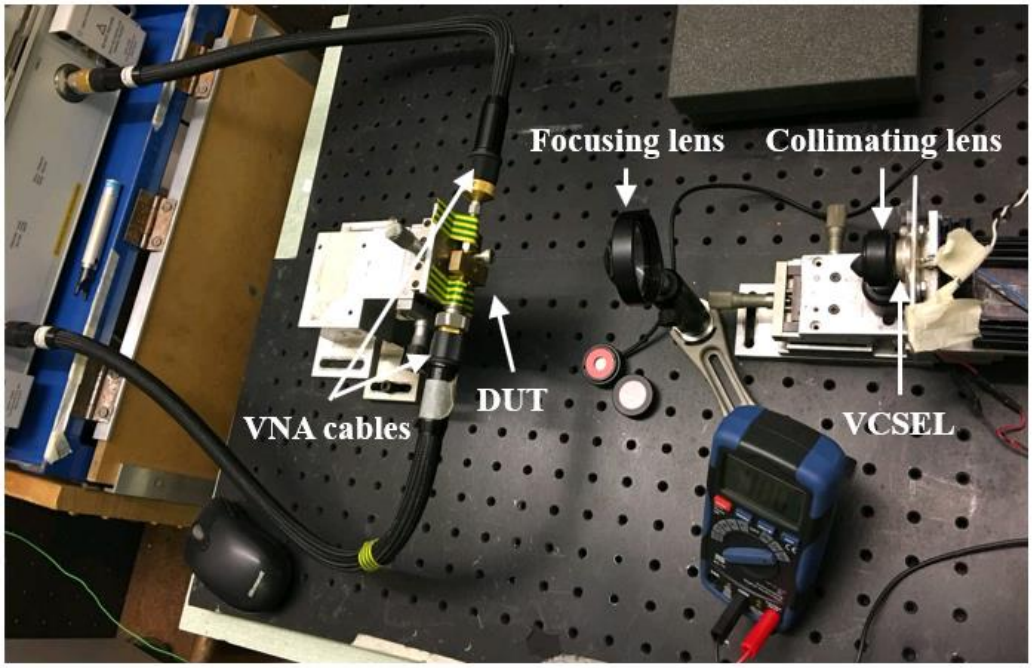

Figure 3.4 Measurement setup with optical illumination provided by VCSEL and optics

As mentioned earlier, the chosen illumination wavelength was in the near infra-red (NIR) region. An NIR reflective surface coated ring was used to capture the illuminated area to calculate the intensity, since these wavelengths are normally invisible to the human eye. The magnified images of the ring on an optical power detector are shown in Figure 3.5 and it was measured and calculated that an intensity of $13.9 W/cm^2$ could be obtained with an illuminated area of about $3mm \times 2mm$. The optical power was uniform and the intensity was almost

constant over the illuminated region due to the relatively large area of emission from the VCSEL, as mentioned above.

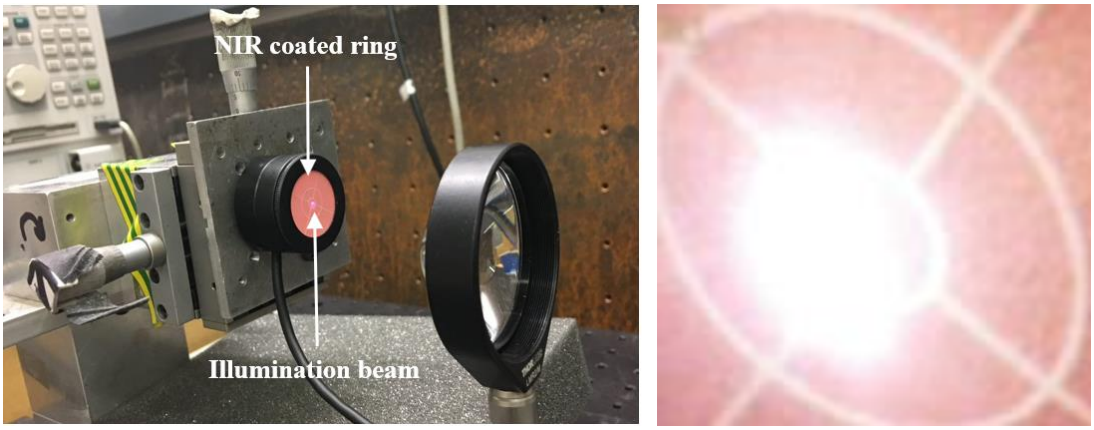

Figure 3.5 Illuminated beam on NIR reflective surface coated ring and magnified image

A further experiment was conducted to check the laser beam illuminating profile. A basic Gaussian profile was observed as expected. Since the beam profile could be measured directly in this experiment, this optical setup could easily be implemented with microwave and millimetre wave devices, which eliminates the need of complex optics. However, it can be still expensive, regardless of some commercially-established samples. Furthermore, the packaging and integration of these bulky optics for base-station applications in telecommunications or other small/medium-scale devices are costly.

Another optical setup solution that benefits from mobility is shown in Figure 3.6. This optical source is an optical fibre coupled laser (RLCO-980-2000-F) [3.17]. Since the original optical fibre is bare and exposure to it can harm the human eye, it was enclosed within a metal box with the addition of a Peltier pad [3.18] for a TEC cooling method [3.19]. A cladded multimode fibre (M56L005) [3.20] was then connected by a FC-SMA adapter, which enabled the transition and simultaneously extended the reach with the mobility. However, since a full optical transition cannot be performed due to the use of adapters, the connection between those two fibres is not optimum, which reduces the power efficiency, to be less than 10%, in terms of the ratio of the optical source to the DC power consumption. This multimode fibre has a diameter of $2.5mm$ and its end is inserted into a drilled hole in the brass block with a push fit. In contrast, the free-space VCSEL can provide up to 60% efficiency.

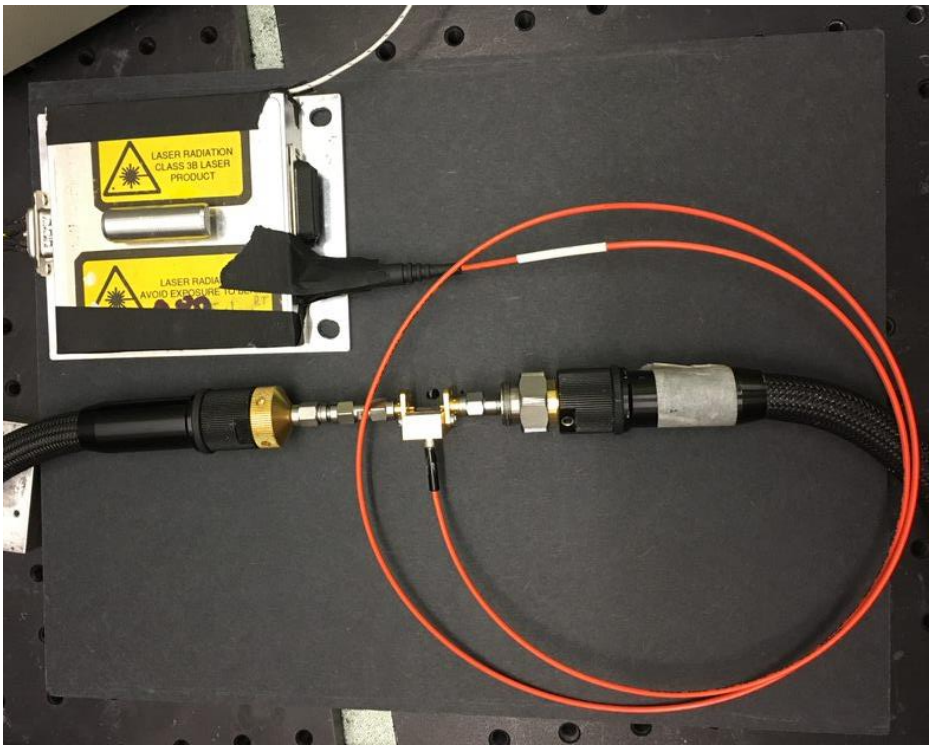

Figure 3.6 Measurement setup with optical illumination provided by fibre-coupled laser

In contrast with the previous method that involved the use of a free space laser, this fibre-based approach shortens the distance between the optical source and the photoconductive region, thereby effectively reducing the loss compared to the light being transmitted in the air. However, as the use of an adapter does not perform a collimation and angles are not aligned at the fibre edges, there is also a considerable loss between the supplied DC power and the radiated optical power.

3.3.2 LED Sources

Light Emitting Diodes (LEDs) are distinguished by their ease of operation and integration. They are free of optics and affordable. The fundamental theory of the emission of light is based on the radiative recombination, as explained in §2.3.2. LEDs have been employed and implemented for package mobility and integration purposes. In this study, mainly in pulsed modulation measurements. The TSHG8x00 series of VISHAY Semiconductors [3.21] have been chosen as basic examples of LEDs because of their high-power operation in the NIR

region, small angle of half intensity, good spectral matching and relatively high-modulation bandwidth. The TSHG8200 model has been selected and its basic ratings characterised in the laboratory have been tested and closely matched to the vendor's data sheets in Figure 3.7. The flat line in Figure 3.7 (Left) suggests that a linear region exists before the forward voltage exceeds 1.5V and the gradient drops where nonlinearity occurs when the forward voltage increases. The main reason for this has been found to be the nonlinear thermal issue in the LED's resistor.

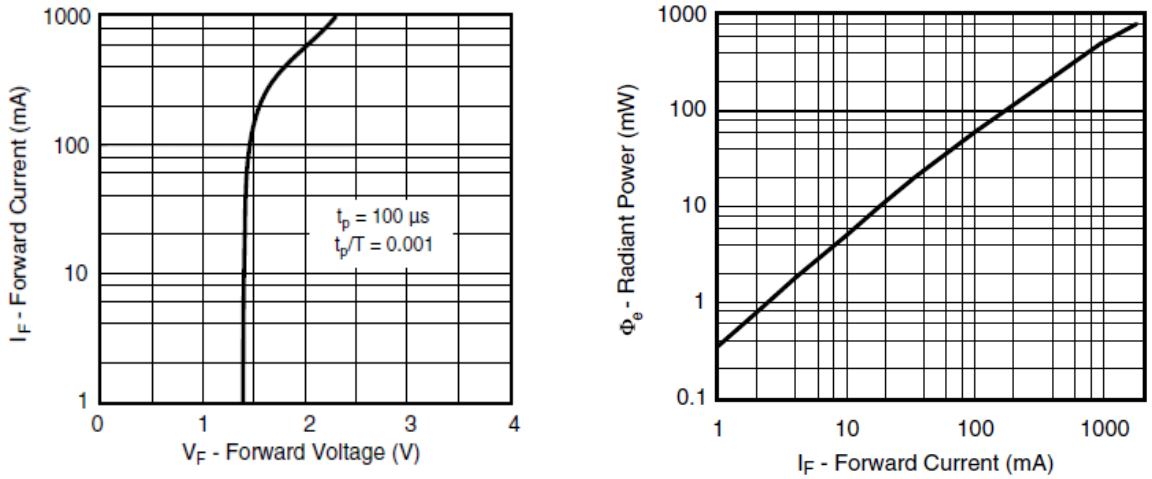

Figure 3.7 Forward current vs. Forward voltage (Left) and Radiant power vs. Forward voltage (Right) from TSHG8200 data sheet [3.21]

This initial characterisation test provided a general idea of the LED. A further pulsed operation with signal generators was conducted on the LED, which will be explained in detail in Chapter 6 along with the implementation of switching and modulation.

3.3.3 Switch Fixture

A switch fixture provides a platform that essentially enables the RF connectors to be mounted and a microstrip, as well as a coplanar waveguide, to be grounded. Since brass is a low-cost metal, it was selected as the main fixture, which is shown in Figure 3.8 below.

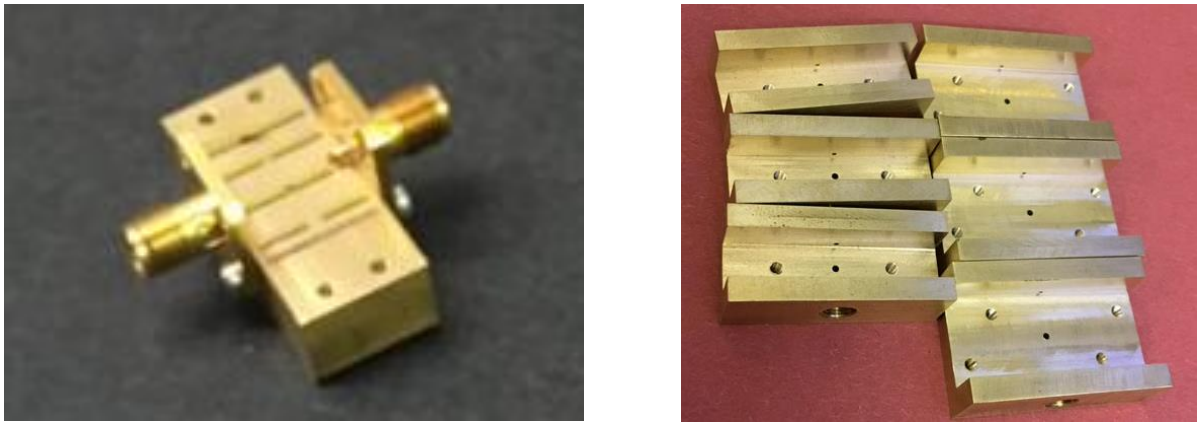

Figure 3.8 Photographs of microstrip (Left) and coplanar waveguide (Right) switch fixtures

In terms of the microstrip circuits, which are mainly discussed in Chapters 4 and 6, female SMA connectors [3.22] were employed to facilitate the transition from a coaxial line in the VNA cables to the microstrip circuits. The connectors were screw-fixed with bolts onto the brass block and attached to the circuit by silver epoxy. For high frequency, as will be discussed in Chapter 5, V connectors/1.85mm connectors were used to reduce the higher modes in the electromagnetic propagation. Additional drilled and threaded holes by tapers contributed to a firmer fixture or sample holding effect. The fixture mounting and connector installation will be described in detail in subsequent chapters.

3.4 Circuit Fabrication

The fabrication techniques for the microstrip and CPW circuits involved in this study will be introduced in this section. There are two main approaches, namely photolithography and PCB laser cutting. The former involves using ultra-violet (UV) optical illumination with masks and chemicals to ensure a more accurate resolution and a good finish on the circuits. The main benefits of the latter may be its low cost, chemical-free and simple procedures. However, the accuracy and resolution are degraded by the laser-cutting technique being implemented through mechanical precision control. Also, since most thermal solutions, as involved in this technique, are extremely sensitive to ambient conditions, it is always difficult to control the depth and edges of the cut so that careful preparation and repeated test cuts are required beforehand. The

main focus of this section is the photolithography fabrication techniques and an example of PCB fabrication by laser cutting for integration purposes will be provided in Chapter 5.

3.4.1 Wafer Coating

Before the photolithography, the first process for the fabrication of a standard semiconductor circuit is the application of the metal material on the semiconductor. The material used in this project was a combination of gold and silicon. Gold was selected because of its high conductivity, oxidation resistivity and resistance to other forms of corrosion. A very thin layer of titanium was added between the gold and the silicon because this has been found to significantly improve the adhesion. The wafer structure of gold, titanium and silicon layers is shown in Figure 3.9.

Figure 3.9 Wafer Structure

Sputter coating is a technique used to depose gold on silicon. In this project, it involved using ion bombardment physics to coat the sample with gold and titanium. After the clean wafers were attached to the coater using an adhesive sticker, the chamber was evacuated in a vacuum condition. Then, a neutral gas, argon in this case, was introduced into the chamber so that the ions would collide with the metal in a high electric field and bring them onto the surface of the wafers.

3.4.2 Photolithography

The standard procedure of optical photolithography, which is also called UV lithography, will be introduced in this section. This involves using microfabrication to pattern microstrips or a CPW line of a substrate. A geometric pattern is formed by a photomask on light sensitive chemical photoresist. The photomask is firstly designed and drawn in CST. The exported image

file is then uploaded to [3.23] for fabrication. The following process generically involves cleaning, photoresist application, UV exposure with a mask, developing and etching. The initial cleaning involves removing dust, organic and inorganic contaminations on the wafer surface using a wet chemical treatment. Acetone, Methanol and Isopropanol were used in this laboratory work. Firstly, all the wafers were put onto a clean plate in a Sonicator with a water bath that made ultrasonic waves around the sample and relatively big particles of dust or impurities were shaken off by oscillation. Then, Acetone was poured onto the plate and Methanol was after 15-20 seconds before the Acetone had dried up. This was left for 20 seconds, after which Isopropanol was used following the same procedure. Finally, soft, de-ionised water that was free of minerals was used to clean the beaker holder and the wafers were dried by a compressed nitrogen gun. The sonicator and chemical solvents are shown in Figure 3.10.

Figure 3.10 Sonicator (Left), and Acetone, Methanol and Isopropanol (Right)

The second step was to apply photoresist to the surface of the semiconductor. In this project, the wafer was covered by photoresist using a spin coater [3.24]. Microposit S1805 [3.25] is a chemical photoresist that is resistant to chemical etchant in the later stages. Tweezers were used to take a wafer onto the centre of the SPIN150, where it was held by the spinning machine using a vacuum. Next, 3 to 5 drops of Microposit S1805 photoresist were applied using an injector based on the sizes of the cleaved or diced samples. The spinner was set to 5000 revolutions per minute (rpm), 30 seconds duration and 10000 rpm per seconds acceleration to dispense the photoresist onto the wafer, thereby forming an equally thick photoresist layer. After ensuring that the wafer was covered uniformly by the photoresist, samples were moved to an oven for stabilisation and baked at 90 degrees Celsius for 30 minutes. If a photoresist application failed or was unacceptable, a process called ashing was used to remove the

photoresist using a liquid resist stripper. With practice, it was possible to fabricate several wafers with similar dimensions in batches at one time for backups and averaging purposes. The corresponding devices and instruments involved in this stage are shown in Figure 3.11.

Figure 3.11 Spin Coating Machine (left) and Oven (right)

After baking, the wafers with the photoresist were exposed to intensive UV light with the desired pattern guided by the mask. As a result, unmasked regions that were exposed under the UV could be removed later by the developer [3.26] while the photoresist in masked areas did not interact with the developer, leaving the circuit pattern. This approach is called positive photoresist, since the photoresist is soluble when exposed to the developer, while unexposed areas remain stable.

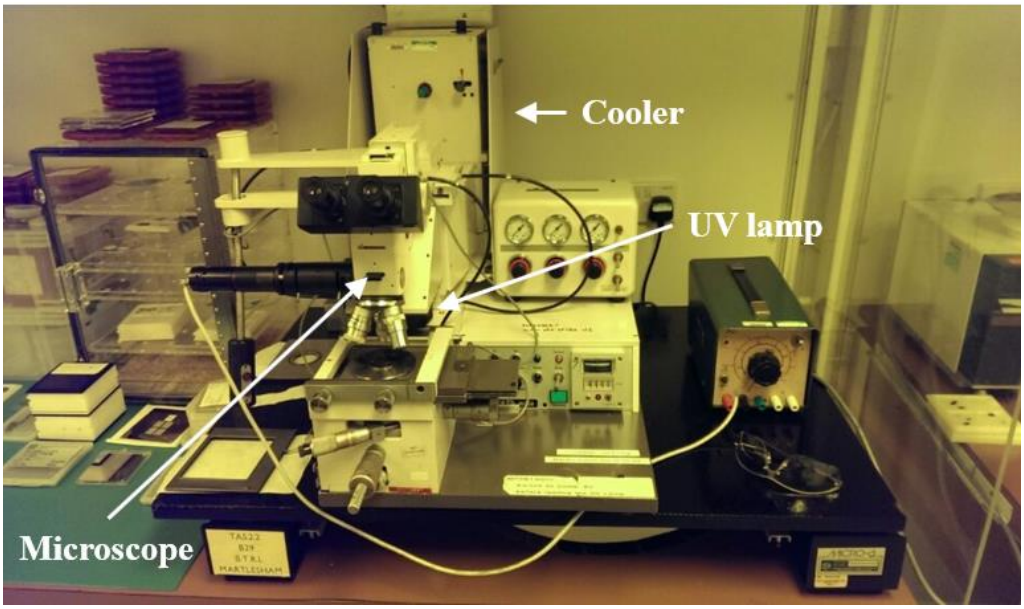

Figure 3.12 Masking and UV Exposure Device

The mask aligner, which was the device used to hold the mask and wafer, and provide UV illumination, is shown in Figure 3.12. It mainly consisted of three compartments, namely, a cooler (the top device at the back), a UV lamp (the box after the Microscope in front of the Cooler) and the microscope. The cooler used Argon and compressed vacuum air to cool the UV light device. The UV exposure time varied based on the different sizes of the wafers and it normally took 100 seconds for 2 to 3 cm^2. Care must be taken to ensure that the instrument is left to cool for 1 to 2 minutes after each use. After the UV exposure, unwanted photoresist needed to be removed by the developer, MF-319 so that the pattern from the mask would be transferred through the photoresist. Masked regions that had not interacted with the UV illumination would be protected from etchants by the photoresist. A 2-minute soaking is normally long enough for a newly-exposed wafer, but a longer time will be expected if the developer stays in the air as a result of oxidation.

Figure 3.13 MF319 Developer (Left), Bath Heater (Middle) and Etched Wafers (Right)

As previously shown in Figure 3.9, from top to bottom, the layers of the wafer had become a photoresist layer that only resided in the masked area, gold layer, titanium layer, and silicon substrate. The etching process normally aims to remove the unwanted upper layers in which the photoresist has been dissolved by the developer in the last process. Highly corrosive Trifluoroacetic acid (TFA) was used to remove the gold for typically 5 to 7 minutes, depending on the proposed wafer thickness and the etch rate. Next, titanium etching was performed by placing the wafers into a preheated 37% hydrochloric acid (HCL) liquid for 3 to 5 minutes with a heat of 67℃. Finally, the sample wafers were cleaned by de-ionised water and dried by a

nitrogen gun. The developer, bath heater, and some microstrip gaplines on the silicon substrate are shown in Figure 3.13.

3.4.3 Cleaving and Wafer Cutting

The fabrication process normally starts with a large wafer that needs to be divided into several fragments. A picture of a 4-inch wafer that arrived from the supplier before it was cut is shown in Figure 3.14. A basic rough cut can be achieved in the first stage by using a cleaver. The cleavage process in crystallographics is based on crystalline planes glass and may produce a result similar to the cleaving process employed in this project. The aim of this technique is to give the sample a flat edge and it usually causes a break perpendicular to the longitudinal axis of the wafer.

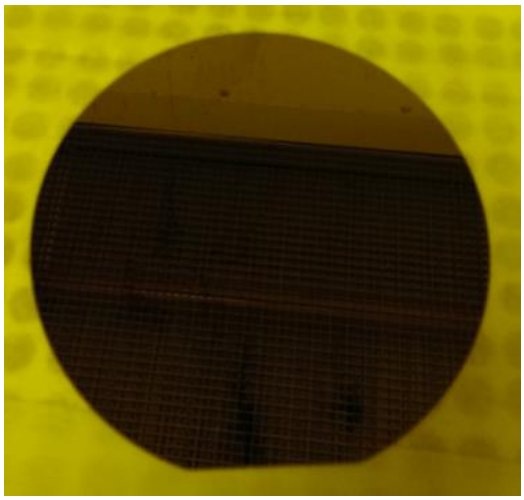

Figure 3.14 4" silicon wafer

Cleaving is used to produce roughly-sized samples. A break line can be generated by firstly nicking two edges of a wafer with a diamond pen and then hand-breaking it simply with two tweezers inserted underneath it as cushions. A more accurate sizing and dicing tool employed in this project was the Microace 3 Dicing Saw [3.27] in a clean room [3.28], which served to produce the desired sizes of samples.

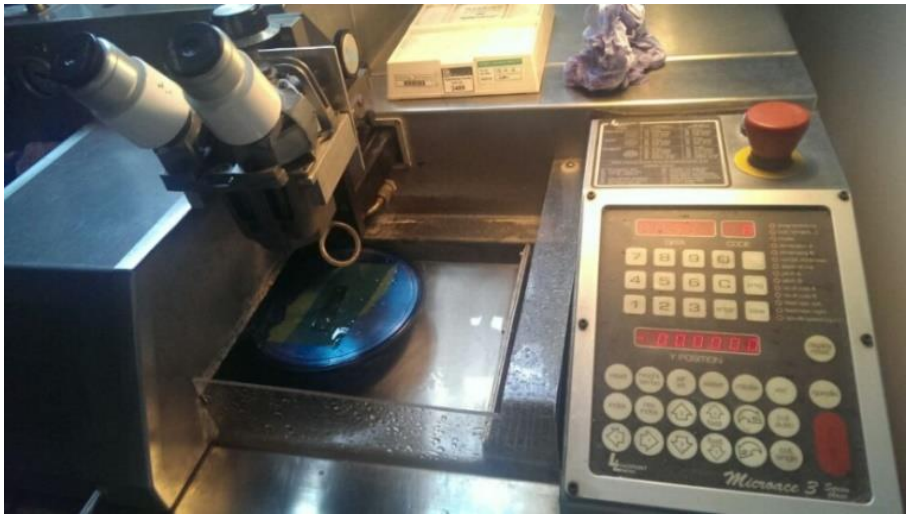

Figure 3.15 Microace 3 Wafer Cutting Machine

As can be seen from the above Figure 3.15, this dicer consisted of three main components, namely, a programming controller (keyboard on the right side), microscope operation platform and high-speed blade (boxed section on the left). Before dicing, the wafers had to be held firmly on the central tray. This problem was solved by designing a flat drum surface using a circular ring band with replaceable green and blue tapes, 0.07mm and 0.08mm thick respectively. The less sticky blue tape was firstly stretched and fastened firmly by a circular rubber band with the sticky side facing up and then the green tape was put on top of it. It is worth noting that any air bubbles between the green and blue tapes should be squeezed out by fingers to form a flat surface. Care should also be taken not to scratch or damage the surface in case the vacuum cavity is broken before the drum can be stuck and locked on the dicer tray. The final step is to put the wafers on the sticky side of the green tape using tweezers. Air bubbles should be squeezed again to ensure a flat surface before mounting the wafers on the dicer tray. Several photographs in Figure 3.16 were taken during the process for a more intuitive explanation.

Figure 3.16 Microscope Section (Left), Operation Platform (Mid) and Flat Tray (Right)

The most important thing at this stage is to carefully calculate all the data that needs to be input to the Microace 3 dicer machine. The first essential parameter is the depth of the cut. For example, here a silicon wafer was measured to be 0.525mm thick, including 10nm titanium and 5nm gold layers. The depth of the cut is calculated as 0.660mm which is the sum of the 0.525mm (wafer thickness), 0.07mm (green tape thickness) and 0.08mm (blue tape thickness). The thickness of the blade (0.3mm) also needs to be considered, as shown in Figure 3.17. A black cross is marked on the microscope lens for calibration, but it only indicates the central position of the blade and this fact needs to be considered when deciding the accurate line of the cut. In other words, if a 13.3mm long wafer is targeted, two extra 0.15mm spaces should be left on both sides in order to compensate for the thickness of the blade, as shown in Figure 3.17.

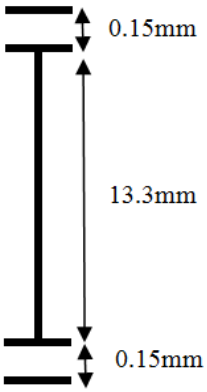

Figure 3.17 Diagram for accurate cutting calculation, blade thickness of 0.3mm, desired sample length is 13.3mm

Having completed the planning and preparation the operation can proceed as follows;

Turn on Vacuum; (eliminate air between the tray and operational platform)
Turn on Water; (for cooling the blade)
Turn on main switches for the cooler, lamp and dicer;
Turn Isolator 90 degrees clockwise;
Fit Sample ring on operational platform;
Wait for machine's self-condition check; (machine stand-by)
Turn on vacuum; (to hold sample in place)

Programme:

- press and select personalised programme and dicing mode,
- dimension width: 50mm (total area coverage of wafers to be cut)
- dimension length: 50mm (total area coverage of wafers to be cut)
- total thickness: 0.660mm (as calculated above)
- depth of cut: 0.660mm (as calculated above)
- feed rate 0.2mm per second (can be faster if no metal coated on surface)
- spindle speed: 25 (kilo rpm)
- align in vertical and horizontal axis
- water on – spindle – single cut (height sense examined)

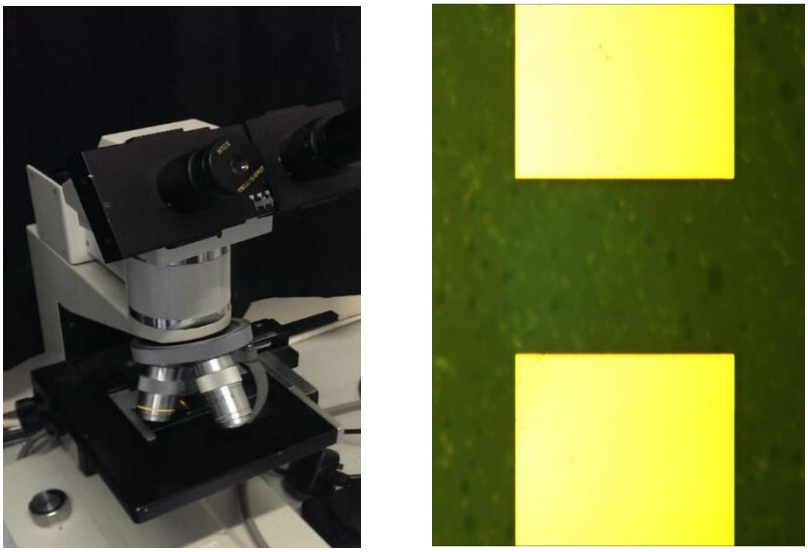

Figure 3.18 Electronic Microscope (Left), View from Digital Microscope (Right)

After the dicing, each piece of the wafer should be checked for the dimensions and cleaned before use. Figure 3.18 (Left) contains a photograph of the electronic microscope in a clean room that was used to observe the microscopic view of the microstrip shown in Figure (Right).

3.5 Conclusion

The relevant standard process of simulation, measurement and fabrication implemented in this research was described in this chapter. The chapter began with a comparison of the distributed element model and the full-wave electromagnetic analysis, which mainly served to expose the limitation of the former. Therefore, a more detailed explanation and comparison was made of the scope of the full-wave analysis, which consists of the FEM, FDTD, FDFD and FIT algorithms. The FIT method, which has evolved from the FDTD method, is distinguished by its computational efficiency and popularity in modern simulation software. The laboratory measurement work was the focus of the final part of the chapter, which included a description of the setup, which was flexible and versatile, and the platform on which optical and RF engineering interacted. Both lasers and LEDs were listed as optical source candidates for different purposes and photolithography-based and laser cutting-based semiconductor circuit fabrication approaches were also discussed.

3.6 References

[3.1] D. M. Pozar, “Microwave engineering”, John Wiley & Sons, 3th edition, 2009

[3.2] M. Costabel, “Principles of boundary element methods”, Techn. Hochsch., Fachbereich Mathematik, 1986

[3.3] R. Courant, “Variational methods for the solution of problems of equilibrium and vibrations”, Lecture Notes in Pure and Applied Mathematics, 1994

[3.4] R. L. Taylor, K. S. Pister, G. L, Goudreau, “Thermomechanical analysis of viscoelastic solids”, International Journal for Numerical Methods in Engineering, vol. 2, no. 1, pp. 45-59, 1970

[3.5] I. Babuška, U. Banerjee, J. E. Osborn, “Generalized finite element methods—main ideas, results and perspective”, International Journal of Computational Methods, vol. 1, no. 1, pp. 67-103, 2004

[3.6] K. Yee, “Numerical solution of initial boundary value problems involving Maxwell's equations in isotropic media”, IEEE Transactions on antennas and propagation, vol. 14, no. 3, pp. 302-307, 1996

[3.7] C. L. Longmire, “State of the art in IEMP and SGEMP calculations”, IEEE Transactions on Nuclear Science, vol 22, no. 6, pp. 2340-2344, 1975

[3.8] A. Taflove, M. E. Brodwin, “Numerical solution of steady-state electromagnetic scattering problems using the time-dependent Maxwell's equations”, IEEE transactions on microwave theory and techniques, vol. 23, no. 8, pp. 623-630, 1975

[3.9] F. Dominec, “Illustration of how the finite-difference time-domain method in computational”, [accessible: https://commons.wikimedia.org/wiki/File:FDTD_Yee_grid_2d-3d.svg]

[3.10] A. Dunn, R. Richards-Kortum, “Three-dimensional computation of light scattering from cells. IEEE Journal of Selected Topics in Quantum Electronics”, vol. 2, no. 4, pp. 898-905, 1996

[3.11] S. H. Chang, A. Taflove, “Finite-difference time-domain model of lasing action in a four-level two-electron atomic system”, Optics express, vol. 12, no. 16, pp. 3827-3833, 2004

[3.12] S. D. Gedney, “Introduction to the finite-difference time-domain (FDTD) method for electromagnetics”, Synthesis Lectures on Computational Electromagnetics, vol. 6, no. 1, pp. 1-250, 2011

[3.13] T. Weiland, “A discretization method for the solution of Maxwell's equations for six-component fields”, Electronics and Communication (AEÜ), Vol. 31

[3.14] ROITHNER LaserTechnik GmbH, RLCO-830-1000-C, [accessible: http://www.roithner-laser.com/ld_fiber.html]

[3.15] Thorlabs, C390TME-B, Mounted Geltech Aspheric Lens, [accessible: https://www.thorlabs.com/thorproduct.cfm?partnumber=C390TME-B]

[3.16] Thorlabs, Mounted N-BK7 Plano-Convex Lenses, [accessible: https://www.thorlabs.com/newgrouppage9.cfm?objectgroup_id=6278]

[3.17] ROITHNER LaserTechnik GmbH, RLCO-980-2000-F, [accessible: http://www.roithner-laser.com/ld_fiber.html]

[3.18] Farnell, APH-127-10-20-S, Peltier Element, Thermoelectric Cooler, [accessible: https://uk.farnell.com/european-thermodynamics/aph-127-10-20-s]

[3.19] R. A. Taylor, G. L. Solbrekken, “Comprehensive system-level optimization of thermoelectric devices for electronic cooling applications”, IEEE Transactions on components and packaging technologies, vol. 31, no. 1, pp. 23-31, 2008

[3.20] Thorlabs, Multimode FC/PC Fiber Optic Patch Cables with Ferrule Ends, [accessible: https://www.thorlabs.com/newgrouppage9.cfm?objectgroup_id=5892]

[3.21] VISHAY, TSHG 8200/8400 series, Opto-electronics, Infrared Emitters, [accessible: http://www.vishay.com/docs/84755/tshg8200.pdf]

[3.22] Radiall Straight 50Ω Panel Mount SMA Connector, Solder Termination, [accessible: https://uk.rs-online.com/web/p/sma-connectors/2956129/]

[3.23] Film Photomasks, JD Photo Data, [accessible: http://www.jd-photodata.co.uk/photo-tooling.html]

[3.24] Semiconductor Production Systems, Europe, SPIN 150, [accessible: www.physics.umu.se/digitalAssets/140/140385_spin-coater--spin150-npp-.pdf]

[3.25] MicroChem, Microposit S1800 series photoresists, electronic material, [accessible: http://microchem.com/products/images/uploads/S1800_Photoresist.pdf]

[3.26] MicroChem, Microposit MF319 series developer, electronic material, [accessible: http://microchem.com/products/images/uploads/MF319_Photoresist.pdf]

[3.27] Loadpoint Limited, MicroAce Series 3 Dicing Saw, Model: Series 3 [accessible: http://www.microp e.com/catalog/microace-series-3-dicing-saw]

[3.28] University of Bristol Cleanroom, H. H. Wills Physics Laboratory, Bristol, BS8 1TL, UK

CHAPTER 4

4. Nonlinearity and Power Handling Characterisation of a Photoconductive Microstrip Switch

4.1 Introduction

The aim of this chapter is to design and optimise a microstrip switch based on previous work [4.1] using the theory of light-semiconductor interaction discussed in previous chapters. Most of the materials shown in this chapter have been presented in [4.2] and [4.3]. The chapter begins with a review of the current standard industrial switches in order to demonstrate that there is room for improvement and illustrate the potential for photoconductive switches. Optimisation and characterisation, especially in terms of nonlinearity and power handling, are described and analysed.

4.2 Reviews and Proposals

According to the discussion in the literature review section in Chapter 1, there are several wireless communication standards that coexist and need to be accommodated by the design and implementation of reconfigurable circuitry and there is growing interest in tunable RF switching circuits. Primarily, the cost and size of systems can be significantly reduced by designing these circuits with tunability, which eliminates the need to duplicate the same circuits for every desired band. Some relatively mature techniques are mainly evident in PIN diodes, Varactors and RF MEMS [4.4-4.8]. Varactor and PIN diodes can be employed to provide low insertion loss and continuous frequency band tuning, but they cannot easily cope with high power signals because of their diode non-linear behaviour [4.4-4.6]. While RF MEMS switches give excellent isolation value and linear behaviour, there are some issues related to reliability and high-power performance, particularly "hot-switching" [4.7-4.8]. One overriding issue with all these approaches is the requirement for DC bias lines and, although this is not a major issue for simple switching/tuning networks at low microwave frequencies, it can become extremely complex with many tens to hundreds of elements. However, the requirement for complex DC biased networks can severely limit the system performance at millimetre wave frequencies and beyond. Optically tunable devices remove the need for bias circuits and a very linear performance should be achievable, since no diode junction or Schottky barrier is required within the structure.

Therefore, despite its relatively lossy behaviour [4.1], photoconductivity-based tuning in a semiconductor could be a strong candidate technology due to a number of significant benefits, which include very high operating frequencies with up to 266GHz operation having been shown in [4.9]. The potential of a very linear performance of a photoconductive switch was first studied in 2003 [4.10] based on a heterostructure of a photoconductive switch with illumination provided from a flip chip VCSEL at a maximum of 15mW. A single tone harmonic nonlinearity test was conducted at 960MHz. The second order intercept point (SOI) was measured to be 115dBm and the third order intercept point (TOI) was 65dBm with RF power up to 1W. This research demonstrated the huge potential of a photoconductive switch for a very linear performance and good power handling ability. Another investigation was undertaken later [4.11] when a single material, silicon, was examined at a higher frequency of 2GHz. The

characterised SOI and TOI were 70dBm and 63dBm respectively in a single-tone non-linearity test with 200mW incident light illumination at 980nm.

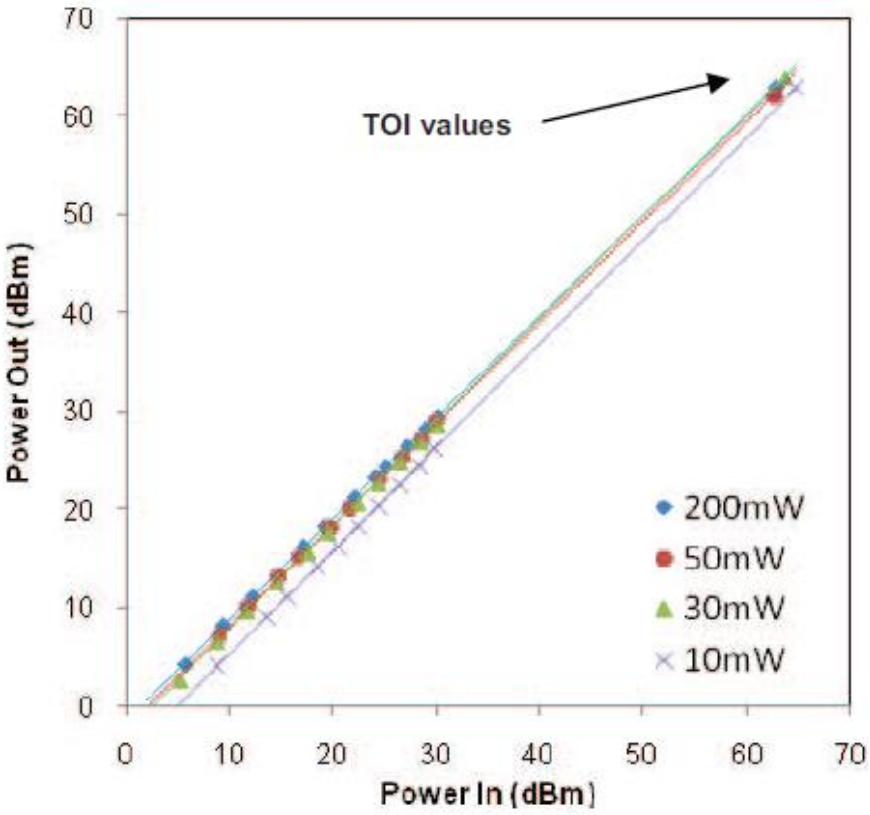

Figure 4.1 Fundamental linearity and second order and third order harmonics [4.11] for different optical power (fundamental tone at 2GHz with maximum power of 1W)

Figure 4.1 obtained from this work indicates that the linearity was constant and independent at an illumination power of over 10mW. This linearity, which is irrespective of the method and power of the controlling terminal, can be considered as an advantage compared to some other RF switches. The linearity of other conventional RF switches will deteriorate when they are not biased at the right voltage because the resistance often depends on the supplied current. On the other hand, since the RF power was limited at up to 30dBm in this experiment, it was also interesting to determine the power handling of this type of switch. A follow-up experiment was conducted later [4.12] and compression was observed when the RF input power was increased to 42dBm (~16W). Meanwhile, the silver epoxy used to fix the silicon began to melt from this point onward.

Although good results have been obtained from the above-mentioned non-linearity test on a photoconductive switch, these results were based on harmonics from a single-tone non-linearity test in which the nonlinear harmonics occur as noise signals at multiple-integer times the frequency of the input tone. This test approach cannot be a good indicator of a circuit used in a channel in which the fundamental tones are close to each other and intermodulation distortion could mask the wanted signals. Therefore, a two-tone non-linearity test for intermodulation distortion observation is firstly proposed in our study, while another study will focus on how to increase the circuit's competitiveness, since its reliability was compromised when the silver epoxy melted at 16W input in [4.12].

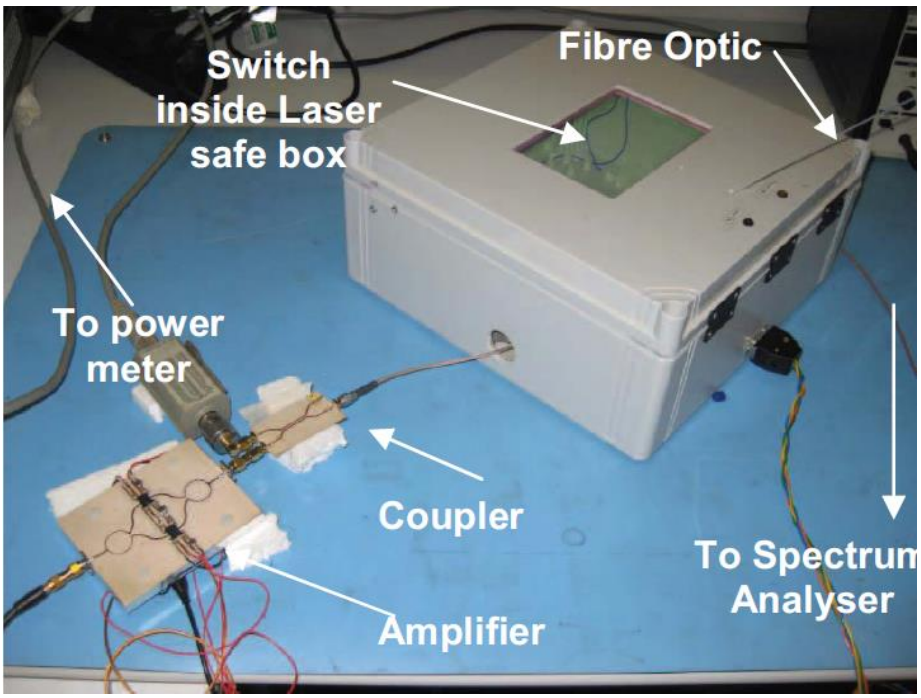

Figure 4.2 Measurement setup for nonlinearity test [4.11] with bulky laser and fibre optics

As for the packaging design, [4.10-4.12] a solution of top illumination was chosen, since this can make the system or chip integration difficult due to the requirement of a specific suspended arm to hold the optical source. Figure 4.2 shows the measurement setup described in [4.11, 4.12]. Since this bulky packaging is unrealistic in practice, a new proposal is made in this thesis and will be discussed later in this chapter.

4.3 Superstrate Microstrip Gapline Design

4.3.1 Insertion Loss Investigation

A gapline structure based on a microstrip transmission line was studied in our previous work [4.1] and a photograph of this microstrip gapline is shown in Figure 4.3. This was based on silicon substrate, which was mounted on a brass block and adapted with SMA connectors which were then connected to the VNA. The transitions for RF were provided by Anritsu K104M K-Type coax [4.13] to microstrip connectors.

Figure 4.3 Photography of a microstrip gapline switch [4.1] for top illumination

Then the DUT was fixed on a Microstage [4.14] where light was focused and incident on the gap area of the microstrip line. As explained in §3.3.1, free-space illumination was provided by a VCSEL with lenses. Figure 4.4 shows the VNA measured S_{21} results of a microstrip gapline with 0.4mm linewidth and 1mm gap illuminated by varying intensities in [4.1]. S_{21} is the forward transmission coefficient in a two-port network in a scattering parameter system [4.15] and used as insertion loss in this scenario. As shown, the insertion loss of un-illuminated microstrip gaplines was considerable, which makes it impractical for commercial use, not to mention competing with other microwave switches. Therefore, the first target was to find the optimised microstrip gapline geometry that had the lowest insertion loss in this structure layout.

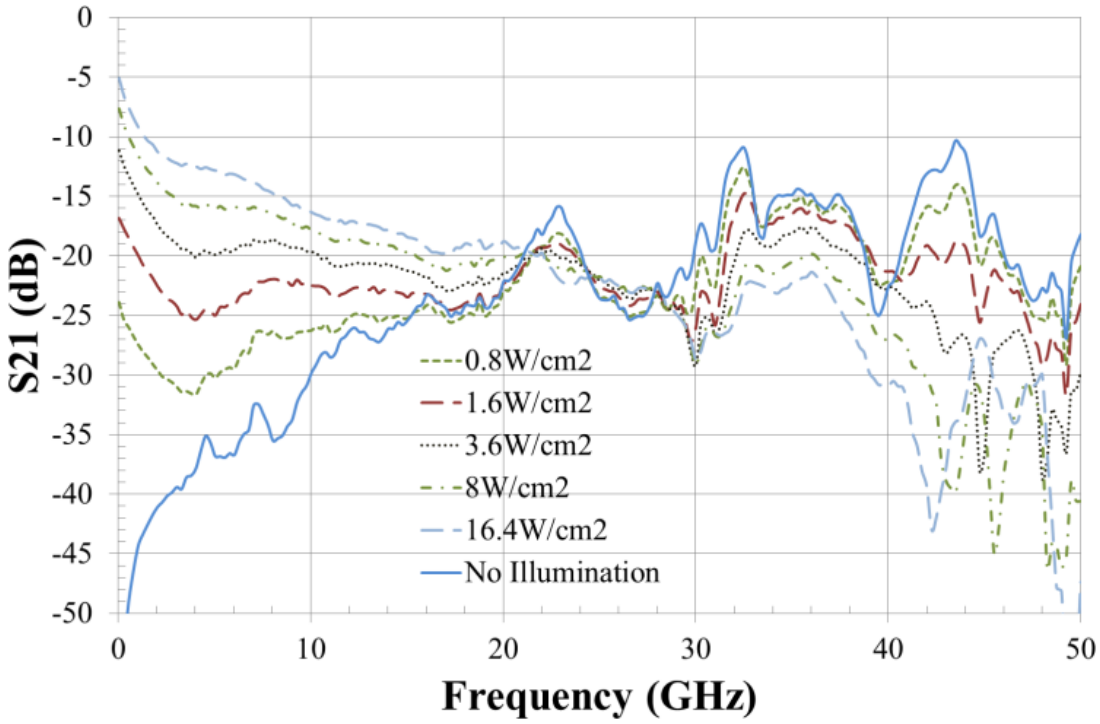

Figure 4.4 S_{21} comparison of the VNA measured results of a microstrip gapline with 0.4mm linewidth and 1mm gap in varying intensities [4.1]

CST simulation was used to find the optimal gapline geometry. To begin with, a fundamental transmission line model needed to be created as a reference indicator, which could then be modified into a gapline structure. Given the thickness of the silicon substrate ($500\mu m$) and the permittivity of silicon (11.9), the width of a transmission line of 50Ω characteristic impedance could be calculated as $400\mu m$, according to [4.16]. The CST simulated and VNA measured S-parameter result of a $400\mu m$ microstrip line are shown in Figure 4.5, which indicates good agreement. In general, the simulated curves accurately predicted the tendencies of the peaks and troughs in the measured results. The degradation in S_{21} after $10GHz$ could have been caused by a manufacturing limitation of the SMA connectors or the transition loss, as mentioned above. This initial test successfully formed a basis and reference for the subsequent research of microstrip gaplines.

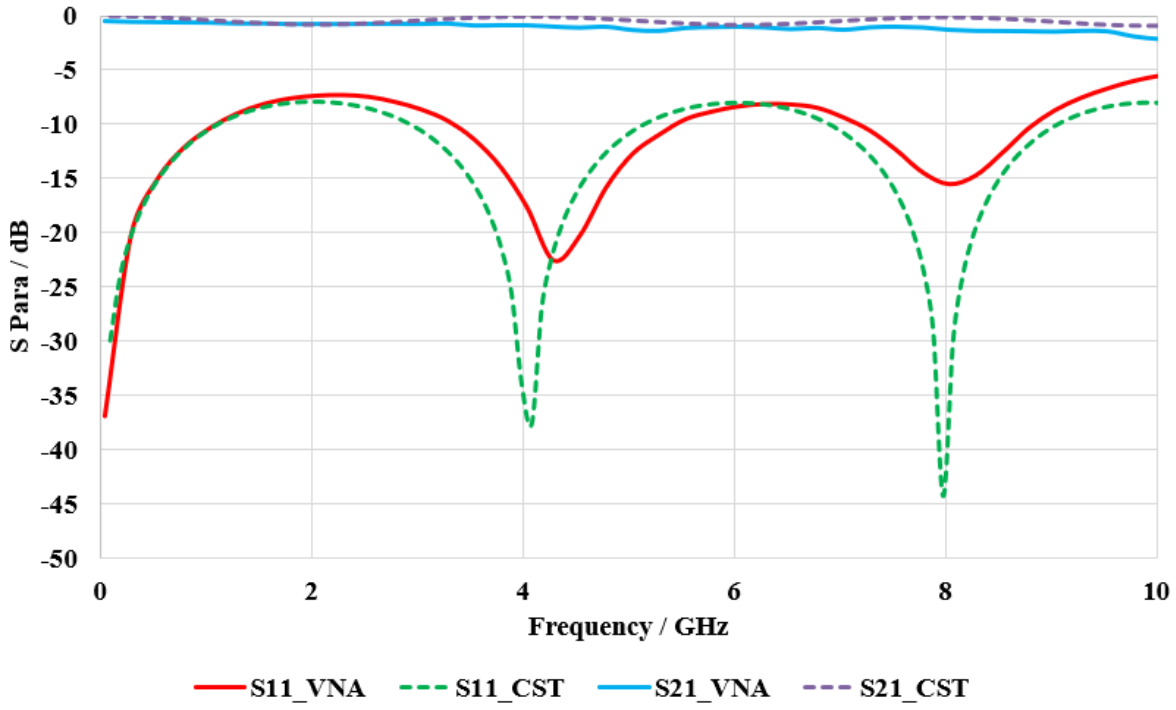

Figure 4.5 S parameter results for a CST simulated and VNA measured microstrip line with 0.4mm linewidth

Having obtained good simulated results for the above circuits, CST-based simulation can be considered to be a good and reliable technique that saves the cost of fabrication and ensures the accuracy of parametric results of a circuit analysis. The height of the silicon substrate in this gapline circuit model is fixed at $500\mu m$, relative permittivity is 11.9, and the thickness of the gold microstrip is $100nm$ to $500nm$. Hence, the optimisation focused on manipulating the other parameters, namely the surface conductivity, the gap length and the linewidth. A sensitivity analysis was conducted using the function of parameter sweep in CST, which can determine the impact of the independent variable or parameter values on the overall results, especially the S_{21}. Firstly, a relatively high conductivity in the microstrip gap region was set to a constant to ensure the independence of conductivity and comparability among different insertion losses of circuits of varying dimensions. After a few rounds of comparing the S_{21} results for varied microstrip line widths, $0.4mm$ was found to be the optimum linewidth selection. The S_{21} results of a $0.4mm$ linewidth microstrip line with varying gap lengths in ranges of $100\mu m$, $200\mu m$, $500\mu m$, $800\mu m$, and $1000\mu m$ are shown in Figure 4.6. The minimum $100\mu m$ gap length is considered to be the lower bound because the isolation value

drops significantly as the gap continues to decrease. Another reason is that the optical efficiency will decrease with the gap shrinking under the area of the illuminated spot because more energy is unused and wasted. The illumination spot is typically $1mm$ in diameter, which is similar to those of other optical sources introduced in Chapter 3.

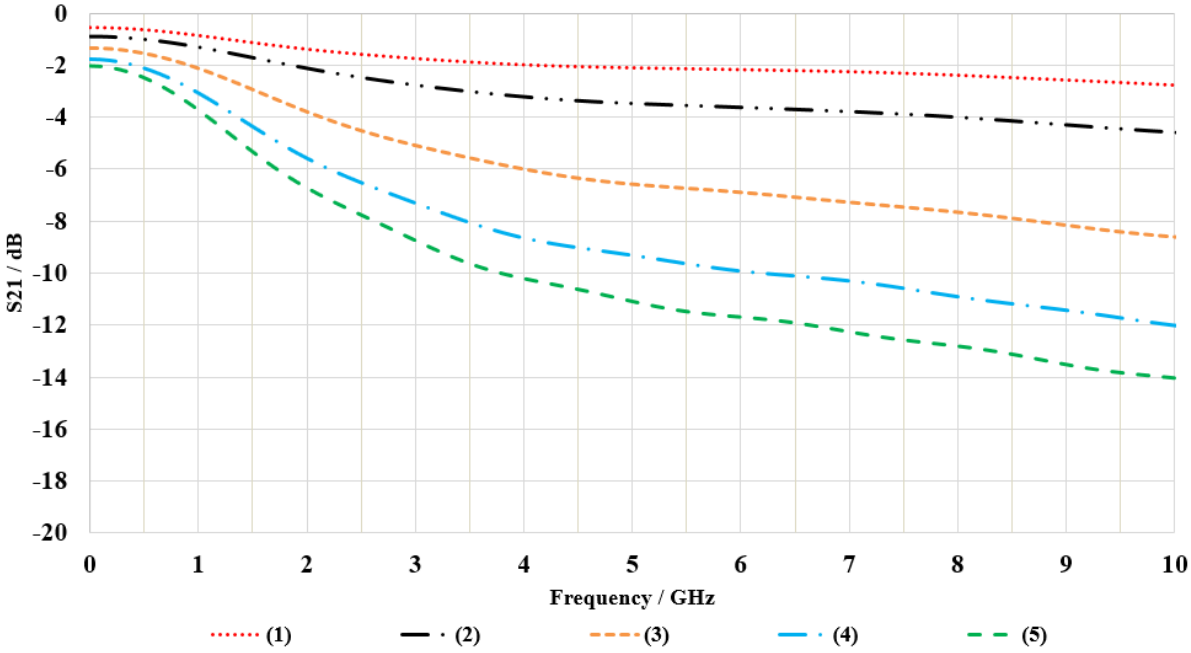

Figure 4.6 S_{21} of 0.4mm linewidth microstrip line with varying gap lengths (μm) (1)100 (2)200 (3)500 (4)800 (5)1000

The insertion losses of varying gap lengths shown in Figure 4.6 demonstrate a gradual tendency to increase as the frequency increases. The main reason for this may be the heat dissipation that occurs in every thermodynamic motion, as well as radiation loss because signals are less confined at higher frequencies. The lowest insertion loss at 10GHz is about 3dB from a $100\mu m$ gap. This loss is still considerably high before reaching the millimetre wave regime and is not ideal in practice. Therefore, the loss mechanism in this structure was analysed [4.1] with the aim of inspiring a better improved structure. A snapshot in cross-section view of the CST simulated E-field magnitude distribution for an instant of time as it propagates through the single-layer-plasma model region at 10GHz is shown in Figure 4.7. The strongest fields exist right below the plasma, which is the low-conductivity region. There are two main factors that can account for the insertion loss, the first of which is the finite conductivity of the plasma. The

order of magnitude of the metal's conductivity normally ranges from 5 to 6 in S/m, whereas the surface conductivity of the plasma only has a few hundreds of S/m. Hence, abruption may be considered to occur when the signal is propagated from the gold track of the microstrip to the plasma surface, where fringing fields tend to break away from the confinement, which causes the loss. The other loss is caused by the superposition of strong E-fields and the low-conductivity region within or below the plasma. This means that the strong fields distributed within the substrate region beneath the plasma are causing the current to drain in a highly resistive region.

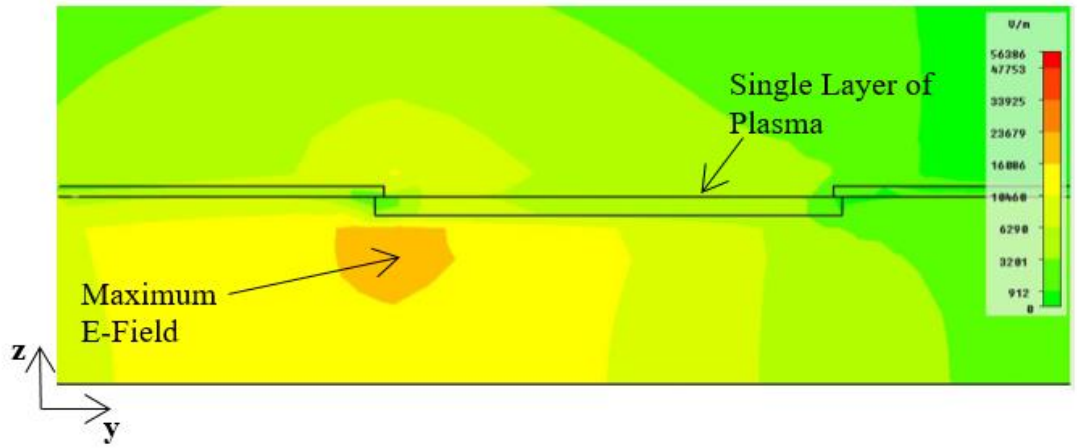

Figure 4.7 A snapshot in cross-section view of the CST simulated E-field magnitude distribution for an instant of time as it propagates through the single-layer-plasma model region at 10GHz [4.1] (Strong electric field distributed within the low-conductivity substrate region beneath the plasma – this superimposed E-field and plasma region cause energy draining and hence the loss)

4.3.2 Superstrate Structure

Since the gapline structure introduces the abruption at microstrip ends, the above-mentioned fringing loss can be inherently difficult to eliminate. However, changing this geometric superposition would reduce the other loss caused by the overlap of the E-field and highly resistive plasma region. It was suggested that this could be achieved by a superstrate structure that would split these two regions away; therefore, based on this idea and our successful work on antenna [4.17], the superstrate structure was implemented in a microwave and millimetre wave switch design. This structure for a superstrate microstrip gapline is shown in Figure 4.8.

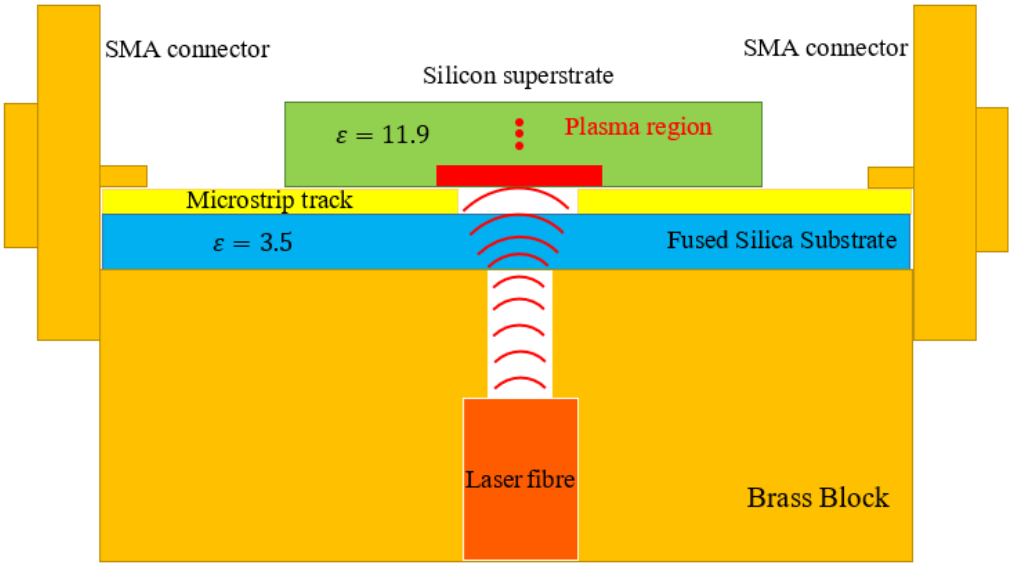

Figure 4.8 Schematic diagram of superstrate microstrip gapline switch

As shown in Figure 4.8, the silicon had flipped over to become a superstrate on top of a microstrip gapline that had a substrate of fused silica glass. As described in §3.3.1 and depicted in Figure 4.8, the optical illumination was firstly delivered by an optical fibre which was push-fitted inside the brass block fixture. The light later came from the fibre end and was incident on the silicon surface through the air and the fused silica. The air represented the space between two microstrips and the hole drilled inside the brass block fixture for holding the sample. The fused silica was highly optically-transparent with low microwave loss. SMA connectors were mounted on the brass block to provide the microstrip-to-coax transitions. This structural design has many benefits, as discussed below.

The first obvious advantage of this superstrate structure is that the above-mentioned high-loss region was eliminated due to the geometric alternation. Silicon above the microstrip circuit meant that the diffusion tail and high-loss region were away from the high microwave field region, which is expected to reduce losses.

Secondly, fused silica glass was chosen as a substrate material based on its low loss tangent (0.00006 at 3GHz) and low relative permittivity ($\varepsilon_r = 3.5$) as opposed to silicon's loss tangent (0.005 at 1GHz) and relative permittivity ($\varepsilon_r = 11.9$) which will further reduce the insertion loss [4.18]. As explained earlier in §2.3.4, the loss tangent is the ratio of the lossy reaction to the electric field to the lossless part of it. The lossy part is caused by bound charge and dipole

relaxation, which contributes to free charge conduction. Fused silica is a transparent insulator that absorbs hardly any light, as well as possessing a very high bandgap. Hence, almost no conduction region can exist around this glass, which may lead to the loss.

In terms of transparency, there is a need to ensure a high percentage ratio, since a high optical efficiency needs to be retained, despite the structural change. Fresnel equations [4.19] can be used in this case to determine the theoretical reflection and transmission for electromagnetic radiation incident on an interface of different media. Assuming normal incidence, the reflection R can be written as follows;

$$R = \left(\frac{n_0 - n_{fs}}{n_0 + n_{fs}}\right)^{\mathbf{2}} = \left(\frac{1 - 1.87}{1 + 1.87}\right)^2 = 9.2\% \qquad 4.1$$

where n_0 is the refractive index of air and n_{fs} is the refractive index of the fused silica. This calculated result implies that a maximum of 90.8% transmittance could be achieved. A follow-up experiment was conducted using the set-up introduced in §3.3.1. An optical power meter was used to record the optical power and compare the values. The only variable was whether fused silica existed in front of the sensor or not. The attenuation was found to be almost 10% and this was considered to correlate with the theoretical answer. Other factors were assumed to have little impact, such as the sample variation of the fused silica, measuring system error or device calibration error.

It is also very important to discuss the bottom-side illumination here. Bottom-side illumination through drilled conventional substrates has been shown previously [4-20], however the use of glass substrates minimises the discontinuity introduced into the microstrip line which will become much more important at higher frequencies where optically controlled switching becomes a very attractive technology. In addition, this hybrid approach with a silicon superstrate provides a good integration possibility that could be easily incorporated into large complex circuits. Finally, the use of the brass block ground plane as heat sink has considerable potential and suitability for high power applications.

4.4 Switch Characterisation

4.4.1 Simulation

Before moving to the fabrication and measurement to characterise the switch's properties, it is recommended to use simulation approach to find the optimum circuit dimensions first. Computer aided design and simulation always give effective, systematic and low-cost options compared with fabrication and manufacture. Detailed discussion has been carried out in §3.2 and FIT-based CST simulation solver has been selected for its advantage on broadband analysis. Figure 4.9 shows the top view of such basic superstrate microstrip gapline model in CST. The brass block behaves like the ground plane, fixture and good heat sink for this device under test (DUT). For the ground plane, both the simulated connectors with coax excitation ports and the fused silica substrate have been ensured to be aligned and sit on the same height which is represented in z-direction.

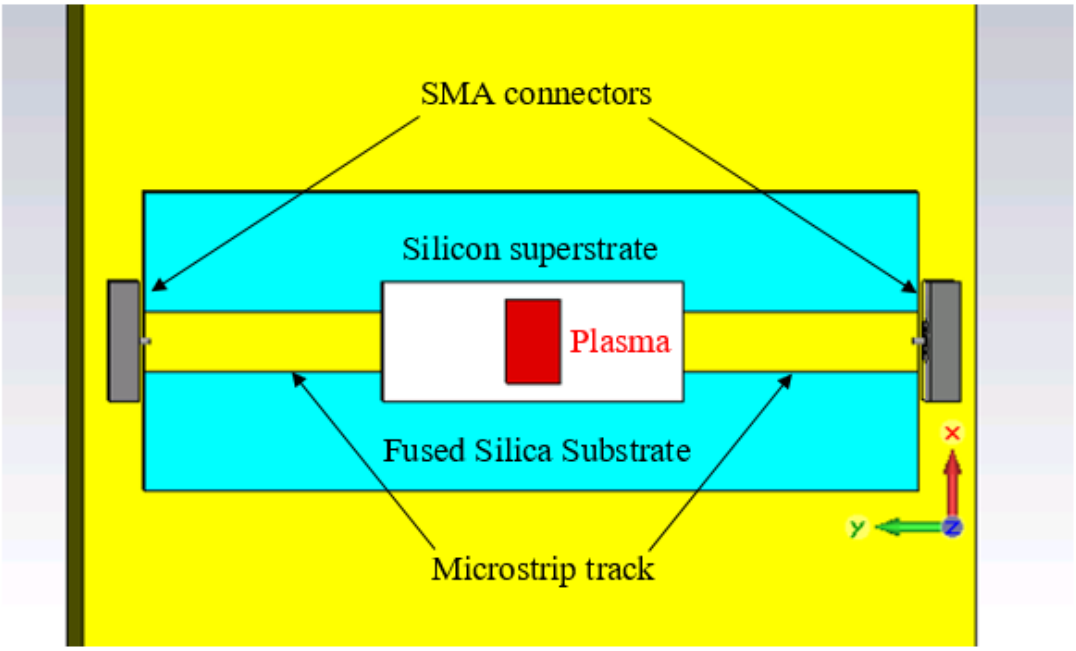

Figure 4.9 Top view of a superstrate microstrip gapline in CST (showing coax connectors, substrate, superstrate and microstrip)

The electron-hole plasma region can be represented by a series of varying conductivity layers as quantified in §2.3.3. In the multi-layer model, each differentiated layer of the created plasma region was assigned with varying conductivity and permittivity values in terms of the material properties. Figure 4.10 shows the conductivity profile used in this work. Figure 4.11 shows the ten cascaded conductive layers derived from Figure 4.10.

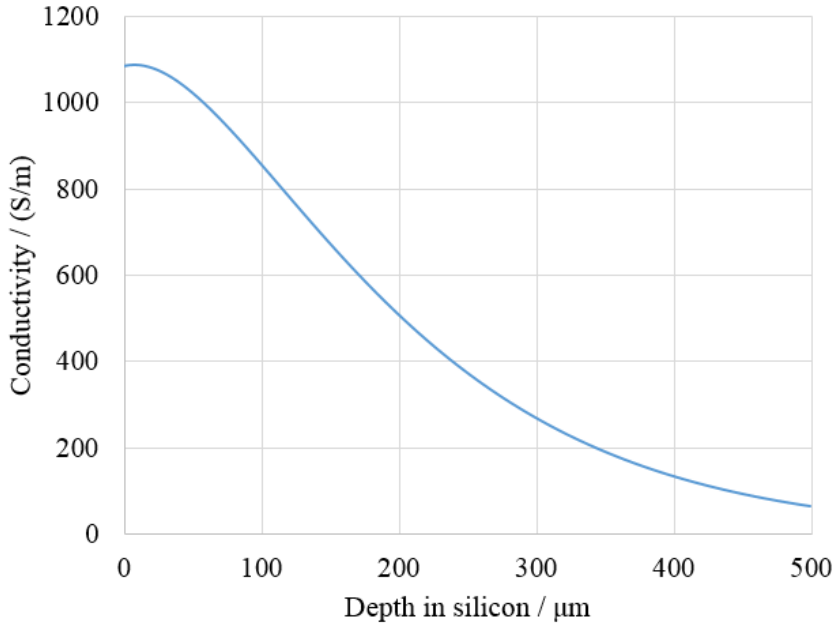

Figure 4.10 Conductivity vs. Depth below the surface of silicon superstrate

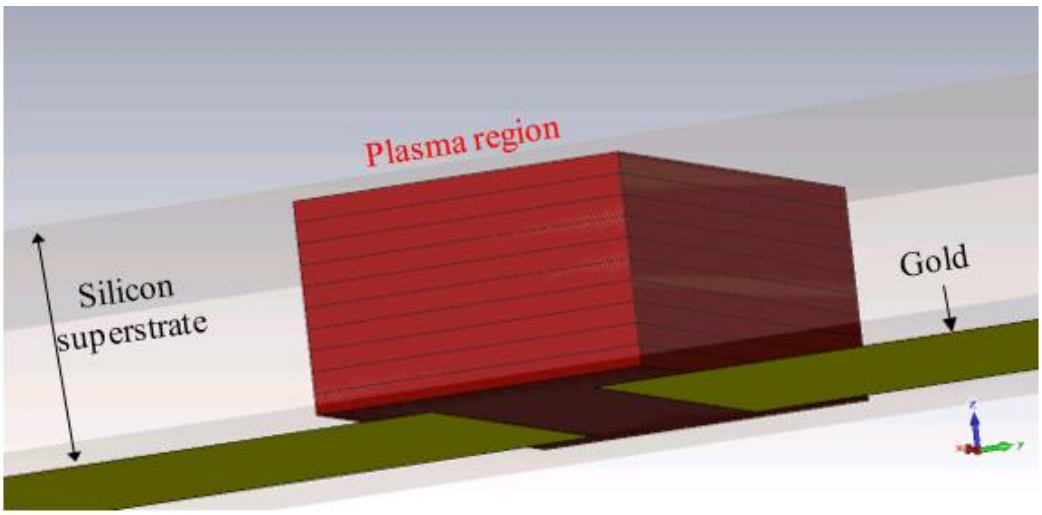

Figure 4.11 Multiple-plasma-layer model within silicon superstrate in CST view

A sensitivity analysis was conducted again through the parameter sweep function in CST to compare the circuits with various dimensions. Based on the experience of §4.3.1, the linewidth was calculated at around $1mm$ for a $50Ohm$ transmission line that now had a substrate of fused silica. Therefore, this was the reference linewidth to begin the parameter sweep. After checking and fixing the linewidth of $1mm$ for other parameter sweeps in a simulation to obtain the optimum insertion loss, an investigation of the optimisation of the gap length was initiated. The surface conductivity was set to 1000S/m, which is the same as that used in the sensitivity analysis for a standard microstrip gapline mentioned above. The S_{21} of a superstrate microstrip gapline of $1mm$ linewidth and varying gap lengths in this illuminated condition is shown in Figure 4.12 and it can be seen that the insertion loss is now much lower than for the silicon substrate case shown in Figure 4.4 as had been expected. Since insertion loss generally rises with an increase in the gap length, a $0.1mm$ gap length gives the lowest insertion loss in this case. In terms of switch performance the dark-state insertion loss, or isolation of the switch is also critical parameter and also needs to be assessed. Figure 4.13 shows the S_{21} of a superstrate microstrip gapline of $1mm$ linewidth and varying gap lengths in a dark condition without any illumination. The isolation values for this switch are given in this graph, which show the degree of attenuation of an unwanted signal when the switch is off. A trade-off was found to be necessary between the insertion loss and the isolation value. As the frequency of interest is set at 2GHz, to achieve a good trade-off between isolation and insertion loss, a gap of 0.4mm was chosen eventually.

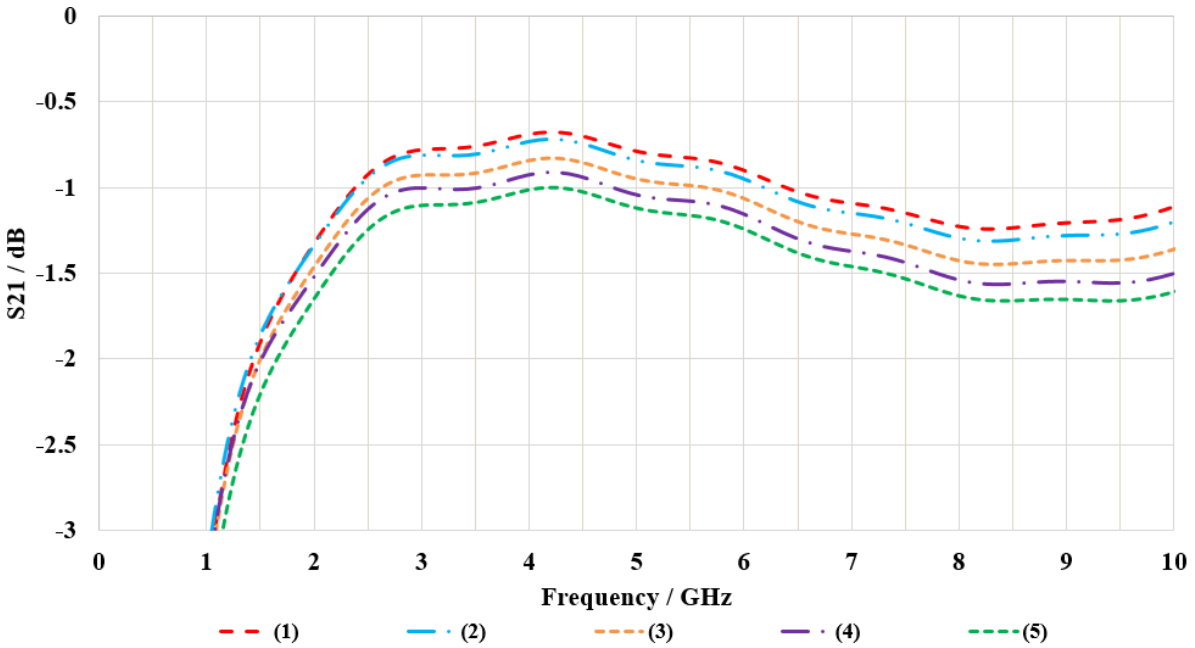

Figure 4.12 Simulated S21 results for a superstrate gapline of 1mm linewidth with varying gap lengths (1)0.1mm (2)0.2mm (3)0.3mm (4)0.4mm (5)0.5mm and surface plasma layer conductivity 1000S/m

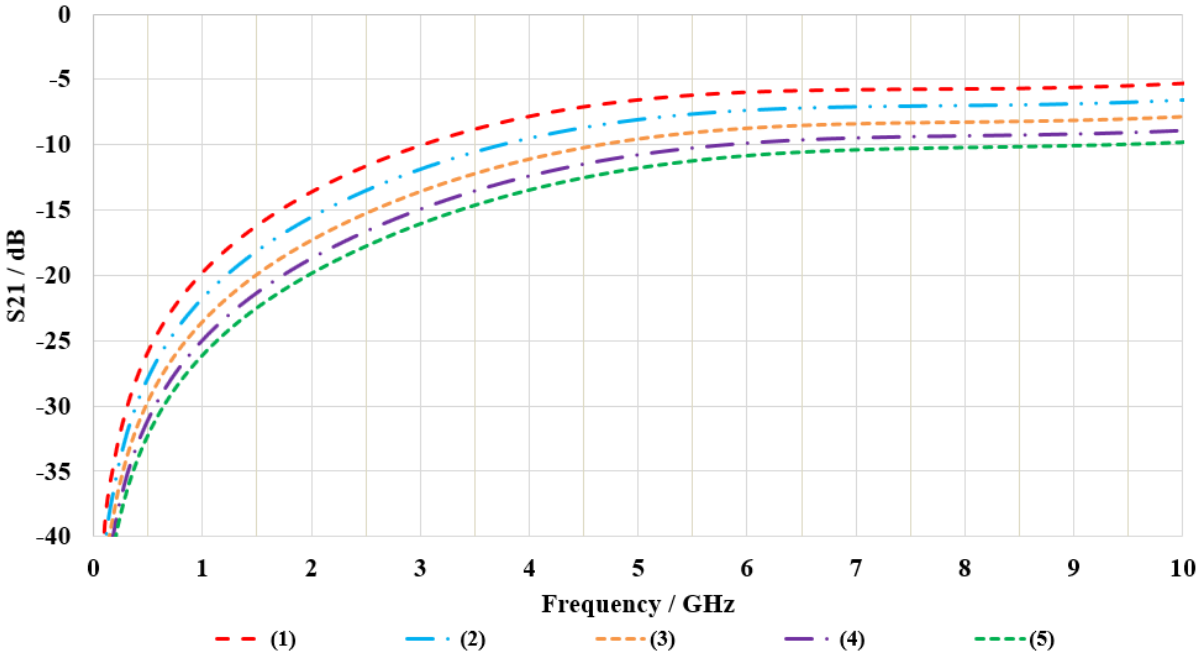

Figure 4.13 Simulated S21 results for a superstrate gapline of 1mm linewidth with varying gap lengths (1)0.1mm (2)0.2mm (3)0.3mm (4)0.4mm (5)0.5mm in dark conditions (no plasma generated)

With regard to the size of the superstrate patch in a sensitivity analysis, almost identical S_{21} results were found from the CST simulations, either when the patch length increased along the y-direction or the patch width varied along the x-direction, as indicated in Figure 4.9. Hence, it seemed that there was no straightforward approach or simple answer. Based on considering the practical or experimental handling and fixing, it is necessary for the superstrate patch to cover the total area of the gap between two microstrip tracks. This means that the patch width should be larger than the microstrip linewidth, $1mm$, and the patch length should be larger than the microstrip gap, $0.4mm$, although a minimum of $2mm \times 2mm$ is desirable for ease of handling and aligning the wafer. Further details about making a decision on the superstrate patch size will be provided in the next section along with the measured results.

4.4.2 Fabrication and Measurement

The fused silica was $500\mu m$ thick and polished on both sides. The silica wafer was initially cleaned using solvents to remove any dust and impurities on the surface, immediately after which it was sputter-coated with 5nm titanium and 350nm gold in an ambient argon atmosphere. This 5nm titanium middle layer was used to improve the adhesion between the gold and the fused silica. Photoresist was then spin-coated on the wafer, which was exposed through a mask to define the circuit. The photoresist was then developed and trifluoroacetic acid (TFA) and hydrochloric acid (HCL) etches were used to remove the gold and titanium respectively. Figure 4.14 contains a microscope magnified view of a microstrip gapline immediately after fabrication with a linewidth of 1mm and a gap of 0.4mm. The fused silica glass substrate ($\varepsilon_r = 3.5$) was mounted on a machined brass block and a piece of silicon ($\varepsilon_r = 11.9$), which was held in place using sellotape. Sellotape was initially chosen based on its low-loss electromagnetic property, but there are more discussions and experiments to decide on the fixing material later. The superstrate silicon was a lightly doped n-type wafer with <100> orientation and resistivity>10KΩ.cm and optical illumination was provided by a 980nm wavelength fibre coupled laser diode (Roithner Lasertechnik). This was chosen due to the high carrier generation efficiency at this wavelength. The fibre laser was coupled through a hole in the block that was designed to have the minimal effect on the microwave response. An electron-hole plasma region was generated in the silicon with the high conductivity region close to the microstrip gap. The lossy, lower conductivity tail was contained within the silicon, far from the

high microwave field region in the gap and the fused silica substrate, which substantially reduced the loss compared to previous configurations [4.1].

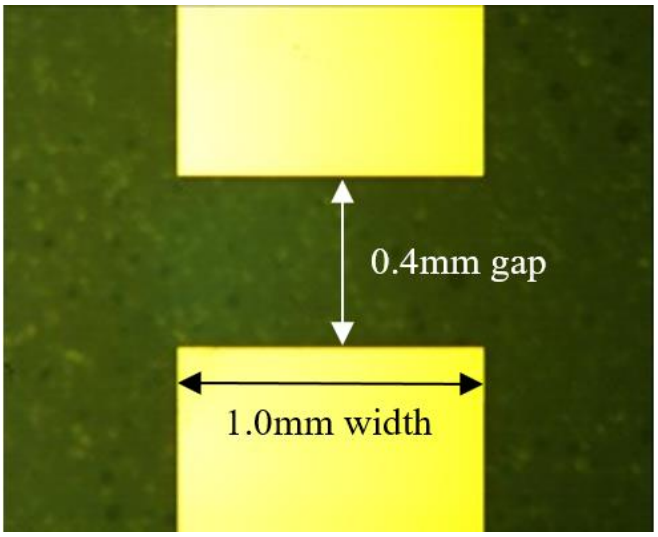

Figure 4.14 Microscope view of a 0.4mm gap in a 1mm wide microstrip line on fused silica glass

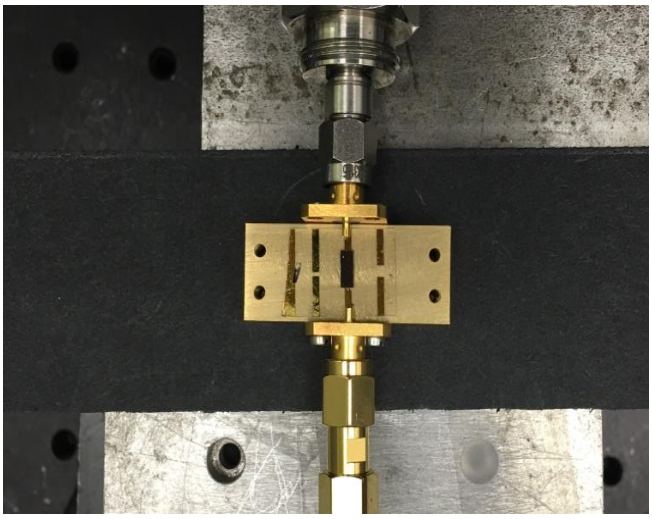

Figure 4.15 Top view of a test circuit mounted on a brass block and connected with coax to VNA

The last section contained a rough estimate of the superstrate patch sizes from simulation and practical consideration. Several tests were undertaken of various superstrate patch sizes to continue to determine the optimum dimensions for this circuit. Firstly, patch lengths were found to have a negligible impact on the results. A $5mm$ length was selected based on its ease

of handling. The S_{21} results for a superstrate switch with various superstrate patch widths are shown in Figure 4.16.

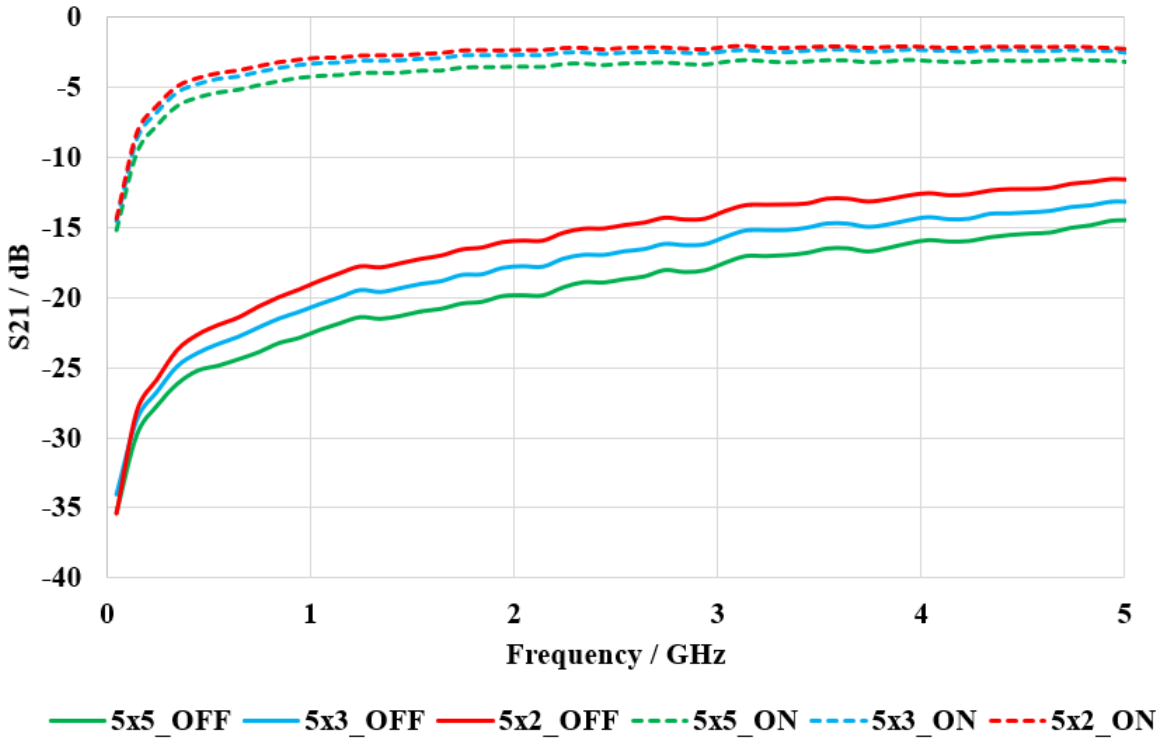

Figure 4.16 Measured S21 results for superstrate gapline of 0.4mm gap and 1mm linewidth with superstrate length of 5mm and varying widths in dark (_OFF) and illuminated (_ON) conditions

As can be seen from Figure 4.16, a combination of 5mm long and 2mm wide superstrate patches caused the least insertion loss while still maintaining a good isolation value. The VNA measured and CST simulated results of a superstrate microstrip gapline switch in illumination ON and OFF conditions are compared and illustrated in Figure 4.17. The microstrip gapline had a linewidth of $1mm$, a gap length of $0.4mm$ and a substrate of $0.5mm$ thick. The dimension of the superstrate patch was $5mm \times 2mm \times 0.5mm$. In the case of illumination ON, there was almost $400mW$ of optical power concentrated on a $1mm^2$ circular spot. Hence, the intensity of this illumination was calculated as $51W/cm^2$. In the CST simulation, the surface plasma conductivity was calculated as $941S/m$ based on the quantified analysis in §2.3.

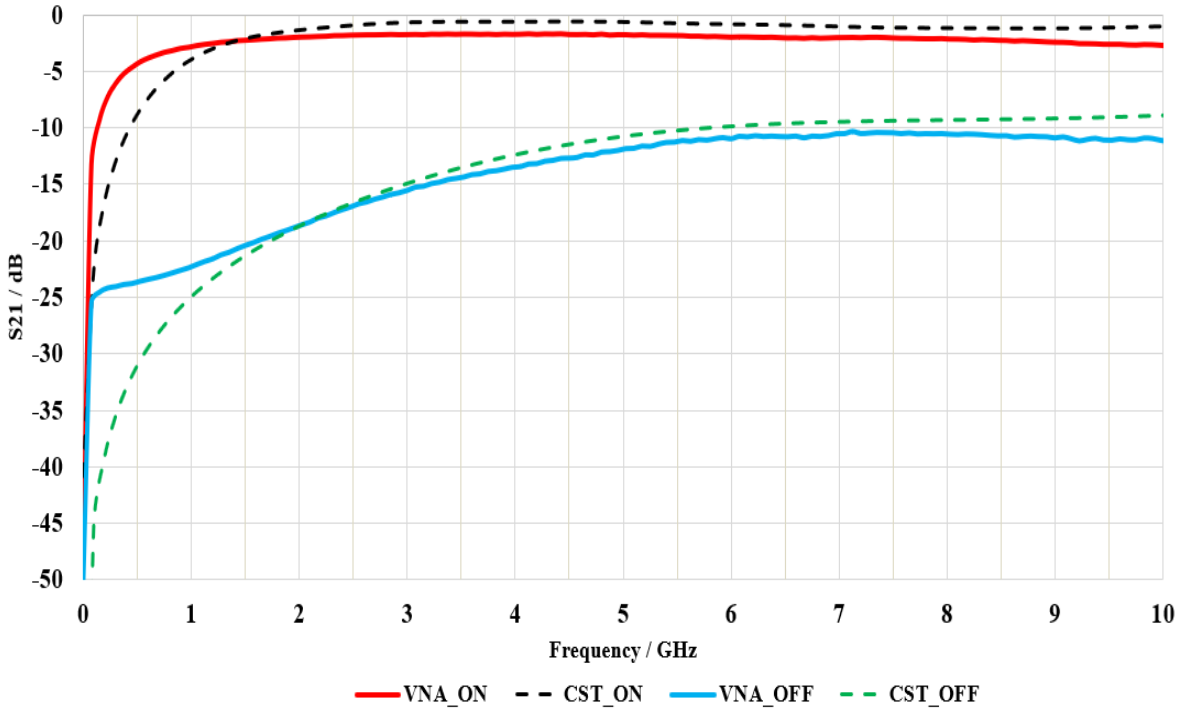

Figure 4.17 S21 Comparison of VNA measured and CST simulated results of a superstrate switch in illumination ON and OFF conditions

According to this graph, there is reasonable agreement between the measurement and the simulation. The simulated and measured curves closely matched one another after $1GHz$, whereas the standard CST approach failed to accurately simulate this trend before $1GHz$. Therefore, distributed element modelling was then implemented with aid of AWR Microwave Office [4.21] to compensate for this disagreement.

4.4.3 Distributed Element Modelling

The derivation of a distributed element modelled equivalent circuit will be described in this section and then compared with the CST simulated and VNA measured results. The plasma models have been derived at the end of microstrip line stubs in previous work [4.22, 4.23], while this work provides the extension of modelling a gap region inserted between two equivalent transmission lines. It will firstly aim for a superstrate microstrip gapline model at dark state. Then, the parameter values attained in the model at dark state will be tested in

condition with illumination so as to prove the assumption and verify the accuracy of such models. Measured results of S_{21} are used for the value acquirement for the equivalent circuit component.

The distributed element for a standard microstrip gapline modelling has been proposed in [4.24]. It consists of a model of three capacitors and a pair of symmetrical microstrip transmission lines that are discussed in §3.2.1. This equivalent circuit modelling has since been widely accepted and used in many researches [4.25]. Figure 4.18 shows the equivalent circuit representation of the gap region in a standard microstrip gapline by discrete element components,

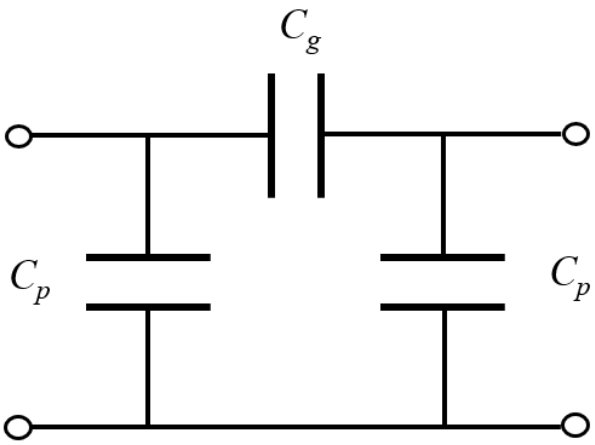

Figure 4.18 Distributed element modelling of microstrip gap region

where C_g is the gap capacitor between symmetrical microstrip lines while C_p is the shunt parallel capacitor between the microstrip track and the ground on each side of the gap.

In the superstrate gapline case, the contact between the superstrate patch and the microstrip tracks are expected to have the same capacitive effect, represented by C_c, but with different values compared with that in the circuit in Figure 4.18. It can be difficult to start the process of comparing the measured and simulated results to directly obtain the values of each individual component. However, at low frequencies, the capacitors can be considered as open circuits, and thus resistors will primarily determine the S_{21} values. Henceforth, the plasma region can

be a breakthrough point. Combining the physics models derived in Chapter 2, the plasma region has been assumed to be represented by a series-thru element [4.25] quantified in impedance values. It can be expressed analytically as,

$$S_{21} = \frac{2}{\frac{Z}{Z_0} + 2} \qquad 4.2$$

where Z_0 is the characteristic impedance of the system and thus is 50Ω in this case. Z is the series-thru impedance which includes the inductive and resistive effect across the plasma region. The value of Z in complex form can be derived from the measured S_{21} in magnitude and phase data results. To simplify this model, lossless environment in low frequency region has been made and hence resistor component is used with the magnitude to represent the plasma region. Data from the S_{21} result in Figure 4.16 has been extracted and used to work out the plasma resistance, R_p. After the resistance derived, capacitance values can be determined by comparing with the measured data plot in Figure 4.17. Figure 4.19 shows the proposed circuit diagram with discrete element components in representation of a superstrate microstrip gapline in the simulation software, AWR Microwave Office (MWO) [4.21].

- Ports ($P = 1$ and $P = 2$) are the simulated coax ports connected to the VNA. $50Ohm$ source and load impedances have been set for the whole system.
- $MSUBs$ ($SUB1$ and $SUB2$) are microstrip line element models in each side of the gap. Detailed parameters in these models have been set with values in reference to the fabricated superstrate switch, which primarily includes the (Nominal) relative permittivity (E_rNom) E_r, substrate height H, and microstrip thickness T.
- As explained above, $C1$ is the gap capacitor, C_g, $C2$ and $C3$ are the shunt parallel capacitors, C_p, $C4$ and $C5$ are the contact capacitors, C_c, $R1$ is the plasma resistor, R_p

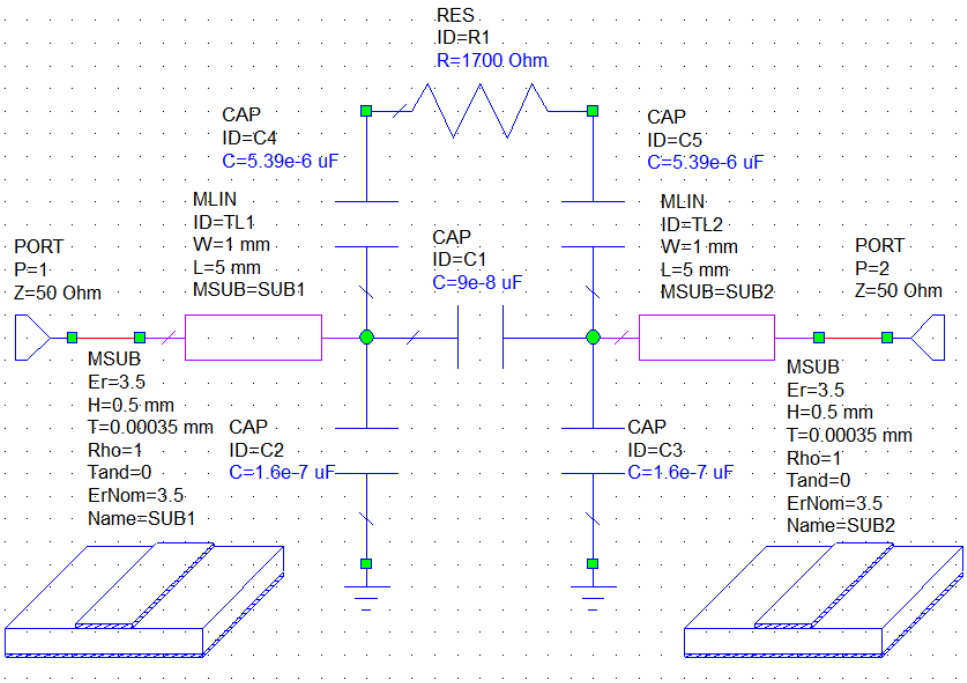

Figure 4.19 discrete element model of superstrate microstrip gapline in AWR Microwave Office

It has been found that R_p and the pair of $C4$ and $C5$ predominately determine the slope of the S_{21} curve below $1.5GHz$. As capacitances have been evaluated by comparing the simulated and measured results, the only variable now is the plasma resistor. To further simplify the model and predictively simulate the circuit instead of comparing results to find the resistance after measurement, a fundamental physics formula has been implemented for use below by linking the electrical resistivity,

$$R_p = \rho \frac{l}{A} = \frac{l}{\sigma w t} \qquad 4.43$$

where ρ is the resistivity, σ is the conductivity, l is the plasma length along the microstrip line, A is the cross section of the plasma which can be decomposed with the plasma width w and the plasma thickness t. By using this formula, the plasma region has been modelled as a single-layer resistor. The resistance value in dark state derived by 4.3 is then assigned into the MWO model. Figure 4.20 shows the S_{21} comparison among the VNA measured, CST simulated and MWO simulated results in both illumination ON and OFF conditions. For the case of switch with illumination ON, plasma resistor has been recalculated by 4.3 with adapting the new resistivity from an optical intensity change. Modelled capacitors remain unchanged as they were with illumination OFF.

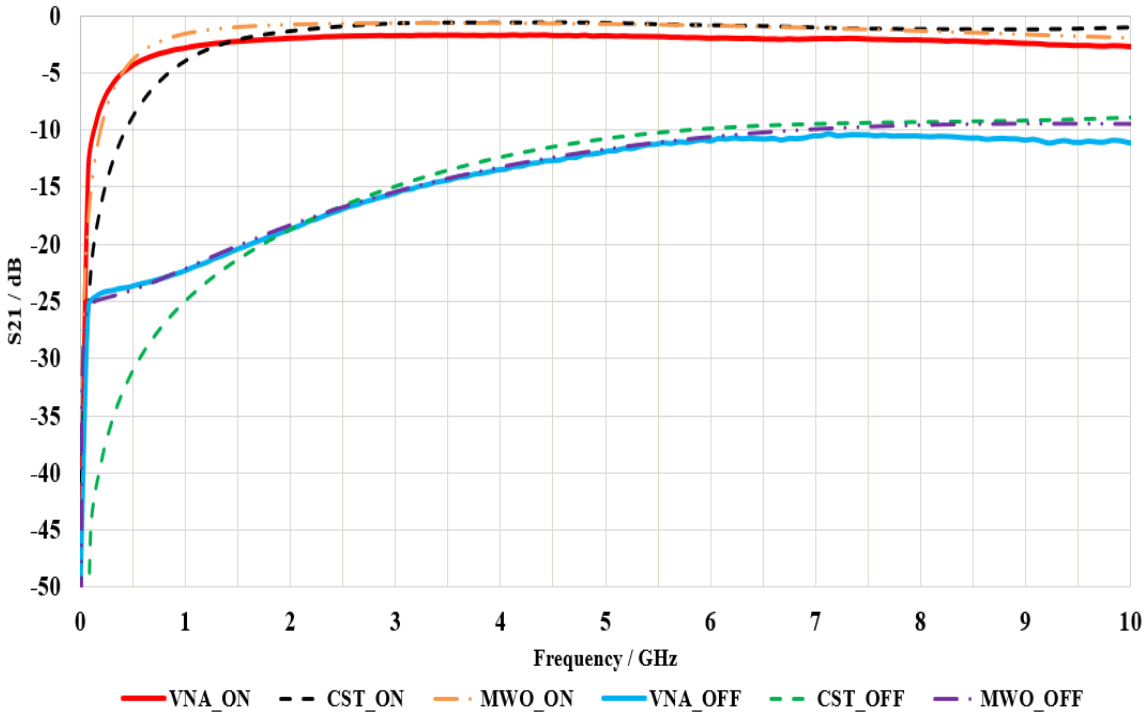

Figure 4.20 S_{21} comparison of VNA measured, CST simulated and MWO simulated results for a superstrate switch in illumination ON and OFF conditions

Figure 4.20 shows good agreement between the MWO simulated and VNA measured results for both cases of illumination ON and OFF. This means that the above derived simplified discrete element modelling has been verified for generalised use. Although MWO simulated result shows good agreement with measured result, especially in the low frequency region below $1.5GHz$, this approach has been implemented based on a single layer plasma model and several ideal assumptions which mainly disregard the phase change. The adaptability has been theoretically limited to certain frequency range by discrete element modelling. It can be improved with more discrete element involved, but a number of pre-calculations are always required, especially when phase and plasma resistor are varied. In contrast, the full-wave simulation tool, CST, still shows an overall strength with electromagnetic field analysis. More detailed discussion and improvement on CST modelling will be followed in §4.6.3.

4.5 Non-linearity Characterisation

After successfully and accurately characterising the insertion loss and isolation of a superstrate microstrip gapline switch, the nonlinearity characterisation that has equally important parameters for high-power RF switch design will be examined in this section. A nonlinear system is a system in which the relationship between the output and the input signals is not proportional. This may cause unpredictable and counterintuitive changes, which can be detrimental to the signal recovery and a noise analysis after a distance of transmission in telecommunication. Moreover, output power efficiency is crucial, since the performance ratings are affected by power consumption and heat dissipation. This work was undertaken based on the proposal of a full two-tone linearity test.

4.5.1 1dB Compression and Third-Order Intercept Point

If communication systems devices such as switches, amplifiers and mixers are nonlinear, harmonic signals will be produced at the output terminal. Normally, the second, third and higher harmonics can be easily filtered out since they are usually outside the bandwidth of the device. Hence, a single-tone nonlinearity analysis may not be sufficiently robust to characterise the device.

In real systems multiple input signals can occur simultaneously and harmonics from these signals can mix with fundamental tones to produce interference signals close to the original signal frequencies. These signals are called intermodulation distortion (IMD) products and they are not easy to eliminate, since they are within the bandwidth of the device. Thus, a third-order intercept point (IP_3), which is based on a two-tone nonlinearity test, is proposed to be a good indicator of a nonlinear system and device. A low-order polynomial modelling can be used to quantify the nonlinearity of a device by means of Taylor series expansion.

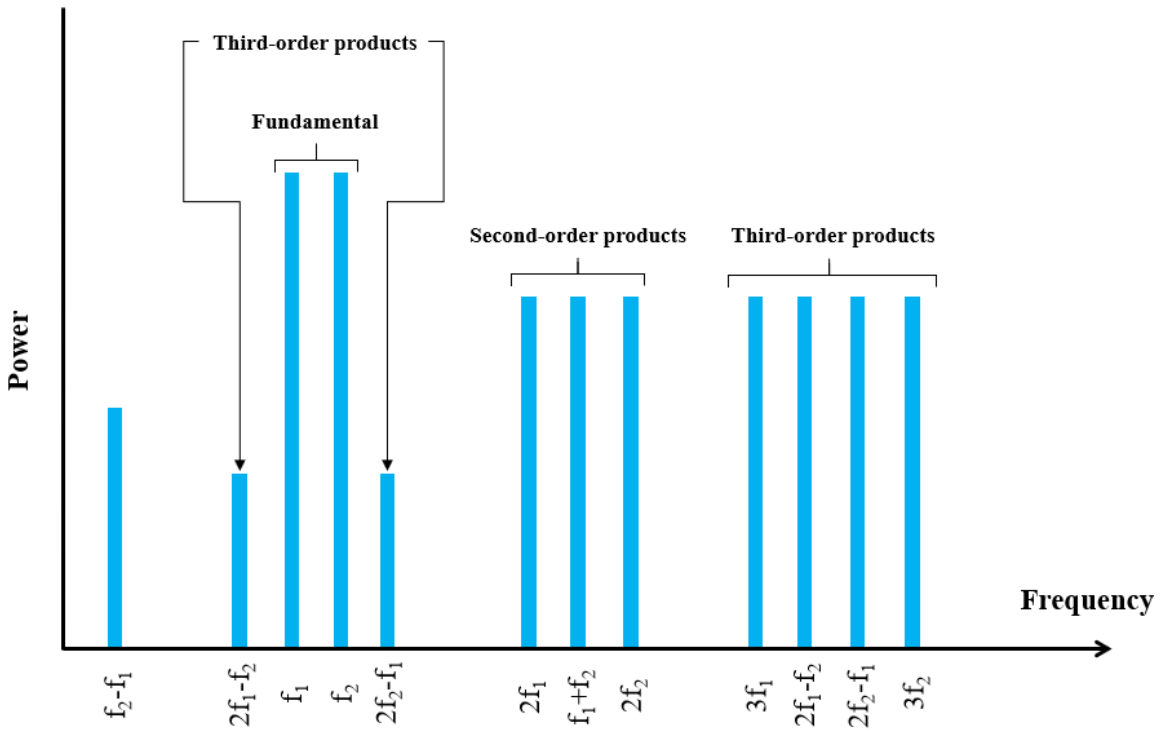

Figure 4.21 Example of two fundamental tones, the harmonics and their higher-order intermodulation distortion products in frequency domain

Two fundamental signal tones, f_1 and f_2, the harmonics and their higher-order IMD products are depicted in Figure 4.21. IMDs, $f_1 + f_2$ and$f_2 - f_1$, are produced from the second-order distortion, but they can be very easily filtered out, since their frequency spacing away from the fundamental tones is relatively wide. However, $2f_1 - f_2$ and $2f_2 - f_1$ are the most problematic third-order IMD products, which are those adjacent to the two fundamental input signals in the frequency regime, as illustrated in Figure 4.21. This is the basic knowledge to derive IP_3 in a two-tone nonlinearity test. The next important step is to plot a curve of output power vs. input power for this DUT. For a linear device, a straight line can be drawn as shown in Figure 4.22. However, the device will not respond like this in practice because, as the input power continues to increase, the curve will flatten, which means that the gradient of the line will begin to decrease at some point. This means that saturation can be reached eventually at some high signal levels, which tends to result in a nonlinear response and distortion, such as harmonics and intermodulations. Hence, it is interesting to determine the point at which the compression starts to occur. This point is defined as 1-dB compression point (P1dB) [4.15] when the input

power incurs a 1dB decrease from the expected linear growth in the output power. This is noted in Figure 4.22 as the 1dB drop from the theoretical response to the actual response.

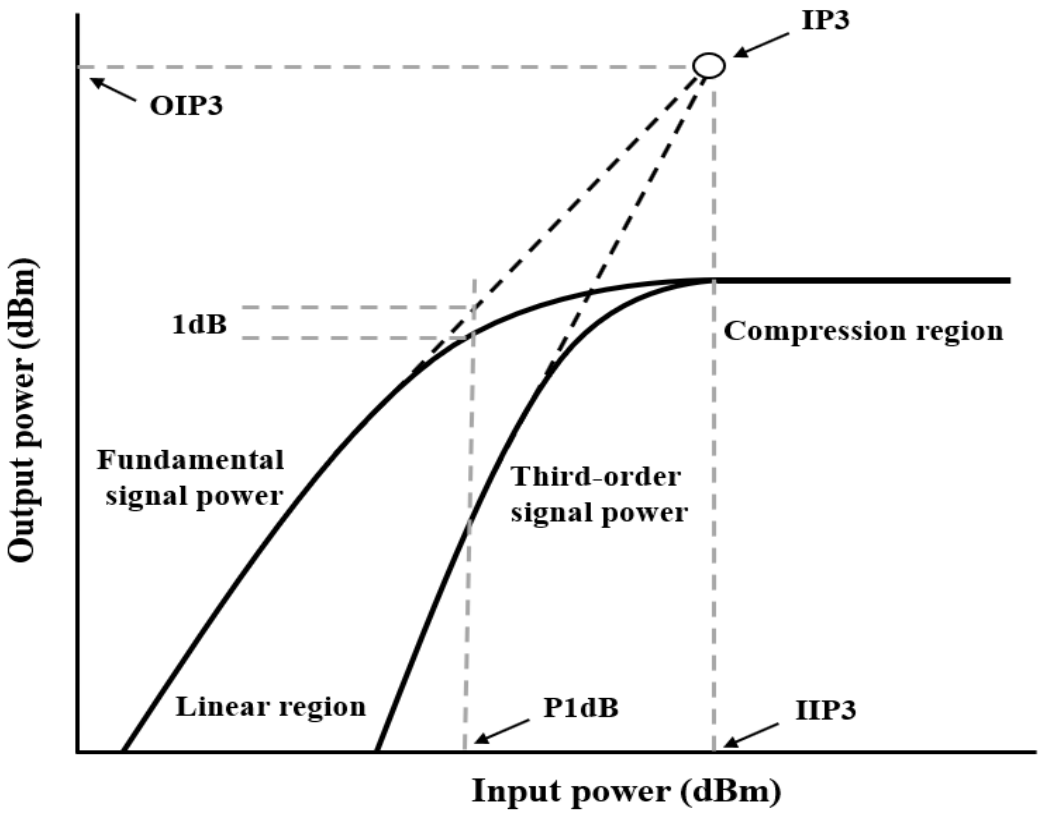

Figure 4.22 Illustration of 1dB compression point (P1dB) and third-order intercept point

In Figure 4.22, the fundamental signal power curve used to derive the P1dB gives a 1:1 gradient within the linear region and this is considered to be the first-order signal plot. The third-order signal power is also plotted in this logarithmic scale with a 3:1 slope. In other words, from a mathematic perspective, an interception can be observed with the slope rate difference between these two lines. This is only based on the assumption that sufficient power can be supplied and compression will not occur before reaching the intercept point, but this is often not the case. However, it is very useful for determining the nonlinearity characteristics of the DUT by extending the linear portions of those two curves to find the intercept point. This point is called the third-order intercept point (IP_3). With different reference to the different power axes, it can be read as IIP_3 for input power, or as OIP_3 for output power. The larger the intercept values, the higher the linearity of the DUT is and the lower the IMD.

4.5.2 Measurement Setup

Large signal characterisation in the presence of a two-tone signal was performed to investigate the non-linear behaviour of the switch in terms of intermodulation products, as well as its ability to handle high power. The frequencies of these two tones were chosen as $2.000GHz$ and $2.001GHz$ based on its usage in current wireless communication standard bands where they vary from 1.4MHz to 20MHz. In the first stage, the frequency spacing was not expected to have a huge impact on the non-linear behaviour, as it does for active devices. More two-tone measurements with different frequency spacing have been planned to confirm this in the next section. The set-up of the two-tone non-linearity measurement is shown in Figure 4.23. The two-tone sinusoidal signals were generated by two signal generators [4.26] and they were synchronised in the same clock cycle by a BNC cable to generate in-phase signals. Two separate generators were used because the use of a single driver with a two-tone generator at its input may result in the observation of the driver's non-linear behaviour rather than that of the microwave switch.

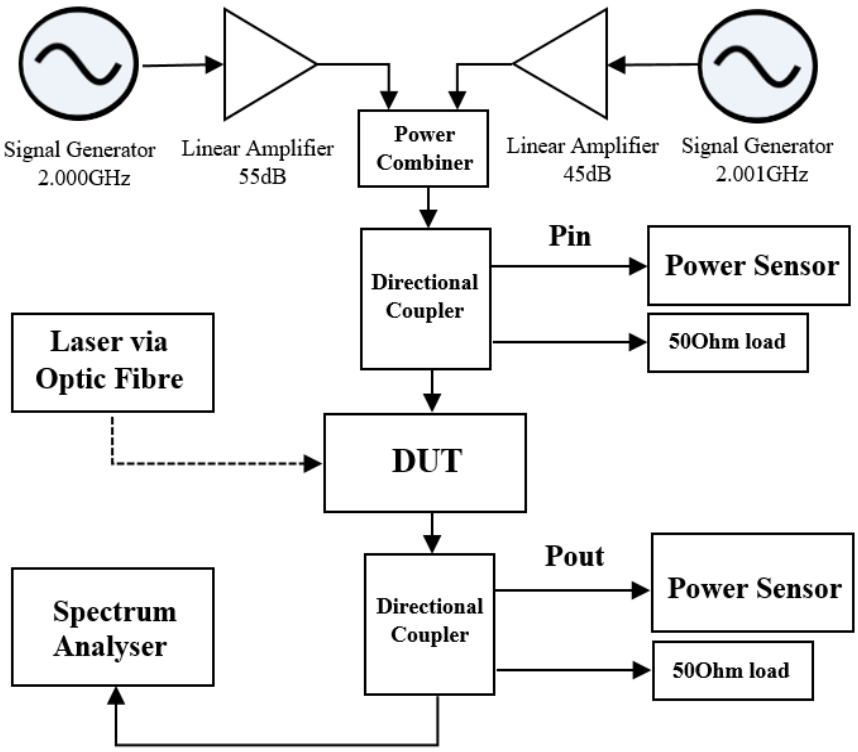

Figure 4.23 Schematic diagram of two-tone nonlinearity measurement setup

Two low-noise linear amplifiers [4.27] were then connected to amplify the signal, since it was limited by the output of the generators. Directional isolators were used after the amplifiers to prevent large-signal reflection and these two amplified signals were later joined by a power combiner [4.28] and delivered to a directional coupler [4.29]. Most of the power was propagated through the DUT, which was subject to IR illumination. A small portion of the signal was split into another path in the coupler, observed by a power sensor and terminated by a 50Ω load. The power sensor [4.30] was employed to monitor the input signal to the DUT and the dummy load was to ensure that no signal was reflected back. A similar approach was also taken to monitor the signal power of the output from the DUT. Care was taken to add appropriate attenuators to protect this sensor from large signals and the sensor meter readings were displayed in real time in R&S power viewer [4.31]. Attenuators must be hired to protect this kind of sensor, since it is very sensitive and has relatively weak power-handling ability; hence, the directly measured results are no longer the actual power. This can be resolved by calibrating the device beforehand and compensating for the difference made by the attenuators. Offset values can be easily set in the sensor interface software. Caution should be employed when implementing a calibration by always starting with a small input of power. In this calibration method, the DUT in Figure 4.23 was firstly replaced by a straight-thru connection to the power sensor for P_{out} directly. Hence, the offset value should be the difference between these two power sensors, for P_{in} and P_{out}, after accounting for the attenuation from the directional coupler. The calibration of a power sensor for P_{in} can be completed by calculating this offset. Next, to calibrate the power sensor for P_{out}, the second directional coupler needs to be added between the straight-thru and the sensor for P_{out}. Since the straight-thru power is now being measured by the calibrated sensor for P_{in}, the offset for the P_{out} sensor can be calculated, thereby calibrating both sensors. Finally, a spectrum analyser was connected, as shown in Figure 4.23, in order to capture the spectrum data for a post-measurement analysis.

Figure 4.24 shows the measured S_{21} results for a superstrate microstrip gapline switch of $0.4mm$ gap and $1mm$ linewidth under varying conditions of illumination. As can be seen, the insertion losses tended to be saturated as the illumination intensity increased. The insertion loss under $25W/cm^2$ was $2.6dB$ at 2GHz and the isolation was $19.3dB$ in dark conditions. The plot of output power against input power in a two-tone nonlinearity measurement for the switch can be seen in Figure 4.25. As shown, the third-order intermodulation distortion product started

to occur when the input power increased beyond $40dBm$, equivalent to $10W$. IIP_3 was extrapolated as $65dBm$ using the above mathematical approach.

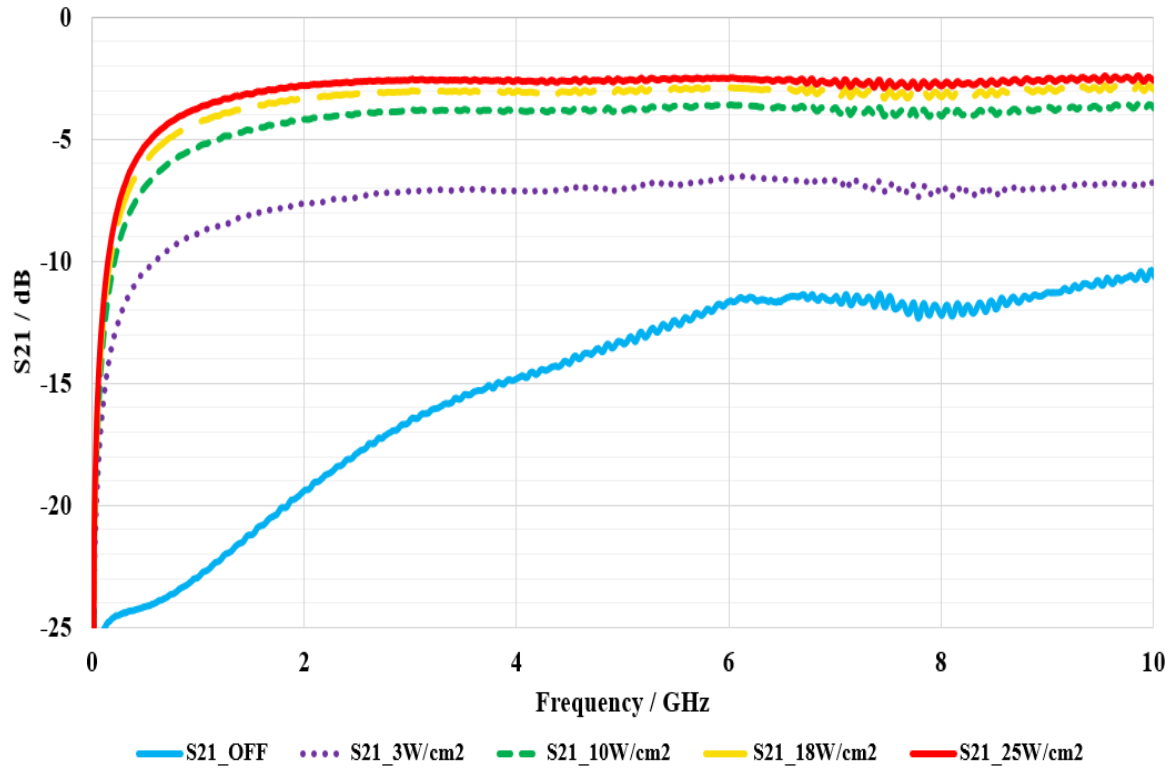

Figure 4.24 Measured S21 results for a superstrate microstrip gapline switch of 0.4mm gap and 1mm linewidth with superstrate fixed by sellotape under varying illumination intensities

The results of insertion loss, isolation and IIP_3 all indicate a considerably good performance. Although it may not be sufficient to compete with the switches [4.5-4.8] mentioned at the beginning of this chapter regarding to insertion loss and isolation, this initial test has demonstrated that this switch has significant potential, especially in terms of nonlinearity. In addition, as shown in Figure 4.26 the sellotape used to fix the superstrate melted and left burn stains when the input power was increased to $43dBm$. Therefore, the power handling ability of the switch also needs to be improved, which will be discussed in detail in the next section.

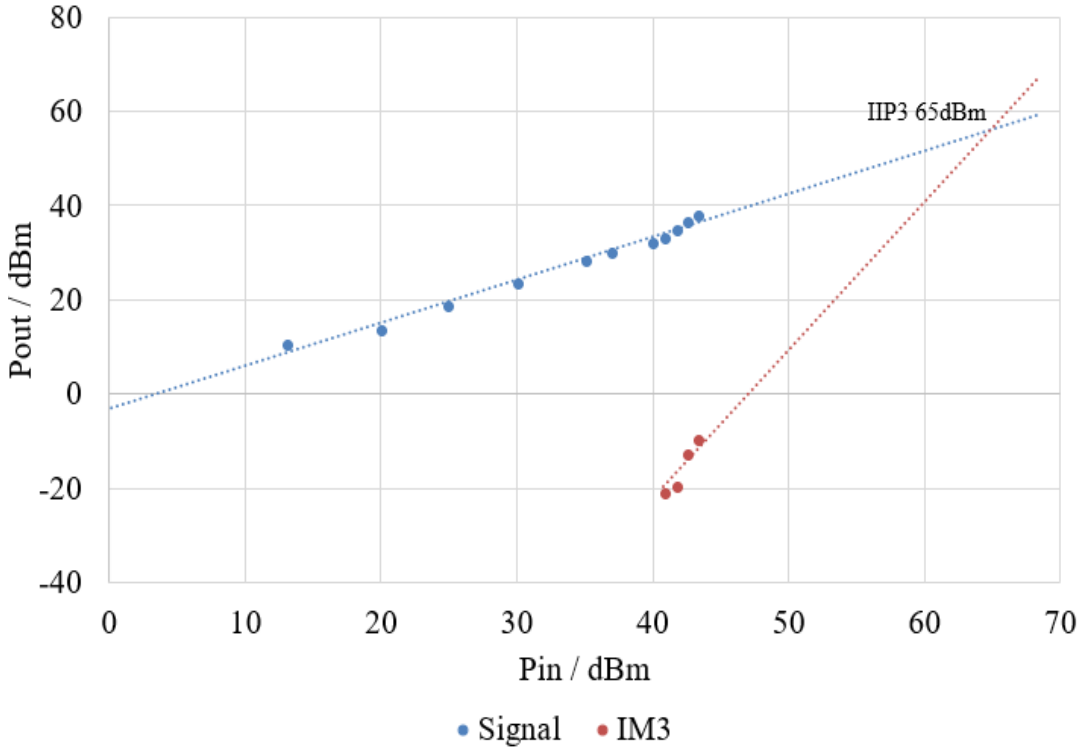

Figure 4.25 Pout vs. Pin in two-tone nonlinearity test for a superstrate microstrip gapline switch of 0.4mm gap and 1mm linewidth with superstrate fixed by sellotape

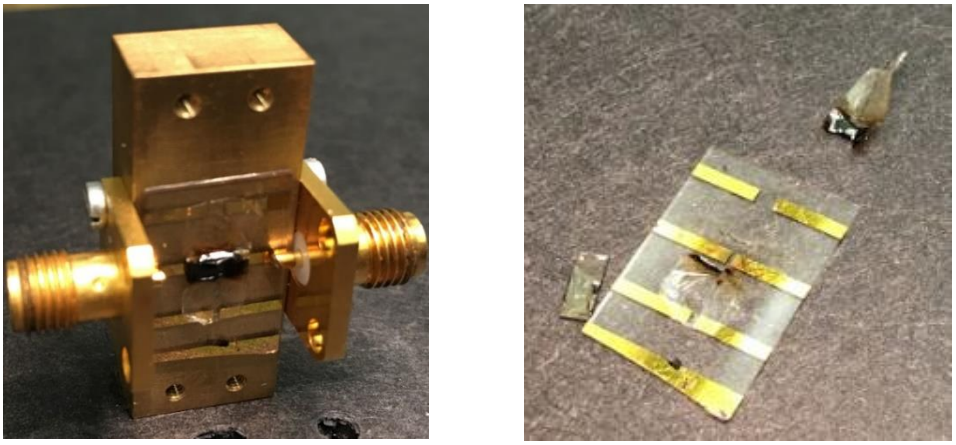

Figure 4.26 Photographs of melted sellotape during nonlinearity measurement

4.6 Nonlinearity and Power Handling Optimisation

4.6.1 Superstrate Fixture

This section contains the details of a further study of the superstrate fixture to improve the switch's power-handling ability. As discussed above, sellotape was initially selected based on its electromagnetic characteristic of low loss. However, it was proved not to survive the heat when the input power increased. Several other materials chosen as superstrate holders were also considered and subjected to an experiment. A photo of the switch with superstrate fixed by a Duroid material [4.32], which has low relative permittivity ($\varepsilon_r = 2.20$), is shown in Figure 4.27. This material is ductile and this property is utilised when bending is needed with the holder being fixed by two screws.

Figure 4.27 Photograph of a superstrate microstrip gapline with superstrate fixed by Duroid

The measured S_{21} results of the superstrate microstrip gapline switch with superstrate fixed by Duroid under varying illumination intensities are shown in Figure 4.28. This result is very similar to that of the switch with superstrate fixed by sellotape, but the rising curve in S_{21} in the frequency region from *5kHz to 500kHz* is steeper in this S_{21} graph. This is believed to be due to better contact and a firmer fixing between the superstrate and the microstrip gapline, which leads to lower insertion loss.

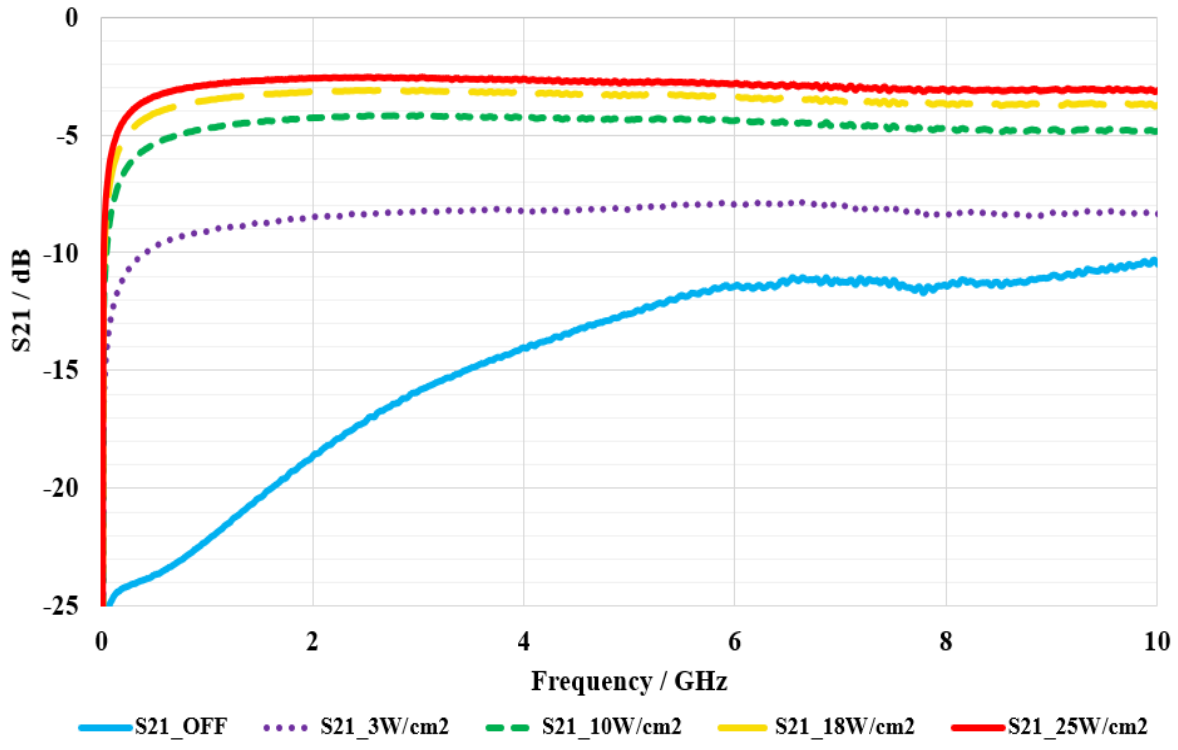

Figure 4.28 Measured S21 results for a superstrate microstrip gapline switch of 0.4mm gap and 1mm linewidth with superstrate fixed by Duroid [4.32] under varying illumination intensities

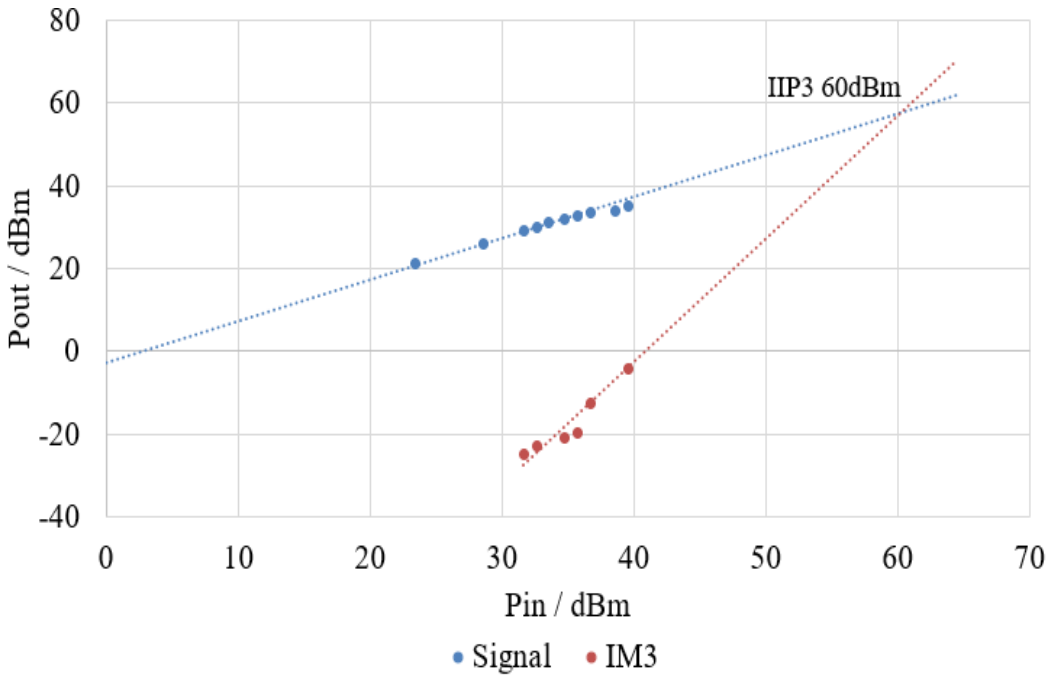

Figure 4.29 Pout vs. Pin in two-tone nonlinearity test for a superstrate microstrip gapline switch of 0.4mm gap and 1mm linewidth with superstrate fixed by Duroid

The IIP_3 of $60dBm$ with the superstrate fixed by Duroid is shown in Figure 4.29. This number has dropped by $5dB$ compared with the IIP_3 in the sellotape fixture test. The reason for this drop is believed to be associated with the firmer contact, as mentioned above, and also with the Duroid's material property.

As for power handling, it was found that the Duroid started to soften and bend after the input power increased above $40dBm$. Also, the Duroid fixture holder cannot be used repeatedly since the damage tends to be permanent. Another approach using a Perspex holder to clamp the superstrate firmly together with screws is illustrated in Figure 4.30.

Figure 4.30 Photograph of a superstrate microstrip gapline with superstrate fixed by Perspex

As shown in Figure 4.31, when the insertion loss at $2GHz$ was decreased to $1.8dB$ and the isolation maintained at around $20dB$, the rising curve in S_{21} in the low frequency region from $5kHz$ to $500kHz$ became even steeper. This again proved that a firmer contact results in a smaller impedance and thus a smaller insertion loss at low frequency. This impedance in superstrate part is composed of a series RC connection as previously discussed in §4.4.3 and shown in Figure 4.19. As the contact between the silicon and the gold tracks is not ideal, pressure will change the surface contact conditions. When more pressure is exerted on the superstrate, a larger surface contact area will decrease the resistance while the resultant reduced distance tends to increase the capacitance. Therefore, this change incurs a lower impedance and a smaller insertion loss at low frequency.

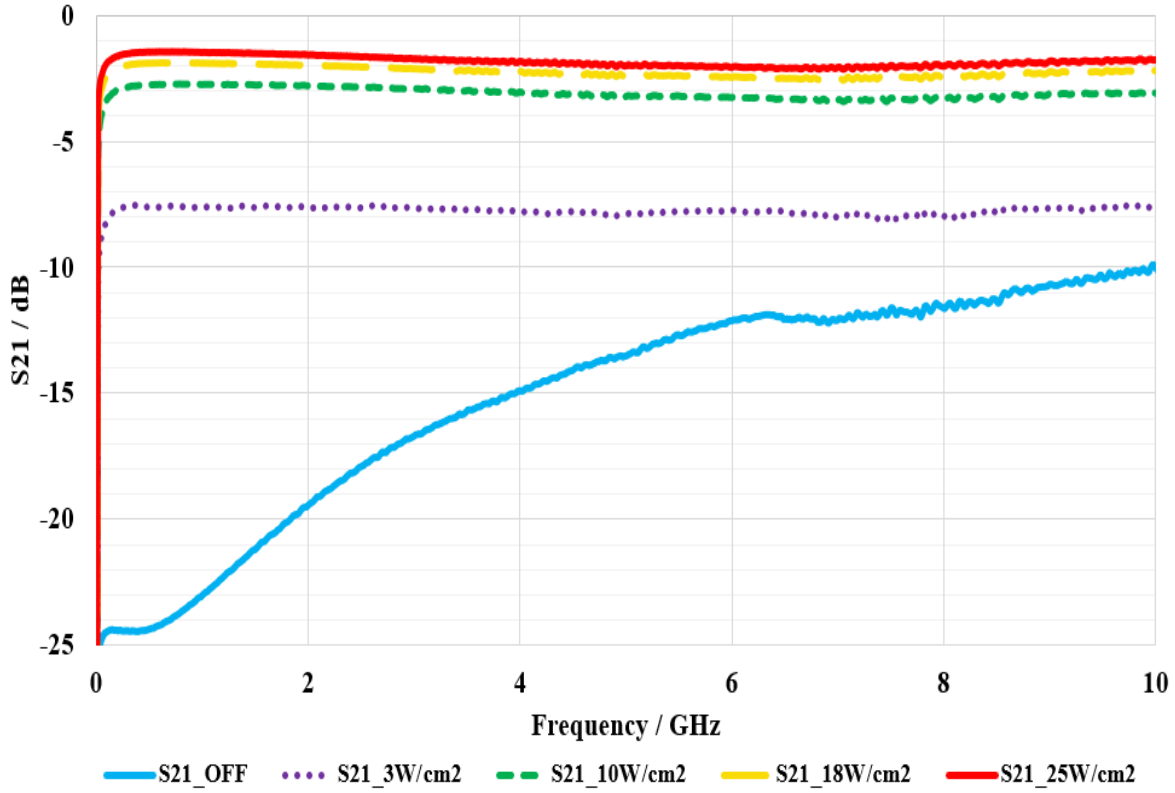

Figure 4.31 Measured S21 results for a superstrate microstrip gapline switch of 0.4mm gap and 1mm linewidth with superstrate fixed by Perspex under varying illumination intensities

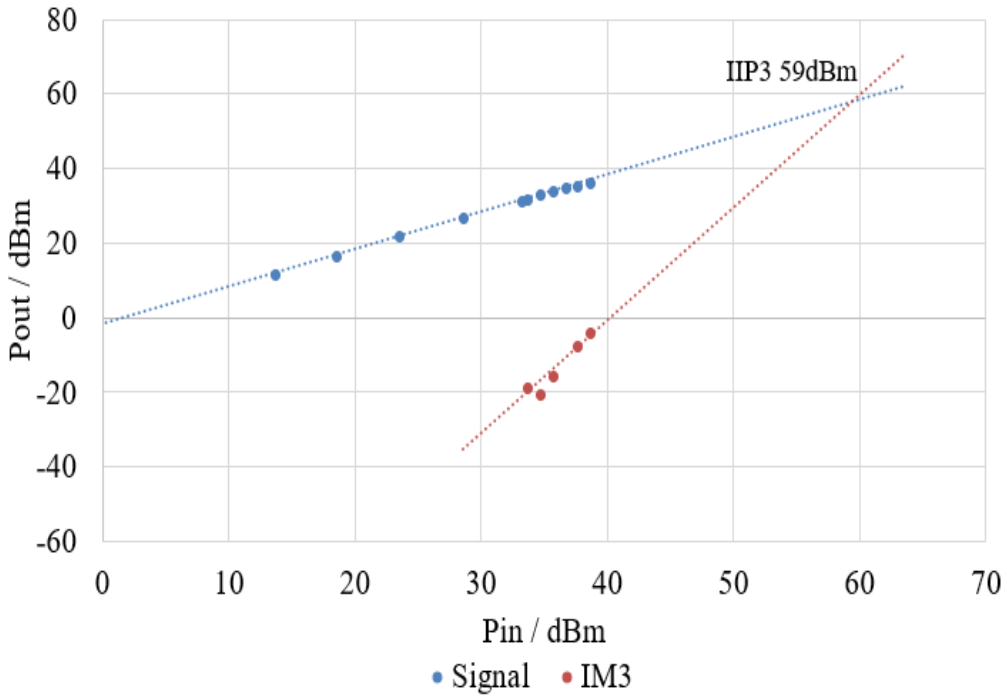

Figure 4.32 Pout vs. Pin in two-tone nonlinearity test for a superstrate microstrip gapline switch of 0.4mm gap and 1mm linewidth with superstrate fixed by Perspex

However, in terms of the nonlinearity characterisation, IIP_3 had decreased to $59dB$ which was $1dB$ lower than that in the Duroid fixture test. This suggests that a firmer contact may affect the switch's linearity. With regard to power handling, a similar problem occurred when the input power was raised above $43dBm$. The heated silicon was gradually squeezed into the melted space from the Perspex fixture bar from this power level onwards.

So far, the fixture material had been changed from sellotape to Duroid and Perspex. Although this led to a better insertion loss, the performance of the power handling was a trade-off and this was not ideal. It has been suggested that it is possible to use another low-loss material with a relatively higher melting point or without conducting much heat from the silicon, while simultaneously maintaining a firm contact between the superstrate and the microstrip gapline for a good insertion loss. A more in-depth analysis and discussion will be provided in the next section.

4.6.2 Passivated Layer and Quartz Insulation

The design of superstrate material and fixture selection is further studied in this section. As discussed above, it can be concluded that a firmer contact between the semiconductor silicon superstrate and the metal gold microstrip gaplines may lead to a better S_{21} performance, but it increases the nonlinearity effect. It is suspected that this silicon-gold junction causes a diode effect and forms a high Schottky barrier. Hence, it is necessary to employ the band diagram again to explain the Schottky barrier and a qualitative discussion will be required, since quantitative calculations need rich knowledge of quantum physics and a massive amount of experimentation. The following text will focus on n-type semiconductors, since this type of material is used to rectify contacts [4.33] in most cases. The band diagrams of a metal and n-type semiconductor before contact are shown in Figure 4.33. At a first glance, there appear to be different Fermi levels (E_F), which can be considered as the key reason for the formation of

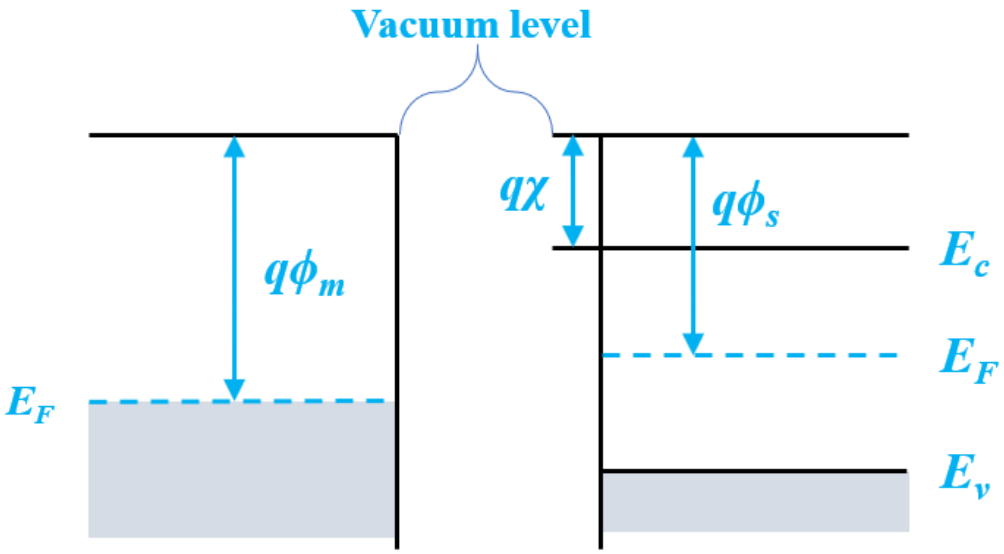

Figure 4.33 Energy-band diagram of a metal and a semiconductor

a Schottky barrier. χ is the electron affinity which is the energy needed to form a negative ion by adding an electron to a neutral molecule, ϕ_m and ϕ_s denote the work functions of metal and semiconductor, respectively, measured in volt. The work function energy measured in electron volt is the minimum energy an electron requires to escape from a solid to a vacuum level immediately above its surface, namely $q\phi$ or $q\chi$. This level of vacuum is also denoted in Figure 4.33. Therefore, it can be seen that $\phi_m > \phi_s$ and the Fermi level in the metal is below that in the semiconductor before contact. When these two materials are combined, electrons from the semiconductor will flow into the metal which has relatively lower energy states to achieve a thermal equilibrium. In this process, a depletion region will be formed through the system which shares a same constant in the Fermi level. The Schottky barrier can now be defined as the potential barrier height, ϕ_b.

$$\phi_b = \phi_m - \chi \qquad 4.2$$

This potential height is seen by electrons as the barrier they must overcome in order to move back to the semiconductor from the metal. The potential barrier can vary from forward bias or reverse bias conditions. The band diagrams are also similar to those of a pn junction [4.33]. The current-voltage characteristics are expected to show exponential behaviour; therefore, the

silicon-gold contact is believed to be a Schottky contact, which can be the major cause of the nonlinearity in the superstrate switch.

Several approaches have been considered to remove or reduce the Schottky effect. The first is to provide an annealed and alloyed contact. This kind of fabrication method normally entails depositing alloy metals on the semiconductor followed by high-temperature annealing to reduce the unintentional barrier at the interface. For example, a typical alloy aluminium can be used with silicon; however, this can be difficult to handle and align in practical fabrication from a circuit design in a micrometre or millimetre scale. In addition, the subsequent annealing at around $500℃$ will further improve the contact resistivity, which may lead to an unwanted drop in the switch's insertion loss. The second method is the tunnelling contact. This phenomenon can be described as particles, such as electrons, tunnelling through a barrier that typically cannot be surmounted. However, it requires a dense carrier concentration, which may need high-level doping and it only occurs where the interface or contact is in the order of few nanometres. Although this is not a realistic approach, the idea of doping is of much interest. Hence, the third method is the semiconductor doping that was introduced earlier in §2.3.2. All three of these methods generically aim to reduce the potential barrier height and are effective with an ohmic contact formation when a low-resistance junction provides the bidirectional conduct between the metal and the semiconductor. Hence, the relationship between the current and the applied voltage can be characterised by a linear function. Both n-type and p-type dopings were considered as a third approach. As suggested, the difference between Fermi levels needs to be reduced before contact in order to reduce the difference between ϕ_m and ϕ_s and thus, the barrier. Both less n-type doping and a high level of p-type doping can lower the Fermi level in a semiconductor to achieve this effect. Nevertheless, since a lightly n-doped silicon (resistivity > $10k\Omega.cm$) has already been employed, even less n-type doping will demand more optical power to prevent more insertion loss. On the other hand, p-type doping can also provide a solution by lowering the Fermi level on the side of the semiconductor and hence reduce the potential barrier. The results of further measurements are shown below.

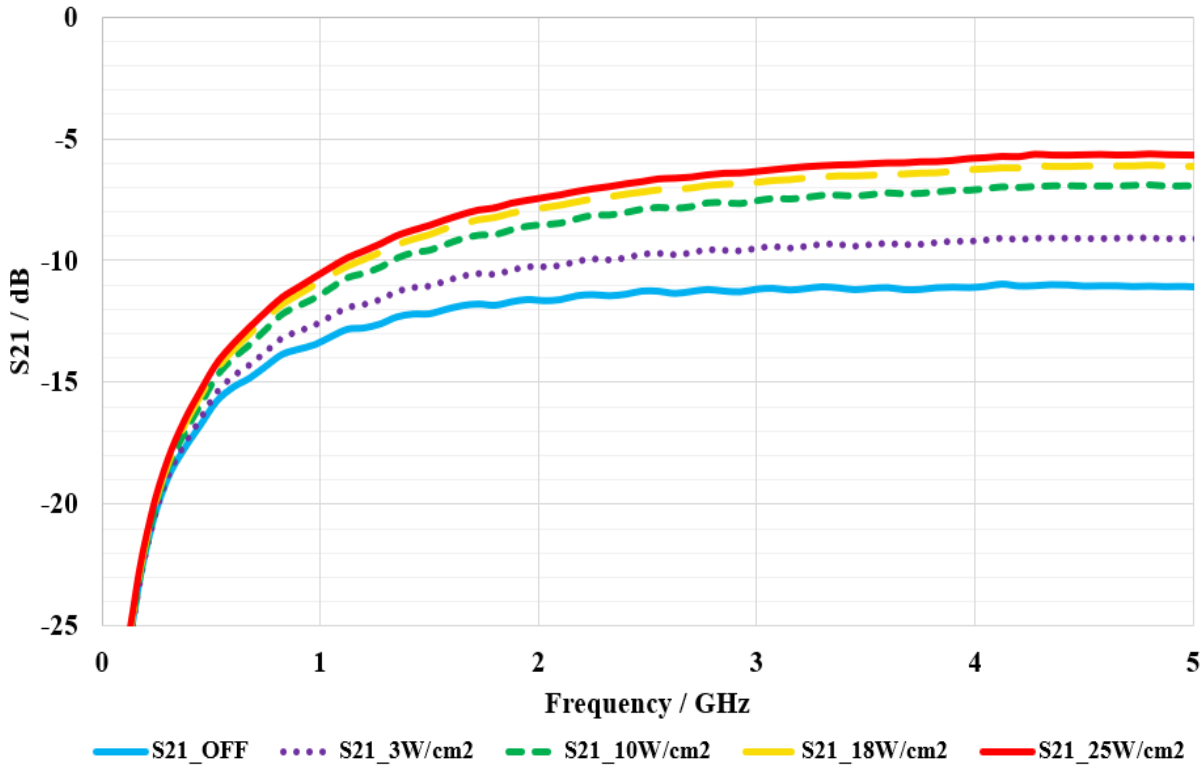

Figure 4.34 Measured S21 results for a superstrate microstrip gapline switch with p-type superstrate silicon (resistivity < 5kΩ.cm) under varying illumination intensities

The measured S_{21} results for an identical microstrip gapline switch in terms of dimensions and optical illumination conditions as investigated above are shown in Figure 4.34. The only change was the doping of the superstrate silicon and its resistivity had been reduced to below $5k\Omega.cm$ compared to the previous $10k\Omega.cm$. The isolation remained lower than 10dB at $2GHz$. Although the isolation value met the basic requirement for an RF switch design, the lowest insertion loss under the strongest illumination had already dropped below $7dB$ at $2GHz$. With regard to the nonlinearity, the rise in IIP_3 of $66dBm$ shown in Figure 4.35 was a good sign of the p-type doping.

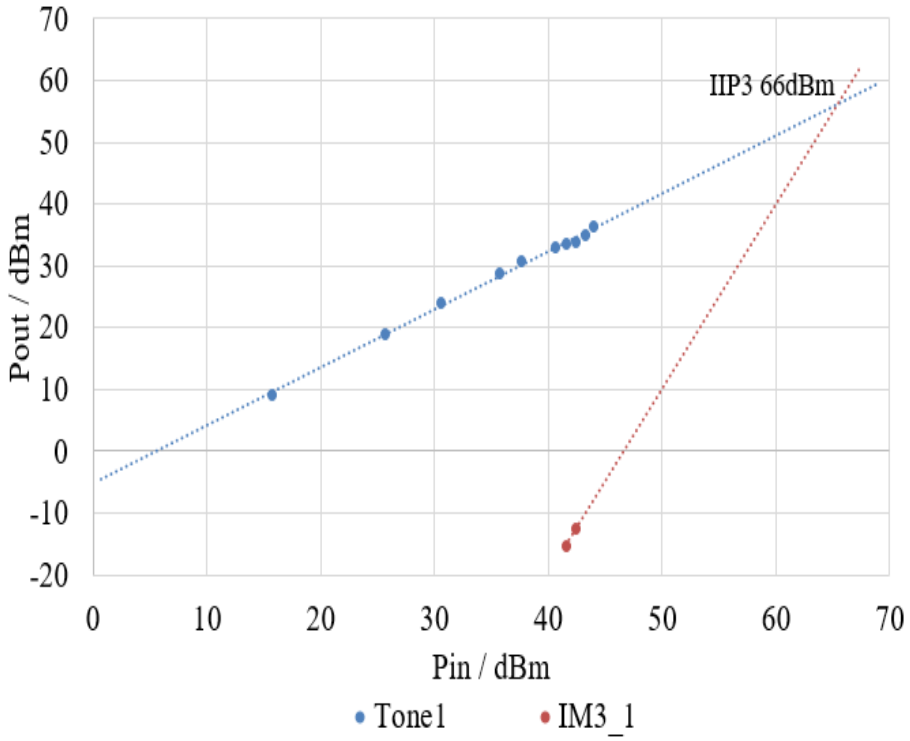

Figure 4.35 Pout vs. Pin in two-tone nonlinearity test for a superstrate microstrip gapline switch with p-type superstrate silicon (resistivity < 5kΩ.cm)

The next measurement was based on superstrate silicon with higher p-type doping and hence, it had lower resistivity (< $1k\Omega.cm$). Figure 4.36 shows the best IIP_3 value so far of $68dBm$, which is competitive with the other above-mentioned switches. However, the isolation value was sacrificed to be less than $10dB$ as shown in Figure 4.37 in spite of a good insertion loss with maximum optical illumination below $2dB$, due to the implementation of higher doping.

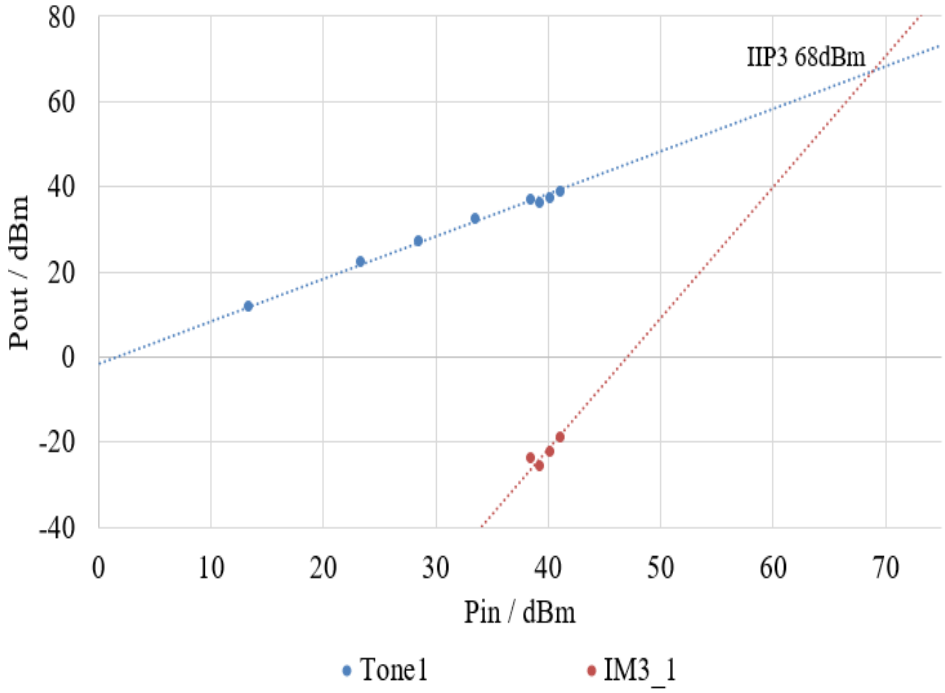

Figure 4.36 Pout vs. Pin in two-tone nonlinearity test for a superstrate microstrip gapline switch with p-type superstrate silicon (resistivity < 1kΩ.cm)

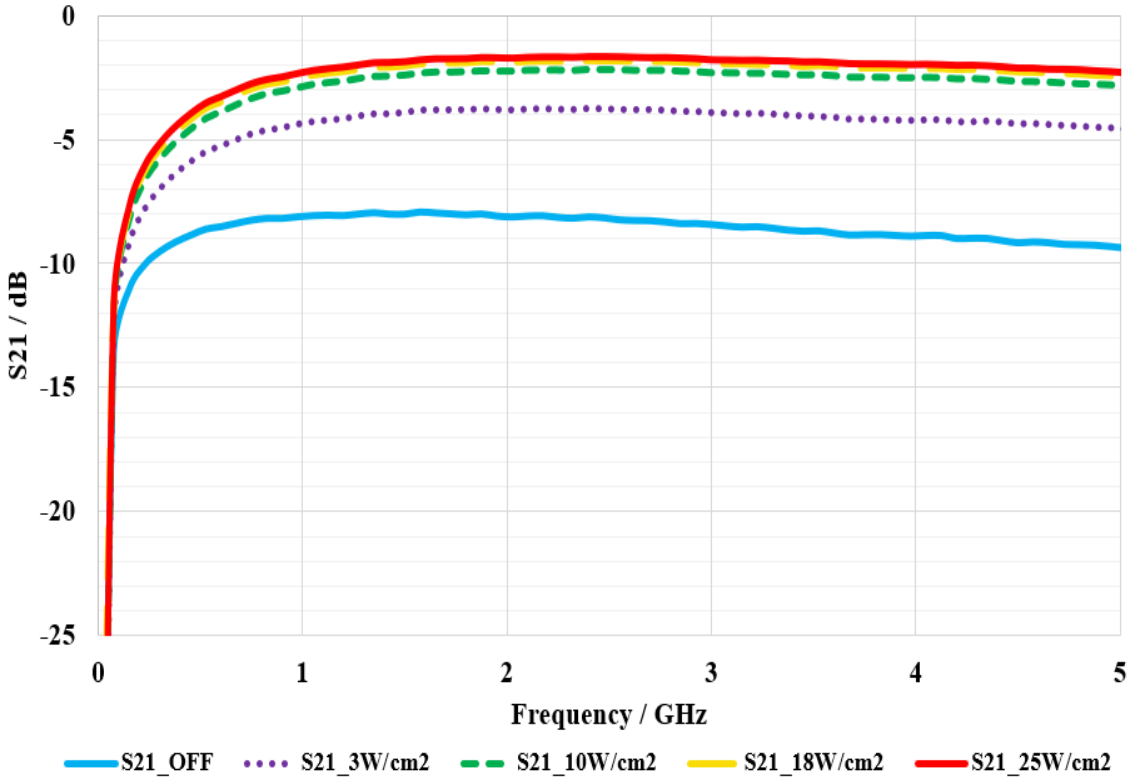

Figure 4.37 Measured S21 results for a superstrate microstrip gapline switch with p-type superstrate silicon (resistivity < 1kΩ.cm) under varying illumination intensities

In summary, it has been suggested that these three methods to reduce Schottky barriers cannot be used to design an RF switch without sacrificing either the isolation or the insertion loss. The fourth method proposed in this study was to add a passivated layer that would inherently replace the metal-semiconductor-contact. Passivation is a very popular technology that is mainly used to coat surfaces and generally make them passive to unwanted interaction with chemicals or simply for anti-corrosion purposes. Researchers of [4.34-4.37] have studied the effect of passivation technology applied to silicon and confirmed the promising outcome. An oxidation layer (silicon dioxide) $100nm$-$300nm$ thick was finally chosen for several reasons. In terms of the material selection, the recommended passivation for silicon is oxide or nitride. The most important reason for selecting oxidation is the expectation of less electromagnetic loss, since the dielectric constants for silicon dioxide and silicon nitride are 3.5 and 7.5 respectively. In addition, oxidation is less costly in terms of fabrication and the transmission of silicon dioxide is also higher than that of silicon nitride in the IR region. As for the thickness of the silicon dioxide (silica) layer, a value lower than $100nm$ may bring about a leakage in that part of the current that can be tunnelled through. Hence, this portion of the metal-semiconductor-contact will revive the Schottky effect and the nonlinearity. On the contrary, with an increase in the thickness of the silicon dioxide layer, more low frequency signals will be blocked by this insulating layer and the insertion loss will be increased.

Furthermore, this low-loss and electrically insulating material are also reminiscent of the use of an allotropy, quartz, for thermal insulating. The schematic and photographic top view of the new design of a superstrate microstrip gapline switch with passivated superstrate silicon and quartz insulator are shown in Figure 4.38 and Figure 4.39. In fact, the original idea was to use quartz to entirely replace the Perspex bar, but quartz is fragile and insufficiently ductile to be bent and fixed by screws. It was broken several times in the tests. However, its characteristic of heat insulation with a melting point of over 1650℃ makes quartz an irreplaceable and outstanding candidate. The new idea of putting and clamping the quartz in the middle of the superstrate silicon and the Perspex holder, as used earlier, is shown in Figure 4.39. It was used to insulate and prevent the collected heat from melting the Perspex and further loosening the fixture and the contact. A detailed discussion of the measured results will be provided in the next section.

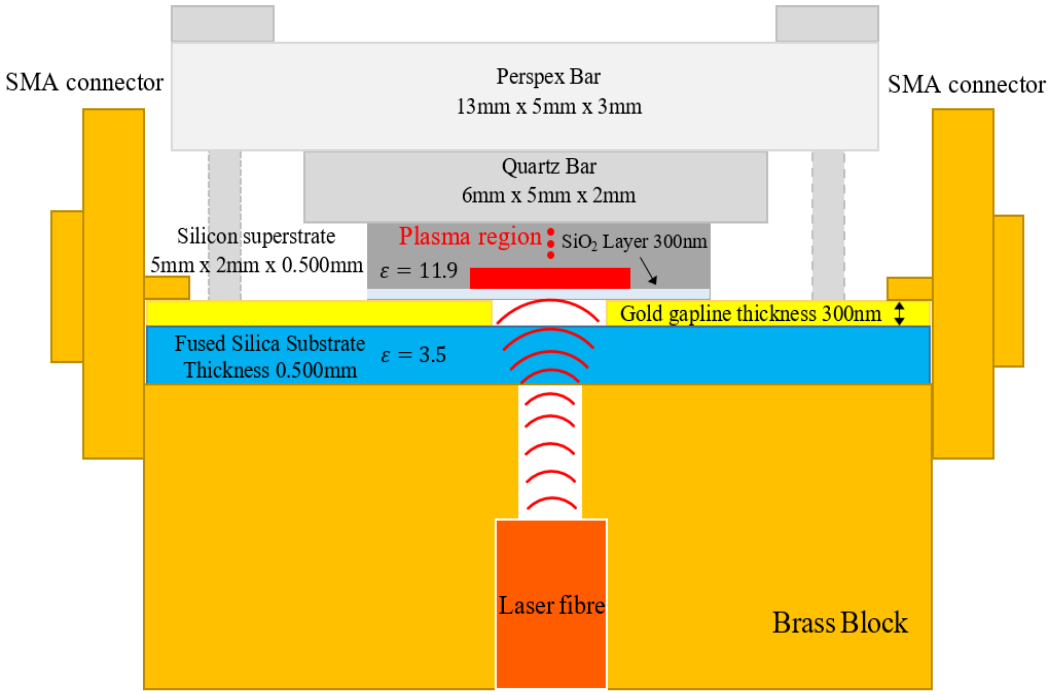

Figure 4.38 Schematic side view of a microstrip line on fused silica with bottom illumination

Figure 4.39 Photographic top view of a fabricated superstrate microstrip gapline switch

4.6.3 Measurement Results

A schematic diagram of the structure is shown in Figure 4.38. The silicon was held in place by a Perspex bar with heat insulation provided by a quartz bar. The original silicon superstrate is lightly n-type doped with <100> orientation and resistivity >10kΩ.cm. It was passivated with 300nm thick silicon dioxide to prevent a Schottky contact from forming between the gold and silicon surface.

Two samples were used in the subsequent measurement for a parametric comparison and a generalised analysis and deduction. Sample 1 had a 0.4mm gap, 1.0mm linewidth and a 1mm diameter hole and Sample 2 had a 0.1mm gap, 1.6mm linewidth and a 2mm diameter hole. The measured S_{21} for the two samples of different geometries with varying illumination intensities is shown in Figure 4.40.

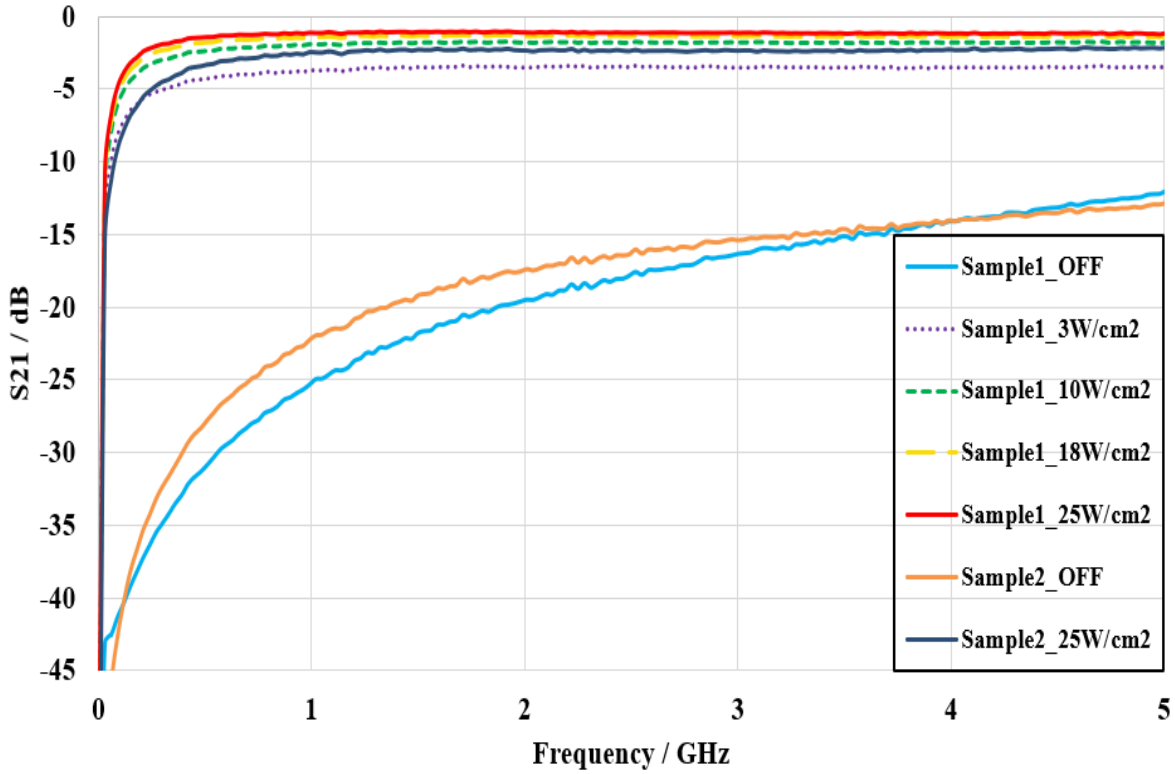

Figure 4.40 Measured S21 magnitude for Sample 1 (0.4mm gap and 1.0mm linewidth) and Sample 2 (0.1mm gap and 1.6mm linewidth) at varying laser power levels

In the no-light case (OFF), $20dB$ isolation was observed for Sample 1 and a rapid rise in S_{21} could be observed at $3W/cm^2$ illumination intensity with saturation occurring around $10W/cm^2$. The insertion loss at $2GHz$ was $1.11dB$ for Sample 1 and $2.35dB$ for Sample 2 at $25W/cm^2$ illumination intensity. It is believed that the increased insertion loss for Sample 2 was caused by the 2mm diameter hole reducing the light focus and thus, reducing the intensity. The rapid roll-off in S_{21} at a low frequency below $0.5GHz$ was caused by the silica passivation layer acting as a series capacitor.

In terms of the switch's characterisation of non-linear behaviour and its high-power handling ability, the frequencies of the two tones varied from (i) $1.999GHz$ and $2.001GHz$, (ii) $2.000GHz$ and $2.001GHz$ and (iii) $2.0005GHz$ and $2.001GHz$ to give spacings of $200MHz$, $100MHz$ and $50MHz$ respectively. The illumination intensities varied from $0W/cm^2$, $10W/cm^2$ and $25W/cm^2$ for Samples 1 and 2. The spectra data was measured using a Rohde & Schwarz spectrum analyser and the result is shown in Figure 4.41, 4.42 and 4.43. This is raw data prior to the use of the offsets needed to compensate for the presence of attenuators in the setup. An initial test was carried out on a 1.0mm wide through line with 50Ohm characteristic impedance to examine the inherent nonlinearity of the setup and the results are shown in Figure 4.41. *Pspec* annotated in vertical axis is the output power observed in spectrum analyser. It can be seen that no third-order IMD products were observed at a P_{in} of +47.85 dBm (~61W).

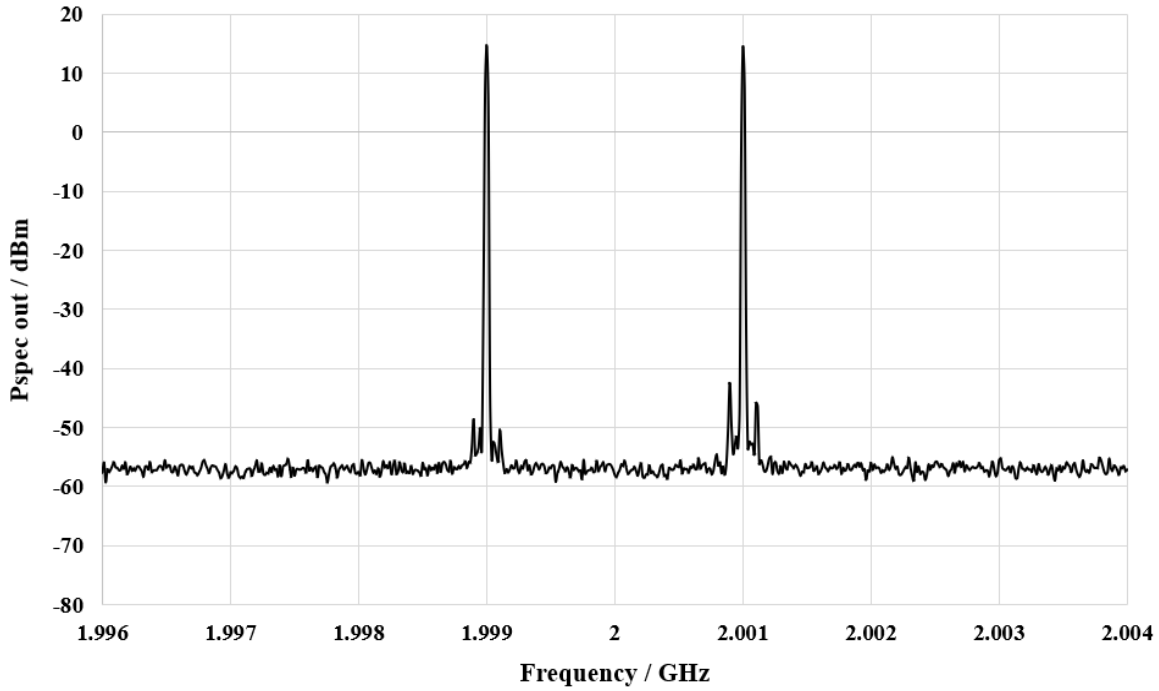

Figure 4.41 Measured output power spectra Pin = +47.85 dBm in a 1.0mm microstrip linewidth (No illumination in passive intermodulation (PIM) measurement)

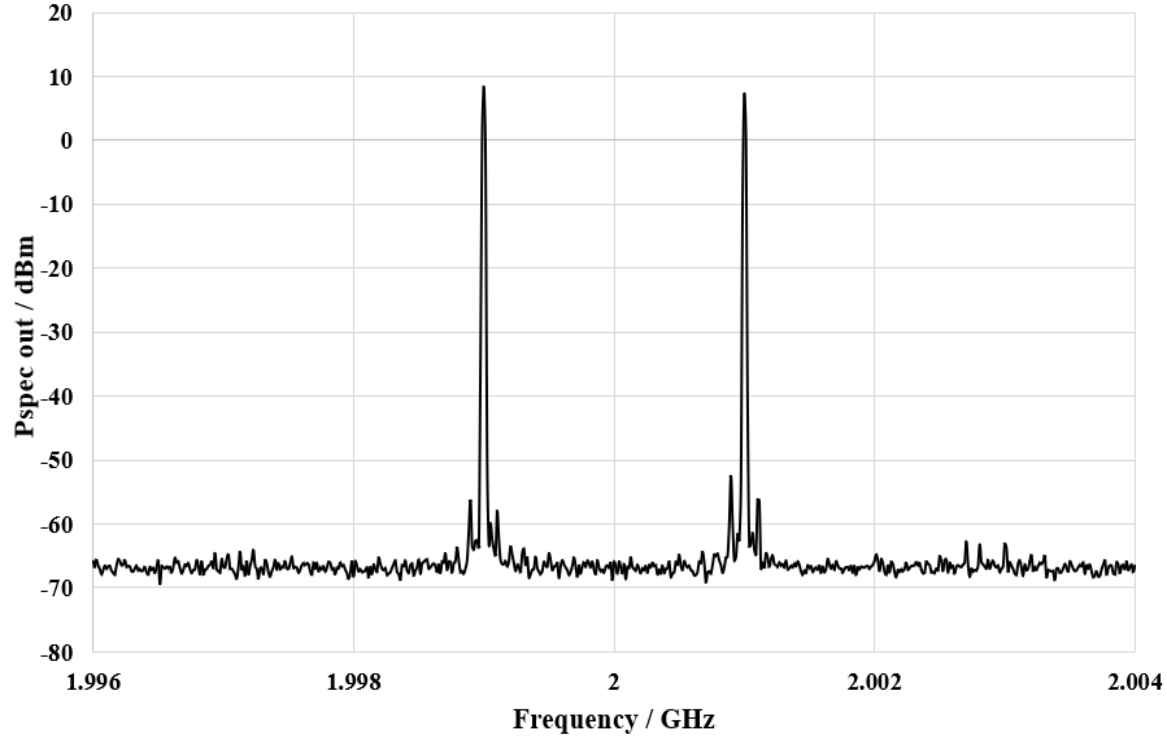

Figure 4.42 Measured output power spectra Pin = +42.77 dBm in Sample 1 (0.4mm gap and 1.0mm linewidth) with 200MHz tone spacing at 25W/cm^2 illumination intensity

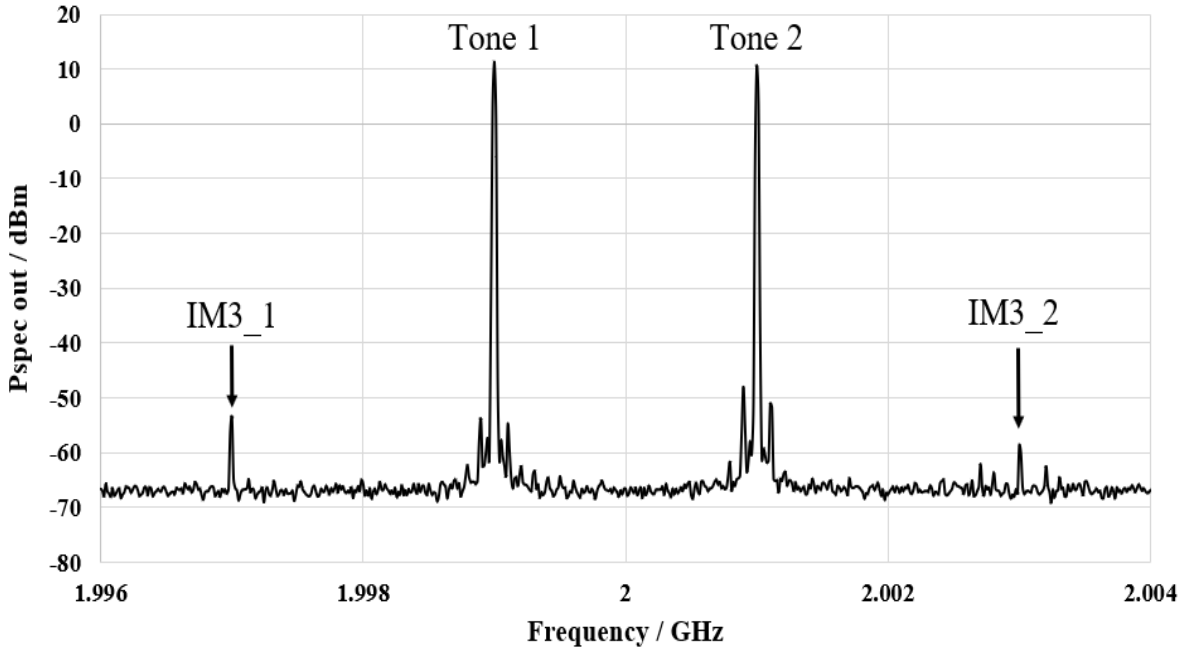

Figure 4.43 Measured output power spectra Pin = +46.22 dBm in Sample 1 with 200MHz tone spacing at 25W/cm^2 illumination intensity

The case of the Sample 1 (0.4mm gap and 1.0mm linewidth) with 200MHz tone spacing at $25W/cm^2$ illumination intensity is shown in Figure 4.42 and no obvious IM_3 was determined, since the input power increased up to +42.77 dBm (~10W per tone). In Figure 4.43, an asymmetric IM_3 pair can be observed at 1.997GHz and 2.003GHz when it was powered up to +46.22 dBm (~21W per tone). The reason for this is that the minor difference between fundamental tones signals causes an imbalanced IM3 output. No material melting or insertion loss deterioration was observed at this power level, which suggests a very robust clamp fixture.

The data for each sample was then plotted as shown in Figure 4.44 with Pout v Pin in order to determine the Third Order Intercept Point referred to Input Power (IIP3) and this was estimated to be +77dBm for Sample 1 with a tone spacing of 200MHz at $25W/cm^2$ illumination intensity.

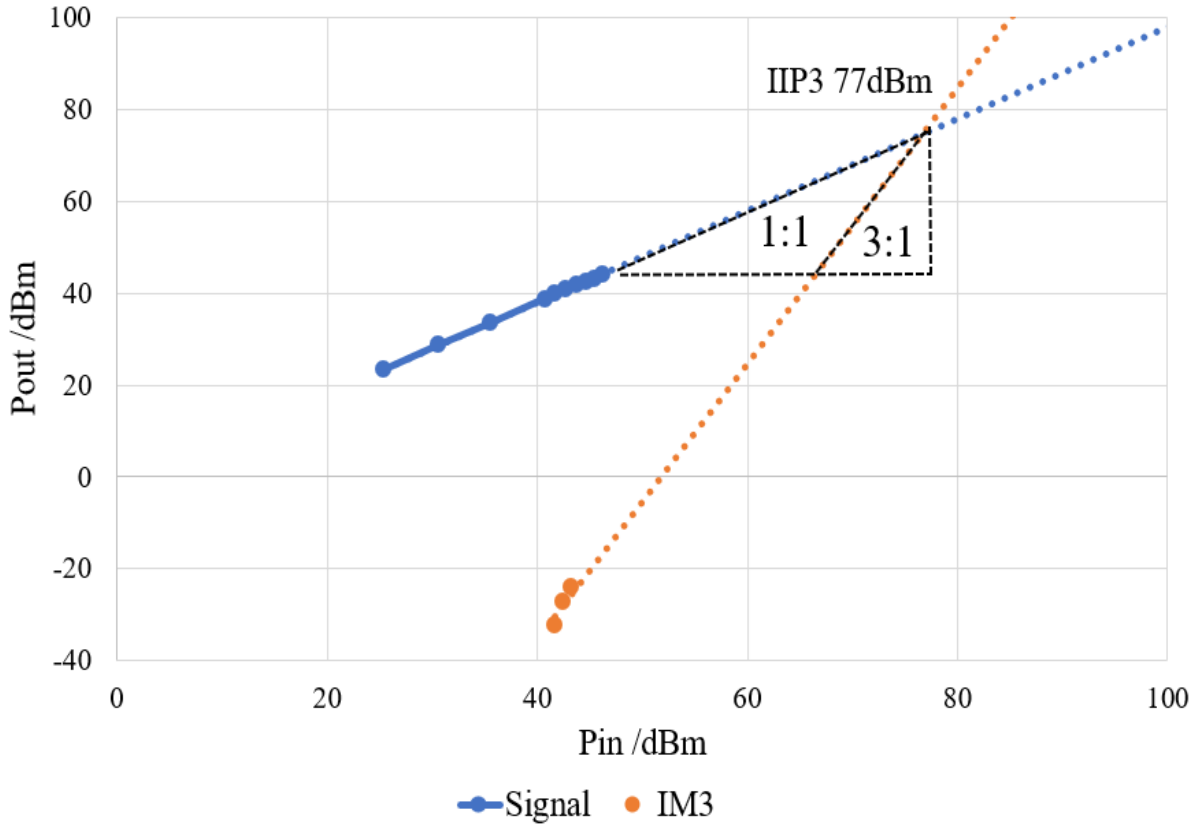

Figure 4.44 Extrapolated IIP3 value for Sample 1 with tone spacing of 200MHz at 25W/cm^2 illumination intensity (IIP3 77dBm)

All the IIP3 data was then collated and is shown in Figure 4.45. Some interesting trends can be observed, particularly the fact that the IIP3 did not improve significantly beyond the $10W/cm^2$ illumination intensity point and, in some cases, it decreased. The best-case frequency spacing was 100MHz for both Sample 1 and 2 at $10W/cm^2$ illumination intensity with a best-case IIP3 of +78.5dBm.

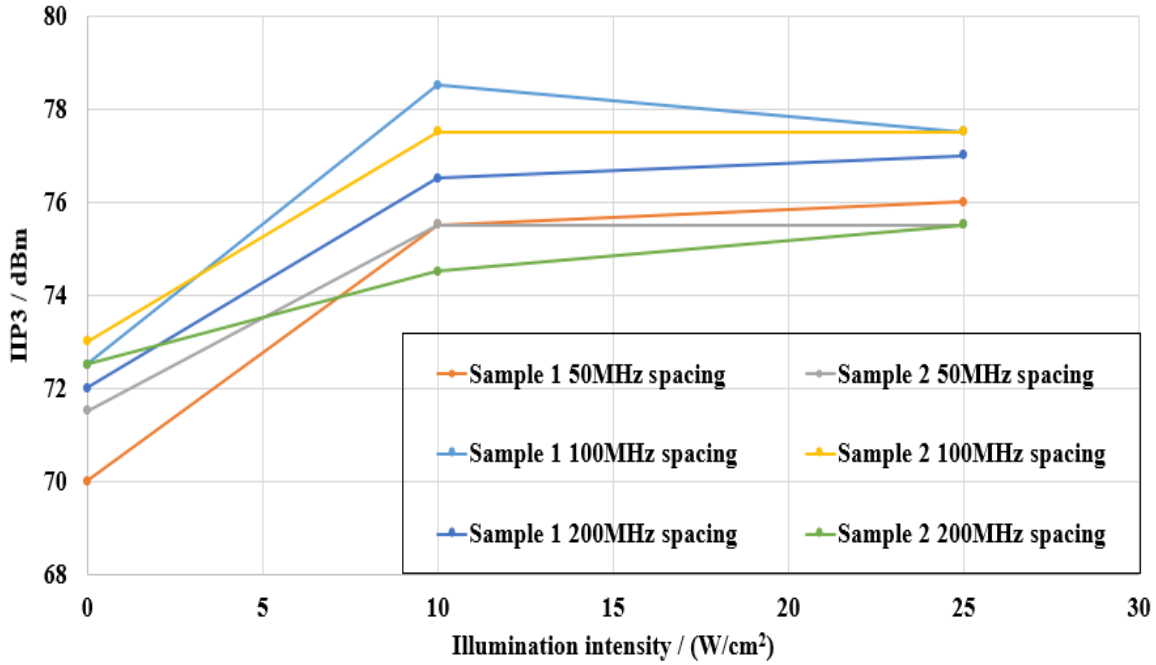

Figure 4.45 IIP3 for different tone spacings and illumination intensities for Sample 1 (0.4mm gap and 1.0mm linewidth) and Sample 2 (0.1mm gap and 1.6mm linewidth)

Finally, a thermal imaging camera was utilised to observe the sample temperature at different RF power levels. Three images taken during the measurement using an NIR sensor camera from FLIR are shown in Figure 4.46. As expected, the whole brass fixture became hot and the central quartz bar acted to thermally isolate the central region. Heat was seen to conduct around the quartz, giving rise to two hot spots on either side.

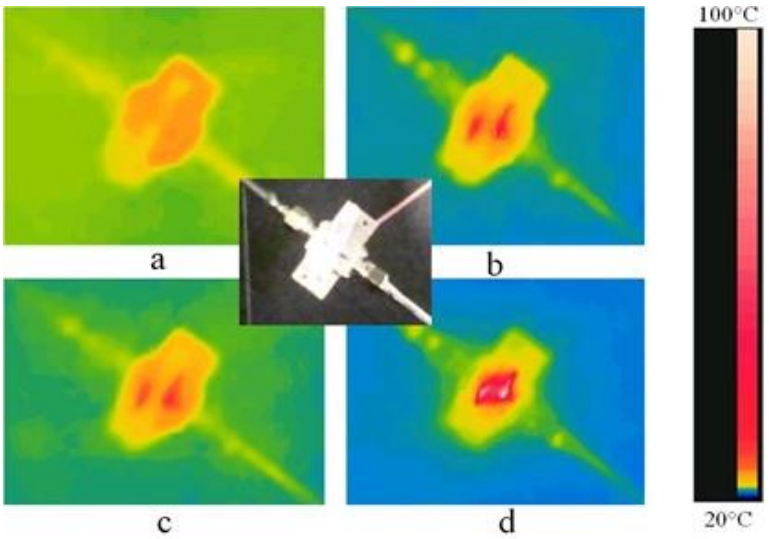

Figure 4.46 Thermal images of Sample 1 at 200MHz tone spacing and 25W/cm^2 illumination intensity with RF input power at (a) 18.53dBm, (b) 36.69 dBm, (c) 43.86 dBm, (d) 46.89 dBm. Inset optical image of the device

4.7 Conclusion

A superstrate-structure microstrip gapline switch was designed and implemented in this chapter based on an analysis of a microstrip gapline switch in previous work. The chapter included a detailed and step-by-step discussion and explanation, which began with a review of popular microwave switches and a comparison of current optically-controlled microwave switches. Several aspects were improved, especially nonlinearity characterisation, power-handling ability and packaging design for integration purposes. Insertion loss has been found to be considerable with existing switches; therefore, the first task was to resolve this problem. To begin with, a physics modelling was created using the simulation software, CST and good agreement was found between the measured and simulated results. Hence, after ensuring the reliability of the simulation, the cause of the large insertion loss was identified with the aid of CST. A new structural design was then proposed to reduce this loss. Meanwhile, further design work was undertaken to characterise and reduce the nonlinearity of the switch. A bottom-illuminated photoconductive reconfigurable microwave switch was finally produced with a minimum insertion loss of 1.11 dB at 2GHz and an isolation of 20dB. There was no observable IM3 in the spectrum when the input power was raised to nearly 20W in a two-tone measurement. However, third order distortion appeared with a further power increase and the best-case IIP3 was +78.5dBm.

4.8 References

[4.1] C. D. Gamlath, D. M. Benton, M. J. Cryan, "Microwave Properties of an Inhomogeneous Optically Illuminated Plasma in a Microstrip Gap", IEEE Trans. Microw. Theory Tech., vol. 63, no. 2, pp. 374-383, 2015

[4.2] A. W. Pang, S. Bensmida, C. D. Gamlath, M. J. Cryan, "Non-linear characteristics of an optically reconfigurable microwave switch", IET Microwaves, Antennas & Propagation, vol. 12, no. 7, pp. 1060-1063, 2018

[4.3] A. W. Pang, S. Bensmida, M. J. Cryan, "Nonlinearity and Power Handling Characterization of an Optically Reconfigurable Microwave Switch", IEEE/MTT-S International Microwave Symposium-IMS, pp. 420-422, 2018

[4.4] R. L. Haupt, M. Lanagan, "Reconfigurable antennas", IEEE Antennas Propagat. Mag., vol. 55, no. 1, pp. 49-61, 2013

[4.5] C. G. Christodoulou, T. Youssef, A. L. Steven, "Reconfigurable antennas for wireless and space applications", Proc. IEEE, vol. 100, no. 7, pp. 2250-2261, 2012

[4.6] C. Rauscher, "Reconfigurable bandpass filter with a three-to-one switchable passband width", IEEE Trans. Microw. Theory Tech., vol. 51, no. 2, pp. 573-577, 2003

[4.7] C. D. Patel, G. M. Rebeiz, "A high-reliability high-linearity high-power RF MEMS metal-contact switch for DC–40-GHz applications", IEEE Trans. Microw. Theory Tech., vol. 60, no. 10, pp. 3096-3112, 2012

[4.8] L. L. W. Chow, J. L. Volakis, K. Saitou., "Lifetime Extension of RF MEMS Direct Contact Switches in Hot Switching Operations by Ball Grid Array Dimple Design", IEEE Electron. Device Lett., vol. 28, no. 6, pp. 479-481, 2007

[4.9] M. Kulygin, G. Denisov, K. Vlasova, “Nanosecond Microwave Semiconductor Switches for 258… 266 GHz”, Journal of Infrared, Millimeter, and Terahertz Waves, vol. 36, no. 9, pp. 845-855, 2015

[4.10] T. Kaneko, T. Takenaka, T. S. Low, “Microwave switch: LAMPS (light activated microwave photoconductive switch)”, IEEE Electronics Letters, vol. 39, no. 12, pp. 917-919, 2003

[4.11] E. K. Kowalczuk, C. J. Panagamuwa, R. D. Seager, “Characterising the linearity of an optically controlled photoconductive microwave switch”, In Antennas and Propag. Conf. (LAPC), Loughborough, U.K., pp. 597-600, 2010

[4.12] E. K. Kowalczuk, R. D. Seager, and C. J. Panagamuwa, “Power handling of a photoconductive microwave switch”, In Antennas and Propag. Conf. (LAPC), Loughborough, U.K., pp. 1-3, 2016

[4.13] Anritsu Europe, K Male Flange Launcher, [accessible: https://www.anritsu.com/en-GB/components-accessories/products/k104m-r]

[4.14] Thorlabs, Manual Stages, 3-Axis MicroBlock Compact Flexure Stages, [accessible: https://www.thorlabs.com/newgrouppage9.cfm?objectgroup_id=1041]

[4.15] D. M. Pozar, “Microwave engineering”, John Wiley & Sons, 3th edition, 2009

[4.16] E. C. Robert, “Foundations for Microwave Engineering”, John Wiley & Sons, 2nd Edition, pp. 150, 2007

[4.17] C. D. Gamlath, A. W. Pang, M. J. Cryan, “Investigation of an optically induced superstrate plasma for tuning microstrip antennas”, IET Optoelectronics, vol. 11, no. 6, pp. 230-236, 2017

[4.18] National Physical Laboratory, Dielectric properties of materials, [accessible: http://www.kayelaby.npl.co.uk/general_physics/2_6/2_6_5.html]

[4.19] G. M. Hale, M.R. Querry, "Optical constants of water in the 200-nm to 200-μm wavelength region", Applied optics, vol. 12, no. 3, pp. 555-563, 1973

[4.20] T. Youssef, C. Joseph, H. Sameer, "Demonstration of a cognitive radio front end using an optically pumped reconfigurable antenna system (OPRAS)", IEEE Trans. on Antennas and Propag., vol. 60, no. 2, pp. 1075-1083, 2012

[4.21] AWR Microwave Office, RF/Microwave Circuit Design, National Instruments, https://www.awrcorp.com/products/ni-awr-design-environment/microwave-office-software

[4.22] J. D. Arnould, A. Vilcot, G. Meunier, "Towards a simulation of an optically controlled microwave microstrip line at 10 ghz", IEEE Transactions on magnetics, vol. 38, no. 3, pp. 681-684, 2002

[4.23] A. Bhadauria, A. K. Verma, E. K. Sharma, B. R. Singh, "Optically controlled microstrip load and stub on silicon substrate", Microwave and Optical Technology Letters, vol. 39, no. 4, pp. 271-276, 2003

[4.24] T. C. EDWARDS, "Fundamentals for microwave circuit design" (J. Wiley and Sons, New York, 1981)

[4.25] R. A. Smith, ″Semiconductors″, Second Edition Cambridge University Press, 1978

[4.26] Rohde-Schwarz, R&S®SMU200A Vector Signal Generator, baseband characteristics, [accessible: https://www.rohde-schwarz.com/uk/product/smu200a-productstartpage_63493-7555.html]

[4.27] Milmega, Rosenkranz Elektronik GmbH, AS0820-100R Linear Amplifier, [accessible: http://international.go-dove.com/en/event-18600/lot-122/Milmega-AS0820-100R-Linear-Amplifier]

[4.28] MiNi-Circuits, ZACS242-100W+ HI PWR SPLTR CMBD / SMA / RoHS, [accessible: https://www.minicircuits.com/WebStore/dashboard.html?model=ZACS242-100W%2B]

[4.29] MiNi-Circuits, Directional, bi-directional, dual-directional couplers, [accessible: https://ww2.minicircuits.com/WebStore/Couplers.html]

[4.30] Rohde-Schwarz, R&S®NRP-Z24 Three-Path Diode Power Sensors, [accessible: https://www.rohde-schwarz.com/uk/product/nrpz24-productstartpage_63493-8581.html]

[4.31] Rohde-Schwarz, R&S®Power Viewer for Windows, [accessible: https://cdn.rohde-schwarz.com/dl_software/powerviewer/PowerViewer-Install10.1.6759.2648.msi]

[4.32] Rogers Corporation, RT/duroid® 5880 Laminates, high frequency PTFE composites, [accessible: http://www.rogerscorp.com/acs/products/32/rt-duroid-5880-laminates.aspx]

[4.33] D. A. Neamen, "Semiconductor physics and devices: basic principles", McGraw-Hill Inc., 4th edition, 2003

[4.34] E. K. Kowalczuk, R. D. Seager RD, C. J. Panagamuwa, "Investigating factors affecting photoconductive microwave switch performance using 3D EM simulation"

[4.35] Z. R. Chowdhury, K. Cho, N. P. Kherani, "High-quality surface passivation of silicon using native oxide and silicon nitride layers", Applied Physics Letters, vol. 101, no. 2, 2012

[4.36] B. Stegemann, K. M. Gad, P. Balamou, D. Sixtensson, D. Vössing, M. Kasemann, H. Angermann, "Ultra-thin silicon oxide layers on crystalline silicon wafers: Comparison of advanced oxidation techniques with respect to chemically abrupt SiO2/Si interfaces with low defect densities", Applied Surface Science, vol. 15, no. 395, pp. 78-85, 2017

[4.37] H. Kakiuchi, H. Ohmi, M. Harada, H. Watanabe, K. Yasutake, “Formation of silicon dioxide layers at low temperatures (150–400 C) by atmospheric pressure plasma oxidation of silicon”, Science and Technology of Advanced Materials, vol. 8, no. 3, pp. 137, 2007

CHAPTER 5

5. Optically Controlled Co-Planar Waveguide Millimetre Wave Switches

5.1 Introduction

The interest of this study moves to higher frequencies in this chapter based on the growing attention to millimetre wave technologies. The chapter will be divided into two parts and most of the materials shown here were presented in [5.1, 5.2]. The first part will contain a proposal for an optically controlled Co-Planar Waveguide millimetre wave switch based on the superstrate design on a fused silica glass substrate and bottom illumination as discussed in the last chapter. The focus of the second part will be an optically controlled millimetre wave attenuator based on the switch proposed in the first part and the ability to easily integrate this with a standard PCB design will be further explored. Studies on the improvement of optical power efficiency will also be discussed. Both designs involve models developed using FIT-based CST simulation, which has helped to choose the optimal dimensions for the components. It is also important to note that measurements based on V and K connectors are compared with the modelled results and show good agreement.

5.2 Reviews and Proposals

As discussed previously, reconfigurable Radio Frequency (RF) microwave and millimetre wave (mmW) switches are important aspects of modern communication systems [5.3]. The increasing demand for faster data rates and more bandwidth has motivated research for next generation wireless communication systems. The millimeter wave bands promise a massive amount of unlicensed spectrum at 28 GHz and 38 GHz and are potential frequency bands for 5G cellular systems [5.4]. Reconfigurable circuitry stands out for its solution to the unprecedented challenge of accommodating multiple wireless standards that reduces the system size and removes the requirement of duplicating the same circuits for every desired band. Mature RF switching technologies are mainly based on varactors, PIN diodes, transistors or RF MEMS [5.5-5.9]. The requirement for DC bias lines is a major issue for all these approaches and this can lead to complex bias circuits and parasitic effects which can degrade their performance at millimetre-wave frequencies and above. Therefore, there is a need for alternative technologies that work well at these very high frequencies.

One such approach is based on Optically-Induced Plasmas (OIPs) [5.10-5.14]. The basic physics of a microstrip gap-based optical switch was described in our previous work [5.15]. Here a microstrip gap is defined on a silicon substrate and the gap is illuminated by light with energy above the band gap of the semiconductor. In this case a plasma region made up of electron and hole pairs is created and this area becomes electrically conductive. Several such switches and switchable antennas have been developed based on microstrip lines and patch antennas [5.15-5.17]; however, microstrips tend not to perform well at millimetre-wave frequencies. CPW particularly reduces surface wave modes and hence reduces dispersion and radiative loss [5.18]. Therefore, the use of a Co-Planar Waveguide (CPW) as a transmission line is explored in this research. Not only does this give a good high-frequency performance, but also the switch topology becomes more flexible since the centre conductor can now be grounded easily, which results in a normally-ON type switch. A silicon substrate CPW switch was previously demonstrated in [5.13] to have good insertion loss and isolation values up to 25GHz. However, its top illumination approach limits the integration with other circuits since a handling fixture may always be required to hold the optical source, whether optical fibre or LEDs. Furthermore, as explained in Chapter 2, the plasma diffusion follows an exponential

decaying profile from the surface incident with illumination. Hence, the highest photoconductivity of the plasma region is not utilised in the aspect of energy efficiency in this top illumination approach. A bottom illumination approach was proposed and discussed in [5.12] and in the last chapter. This hybrid integrated approach with a silicon superstrate makes it likely that this circuit can be easily incorporated into large complex circuits. In addition, [5.12, 5.13] have only reported a switch performance up to $7GHz$ and $25GHz$ respectively, whereas this proposed study will lift this boundary into the millimetre wave regime up to $50GHz$ with V connectors. Detailed 3D electromagnetic modelling will also be studied.

The fabrication procedure of the high-resistivity-silicon optically controlled CPW RF switch with a surface area of $400\mu m \times 400\mu m$ is shown in Figure 5.1. This is much smaller than the proposed circuit scale in the last chapter.

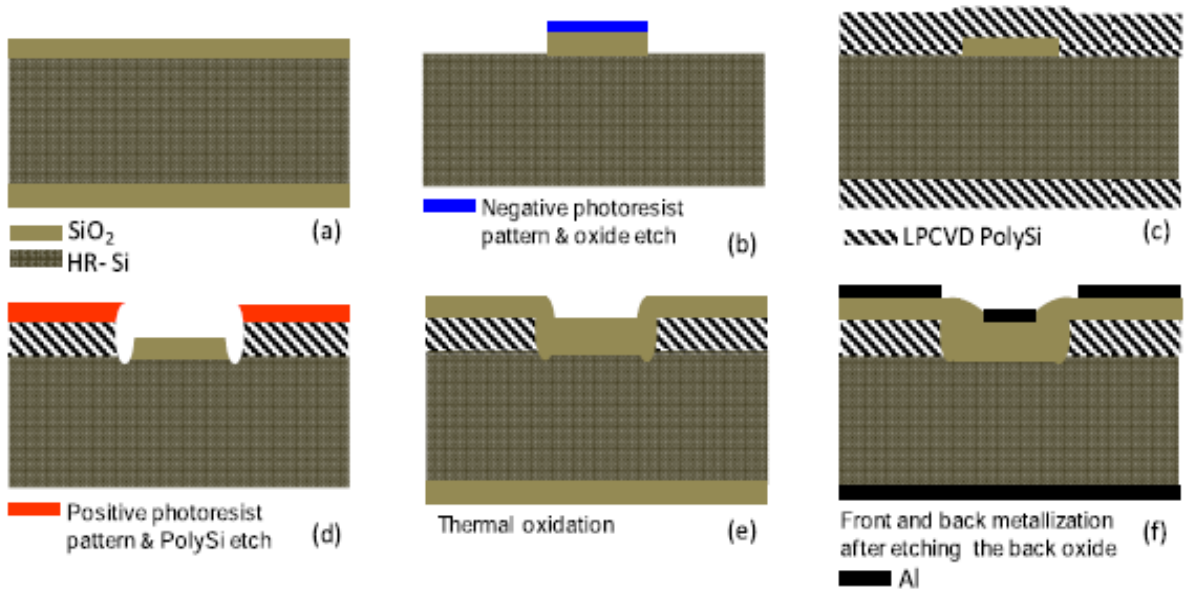

Figure 5.1 Process steps for a trap-rich HR-Si optically controlled CPW RF switch [5.13]

OIP-based switches have been shown to have very good linearity at high power levels, such as an input power of 30dBm in [5.10] and 46dBm in the results of the last chapter. The hybrid integration approach is considered to be more suitable for high power applications, since it involves the use of bottom illumination, which enables simple integration and heat sinking of

the light source. A smaller size of circuit shown in Figure 5.1 will inevitably degrade the heat sinking and power handling ability.

As introduced above, an optically controlled CPW millimetre transmission line switch based on a superstrate structure, bottom illumination and a considerable size for power handling will be studied first. After the successful development of this newly-proposed millimetre switch, the further improvement of the isolation, optical source efficiency and low-cost fabrication will be discussed. The requirement of DC power for the light source is generally the main shortcoming of optically controlled switches. However, applications like Radar and wireless communication basestations, which already consume a large amount of power, may not be affected by an additional 1-2W in the power budget. The second part of this chapter will be devoted to the employment of affordable LEDs in the proposed device and the improvement of optical efficiency. There are also new light source technologies, such as microLEDs, which have high optical intensity and can be easily integrated with our approach in the future [5.19].

With regard to improving the isolation, many microwave switches have reached an isolation of more than 10 dB with either LEDs or fibre-coupled lasers. The first exploration of the OIP along CPW gaps found a 1.3 dB attenuation up to 20 GHz on a silicon substrate [5.20]. Later, over 20 dB attenuation with LED illumination was reported in [5.21] based on a meandered CPW attenuator. However, the performance deteriorated when the frequency was raised over 7 GHz due to the effect of a low pass filter (LPF) from the meandered structure. Although good attenuation was achieved in [5.13], this complex fabrication process can be difficult and time-consuming, as shown in Figure 5.1. In addition, since the small area of illumination is not easily achieved using low cost LEDs, it is also useful to explore the fabrication of a standard PCB circuit without photo-lithography fabrication and flip-chip integration techniques [5.22]. Therefore, a LED-controlled CPW millimetre-wave attenuator will be proposed in the second part of this chapter to provide a low-cost and flexible approach integrated with an on-board millimetre circuit.

5.3 Optically Controlled CPW Millimetre Wave Switch

5.3.1 GCPW Line Introduction and Modelling

As mentioned in the last section, microstrips tend not to perform well at millimetre-wave frequencies and CPW reduces the surface wave modes, thereby reducing dispersion and radiation loss [5.18]. It is important to firstly introduce the CPW and compare it to a microstrip. The CoPlanar Waveguide (CPW) was invented by Cheng P. Wen in 1969 [5.23] and a classic CPW consists of a central conductor that is separated from a pair of ground planes. These metal tracks sit on a dielectric medium and the thickness of this dielectric material is assumed to be infinite, while, in practice, it should be sufficiently thick for the electromagnetic fields to die out before leaking from the dielectric medium. Hence, a variation of the standard CPW was created, which adds another ground plane on the opposite side of the dielectric material. This is called a Grounded coplanar waveguide (GCPW). A Grounded CPW approach was adopted in this study for several reasons, the first of which is that the GCPW provides mechanical convenience for the alignment of the optical circuit and better integration with a brass block fixture with V-connectors. Since one of the disadvantages of the CPW is poor heat dissipation, a brass block as part of the ground plane is a good heat sink metal for the optical source, especially when an LED is mounted as a replacement.

The electromagnetic field line diagrams of a microstrip line and a GCPW line are shown in Figure 5.2. Both GCPW and microstrip propagate electromagnetic waves in quasi-TEM mode. This “quasi” here means that the waves propagate through different media, namely, air on one side and dielectric on the other. Hence, there can be different speeds in these regions. While they both have relatively low radiation losses in a microwave frequency regime, high loss can be seen in the microstrip lines in millimetre-wave frequencies. At these high frequencies, these transmission lines also support higher modes and surface modes that deteriorate the performance. Mode suppression means to suppress the unwanted modes from a quasi-TEM. Microstrips find it difficult to suppress higher order modes at millimetre-wave frequencies, which can create more radiation loss. The unwanted modes can rise and disturb the quasi-TEM from propagating correctly, thereby causing dispersion. For the microstrip design, only

substrate thickness and conductor width can be varied to provide higher mode suppression. In contrast with the GCPW, both the width of the central conductor and the spacing between the ground planes and the conductor can be altered, as shown in Figure 5.2. In addition, vertical interconnect access (via) can also be introduced to reduce CPW's surface modes.

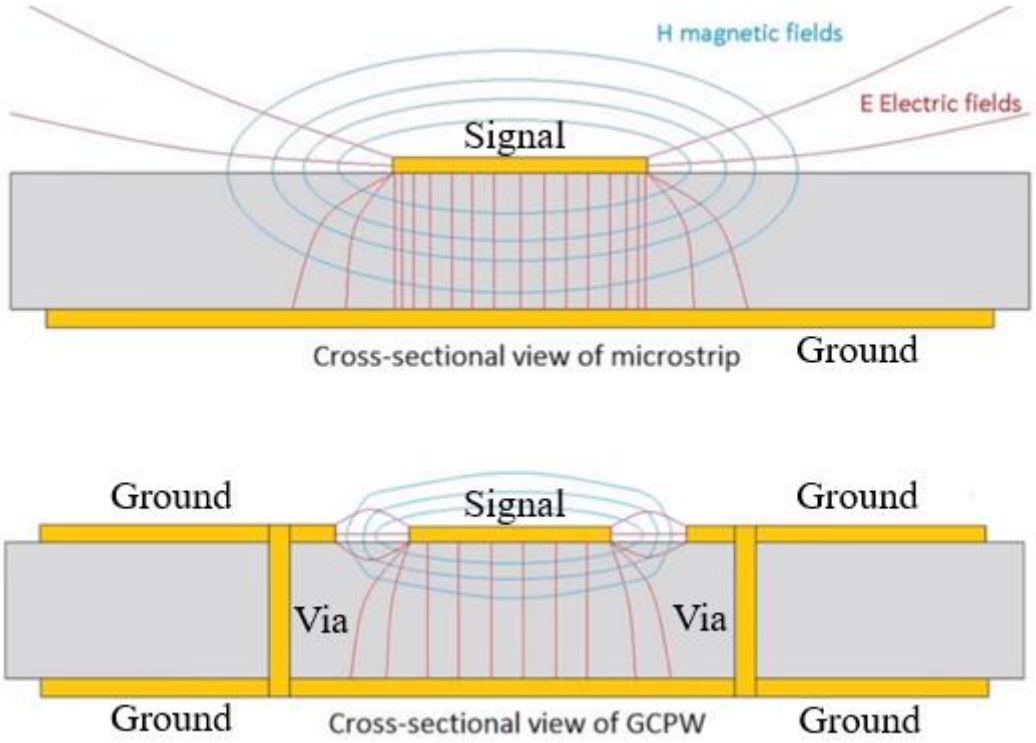

Figure 5.2 Cross-sectional diagrams of electric field lines for a microstrip line and a GCPW line

In Figure 5.2, most electric field lines are concentrated between the signal line and the ground plane. However, there is also another portion of field lines at the edges that forms a fringing field with high current density that cannot be easily returned to the ground and thus produces losses. With regard to the GCPW, in addition to the strong field that exists between the signal line and the bottom ground plane, it is further constrained to ground planes on both sides. The benefit of these additional coupling areas distinguishes the GCPW from microstrips in higher frequencies. The tight spacings between the ground planes and the signal line effectively reduce the number of spurious modes. Furthermore, the variables of the central conductor linewidth of the GCPW and the spacing between the conductor and ground planes allow many possible combinations, even for a single characteristic impedance value. Therefore, sensitivity analysis

was conducted in a CST simulation to select the optimum dimension for an optically controlled GCPW switch based on a transmission line model. An important aspect of GCPW design is the interface between the transmission line and the connector. Geometric misalignment at the interface normally brings discontinuities and impedance mismatch. This mismatch with system and load impedance will cause more reflection and less power transfer. Hence, more return loss will be created and less wanted signal can be transmitted through the microstrip or CPW.

An SMA connector was firstly examined due to its low cost and ease of mounting. A mechanical drawing of a SMA connector from [5.24] is shown in Figure 5.3.

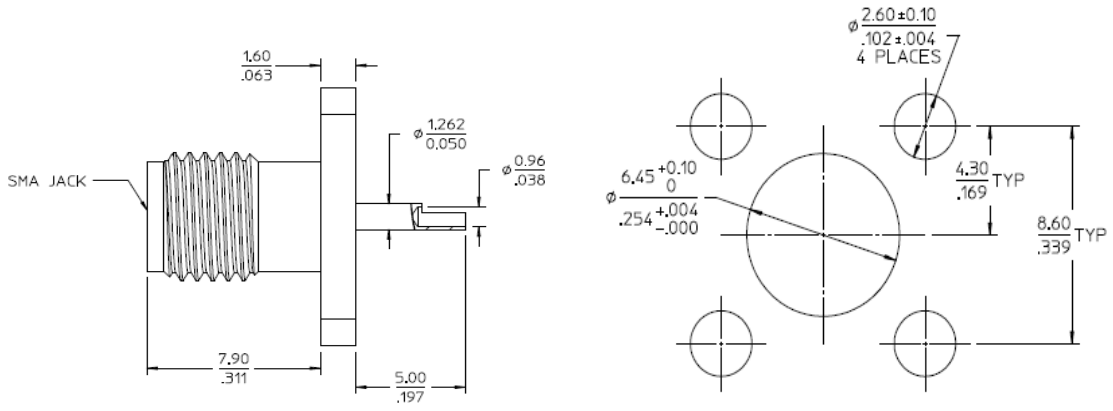

Figure 5.3 Mechanical drawing of a SMA connector [5.24]: Side view (Left), End view (Right)

As can be seen, the diameter of the inner central conductor is 1.262mm and that of the coax outer boundary at the filing material is 6.45mm, which gives nearly 50Ohm impedance. To ensure good geometric alignment and thus impedance match, the recommended dimensions should be taken as close to the coax connector size as possible; the signal linewidth and the spacing between the signal line and the ground of the GCPW are chosen close to the inner and outer coax diameter values respectively. Figure 5.4 shows a perspective view of the connector-GCPW interface in CST. The diameter of the inner central conductor is 1.3mm and that of the coax outer boundary at the filing material is 6.5mm. The central conductor of the GCPW has a linewidth (w) of 1.1mm and the spacing (s) between the central conductor and the ground is 0.62mm.

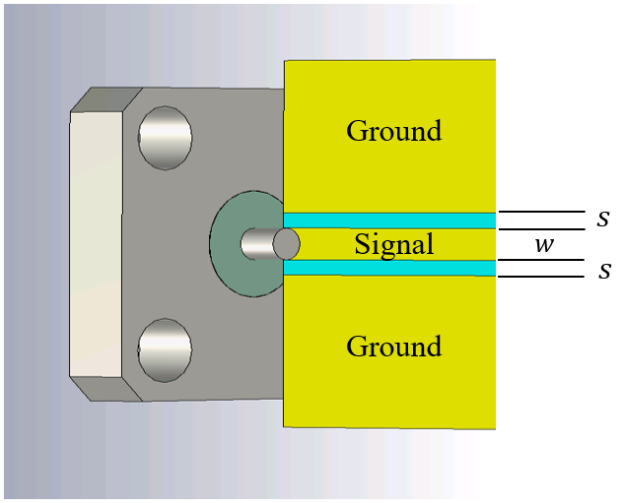

Figure 5.4 Perspective view of the connector-GCPW interface in CST modelling

SMA connector was introduced and employed as pilot, but this type of connector is not suitable for millimetre wave designs. K and V connectors were chosen later for their use at higher frequencies, since they can work up to $35GHz$ and $65GHz$ respectively. A mechanical drawing of a V connector is shown in Figure 5.5. Since different coax lines have different filling material, PTFE was used for the SMA connector, while the filling for the V connector was air, which reduces the dielectric constant and loss for use at higher frequencies. Since the outer shield has a diameter of $1.85mm$ (denoted by C in Figure 5.5), the V connector is also called a $1.85mm$ connector. The inner conductor pin has a diameter of $0.5mm$ (denoted by G) and this value was used as the initial central conductor linewidth in parameter sweep in CST simulation for the V connector GCPW switch design.

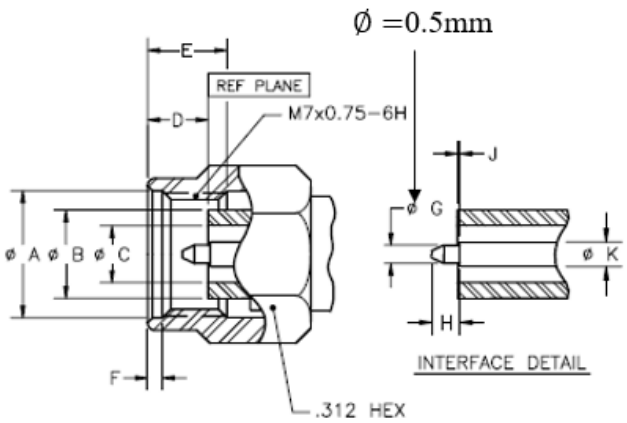

Figure 5.5 Mechanical drawing of a V connector [5.25]

A parameter sweep was conducted of various combinations of central conductor linewidth (w) and spacing (s) between the central conductor and ground planes in CST. These combinations are listed in Table 5.1 for comparison and they all produced a 50Ω characteristic impedance for good impedance match with the whole system.

Index number	Linewidth (w) (μm)	Spacing (s) (μm)
(1)	1000	345
(2)	1100	620
(3)	1200	800
(4)	500	60
(5)	600	80
(6)	700	110

Table 5.1 Geometric dimension combinations of linewidth and spacing for 50Ω GCPW line

The top view of the GCPW model on which the parameter sweep has been based is shown in Figure 5.6. The extended arms around the simulated connector are always in contact with the ground planes on each side. This provides the GCPW with an ideal grounding and connection between these two planes and the bottom ground plane for a better performance.

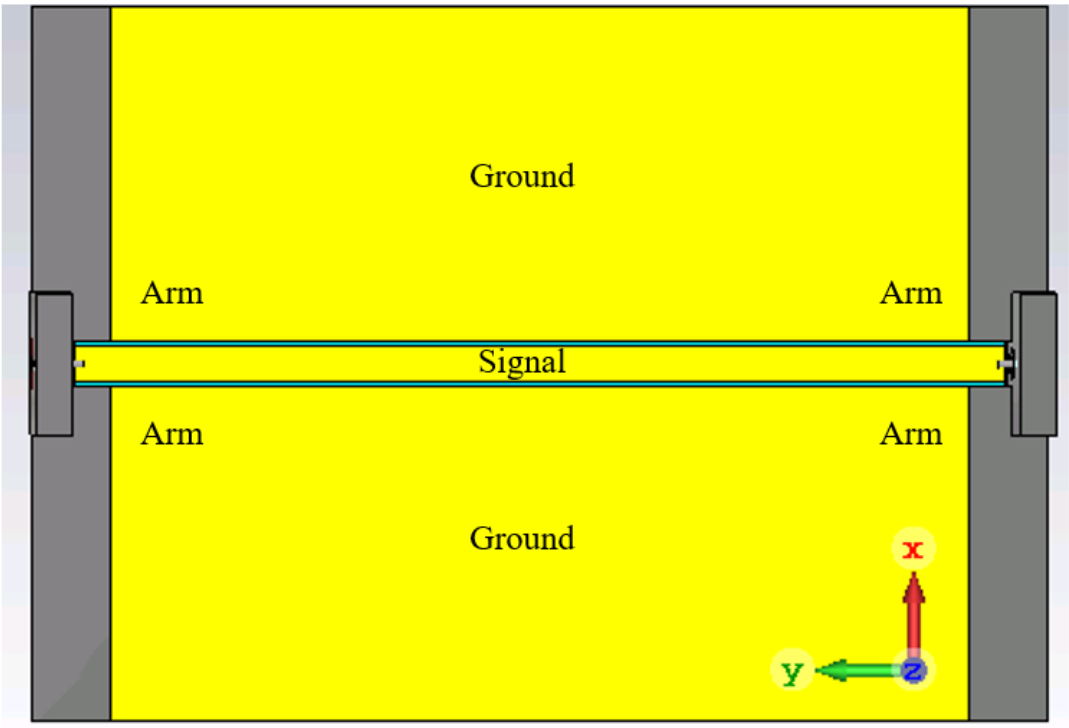

Figure 5.6 Top view in CST of a GCPW transmission line model with grounded arms shown

The simulated S_{11} and S_{21} results are shown in Figure 5.7. The number in the legend of the Figure 5.7 corresponds to the index number of dimension combinations in Table 5.1. As can be seen from Figure 5.7, the trend of increasing S_{11} and decreasing S_{21} suggests that electromagnetic waves more easily lose energy as radiation loss with a raised frequency and this corresponds with the statement explained above. For S_{11}, the results of GCPWs in various dimensions are very similar to each other. Taking each peak of these several ripples in S_{11}, the general trend shows a gradual rise. With regard to the S_{21} results, the values gradually decrease, with the highest insertion loss reaching $12dB$ at $50GHz$. The reference dimension combined with an $0.5mm$ linewidth shows the lowest insertion loss at $4dB$, and this value is shared with several other cases with narrower linewidths. Therefore, this can be considered to be the saturation and optimum point achieved after circuit-connector geometric matching. A comparison of the best case and another similar case is always recommended in practice. Based on this simulated result in Figure 5.7 and the above discussion of the geometric continuity as well as impedance matching, GCPW line with $1.1mm$ central linewidth and $0.62mm$ spacing to ground has been chosen to work with SMA connector while GCPW line with $0.6mm$ central linewidth and $0.08mm$ spacing to work with V connector.

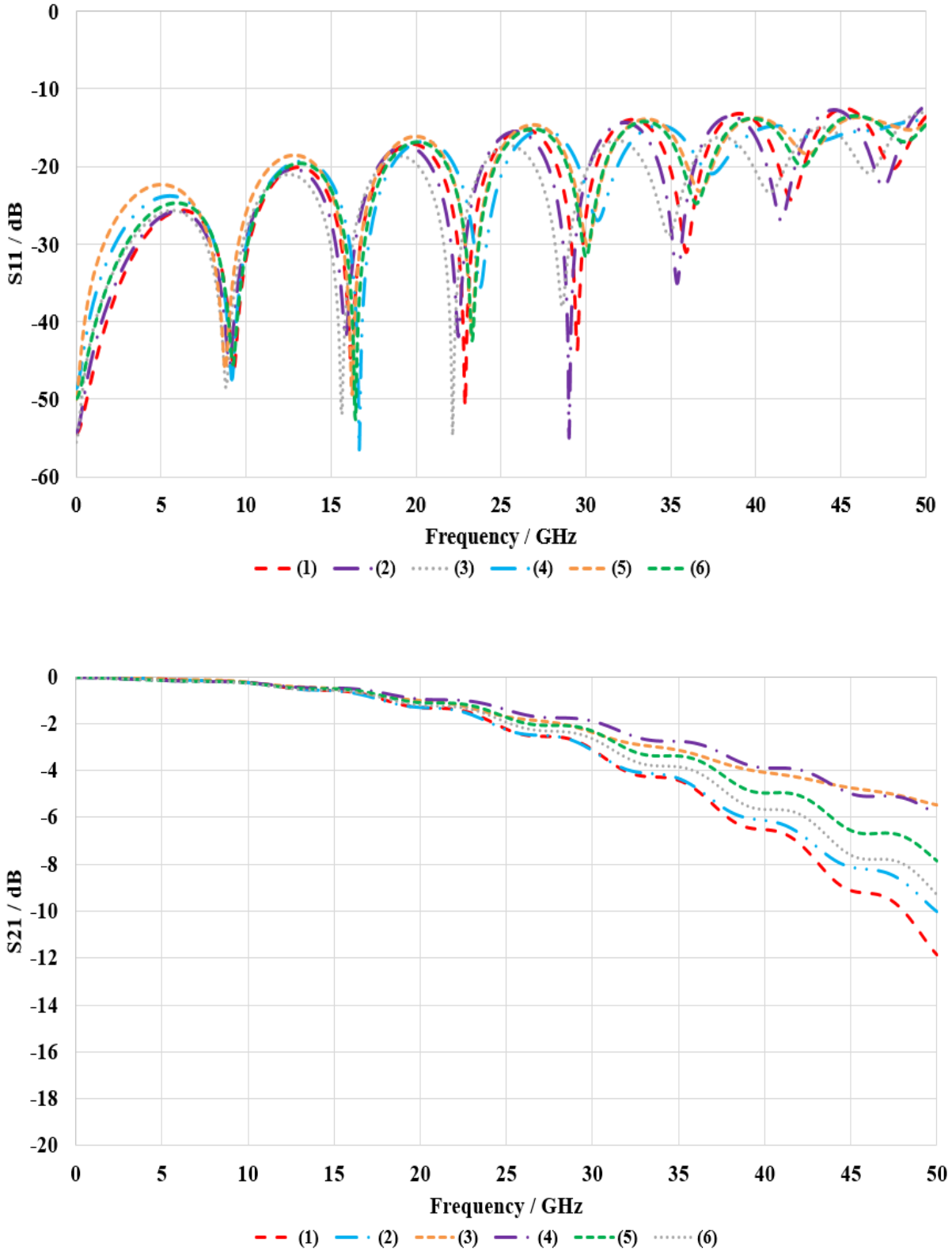

Figure 5.7 Parameter sweep S_{11} (Top) and S_{21} (Bottom) results of different GCPW dimension combinations in linewidth and spacing

5.3.2 SMA GCPW Switch

After the GCPW transmission line was modelled in CST, a good foundation had been built for a GCPW switch design. The initial idea for constructing an optically-reconfigurable switch was to use the same mechanism for the microstrip gapline utilised in the last chapter; however, there were concerns about the plasma diffusion characteristic. Due to the relatively small spacing between the central conductor and the pair of ground planes, plasma can diffuse spontaneously further away and this is likely to create a resistive path from the central conductor to the ground. The resistance of the path largely depends on the intensity of the optical illumination. Manipulating the optical source can be controversial because, although higher intensity is expected to reduce the loss of insertion in the central gapline, increased diffusion will also effectively create resistive paths to the grounds, possibly causing even more loss in this region. Although this plan was rejected, a new idea was formed using these resistive paths to the grounds. As shown in Figure 5.8, the proposed switch topology involves reversing the working scheme for a normal optically-controlled switch. In fact, illumination-ON gives a switch-OFF condition by shorting the central signal line to the ground planes, whereas illumination-OFF yields a switch-ON with the GCPW working as a normal transmission line.

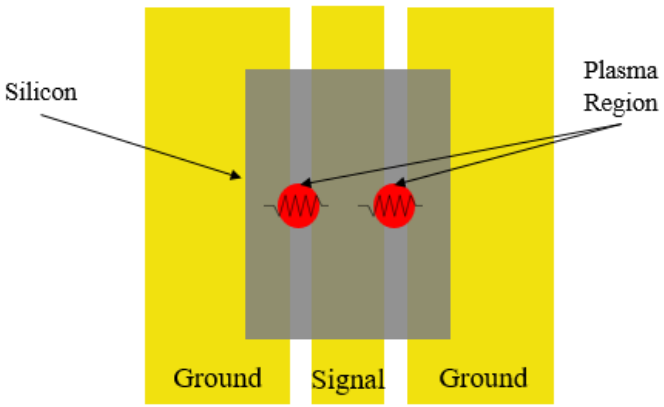

Figure 5.8 Schematic top view of optically controlled GCPW switch layout

The first test was conducted on a transmission line without superstrate as a reference line with 50Ω characteristic impedance. The linewidth and spacing were chosen to be $1.1mm$ and $0.62mm$ respectively from the previous simulated results. An important feature of this work was the continued use of optically-transparent fused silica glass ($\varepsilon_r = 3.5$) as a low loss

microwave substrate. This allows bottom side illumination which produces a highly-integrated device. The fused silica substrate was $500\mu m$ thick and lithographically processed to create gold CPW transmission lines, as outlined in the following text. Piranha Solution was used for the initial cleaning to remove the organic impurities and dust on the surface. It was then sputter coated with $5nm$ titanium and $500nm$ gold in an ambient argon atmosphere. The circuit was defined by spin coating, thereby exposing and developing negative photoresist on the wafer. Finally, the exposed gold and titanium were removed with wet etching. A photograph of a GCPW line with $1.1mm$ central linewidth and $0.62mm$ spacing to ground is shown in Figure 5.9. As can be seen, a large amount of silver epoxy was used to ensure the connection of the ground planes.

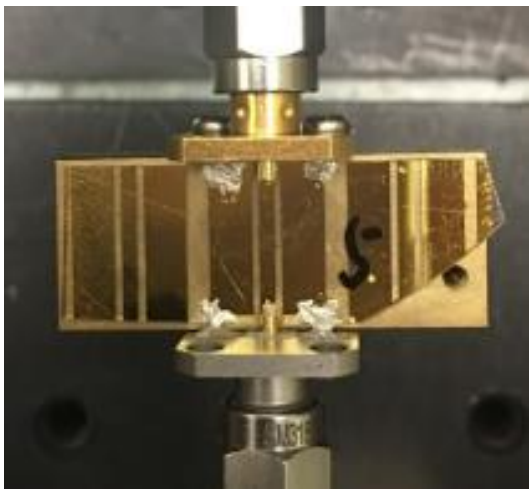

Figure 5.9 Photograph of a GCPW line with 1.1mm central linewidth and 0.62mm spacing to ground with SMA connectors

The measured results are shown in Figure 5.10 from which it can be seen that a good performance was obtained up to 15GHz in spite of some small ringings in S_{21} that occurred at around $5.6GHz$, $8.5GHz$, $11GHz$ and $13.5GHz$. These minor losses are due to circuit defects and scratches.

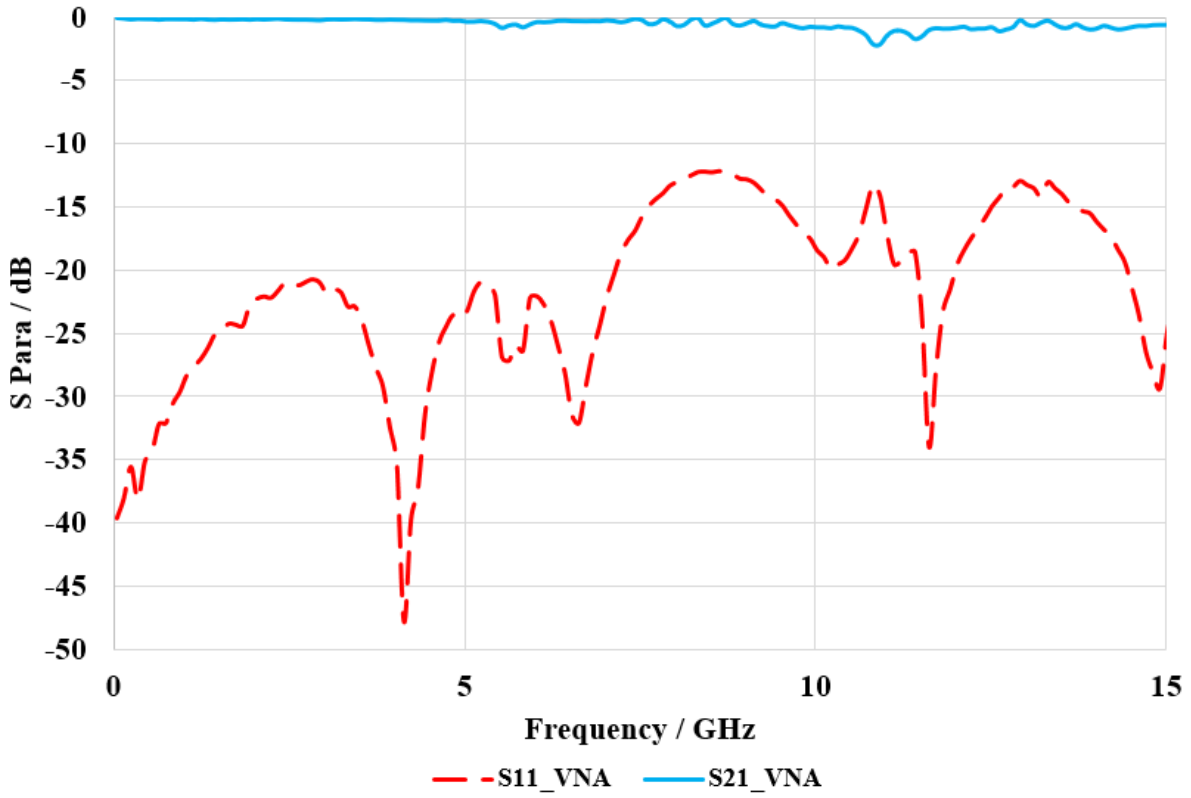

Figure 5.10 Measured S_{11} and S_{21} for 50 Ω GCPW line with 1.1mm central linewidth and 0.62mm spacing to ground with SMA connectors

The schematic end view and top view images of the test fixture of the optically-controlled CPW microwave switch are shown in Figure 5.11 and Figure 5.12 respectively. A piece of silicon, 3mm x 3mm x 0.5mm ($\varepsilon_r = 11.9$), was used as a superstrate, which was held in place using a thick Perspex bar, and covered the CPW gaps to the ground. The silicon superstrate was a lightly doped n-type wafer with <100> orientation and resistivity$> 10\ k\Omega.$ cm. A $300nm$ thick silicon dioxide layer was deposited on the silicon surface to remove the Schottky contact between the metal and the semiconductor interface. Optical illumination was provided by a 980nm wavelength fibre-coupled laser diode (Roithner Lasertechnik) [5.26]. The fibre laser was coupled through a hole in the block, which was designed to have a minimal effect on the microwave response. Two electron-hole plasma regions were generated in the silicon with the high conductivity region close to the CPW gaps.

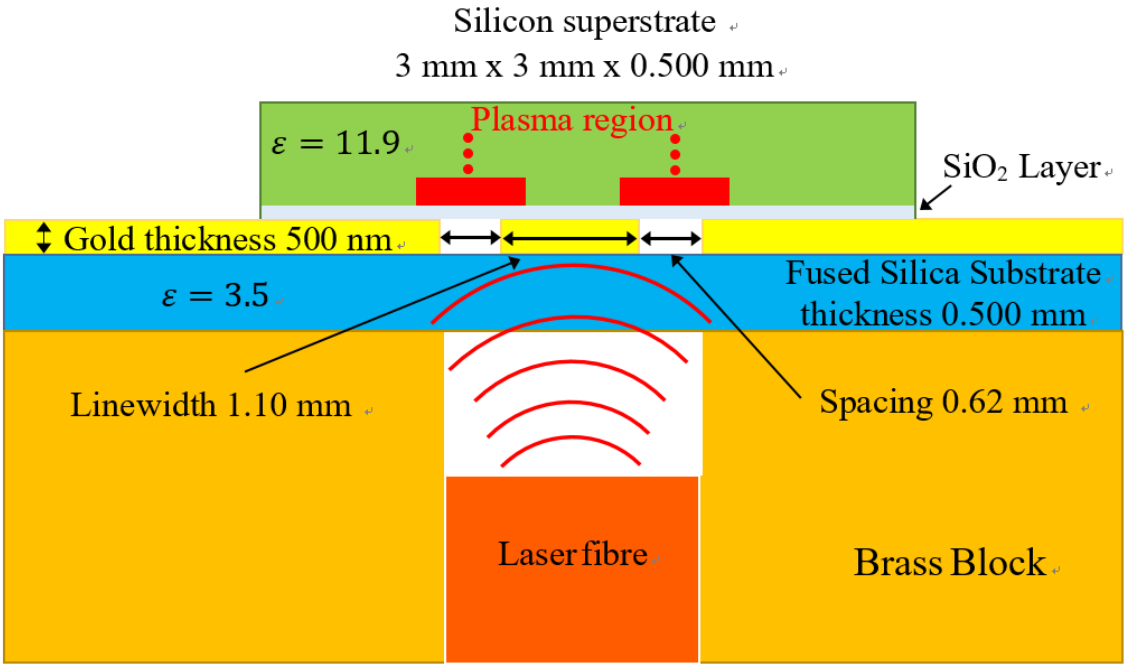

Figure 5.11 Schematic end view of superstrate optically controlled GCPW switch with bottom illumination (1.1mm central linewidth, 0.62mm spacing to ground and 3mm x 3mm x 0.5mm superstrate silicon)

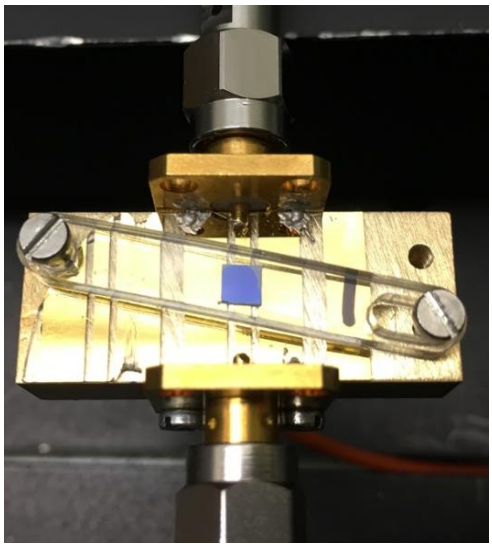

Figure 5.12 Photographic top picture of superstrate optically controlled GCPW switch with bottom illumination (1.1mm central linewidth, 0.62mm spacing to ground and 3mm x 3mm x 0.5mm superstrate silicon)

CST was used as a full wave 3D Electromagnetic modelling tool with the implementation of cascaded layers of varying conductivity to represent the plasma region, as described in Chapter 4. A detailed description of the simulation is included in the next section. The VNA measured and CST simulated S_{21} of the CPW in the ON and OFF conditions is shown in Figure 5.13. This switch has a reasonably good insertion loss up to 20GHz with no laser illumination. When illumination is provided, the central track in the CPW will be shorted to ground and insertion loss will increase to more than $10dB$ above $15GHz$. An illumination intensity of 18W/cm^2 was used in the measurement and 800S/m conductivity at the plasma surface layer were used in the CST simulation. Reasonably good agreement between the simulated and measured results was achieved up to 20GHz, which was mainly limited by the connector transitions.

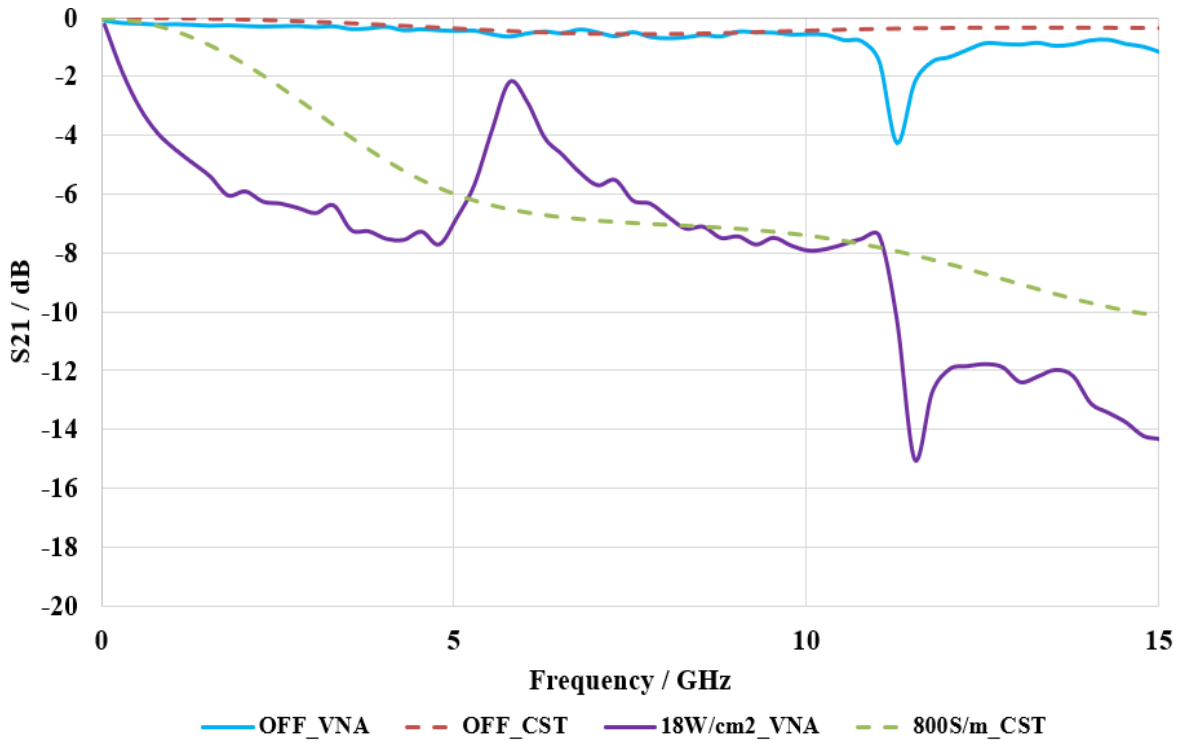

Figure 5.13 Measured S21 magnitude for optically controlled CPW microwave switch with 1.10 mm central linewidth and 0.62 mm spacing to ground

The predicted performance in CST of a similar switch with a 0.62 mm central linewidth and 0.1 mm spacing to ground with a 2 mm x 2 mm x 0.5 mm silicon superstrate up to 60GHz is shown in Figure 5.14. Increasingly good isolation values up to 25 dB at 50 GHz can be observed here, which is very promising for the experiments with V connectors.

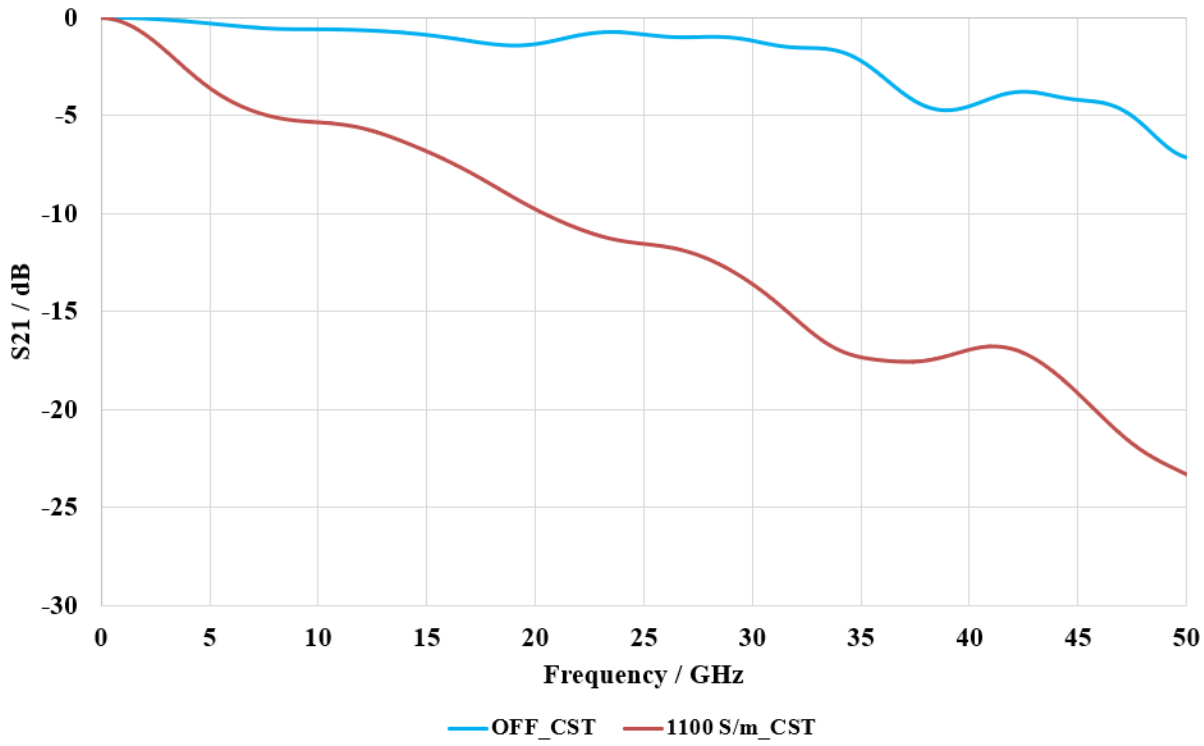

Figure 5.14 CST Simulated S21 magnitude for optically controlled CPW microwave switch of 0.62 mm central linewidth and 0.10 mm spacing to ground (optical intensity at 25W/cm^2)

This section contains a report on a bottom-illuminated optically controlled microwave CPW switch with a low insertion loss up to 20 GHz and an off-state isolation over 10 dB from 15 GHz to 20 GHz. Good agreement with electromagnetic modelling has been shown and a very good isolation behaviour up to 50 GHz can be predicted using a similar switch. It is believed that the implementation of a V connector and the optimisation in GCPW will further improve the performance of the switch. Since the optically induced plasma used here is inherently frequency independent in nature, it is envisaged that the millimetre wave performance of such devices will be equally good. This is particularly encouraging since conventional switching approaches become much more difficult to implement in those frequency ranges.

5.3.3 Millimetre Wave Design with V Connector

A GCPW switch based on a V connector is discussed in this section. Since electromagnetic waves can be less constrained in high frequency and tend to escape from the strip or waveguide

structures, the fundamental geometric matching of the coax connector and the circuit is considered to be extremely important. Therefore, much effort was made in this research to find a good alignment technique. A picture of the V connector used in this study is shown in Figure 5.15. This is a VF116 screw-in and hermetic model from Anritsu [5.27].

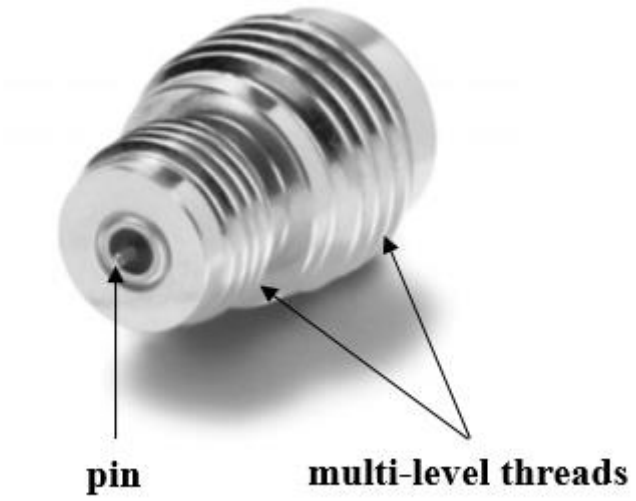

Figure 5.15 V116F connector from Anritsu [5.27]

There are several good reasons for this choice. Firstly, as can be seen from Figure 5.15, this connector has two parts of threads, which is convenient for mechanically mounting fixtures and it also leaves room to extend the reach of the pin. The next is the glass beads. As mentioned earlier, the filling material for a V connector is air. Transition issues can occur when this coax connector is transferred to another strip or waveguide circuit, which can result in a serious return loss. Glass beads can facilitate the transition from the main connector, through a housing wall, to a microcircuit. Fortunately, these tiny beads are already installed in the connectors of this model. Another important benefit of this V116F is the purposely designed supplementary sliding contact. When mechanical tolerance causes uncertainty, these sliding contact sleeves can enable a further extension of the connector pin. The sliding contact and its installation schematic diagram are shown in Figure 5.16.

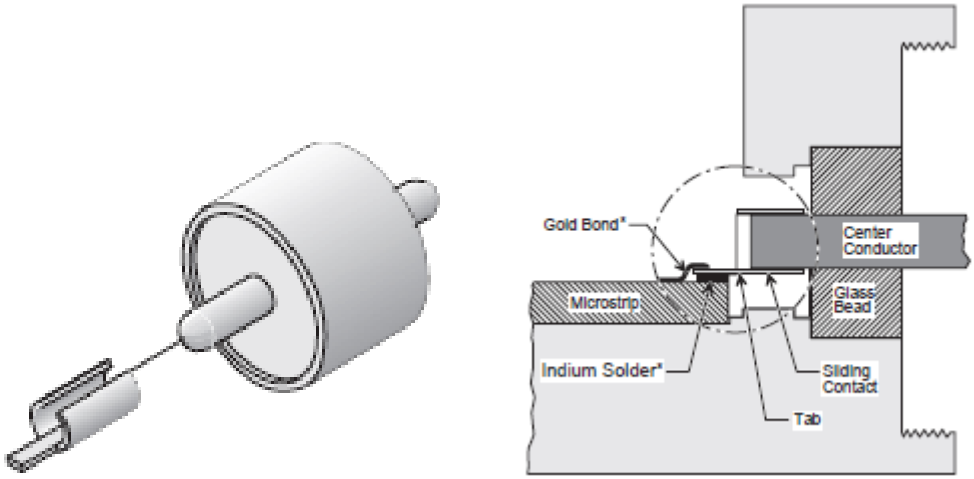

Figure 5.16 V110 Anritsu sliding contact (Left) and Schematic diagram of sliding contact installation (Right) [5.28]

In terms of this installation diagram, Anritsu recommends the machining dimensions for the mounting hole shown in Figure 5.16. As can be seen, the thickness can be as little as around $3.5mm$ from the outer surface and the inner hall. Such a thin metal plate can risk being broken in milling machine work.

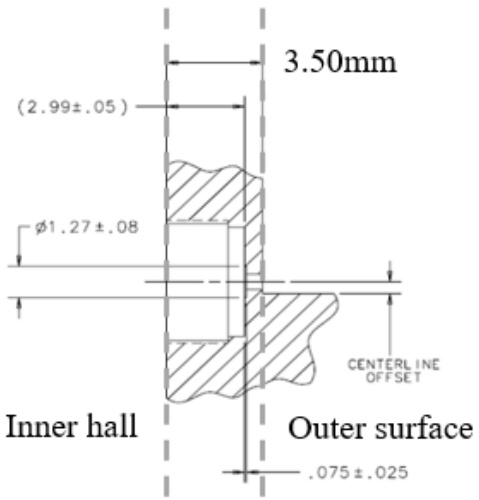

Figure 5.16 Machining dimensions for V116F mounting hole [5.28]

However, this thin metal hall can make more room for an alignment between the connector pin and the GCPW circuit. Hence, it is expected that a sliding contact can be a helpful and essential tool in this respect. A brass block was redesigned for this V connector based on the original

microstrip fixture. The side cross-section view of the proposed machining dimensions of the brass block fixture for the V connector is shown in Figure 5.17. Multi-level threaded holes were drilled on both sides for a firmer fastening.

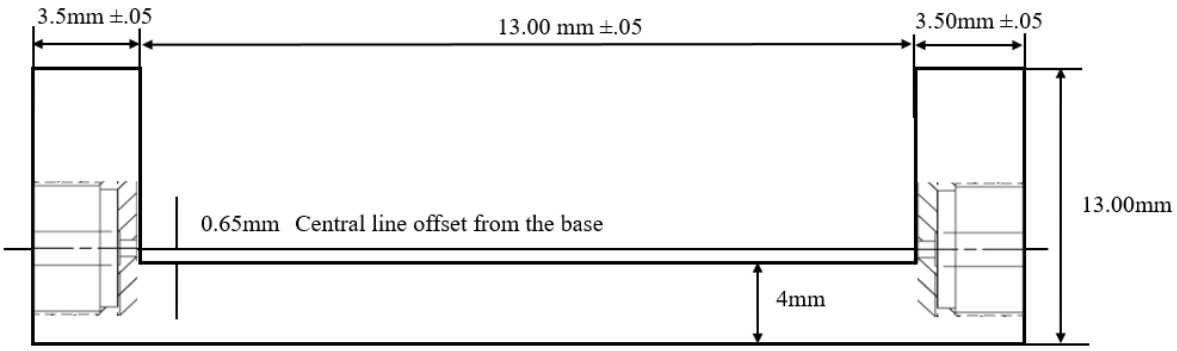

Figure 5.17 Side view cross section of machining diagram for V connector brass block fixture

As mentioned earlier, the conductor pin diameter of the V connector can be as small as $0.5mm$. The sliding contact needs to be mounted under a microscope. The photographic microscope view of the mounted V connector and sliding contact is shown in Figure 5.18 and Figure 5.19. This illustrates how difficult it is to handle a sliding contact with hands or even tweezers. It normally takes a few hours to install the standard packaging of a GCPW switch with a V connector and sliding contact, and the following process is recommended;

- File brass block to remove metal burrs and surface defects; this provides a good contact for the bottom ground plane
- Place circuit wafer in the approximately right place and use plastic screws and washers to hold the sample
- Use tweezers and a microscope to mount the sliding contact sleeves on the V connectors at this stage instead of mounting them after they are screwed into the brass block
- Screw the V connectors into the brass block and adjust the orientation of the sleeves to make contact with the GCPW line
- Use Loctite [5.29] to glue the V connectors onto the fixture
- Very carefully put silver epoxy [5.30] between the sliding contact and the central line
- Carefully put more silver epoxy on every contact area between the brass block and the ground planes

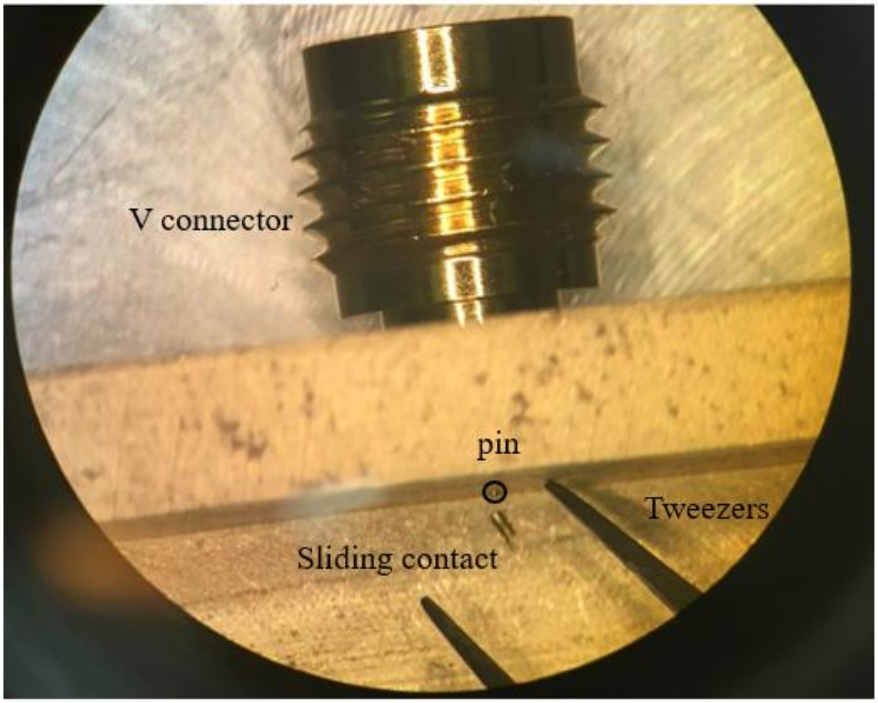

Figure 5.18 Photographic microscope view of a mounted V connector and a sliding contact

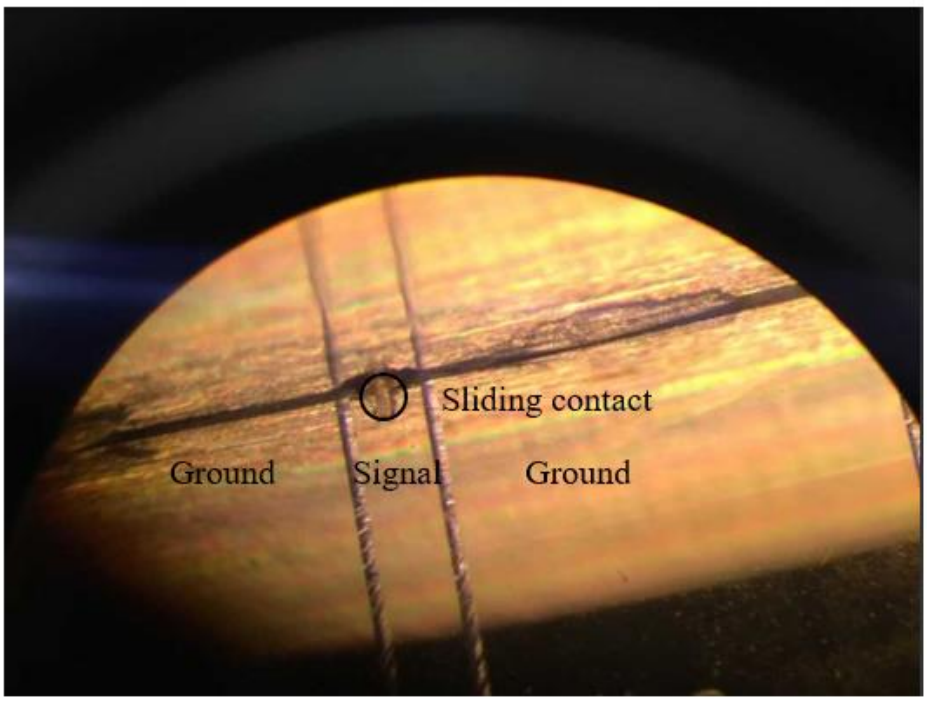

Figure 5.19 Photographic perspective view of a mounted V connector and a sliding contact

5.3.4 V GCPW Switch

A V connector GCPW switch is fabricated following the same procedure as that introduced in §5.3.2. The schematic end view of the GCPW circuit sample covered by a silicon superstrate and mounted on a brass block fixture is shown in Figure 5.20. The central line width (w) is 0.6mm and the spacing (s) between the central line and the grounding planes is 0.08mm.

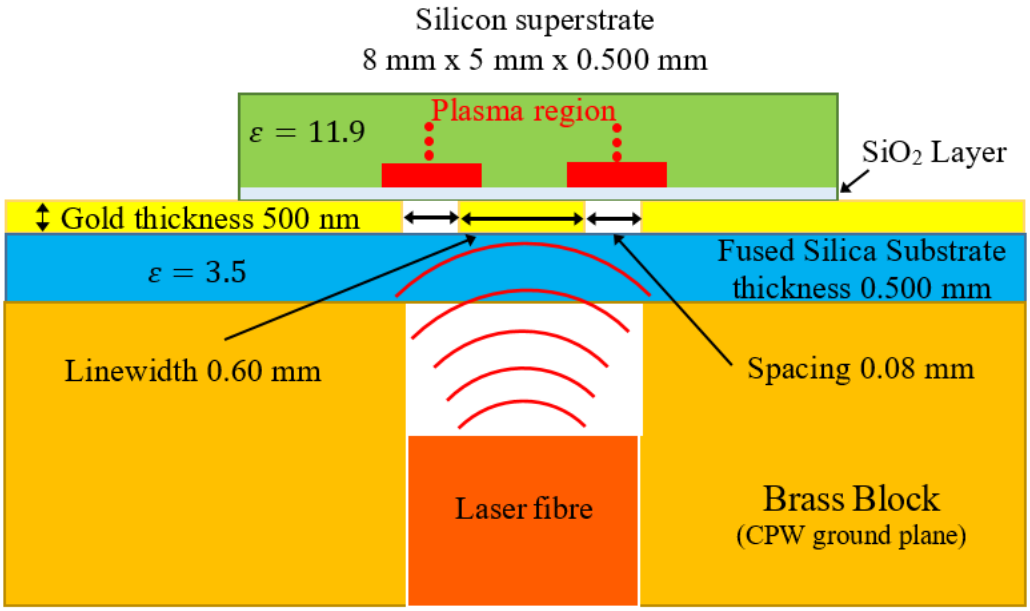

Figure 5.20 Schematic end view of optically controlled GCPW switch with bottom illumination

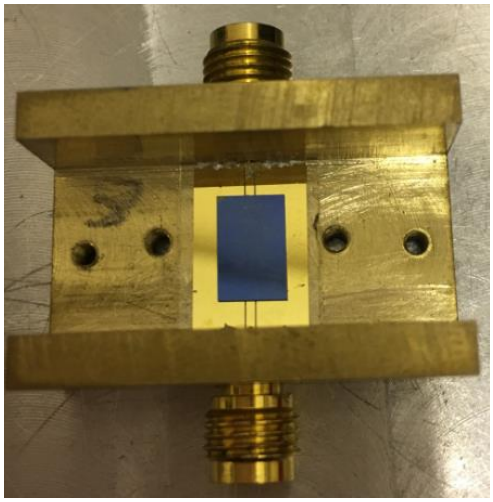

Figure 5.21 Photographic top view of GCPW circuit sample with line width (w) 0.6mm and spacing (s) 0.08mm

The photographic top view of the switch with two illuminated regions in the spacing of the CPW are shown in Figure 5.21. The low resistance of the plasma regions short circuit the CPW line when illuminated from below. A piece of silicon, 8mm x 5mm x 0.5mm (ε_r=11.9) was used as a superstrate which was placed over the GCPW. Figure 5.21 also demonstrates how the light source was integrated into the system. The majority of the laser power was not being used to illuminate the silicon in this case due to the nature of the CPW gaps. This low optical efficiency will be discussed and improved in the second part of this chapter. The plasma region can be represented by a series of varying conductivity layers, as described in [5.15] and the conductivity profile used in this work is shown earlier in Figure 4.10. The corresponding parameters used were absorption depth = 96μm [5.31], bulk recombination time = 10μs, diffusion length = 120μm [5.15]. Illumination power of 175 mW was used in the measurement which corresponds to 1100 S/m conductivity at the plasma surface layer for the CST simulation. The ten cascaded conductive layers are shown in Figure 5.22. There were two plasma regions, each of which was 1200μm x 480μm in area and 480μm high. The size of these regions was chosen to represent (i) the illumination spot size, (ii) the effect of the sideways carrier diffusion, and (iii) the vertical exponential decay in conductivity. In addition, a gap was left between the gold layer and the bottom conductive layer of 20μm to simulate the metal-insulator-plasma contact transition and obtain good agreement at low frequencies.

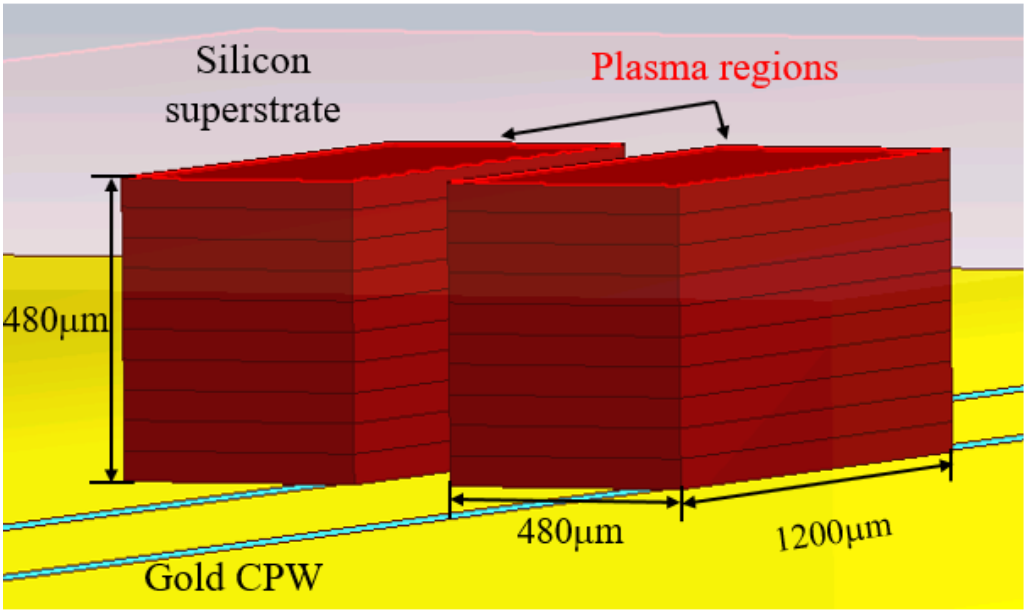

Figure 5.22 Plasma layers within silicon superstrate in CST view

The simulated CST and VNA measured S_{21} of the GCPW in the ON and OFF conditions are shown in Figure 5.23, which indicates good overall agreement. With no laser illumination, this switch was found to have reasonably good insertion loss with less than 4dB through a frequency band of DC to 50GHz. When illumination was provided, a conductive path was created between the central track and the ground planes of the GCPW. This low resistance increased the insertion loss to more than 15dB above 32GHz and there was a large dip of 28.7dB at 46.5GHz. It is believed that the resonant dips around 33GHz and 39GHz were associated with spurious higher order modes on the surface. As mentioned earlier, vias can be used to suppress these modes and hence the ringings of S_{21} in the switch OFF condition can be expected to be smoothed. However, drilling holes through silica glass and installing metal vias are practically difficult. This will be discussed further in the next section. Additionally, an important aspect of these results is that the CPW spacing defines the plasma illumination area and hence, the resistance to ground. Since there was a thin insulating layer between the silicon and the gold, these effects in DC and the low frequency region were masked in this case.

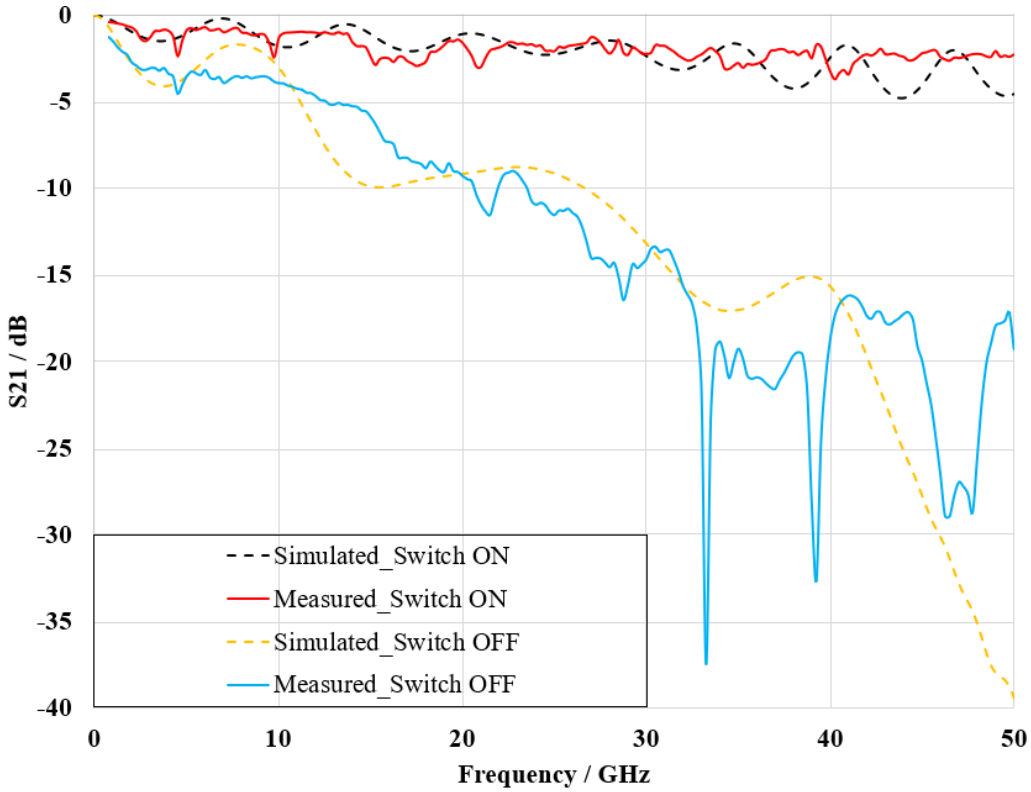

Figure 5.23 Measured and Simulated S21 of GCPW with linewidth, w=0.6mm and spacing, s=0.08mm at Switch ON/OFF conditions (optical intensity at 25W/cm^2)

The CST simulated results for three different CPW spacings are shown in Figure 5.24. It can be seen that only very small differences occurred in these cases. Similarly, other simulations in a sensitivity analysis of the length, width and thickness of the superstrate dimensions have not shown considerable differences. Therefore, the results are expected to largely depend on the practical measurement.

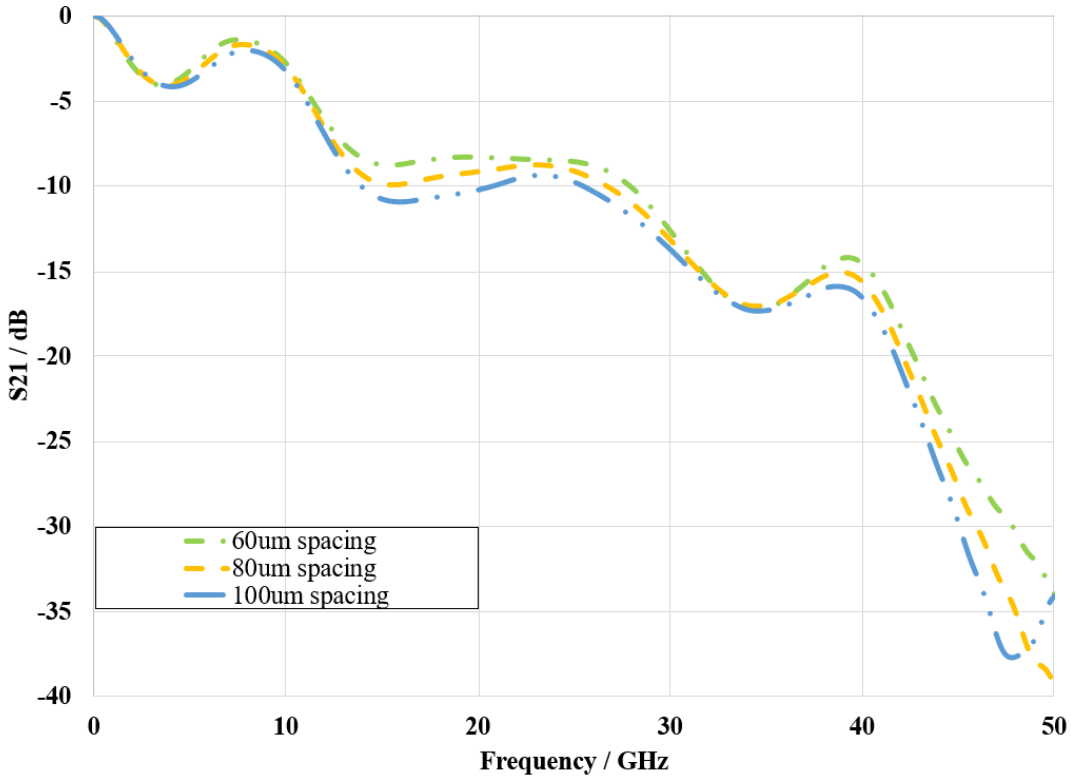

Figure 5.24 Simulated S_{21} of GCPW with linewidth, w=0.6mm and varying spacing values at Switch ON condition (optical intensity at 25W/cm^2)

This section contains a report of a bottom illuminated optically-controlled millimetre wave GCPW switch with a low insertion loss up to 50 GHz and an off-state isolation greater than 15dB from 32GHz to 50GHz. Good agreement with electromagnetic modelling was shown. It is believed that the optimisation of the GCPW geometry, more efficient use of the available optical power and the modification of the circuit grounding and laser coupling will further improve the switch performance. The next part of this chapter will focus on the discussion of work to achieve this improvement.

5.4 Optically Controlled PCB GCPW Millimetre Wave Switch

As discussed earlier, firstly, spurious modes can be found in S_{21} for a fused silica substrate switch, since vias cannot be easily fabricated through the glass substrate and hence, cannot largely reduce the surface current. Secondly, significantly low optical efficiency has been noted based on the small spacing between signal line and ground planes so that only a small proportion of the illumination can pass through it. Thirdly, fibre couple laser can be replaced by LED as a more portable and low-cost optical source. Finally, to further improve the integration with other microwave and millimetre wave circuits, a standard PCB material can be used, which also provides an opportunity to implement vias. All of these factors have been taken into consideration when designing a PCB-based GCPW switch. The proposed substrate fabrication is based on the double-side laminated Rogers RO4003C [5.32]. This low-loss material has a relative permittivity of 3.38 and is 0.508mm thick. It has similar values with the fused silica used above that relative permittivity is 3.5 and thickness is 0.500mm.

5.4.1 PCB GCPW Slot Switch

As the substrate has been changed to ceramics in RO4003C, the previous optically transparent property of a fused silica cannot be relied on. To implement the bottom illumination, it is important to vacate the spacing area between signal line and ground planes in a GCPW to allow optical illumination to go through. The first idea was to use the same laser-cutting machine to burn off the spacing material to form a slot for illumination passing. SMA connector was used as a pilot due to its low cost. Figure 5.25 shows the first test circuit as a GCPW switch which was based on a transmission line of 50Ω characteristic impedance.

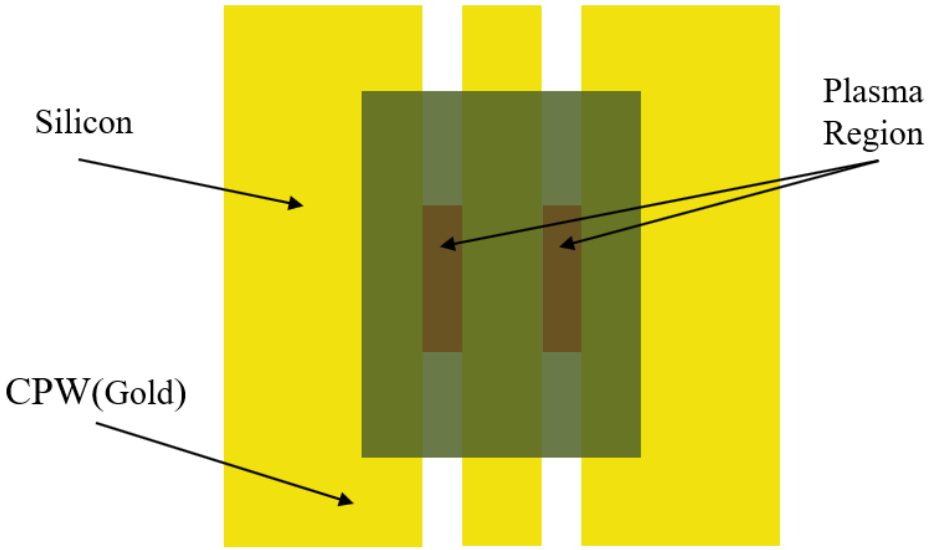

Figure 5.25 Schematic top view of PCB GCPW switch with slot illumination

The linewidth and spacing were chosen to be $1.1mm$ and $0.62mm$ respectively on account of its good impedance matching as discussed earlier. Optical illumination was provided by the fibre-coupled laser, as introduced before. Vacated slot pair has dimensions of $1.0mm \times 0.5mm$. Due to the limitations of the thermal control in hardware, $0.5mm \times 0.5mm$ is the minimum resolution of the laser-cutting machine that was introduced in Chapter 3. This means that the alignment of laser cutting only allowed $0.12mm$ for tolerance. Two rows of holes of diameter $0.3mm$ were drilled through the RO4003C and electrically conductive silver epoxy was then flown through the holes to form the vertical-interconnect vias.

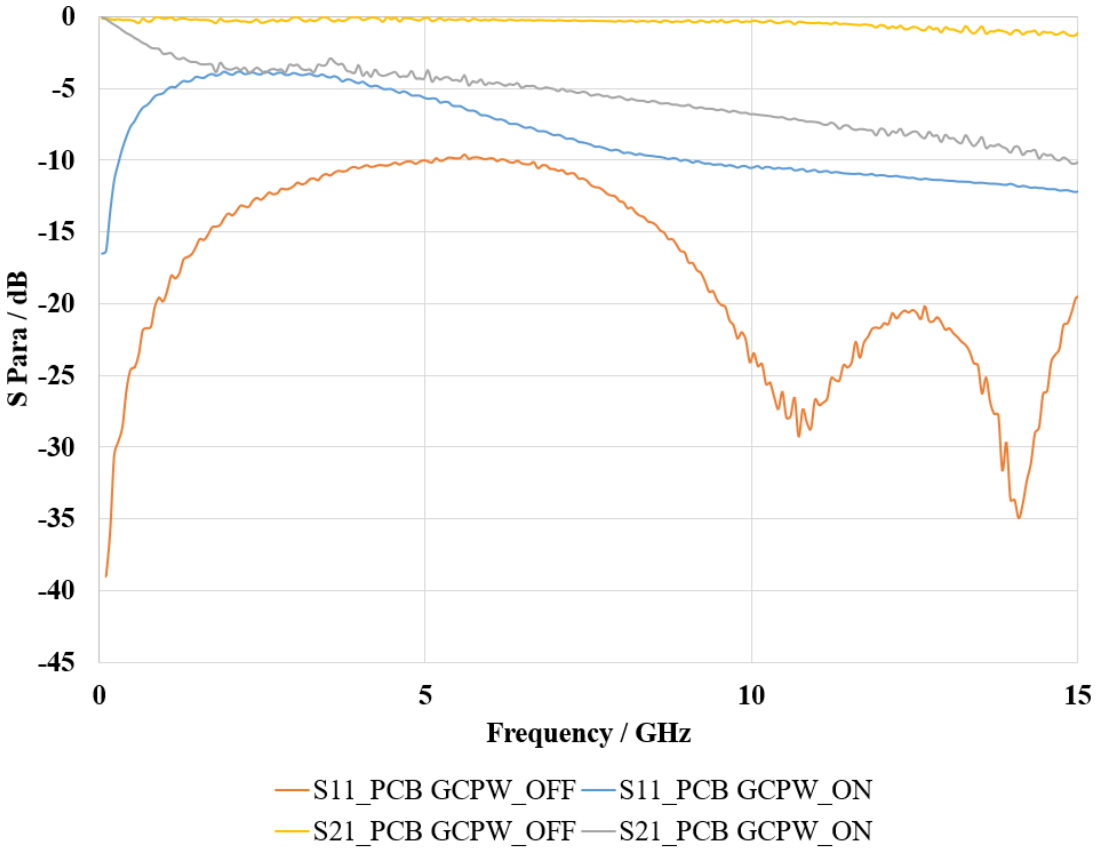

Figure 5.26 S_{11} and S_{21} results comparison of PCB GCPW switch with slot illumination ON/OFF

Figure 5.26 shows the S_{11} and S_{21} results comparison of this test circuit in illumination ON and OFF conditions. The insertion loss obtained in illumination OFF condition maintains a similarly good performance compared with the result in Figure 5.23. From this comparison, a smoother curve and less ringings can be observed here and it is believed to be associated with the introduction of the vias, which has effectively suppressed higher order modes. However, the isolation value obtained in illumination-ON condition is not ideal. It is suspected that less excess carriers can be generated when substrate material hindered the transmission of optical illumination. On the other hand, Figure 5.26 also suggests that signal reflection increases when illumination is provided on the superstrate as a general rise in S11 values can be observed from switch OFF to switch ON conditions.

5.4.2 PCB GCPW Switch Improvement

As discussed in the last section, the slot illumination provided by the fibre-coupled laser failed to excite a large number of electron-hole pairs which can meet the isolation requirement, namely over $10dB$, for a good RF switch. Therefore, improvement has been carried out towards increasing the optical illumination regions which subsequently create more short circuits to ground and thus enhance the isolation. LED/IRED optical sources have been employed to provide a larger illumination coverage and a better integration with PCB circuits as described earlier. Figure 5.27 shows the schematic top view of a proposed GCPW PCB switch.

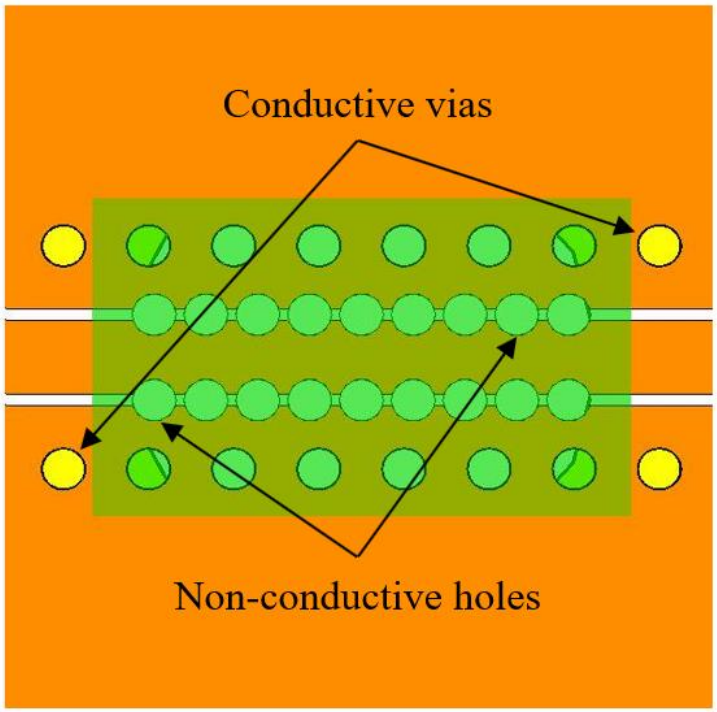

Figure 5.27 Schematic top view of a PCB GCPW switch with dotted holes

As this PCB GCPW switch is designed to work in the millimetre wave frequencies, smaller geometric circuit size is expected to minimise the GCPW spacing between the central signal line and the ground planes for better isolation value in the switch-OFF condition. As introduced in the last section, the minimum size of the holes that can be created are of 0.3mm diameter by drilling. The central signal linewidth and the spacing to the ground planes were chosen to be

0.6 mm and 0.08mm respectively to give a characteristic impedance close to 50Ω for good impedance matching with connectors. A high-powered IRED [5.33] at 940nm wavelength was selected due to its compact and highly-focus characteristics. This IRED has a lens of $3.3mm$ diameter and was inserted into a hole drilled underneath a brass block that was used to provide bottom ground planes for the GCPW and heat sinking for the PCB. The drilled hole of the brass block had the same diameter as the LED lens in order to maintain a relatively high optical intensity without losing much optical power. The non-conductive through-holes created more light paths as indicated in Figure 5.27. Compared to the above GCPW switch design, this approach effectively increased the spacing length for higher attenuation in the illumination ON (switch-OFF) condition, while causing a small insertion loss in the illumination OFF (switch-ON) condition. The conductive vias holes at outer rows are designed to suppress spurious modes.

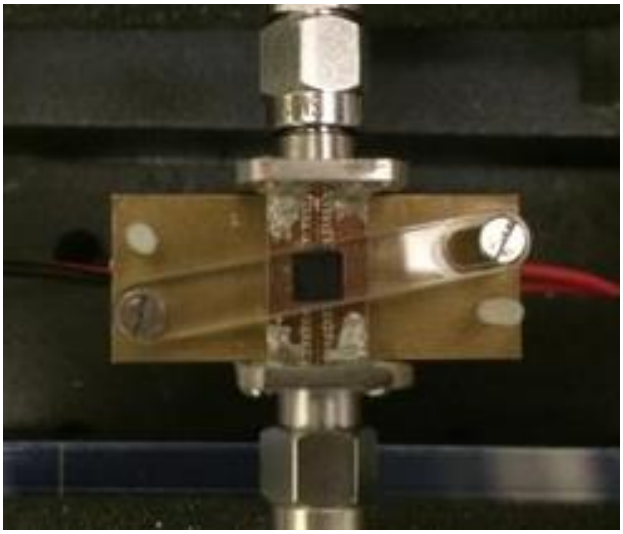

Figure 5.28 Photographic top view of PCB GCPW switch with linewidth w=0.6mm, spacing s=0.08mm, superstrate of 5mm x 5mm x 0.5mm fixed by brass block and Perspex bar

Figure 5.28 shows the photographic top view of this PCB GCPW switch which was mounted onto a brass block and then soldered with two K connectors [5.34]. This K connector can work up to $35GHz$ and it was selected due to its compromise between cost and performance. A Perspex bar holder was screwed onto the brass block to hold the silicon superstrate. S-parameters were measured by a network analyser (Agilent E8364A [5.35]). The side length of the square silicon superstrate was set to 5mm, which was sufficiently large to cover the holes

and diffusion area. The selected high-power IRED [5.33] provided a maximum $1.2W$ radiant power at wavelength of $940nm$ at a DC power consumption of $2.5W$. An initial test was conducted that the 86% of the IRED nominal radiant flux was transmitted through the brass block hole. The maximum intensity obtained with the IRED in measurement was $14W/cm^2$.

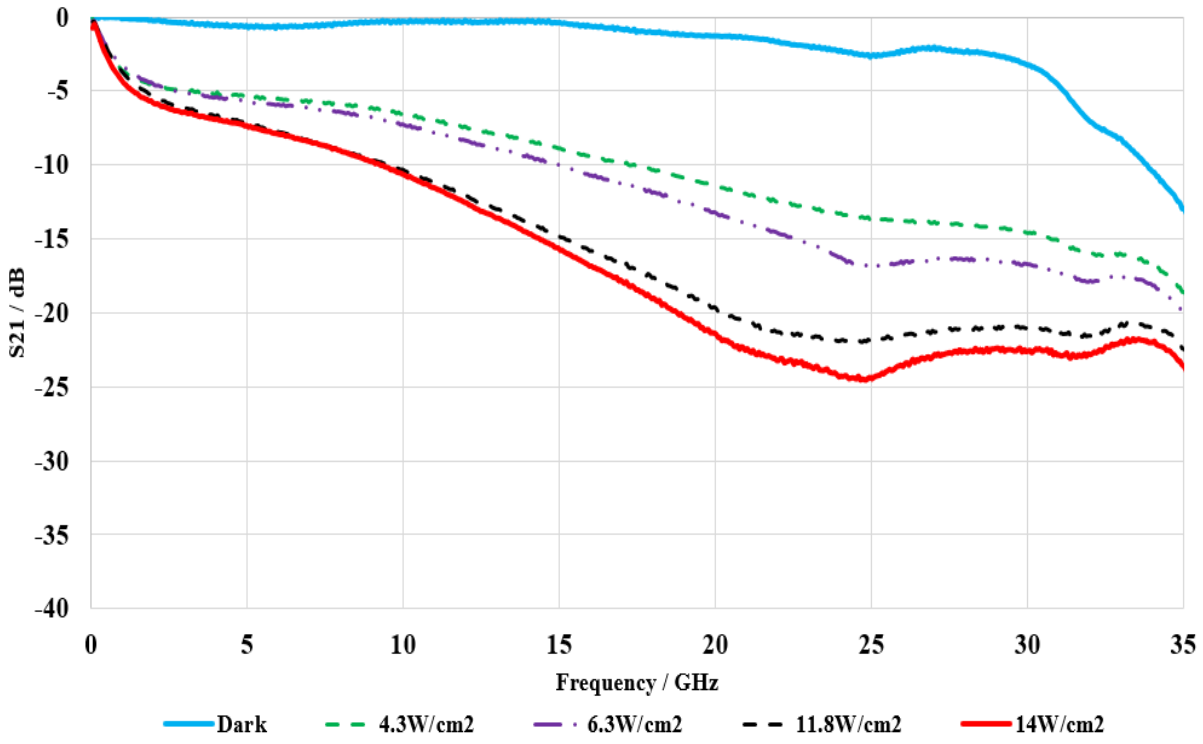

Figure 5.29 Measured S_{21} result of PCB GCPW switch with various optical intensities by a 1.2W IRED [5.33] at 940nm

Figure 5.29 shows S_{21} results of this PCB GCPW switch with various optical intensities. In dark state, good transmission can be observed and the insertion loss is less than $4dB$ through the frequency region of DC to $30GHz$. However, a rapid increase in insertion loss can be seen when frequency is higher than $30GHz$. This means the RO4003C substrate may not be able to constrain the electromagnetic signal within the GCPW and radiative loss is largely increased. The good effect of higher-order mode suppression by vias has been proved again when compared with GCPW with fused silica substrate. In terms of isolation, a general increasing trend can be found with frequency rising up in all cases for different optical intensities. The maximum optical intensity gives $24.5dB$ isolation at close to $25GHz$. Isolation values higher

than $20dB$ can be obtained when frequency is increased over $18GHz$. This reached a similar attenuation level as the glass-substrate GCPW has achieved. Nevertheless, due to the low optical efficiency of an IRED, radiant power has been raised to be as high as $1.2W$ which is compared with the optical power of $175mW$ used in the glass-substrate GCPW.

A single IRED-controlled PCB GCPW millimetre wave switch with RO4003C PCB substrate was presented in this section. It is important to conduct a further comparison with the GCPW switch with fused silica substrate introduced in the first part of this chapter. PCB GCPW has shown its advantage of higher-order modes suppressions and thus produced a smooth S_{21} result. Although glass GCPW suffered from the spurious surface modes, the loss in transmission is under $4dB$ with frequency less than $50GHz$. As for isolation, both circuits have demonstrated considerably good attenuation. With regards to the optical illumination, both need DC supply to the optical sources, namely laser and LED/IRED. The latter can be more attractive as the integratable optical source, LED/IRED, can be easily mounted onto the brass block fixture, but very high power is required due to its dispersive nature and low optical efficiency. With respect to the fabrication, the PCB GCPW is possible to be made with rapid and low-cost laser-cutting by employing through-holes to illuminate a silicon superstrate that can be easily integrated with other microwave and millimetre-wave circuits. However, as discussed above, either the difficulty in control of thermal cutting or the incompatible minimum drilling size ($0.3mm$ diameter) and GCPW spacing (0.06- $0.08mm$) can be the limiting factor in PCB GCPW fabrication. The circuit patterning can be easily controlled through optical aperture and this photolithographically defined glass GCPW is more accurate which also provides the flexibility.

To further increase the optical efficiency for PCB GCPW, a follow-up study has been carried out by another colleague [5.2]. It has converted a straight GCPW transmission line into a stepped-impedance structure and effectively extends the CPW spacing area, thereby achieving higher attenuation. The problem is the band limiting due to the nature of the slow wave structure design.

5.5 Conclusion

The focus of this chapter was the design of devices at higher frequencies in a millimetre wave region. The chapter began with a review of the literature and a proposal of several aspects for improvement. An optically controlled PCB GCPW switch operating in the millimetre wave region was demonstrated in the first part of this chapter. A full wave electromagnetic analysis was used as a multi-layer model to simulate photoinduced plasmas and good agreement was achieved between the measured and simulated results. The insertion loss was less than 4dB and the isolation was greater than 15dB from 32GHz-50GHz. This approach required the use of 175mW of optical power at a wavelength of 980nm, but it removed the need for bandwidth limiting electrical bias networks.

A millimetre-wave PCB GCPW switch controlled by a single IRED was designed and presented in the second part of the chapter. Less than $4dB$ insertion loss has been obtained in the frequency region of DC-$30GHz$, while a big drop in transmission over $30GHz$ can be found due to the PCB material loss. From $18GHz$ onwards, good isolation values higher than $20dB$ can be expected. The drawback is such ratings require large optical power of $1.2W$ to reach the same attenuation level as the first-part approach does. Finally, comparison between these two approaches has been conducted and new structure layout has been proposed to further increase the optical efficiency.

5.6 References

[5.1] A. W. Pang, C. D. Gamlath, M. J. Cryan, "An Optically Controlled Coplanar Waveguide Millimeter-Wave Switch", IEEE Microwave and Wireless Components Letters, vol. 28, no.8, pp. 669-71, 2018

[5.2] Y. Zhang, A. W. Pang, M. J. Cryan, "Optically Controlled Millimeter-wave Attenuator with Stepped-Impedance Lines", to be submitted, Oct. 2018

[5.3] R. Berezdivin, R. Breinig, and R. Topp, "Next-Generation Wireless Communications Concepts and Technologies," IEEE Commun. Mag., vol. 40, no. 3, pp. 108-116, 2002

[5.4] S. Rangan, T. S. Rappaport TS, E. Erkip, "Millimeter-wave cellular wireless networks: Potentials and challenges", Proceedings of the IEEE, vol. 102, no. 3, pp. 366-385, 2014

[5.5] C. G. Christodoulou, *et al*., "Reconfigurable antennas for wireless and space applications," Proc. IEEE, vol. 100, no. 7, pp. 2250–2261, 2012

[5.6] N. Behdad and K. Sarabandi, "Varactor-tuned dual-band slot antenna," IEEE Trans. Antennas Propag., vol. 54, no. 2, pp. 401–408, 2006

[5.7] S.-J. Wu and T.-G. Ma, "A wideband slotted bow-tie antenna with reconfigurable CPW-to slotline transition for pattern diversity," IEEE Trans. Antennas Propag., vol. 56, no. 2, pp. 327–334, 2008

[5.8] J. G. Yang, and K. Yang, "Ka-band 5-bit MMIC phase shifter using InGaAs PIN switching diodes." IEEE Microw. Wireless Compon. Lett., vol. 21, no.3, pp.151-153, 2011

[5.9] T. Boles, *et. al*., "AlGaAs PIN diode multi-octave, mmW switches," In Microwaves, Communications, Antennas and Electronics Systems (COMCAS), IEEE International Conference, pp. 1-5, 2011

[5.10] T. Kaneko, *et. al*., "Microwave switch: LAMPS (light activated microwave photoconductive switch)', IEEE Electron. Lett., vol. 39, no. 12, pp. 917-919, 2013

[5.11] C. J. Panagamuwa, A. Chauraya, and J. C. Vardaxoglou, "Frequency and beam reconfigurable antenna using photoconducting switches," IEEE Trans. Antennas and Propag., vol. 54, no. 2, pp. 449-454, 2006

[5.12] J.R. Flemish, and R. L. Haupt, "Optimization of a photonically controlled microwave switch and attenuator," IEEE Trans. Microw. Theory Tech, vol. 58, no. 10, pp. 2582-2588, Oct. 2010

[5.13] K. B. Ali, *et. al*, "Photo-Induced Coplanar Waveguide RF Switch and Optical Crosstalk on High-Resistivity Silicon Trap-Rich Passivated Substrate," IEEE Trans. Electron Devices, vol. 60, no. 10, pp.3478-3484, 2013

[5.14] M. Kulygin, *et. al*, "Nanosecond Microwave Semiconductor Switches for 258… 266 GHz," Journal of Infrared, Millimeter, and Terahertz Waves, vol. 36, no. 9, pp. 845-855, 2015

[5.15] C. D. Gamlath, D. M. Benton, M. J. Cryan, "Microwave Properties of an Inhomogeneous Optically Illuminated Plasma in a Microstrip Gap," IEEE Trans. Microw. Theory Tech, vol. 63, no. 2, pp. 374-383, 2015

[5.16] A.W. Pang, S. Bensmida, C. D. Gamlath, M. J. Cryan, "Non-linear characteristics of an optically reconfigurable microwave switch", IET Microwaves, Antennas & Propagation, vol. 12, no. 7, pp. 1060-1063, 2018

[5.17] C. D. Gamlath, A. W. Pang, M. J. Cryan, "Investigation of an optically induced superstrate plasma for tuning microstrip antennas", IET Optoelectronics, vol. 11, no. 6, pp. 230-236, 2017

[5.18] N. Vahabisani, and M. Daneshmand, "Monolithic Millimeter-Wave MEMS Waveguide Switch", IEEE Trans. Microw. Theory Tech, vol. 63, no. 2, pp. 340-351, 2015

[5.19] A. H. Jeorrett, *et. al*, "Optoelectronic tweezers system for single cell manipulation and fluorescence imaging of live immune cells," Optics express, vol. 22, no. 2, pp. 1372-1380, 2014

[5.20] M. Riaziat, R. Majidi-Ahy, I. J. Feng, "Propagation modes and dispersion characteristics of coplanar waveguides", IEEE transactions on microwave theory and techniques, vol. 38, no. 3, pp. 245-51, 1990

[5.21] G. M, Rebeiz, and J. B. Muldavin, "RF MEMS switches and switch circuits," IEEE Microwave magazine, vol. 2, no. 4, pp. 59-71, 2011

[5.22] L. L. W. Chow *et al*., "Lifetime Extension of RF MEMS Direct Contact Switches in Hot Switching Operations by Ball Grid Array Dimple Design," *IEEE Electron Device Letters*, vol. 28, no. 6, pp. 479-481, 2007

[5.23] C. P. Wen, "Coplanar waveguide: A surface strip transmission line suitable for nonreciprocal gyromagnetic device applications", IEEE Transactions on Microwave Theory and Techniques, vol.17, no.12, pp. 1087-90, 1969

[5.24] Radiall Straight 50Ω Panel Mount SMA Connector, Solder Termination, [accessible: https://uk.rs-online.com/web/p/sma-connectors/2956129/]

[5.25] Southwest Microwave, End Launch Connector (65 GHz), 1.85 mm (V) Connectors, [accessible: http://mpd.southwestmicrowave.com/products/family.php?family=236]

[5.26] ROITHNER LaserTechnik GmbH, RLCO-980-2000-F, [accessible: http://www.roithner-laser.com/ld_fiber.html]

[5.27] Anritsu, Components and Accessories, Integrated V Female Sparkplug Connector V116F, [accessible: https://www.anritsu.com/en-us/components-accessories/products/v116f]

[5.28] Anritsu, Components and Accessories, Integrated V Female Sparkplug Connector V110, [accessible: https://www.anritsu.com/en-GB/components-accessories/products/v110-1-r]

[5.29] Loctite, Adhesive, Thread locking, Low Strength, Low Viscosity, Purple, Bottle, 10 ml [accessible: http://www.loctite.co.uk/homepage.htm]

[5.30] CircuitWorks, CW2400 Adhesive, Conductive, Epoxy - 2 Part, Silver, [accessible: https://uk.farnell.com/chemtronics/cw2400/epoxy-silver-conductive-syringe]

[5.31] M. A. Green, and M. J. Keevers, "Optical properties of intrinsic silicon at 300 K", Progress in Photovoltaics: Research and Applications, vol. 3, no. 3, pp. 189-192, 1995

[5.32] Rogers Corporation, RT/duroid® 4003C woven glass reinforced hydrocarbon/ceramics, [accessible: http://www.rogerscorp.com/acs/products/54/ro4003c-laminates.aspx]

[5.33] LUMILEDS, High power infrared emitters for high efficiency and beam control [accessible: https://www.mouser.co.uk/ProductDetail/Lumileds/L1I0-0940060000000]

[5.34] Radiall, 50 ohms / part series R127, Sub miniature screw-on connector, [accessible: https://uk.rs-online.com/web/p/sma-connectors/2956129/]

[5.35] Keysight, E8364A PNA Series Network Analyzer, 45 MHz to 50 GHz, [accessible: https://uk.rs-online.com/web/p/sma-connectors/2956129/]

CHAPTER 6

6. Microwave Switch Mixing and Modulation

6.1 Introduction

Based on an interest in developing and characterising the electrical response of the designed optically-controlled microwave switch to pulsed optical excitation, this chapter contains an investigation of this device in an environment with a pulsed optical signal in modulated microwave communication signals. Various optical sources were tested and compared with a list of pros and cons. The chapter is divided into two parts, the first of which will contain a description of the test on silicon. Numerous results, analyses and recommendations will be provided. Tests with GaAs will be the focus of the second part. Feasible and practical experiments and simulations were undertaken based on the properties of this material. Some proposals and recommendations for improvement will also be made at the end of the chapter.

6.2 Silicon-based Switching Test

Having successfully designed and characterised several optically controlled RF switches under a CW optical illumination, the next step was to determine how these devices would perform under pulsed optical excitations. Compared with the GCPW millimetre wave switch proposed in Chapter 5, the superstrate microstrip gapline switch designed in Chapter 4 was taken as a sample circuit for the test due to its good overall properties and superior optical efficiency in terms of illumination region. Both lasers and LED/IREDs are used as optical sources in pulsed mode in order to study the switching characteristics.

The switch testing was designed based on a standard amplitude modulation (AM) of the optical signal. As is known, modulation in telecommunications changes some property of a periodic waveform called a carrier signal. This change is made by varying the amplitude, frequency and/or phase that contains information to be carried and sent. As discussed in Chapter 2, both conductivity and permittivity can be effectively varied in the illuminated plasma region Amplitude modulation was chosen because it is the most simple and straightforward solution for an initial test. A schematic diagram of amplitude modulation is shown in Figure 6.1. The information signal conveys a stream of messages at binary or digital bit levels. The carrier signal in this case is free of any change in frequency or difference in phase. A modulated signal is formed after mixing these two signals in that a carrier signal has been modulated and changed in amplitude according to the information coding. In the case of this study the mixer will be the superstrate switch proposed in Chapter 4. Pulsed optical excitation will control the ON and OFF switches and produce a stream of bits in the information signal. The carrier wave will be the periodic microwave signal that propagates through the coax cable and microstrip line.

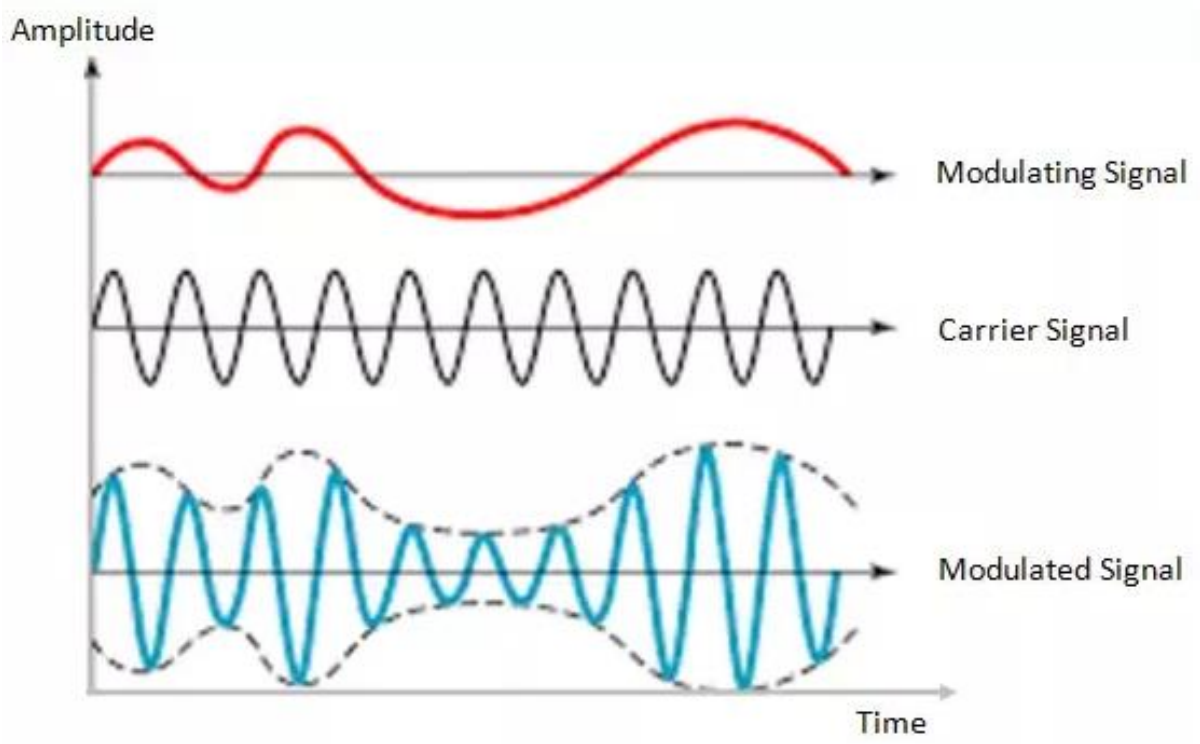

Figure 6.1 Schematic diagram of amplitude modulation (AM)

On the other hand, this test also aimed to obtain data about its switching speed. As explained in Chapter 2, this switching speed mainly depends on the lifetime of the excess carriers and how fast the optical source can be operated. A typical value of the lifetime for silicon is tens of microseconds. A package of pulsed laser diode and laser driver was used to determine the lifetime in the first experiment. This laser diode (905D1S3J09UA from [6.1]) is a portable hermetic device with very good temperature stability. The working wavelength is at $905nm$, which is within the recommended optimum wavelength region concluded in §2.2.3. To prevent from overheating, the maximum pulse duration and duty factor are set to $1\mu s$ and 0.1% respectively. The duty factor is the ratio of the pulse duration that the laser diode is active to a period that a signal completes an on-and-off cycle. Figure 6.2 depicts the pulse width and a full cycle of the signal operation.

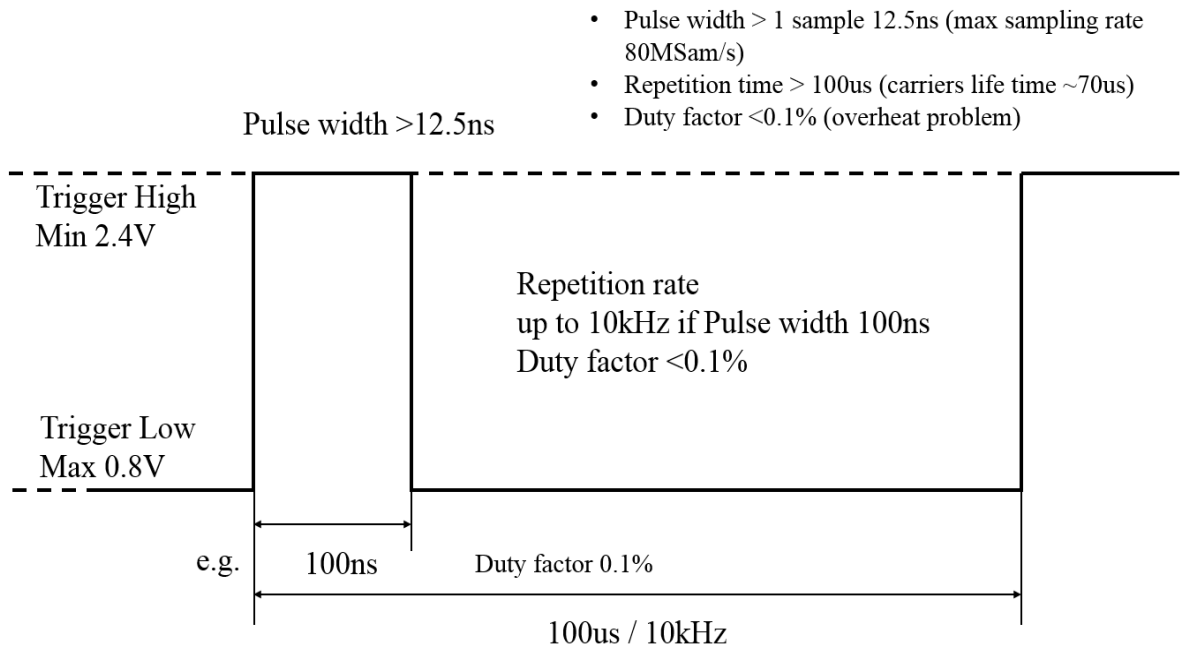

Figure 6.2 Signal level conditions required by laser and laser driver

The supporting laser driver is a compact chip (LDP-V 10-70) from PicoLAS [6.2] which shares the same ratings of maximum pulse duration and duty factor, while the minimum pulse duration is $10ns$. A photography of this device and the schematic diagram of the suggested pin connections are shown in Figure 6.3 and Figure 6.4 respectively. The names and descriptions of each connection with pinheader are illustrated in Table 6.1.

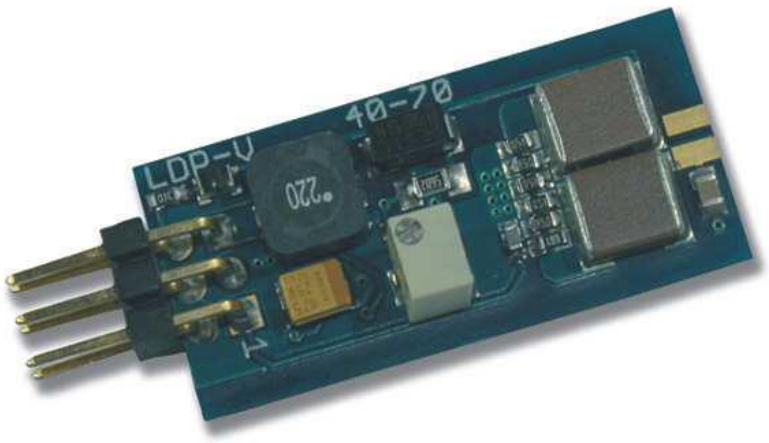

Figure 6.3 Photography of laser driver

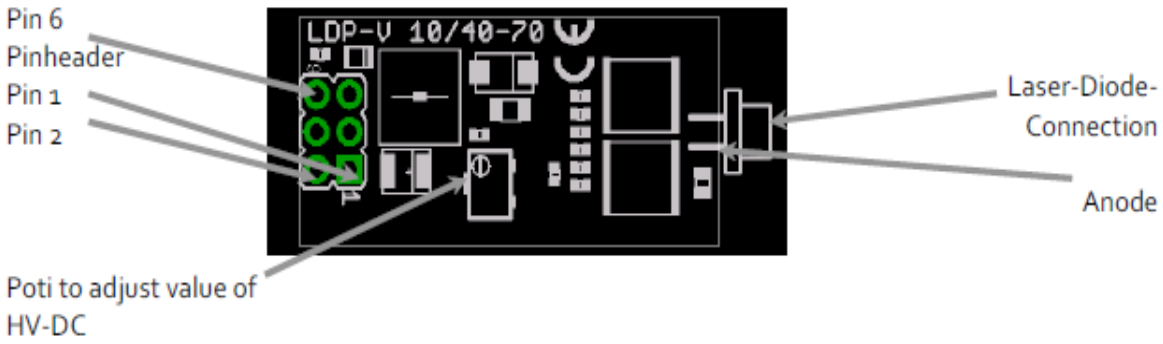

Figure 6.4 Schematic diagram of pin connection [6.2]

Pin	Name	Description
1	I_mon	Current monitor output into 50 Ohm. Scale: 2 A/V (LDP-V 10-70) / 20 A/V (LDP-V 40-70)
2	GND	Ground return
3	Trigger_In	Trigger Input into 50 Ohm
4	GND	Ground return
5	+15V	Supply Voltage, connect to a power supply.
6	U_HV_Ctrl	External HV setpoint input allows control over the internal HV-DC source.

Table 6.1 Pin number, Name and Description of each connection with pinheader [6.2]

This laser driver uses the current monitor as feedback from which the waveform can be observed through an oscilloscope. The current monitor output has a scale of $2A/V$ with a negative signal output. It has a source of 50Ω and must be terminated with 50Ω to achieve the correct scale. With regard to the trigger input, the minimum signal voltage level to be acknowledged is $2.4V$ when signal low moves to high, whereas the maximum is $0.8V$ when signal high moves to low. The specific trigger input signal requirement is summarised in Figure 6.2 for clarification.

Since a very fast switching device needs to be utilised to provide the required signal, a R&S®SMU200A Vector Signal Generator [6.3] was used based on its high sampling rate of up to $80MSa/s$. However, since the maximum duty factor used to protect the chip and laser from overheating is as low as 0.1%, it cannot be achieved under normal operation and settings. Fortunately, this signal generator was supported by remote control and the Matlab [6.4] code

created for connection was open-sourced. The drawback was having to sacrifice the output amplitude. Based on remote control, this signal generator can only be used as a baseband generator which produces a maximum $1V$ voltage output; hence, it becomes a programmable source. The only bridge to build between the signal generator and the laser driver at this stage may be an amplifier that can increase the $1V$ baseband voltage beyond $2.4V$ but does not increase the signal low voltage to over $0.8V$. A non-inverting current feedback amplifier (TH3201 from Texas Instruments [6.5]) on a printed circuit base board (DEM-OPA68xU from Burr-Brown [6.6]) was selected and is shown in Figure 6.5.

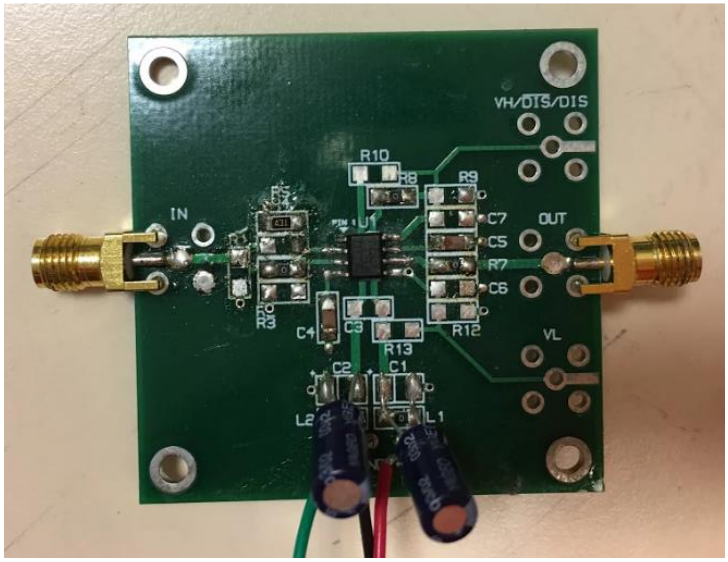

Figure 6.5 Non-inverting current feedback amplifier (TH3201 from Texas Instruments [6.5]) on a printed circuit base board (DEM-OPA68xU from Burr-Brown [6.6])

According to the user manual for the amplifier [6.5], feedback resistor R_f and ground resistor R_g were chosen to be 576Ω and 144Ω respectively, which gave a gain of 5 calculated from the following standard non-inverting feedback gain equation;

$$\frac{V_{out}}{V_{in}} = \frac{R_f}{R_g} + 1 \qquad 6.1$$

The block diagram and a photo of the system design are shown in Figure 6.6 and Figure 6.7 respectively.

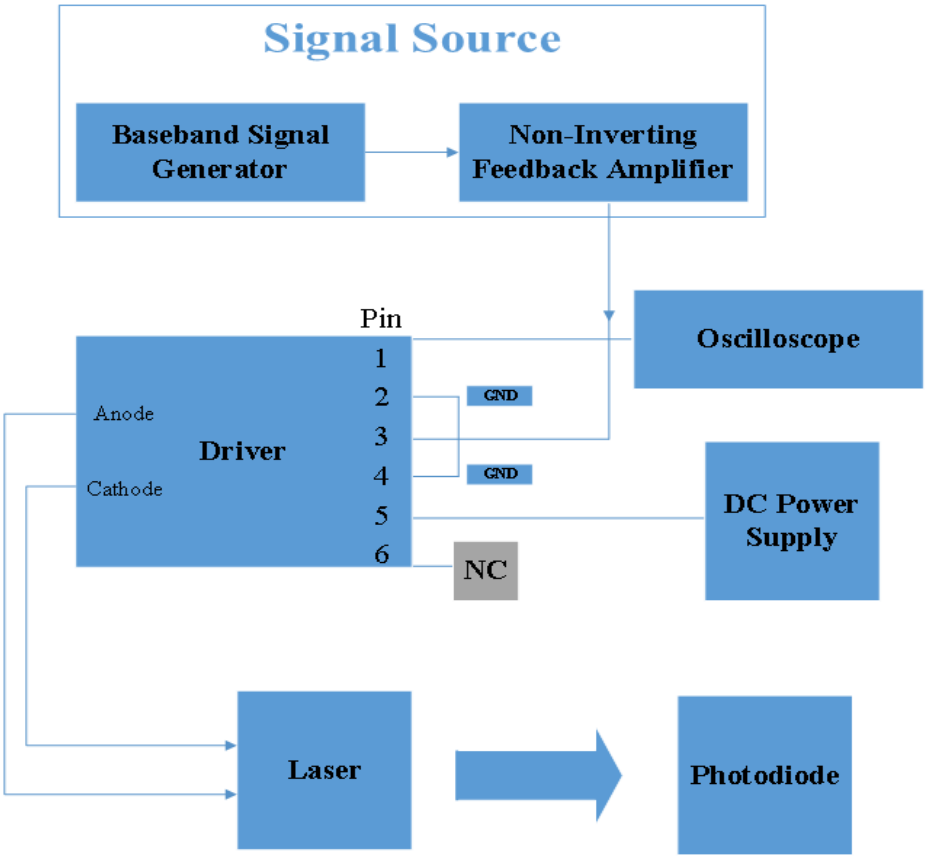

Figure 6.6 Block diagram of signal generation system

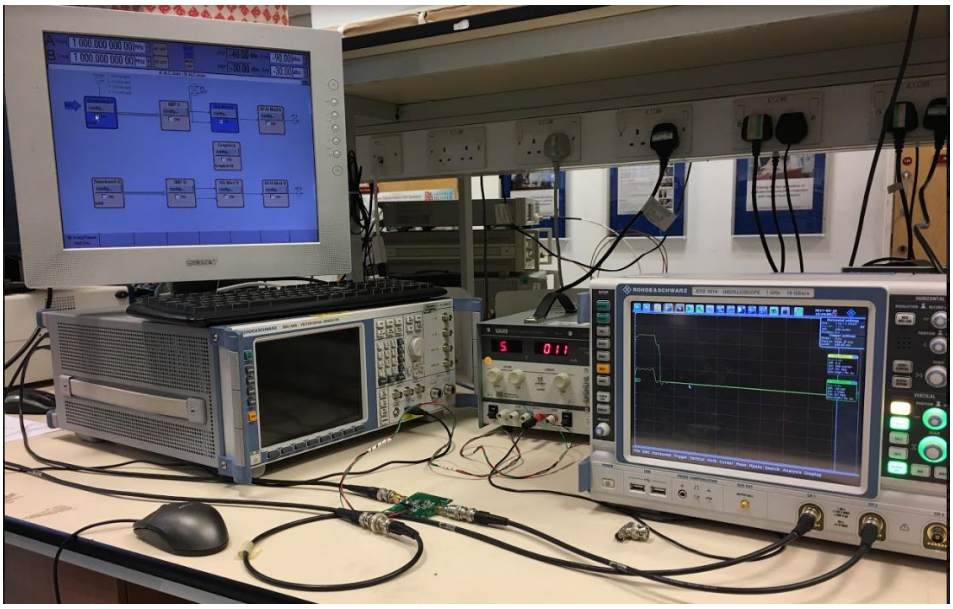

Figure 6.7 Photography of signal generation system

The next test was to use a photodiode detector and oscilloscope to capture this pulsed response as the optical meter used in Chapter 4 was unable to. The photodiode detector used was an InGaAs amplified detector from Thorlabs (PDA10CF [6.7]), which can capture light at wavelengths from 800 to 1700nm and a bandwidth at 150MHz, which is equivalent to about 6.67ns. It converts light into an electrical current which can be then observed through an oscilloscope. This conversion can be implemented using responsivity, which is expressed in units of amperes per watt of incident radiant power. This responsivity can be found in the technical data sheet from [6.7]. The radiant power can then be calculated by using the voltage values captured by the oscilloscope [6.8] divided by the coupling impedance. The oscilloscope has a 1GHz bandwidth which can detect an electrical signal as short as 1ns. Three waveforms superimposed with the output from the signal generator, laser driver current monitor and photodiode detector are shown in Figure 6.8. As can be seen, the outputs of the photodiode detector and the current monitor are in phase, while they both have a trigger delay of 60ns from the output of the signal generator as indicated from laser driver's data sheet [6.2].

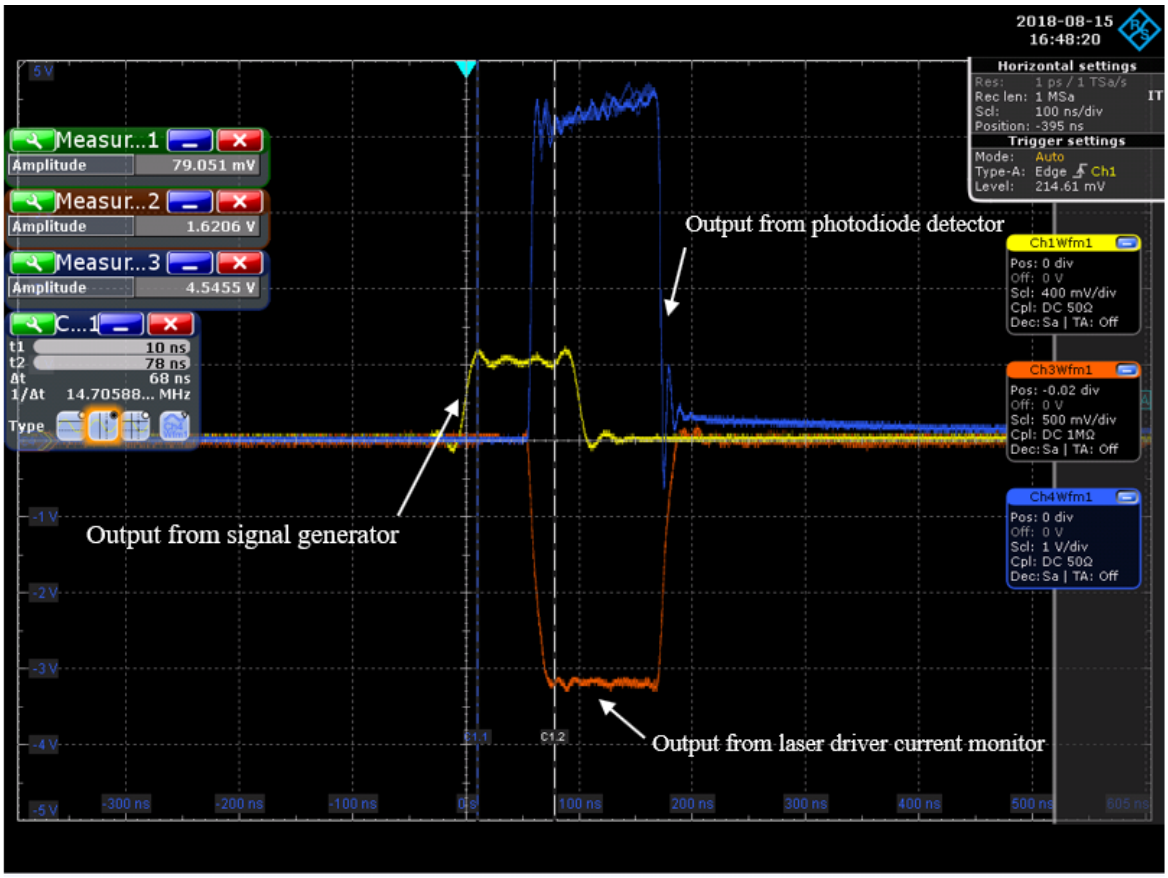

Figure 6.8 Oscilloscope view of three output signals superimposed

After adding a $2GHz$ carrier signal, the modulated waveform is shown in Figure 6.9. The cursor function has been used to measure the excess carrier lifetime and the value is about $80\mu s$. By zooming in on the timescale, the rise time can be found to be around $600ns$ and the fall time around $77\mu s$.

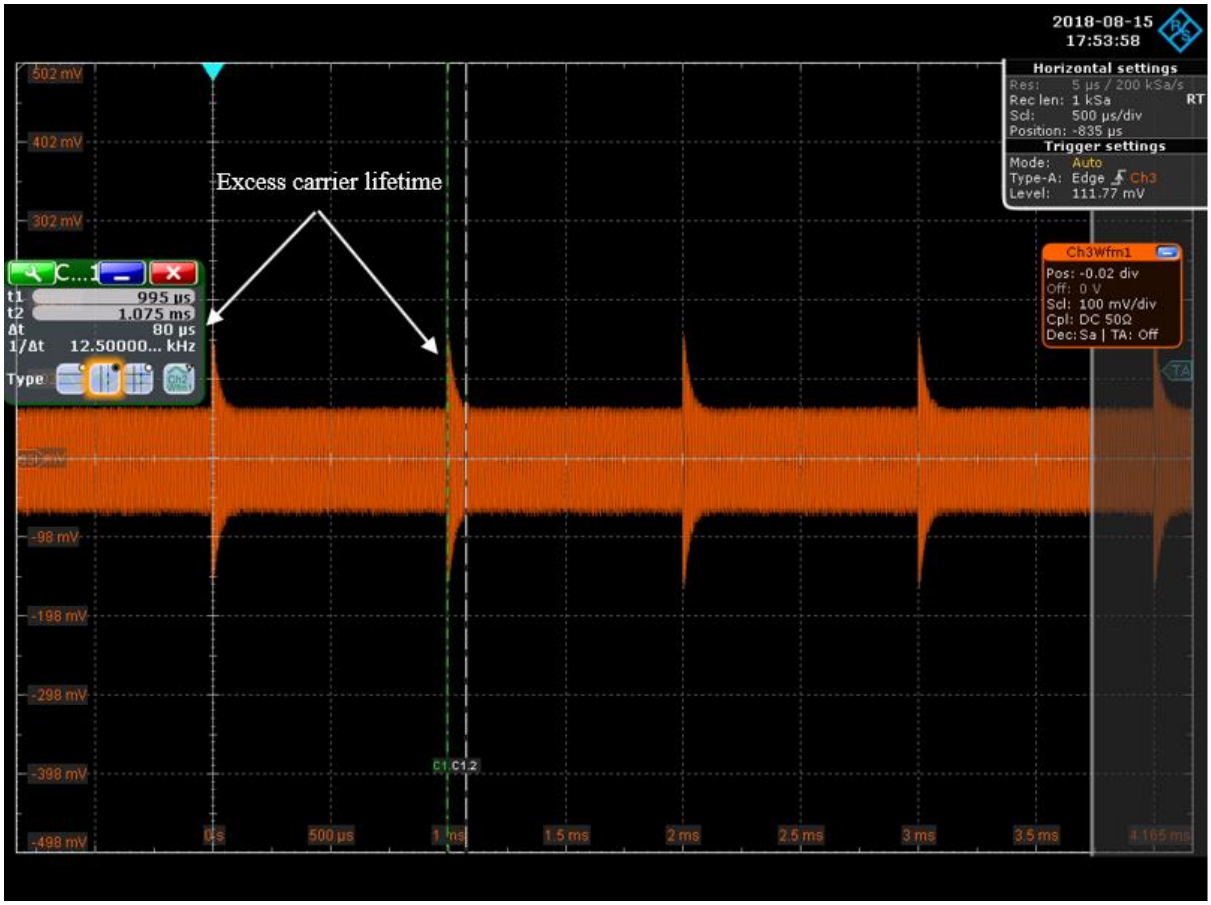

Figure 6.9 Excess carrier lifetime measured by the oscilloscope as 80µs

A high recombination rate is important for the fast switching of applications and steady state plasma needs to be extinguished in a very short time. This lifetime was found to be considerably long, which led to a switching frequency of only $1/80\mu s = 12.5kHz$. According to [6.9, 6.10], the lifetime can be shortened by reducing the passivation layer or introducing surface defects, such as radiation damage, but these approaches may impair the insertion loss, isolation or cost-efficiency of the switch. Essentially, a huge reduction in the order of magnitude in the lifetime cannot be expected. Therefore, GaAs superstrate will be proposed in the next section based on the advantages of its properties, as discussed earlier in §2.3.5.

6.3 GaAs-based Switching Test

The lifetime in the photoconductive region can be reduced to a nanosecond or even a picosecond scale by switching the superstrate material to GaAs [6.11]. As discussed in §2.3.5, this direct-band semiconductor GaAs has a higher band gap than silicon and is expected to have a good isolation value in low frequencies, but, in turn, it requires higher photon energy and thus, a lower wavelength optical source for photo-excitation. As mentioned in Chapter 1, a picosecond optoelectronic switching based on silicon was first demonstrated in 1975 at Bell Laboratories in Austin, Texas [6.12]. This switching was implemented by providing $530nm$ and $1060nm$ picosecond excitation to achieve switch ON and OFF conditions respectively. A year later, Lee pointed out that the switching time was fast, but the repetition rate was rather slow due to the slow recombination in silicon. In addition, the power handling capability was limited when silicon was used as an insulator, which may have been because of the lower electric breakdown voltage. Hence, the first photoconductive GaAs high-speed switching has been proposed and tested [6.13]. However, both of these experiments required a great deal of power and bulky lasers, which is not practical in modern communication systems. The use of GaAs has been increasingly developed since 1975 and many THz switches have been designed, but most of these were used for antennas [6.14]. The GaAs was low temperature-grown GaAs (LT-GaAs), which created surface defects and aimed to reduce the lifetime for faster operation. Another reason for using LT-GaAs was to lower the power demand to achieve a considerable insertion loss, but this also significantly reduced the isolation value. Semi-Insulating GaAs (SI-GaAs) was employed for the subsequent tests, which meant sacrificing some extents of the lifetime in exchange for better isolation.

The S_{21} of a microstrip gapline switch with GaAs superstrate at dark state is shown in Figure 6.10. This measured switch had the same dimensions as the proposed switch in Chapter 4. The microstrip gapline was of $0.4mm$ gap and $1mm$ linewidth. The superstrate dimension was $5mm \times 2mm \times 0.5mm$. The obtained S_{21} curve profile was quite similar to that of silicon superstrate switches at dark state, as discussed in Chapter 4. A minimum $10dB$ isolation value could be guaranteed in this frequency region.

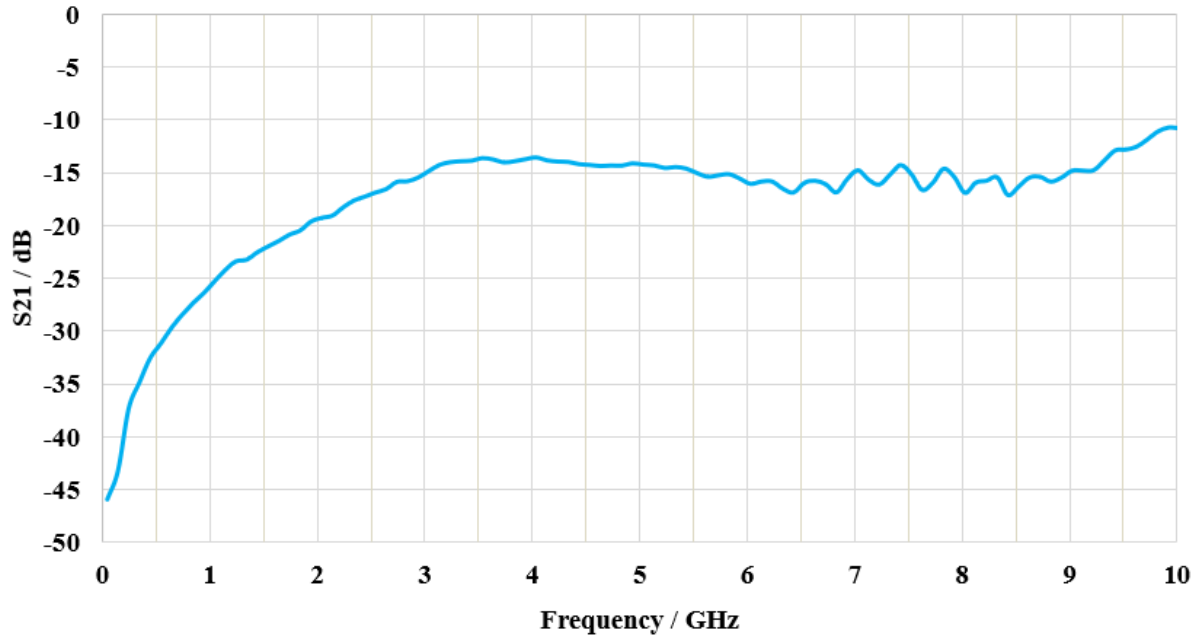

Figure 6.10 VNA measured S_{21} result of a microstrip gapline switch with GaAs superstrate at dark state

To start the pulsed optical excitation, the GaAs was repeatedly tested using the measurement setup shown in Figure 6.7 for silicon switching with the pulsed high-power laser. However, there was no observable change when $3W$ optical illumination was provided. It was suspected that the wavelength of $905nm$ illuminated from this laser had already been in the cut-off region, since it could not provide sufficient photon energy for GaAs with a $1.42eV$ energy gap. The next proposed optical sources were LEDs and IREDs on account of their compact use and for integration purposes. After a comprehensive screening of various low-cost commercial LEDs and IREDs, a powerful IRED TSHG8200 from manufacturer VISHAY Semiconductor [5.15] was chosen, mainly due to its working wavelength of $830nm$ which is below the cut-off wavelength ($\sim 875nm$). It also has a high modulation bandwidth of $18MHz$. This is suitable for high pulse current operation and spectral matching with CMOS cameras [5.15]. The angle of half intensity is $\pm 10°$ and the maximum radiant power can reach nearly $1W$. A TSHG8200 was carefully removed from an anti-electrostatic discharge package for a characterisation test, which was conducted with the optical meter used in §3.3 with a DC power supply. The results shown in Figure 6.11 and Figure 6.12 of forward current vs. forward voltage and radiant power vs. forward current respectively have been found to be fairly close to the technical data shown earlier in Figure 3.7 in §3.3.2.

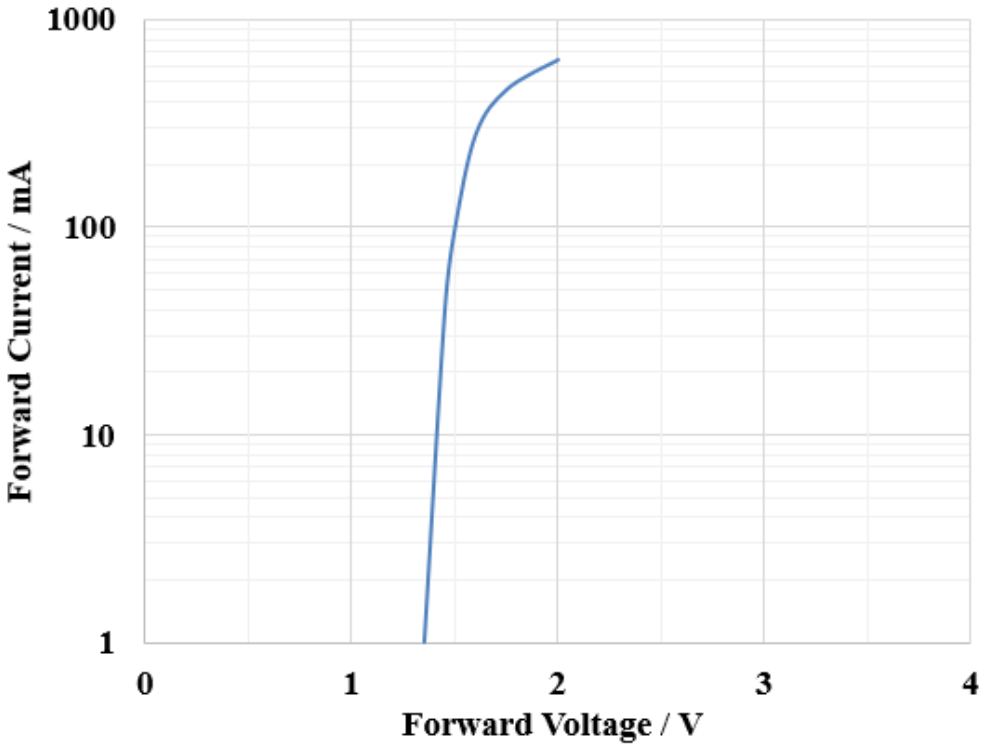

Figure 6.11 Forward current vs. Forward voltage

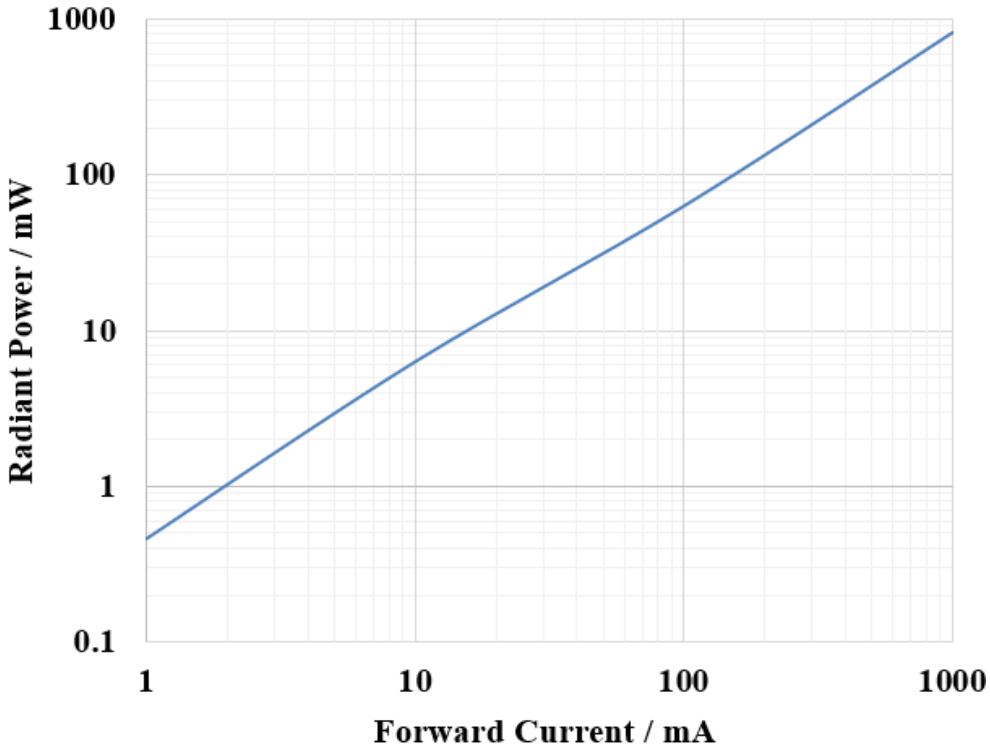

Figure 6.12 Radiant power vs. Forward current

With regard to the pulsed operation on this IRED, the first signal source used was a standard signal generator [6.16] with a maximum bandwidth up to 15MHz. A brass block was drilled with a $6mm$ diameter hole to better mount and fix this IRED at the bottom to deliver the optical illumination. This IRED connected by DC wires and a brass block with a $6mm$ diameter hole for mounting is shown in Figure 6.13.

Figure 6.13 IRED connected by DC wires and brass block with a 6mm diameter hole for mounting

The signal generator was set to generate a standard square wave with 50% duty cycle for easy observation through an oscilloscope. The signal level from the signal generator was set to provide an $8V$ peak-peak voltage (V_{pp}) on a $4V$ DC offset level. These numbers were chosen because considerable optical power can be produced for use when $8V$ V_{pp} is close to the maximum supported voltage rating of the signal generator, $10V$ V_{pp}. The derivation of the optical power value can be calculated as follows. As can be seen from Figure 6.11, a linear relationship between the forward current and forward voltage was demonstrated before the forward voltage reached $1.5V$. Then, the curved I-V plot emerged after this forward voltage level, which is assumed to have been associated with the thermal nonlinearity of the IRED resistor. As a compromise and average between the linear and nonlinear region, this IRED internal resistance value can be calculated as 15Ω by reading the forward current value, 0.1A, at $1.5V$ in Figure 6.11. By knowing the system-coupled internal resistor as 50Ω, the forward current value can be determined as 0.125A from an $8V$ voltage excitation divided by $(50 + 15)\Omega$. Hence, nominal radiant power can be read off as $35mW$ from Figure 6.12.

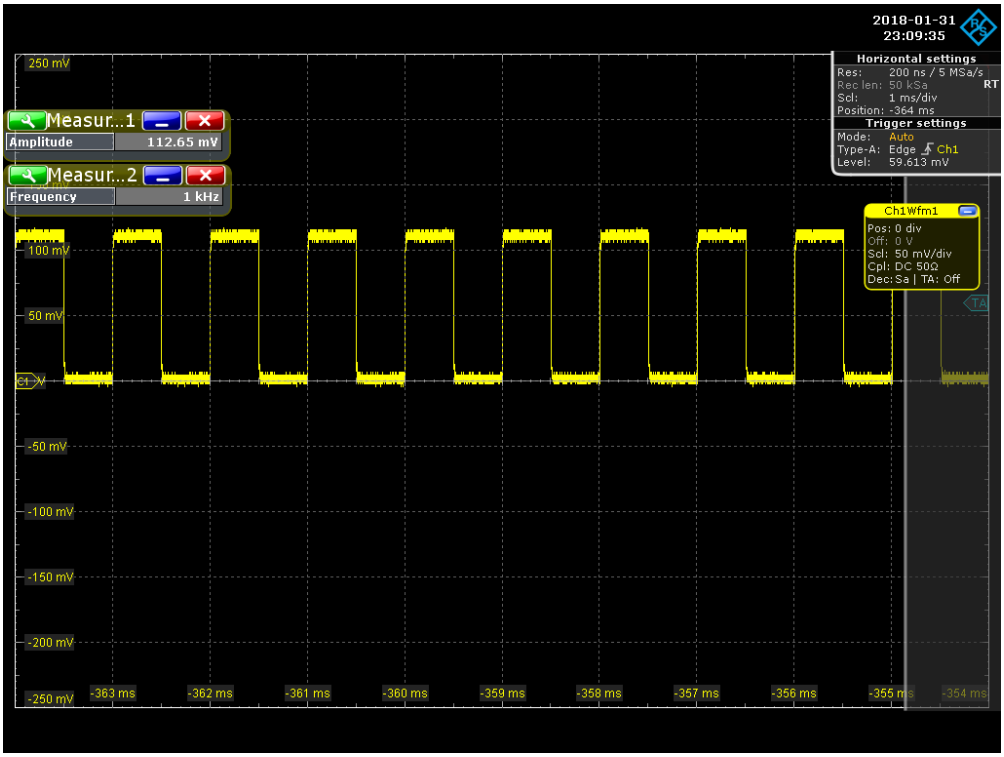

Figure 6.14 Photodiode waveform observed through oscilloscope at 1kHz

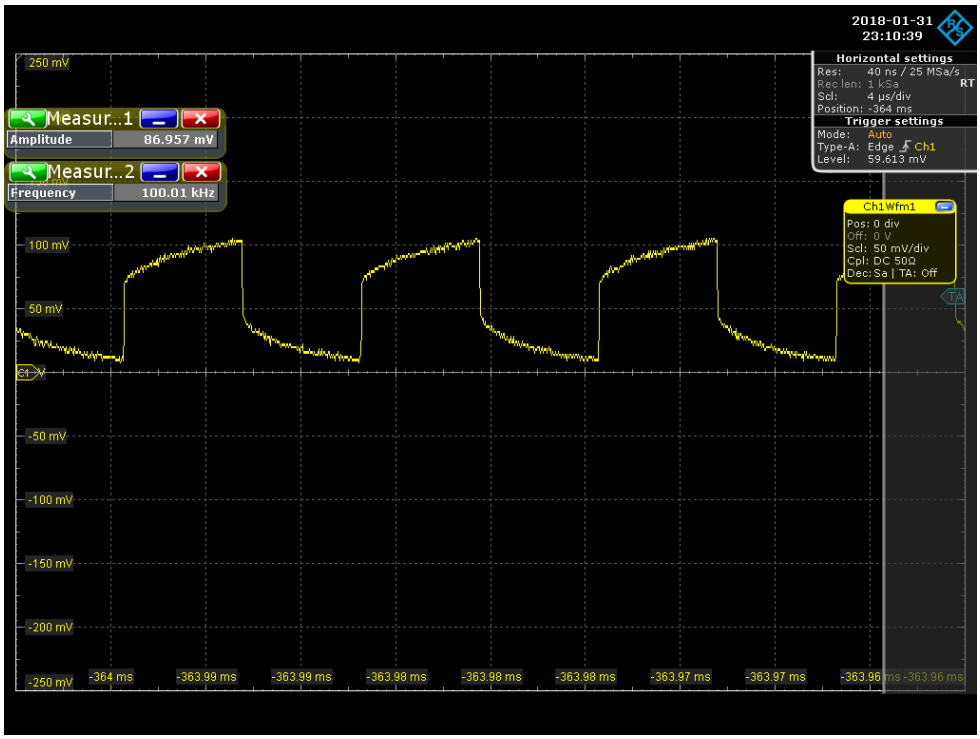

Figure 6.15 Photodiode waveform observed through oscilloscope at 100kHz

Figure 6.14 and Figure 6.15 show the measured waveform from the photodiode detector output. This waveform was repeated at $1kHz$ and had a $112.65mV$ amplitude at signal high. As discussed in the last section, the optical power could be calculated by knowing the responsivity from the user manual [6.7], and it was $11.27mW$. The discrepancy between this value and the nominal power calculated above, $35mW$, could have been caused by several possible factors, but the primary factor is optical loss. As shown in Figure 6.13, there were two drilled holes with different diameters and depths. The outer circle was drilled for IRED mounting, as explained above. The inner through hole at the bottom was used to provide a light path to illuminate the superstrate. The transition area between these two holes was designed with an inclining and tapered angle, which was used to confine the light from the outer circle. Since this IRED had relatively dispersive radiation angles compared with the optical fibre used previously, the confinement failed to focus a considerable portion of light into the inner hole. Therefore, a wider through hole had been proposed, but the simulation does not suggest it since the existence of a bigger hole beneath the substrate would cause great discontinuity and thus, more insertion loss. The second factor could be the impedance mismatch between the 50Ω coax cable and the IRED. As shown in Figure 6.13, the IRED did not produce an impedance-matched PCB circuit, and its anode and cathode were directly connected with the wires inside by a coax cable connected to the signal generator on the other side. This inevitably deteriorates the power transfer. When frequency was raised higher at $100kHz$ as shown in Figure 6.15, the optical power dropped to $8.70mW$ and the phenomenon of an impedance mismatch became more obvious. The significant increase in the rise time and fall time represented by the curves highlighted the inductive and capacitive characteristics. As for other factors that could have caused the discrepancy, system errors and device defects could be considered, but these would not make such a huge difference. Impedance matching techniques could be employed with an L-C circuit to improve the performance of this IRED in pulsed operation, but it may only work with narrowband use due to the limited electrical length from the distributed components, as discussed in Chapter 3.

The microstrip switch with GaAs superstrate was tested based on the current measurement established for this IRED before proceeding further with impedance matching and electronics design. However, no observable difference in S_{21} was found between the switch ON and OFF conditions with IRED used in both DC and pulsed operations.

6.4 GaAs Bias Test

Since the above-discussed GaAs switching test failed to produce satisfactory results, the SI-GaAs (intrinsic GaAs) will be investigated in this section. To begin with, it was assumed that the optical intensity was insufficiently high for an intrinsic GaAs to create sufficient excess electron-hole carriers and this was why negligible conductivity variation could be observed through S_{21}. Therefore, the first amendment involved changing the optical source back to the CW laser, as introduced in §3.3.1. Meanwhile, a current meter can be used to monitor the small photocurrent for a very low electrical conductivity change. This photocurrent refers to the current through the photoexcited region created by optical illumination incident on GaAs. Last, but not least, a dual-port DC supply was prepared to provide a DC bias voltage up to $30V$ across the DUT. This DC bias voltage can theoretically provide an electrical field that exerts a pulling force on electrons and holes and this can effectively hinder their recombination mechanics. A schematic diagram is shown in Figure 6.16.

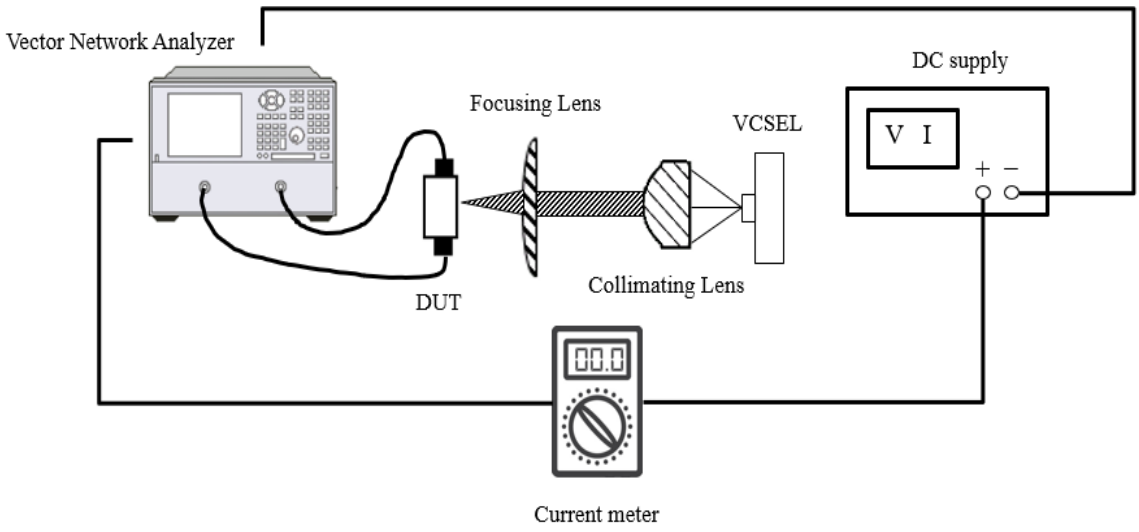

Figure 6.16 Schematic diagram of DC bias test

As a result, the lifetime can be significantly increased if a sufficiently large voltage is used. A photo of the set-up of this proposed GaAs bias test is shown in Figure 6.17. A maximum of $1.5W$ optical illumination at $830nm$ was provided by the VCSEL laser, collimated and focused by lenses and delivered to the DUT. The superstrate microstrip switch was fixed on a microstage and connected to the VNA. This microstage was used for a full dimensional alignment between the illumination spot and the superstrate by fine-tuning with the knobs. A DC power supply was connected in the series with the VNA and the current meter which had a minimum scale of μA.

In addition to the intrinsic GaAs mentioned above, Epilayer GaAs were added for comparison and the properties of these three kinds of samples are shown in Table 6.2. The first one was a double-side-polished (DSP) intrinsic GaAs which was used in the above IRED test. The second had $AlAs$ sandwiched between the GaAs to increase the conductivity at dark state. The third sample was an unpolished GaAs. A bias test was conducted on these three superstrate samples. Yet another microstrip gapline was also added for comparison. This one had a smaller gap of $0.1mm$, in contrast with the above proposed $0.4mm$ gap, for which the DC resistance was expected to be reduced proportionally by a factor of approximately 4.

Sample Type	Thickness (um)	Carrier concentration (cm^{-3})	Resistivity (Ohm.cm)
DSP GaAs	350±25	6.67E6 to 7.69E6	1.43E8 to 1.62E8
Epilayer GaAs	550+3.925(Epi)	9.76E6 to 1.16E7	1.05E8 to 8.9E7
Unpolished GaAs	550±25	9.76E6 to 1.16E7	1.05E8 to 8.9E7

Table 6.2 Properties of Double-Sided-Polished GaAs, GaAs with Epilayer and Unpolished GaAs

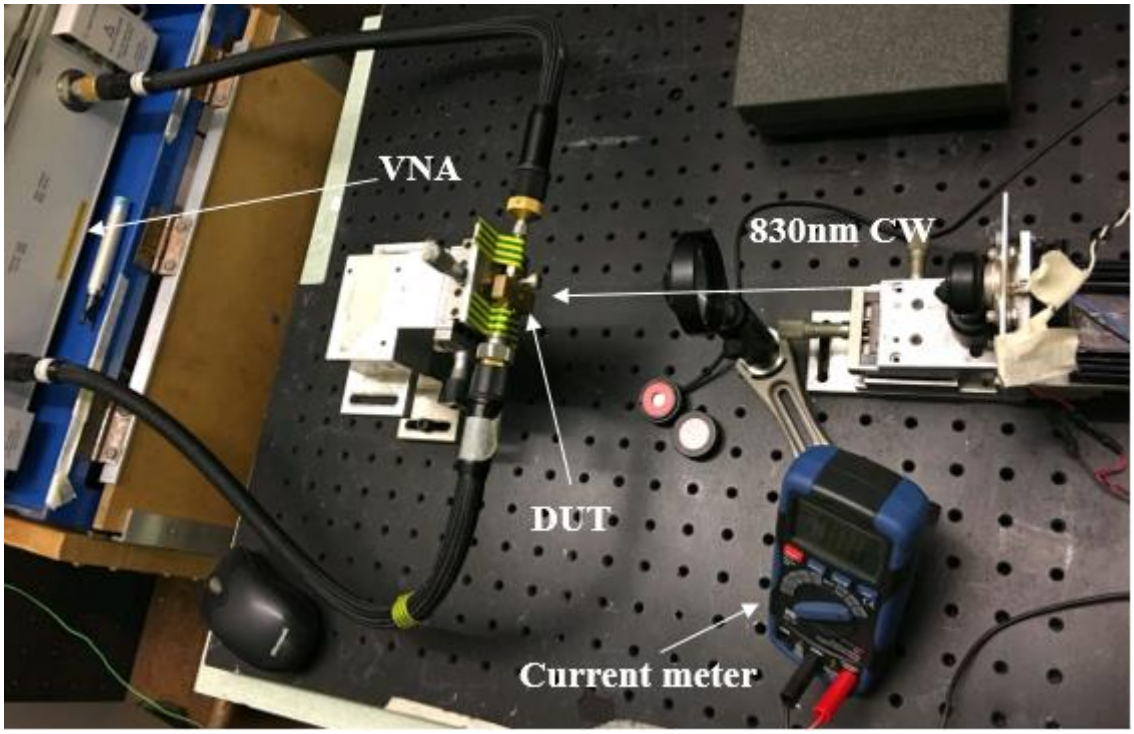

Figure 6.17 Photography of GaAs bias test set-up (with 830nm CW VCSEL, VNA, DUT and Current meter)

The result of the bias current against optical power of the three different superstrate samples on a microstrip gapline of 0.1mm gap and 1mm linewidth under a constant bias voltage ($15.13V$) can be seen in Figure 6.18. The bias current vs. bias voltage of these three superstrate switches under 1240mW optical illumination is shown in Figure 6.19. It can be seen that the unpolished GaAs demonstrated the best performance of highest bias current in both situations. It is believed that the surface defects reduced the optical reflection where light could be more easily trapped into the surface structure and thus, increased the absorption to excite more excess carriers.

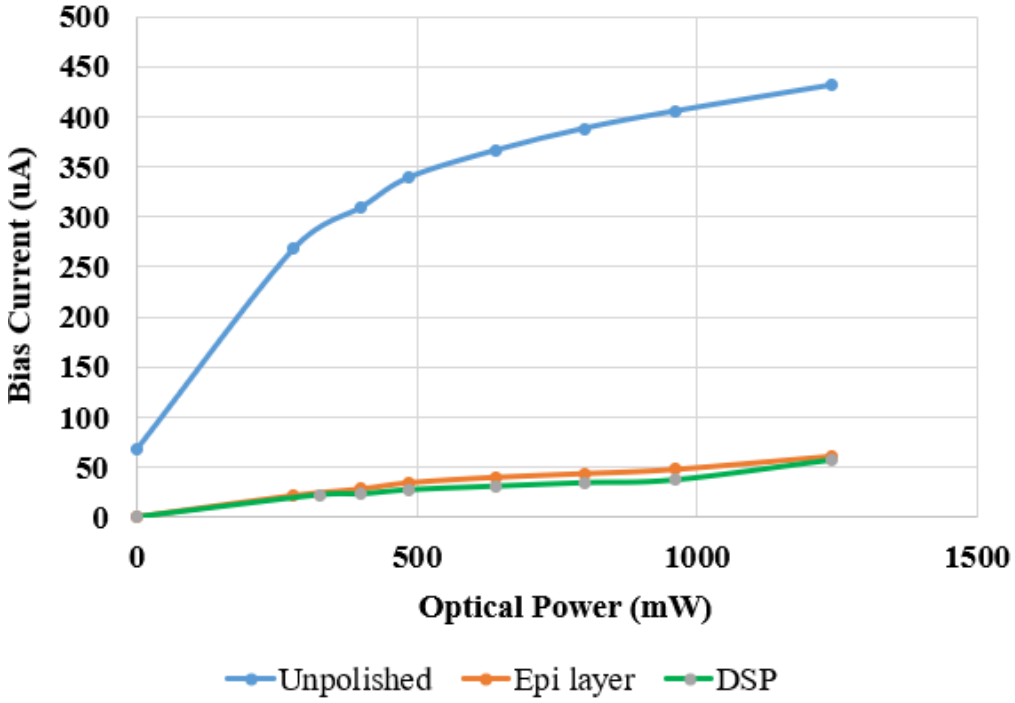

Figure 6.18 Bias current vs. optical power on DSP GaAs, GaAs with Epilayer and Unpolished GaAs on a microstrip gapline of 0.1mm gap and 1mm linewidth under 15.13V bias voltage

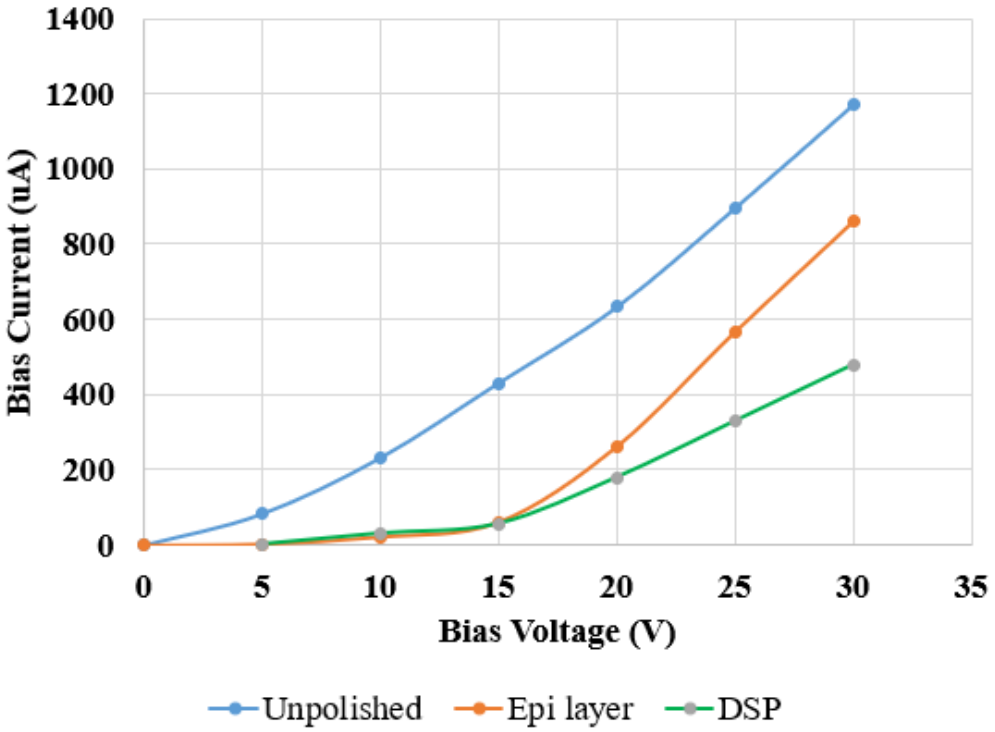

Figure 6.19 Bias current vs. Bias voltage on DSP GaAs, Epi-GaAs and Unpolished GaAs on a microstrip gapline of 0.1mm gap and 1mm linewidth under 1240mW optical illumination

The plasma region was considered as an equivalent photoresistor for a further analysis. This resistance was quantified by the ratio of the bias voltage to the bias current. Taking the highest bias current of $1171\mu A$ and the corresponding bias voltage of $30V$ in unpolished GaAs case, the photoresistor could be calculated as $25.6k\Omega$. By linking this assumption with the simplified distributed element modelling in §4.4.3, this photoresistor is depicted in Figure 6.18. By considering a microstrip gap of 0.4mm, plasma width 1mm, plasma thickness 10um, and substituting photoresistance into 4.3, the conductivity can be calculated as follows;

$$\rho = \frac{RA}{l} = \frac{25.6E3 \times 10E-6 \times 1E-3}{0.1E-3} = 0.256\ \Omega.m$$

$$\therefore \sigma = 3.90625\ S/m$$

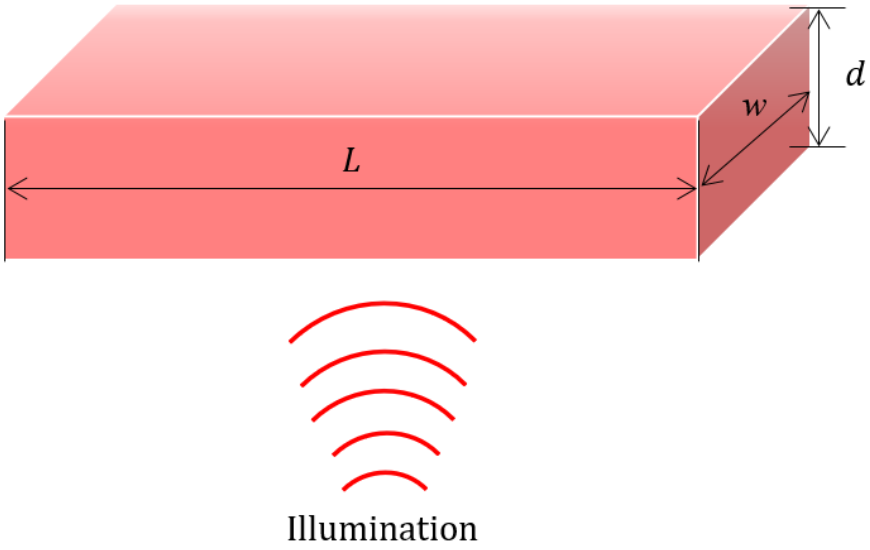

Figure 6.20 Equivalent photoresistor model (gap length L = 0.4mm, plasma width w = 1mm, plasma thickness d = 10um)

Compared to the derived plasma simulation model in Chapter 2, intensity can be calculated with 1240mW optical power incident on the circular illumination area, $(0.15)^2\pi cm^2$, in this experiment,

$$Intensity \sim = \frac{1240E-3}{0.125^2\pi} = 25.26W/cm^2$$

Other parameters for simulations were obtained such as the recombination time $1nm$, the quantum efficiency0.654, the surface recombination velocity $5.4 \times 10^5 cm/s$, the diffusion length $10\mu m$, the absorption coefficient at $830nm$, the electron mobility of intrinsic GaAs at room temperature $8500cm^2/(V.s)$, the hole mobility of the GaAs at room temperature $400cm^2/(V.s)$, and the intrinsic carrier concentration $2.1 \times 10^6 cm^3$. The conductivity against depth in substrate was plotted by substituting these numbers into the plasma modelling created in Chapter 2 and the result is shown in Figure 6.19. As can be seen, the two conductivities derived from different modelling and measurements showed considerably good agreement in the same order of magnitude. As for the $0.4mm$ gapline case, the resistance derived by the bias voltage and bias current was $108.6k\Omega$ which was expected to be about four times the other one. The conductivity calculated from the bias test with the photoresistor model and the simulated conductivity from the plasma model in Chapter 2 are 3.9S/m and 5.7S/m respectively. These two numbers closely matched in the same order of magnitude, which can be considered to be an accurate simulation. Therefore, based on this accuracy, a CST simulation was undertaken to determine the required conductivity that can achieve an S_{21} performance similar to that of the silicon superstrate switch.

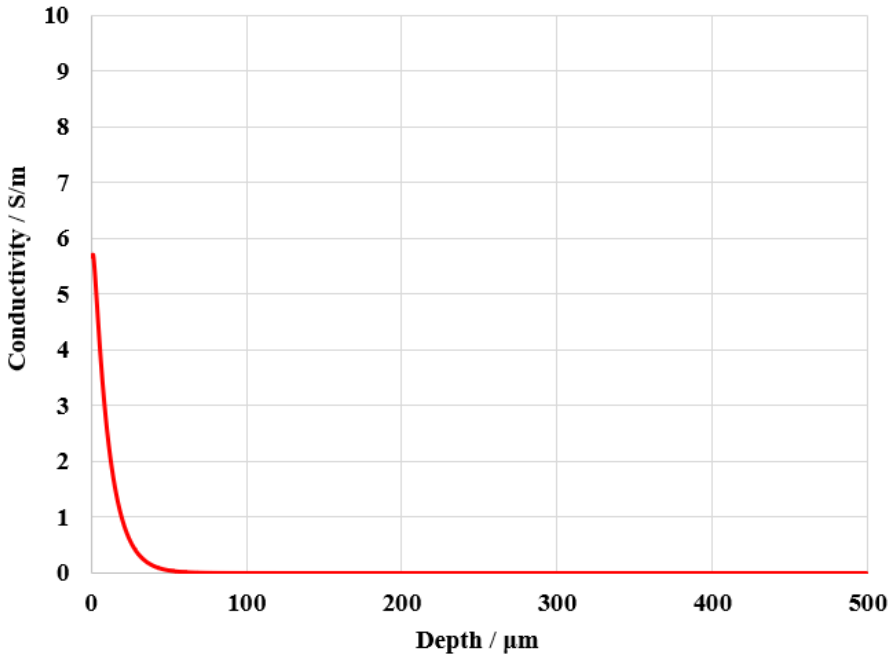

Figure 6.21 Simulated conductivity vs. Depth in substrate for unpolished intrinsic GaAs

The CST-simulated S_{21} results of different plasma surface layer conductivity under various illumination intensties are shown in Figure 6.20. These results illustrate that a $500S/m$ was found to be saturated so that the insertion loss could not be reduced by increasing the conductivity at this order of magnitude. After $4GHz$, the insertion loss and isolation were within the ranges of 2~3dB and 9~11dB respectively.

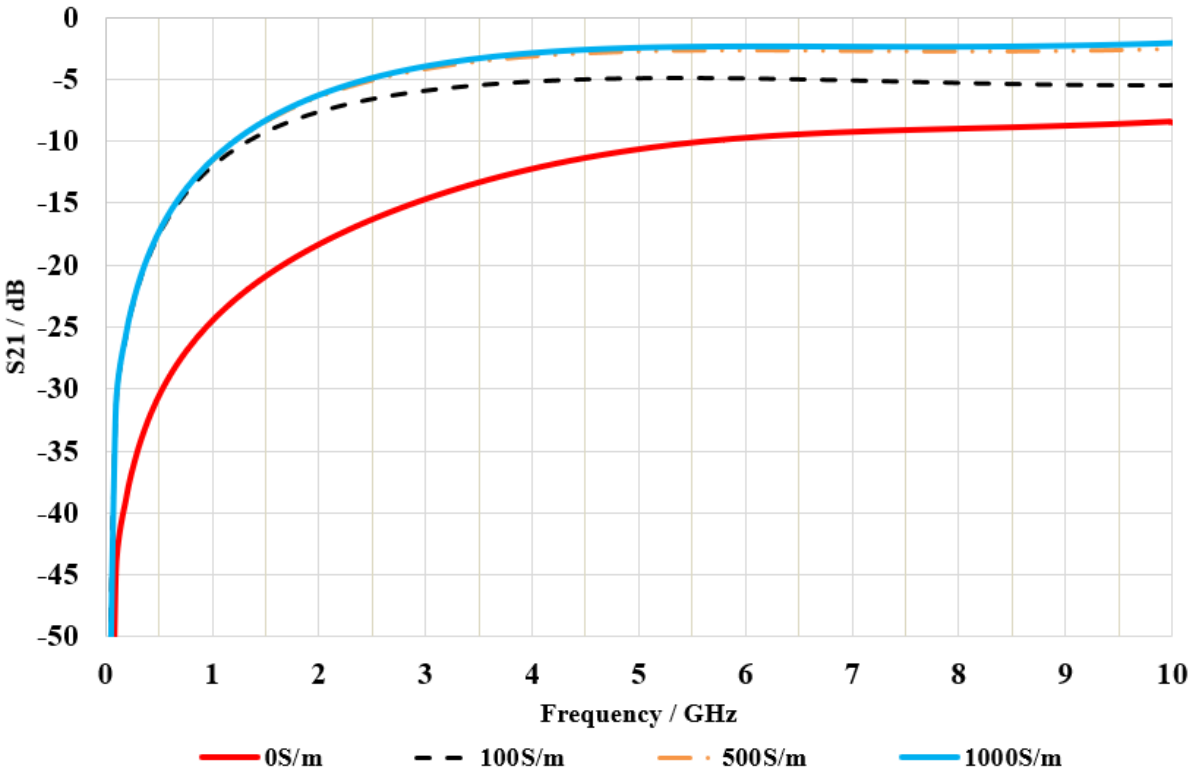

Figure 6.22 CST simulated S_{21} results for varying conductivity

Therefore, it would be interesting to know the intensity at which this good combination of insertion loss less than $2dB$ and isolation larger than $10dB$ could be found in a SI-GaAs superstrate microstrip gapline switch. Therefore, the reverse calculation was conducted, and it was found that the minimum intensity required would be at MW/cm^2. This huge number suggests that the approach of a LED or IRED optical excitation is unrealistic, but a highly focused laser may be able to deliver the desired results. On the other hand, a change of material and the development of new structure could be considered. Other recommendations and future work will be presented in the next chapter.

6.5 Conclusion

This chapter firstly contained a proposal to use a silicon superstrate microstrip gapline switch as a mixer in an AM modulation communication system. Pulsed laser and a laser driver were successfully operated after building an ad-hoc signal generation system with a programmable baseband signal generator. This system was designed for a recombination time measurement of excess electron-hole carriers in silicon, which were created by optical illumination. Since this excess carrier lifetime was found to limit the switching speed, GaAs was proposed as a superstrate due to its much shorter lifetime. A plan of LED/IRED switching toward a pulsed optical illumination was implemented. The optical loss and impedance mismatch of the IRED that prevented it from being a good candidate were discussed in detail. Next, an investigation of the measurement and simulation modelling were encouraged due to the significantly low carrier concentration and photoconductance from an SI-GaAs. Lastly, the power requirement for GaAs switching was raised and future work will be discussed in the next chapter.

6.6 References

[6.1] Laser Components, 905D1S3J09UA, High End / Low Cost Pulsed Laser Diodes, [accessible: https://www.lasercomponents.com/de]

[6.2] Picolas, LDP-V 10-70 Laser Driver 3, Ultra-compact Driver Module for Pulsed Lasers, [accessible: https://uk.rs-online.com/web/p/laser-drivers/6665647/]

[6.3] Rohde-Schwarz, R&S®SMU200A Vector Signal Generator, baseband characteristics, [accessible: https://www.rohde-schwarz.com/uk/product/smu200a-productstartpage_63493-7555.html]

[6.4] MathWorks, makers of MATLAB & Simulink, multi-paradigm numerical, Matlab 2016, [accessible: https://www.mathworks.com/products/matlab.html]

[6.5] Texas Instruments, 1.8-Ghz, Low Distortion, Current-Feedback Amplifier, [accessible: https://uk.rs-online.com/web/p/laser-drivers/6665647/]

[6.6] Burr-Brown, demonstration board, unpopulated PCB for high speed single op amps, [accessible: http://www.ti.com/lit/ug/sbou016b/sbou016b.pdf]

[6.7] Thorlabs, PDA10CF - InGaAs Fixed Gain Amplified Detector, 150 MHz BW, [accessible: https://www.thorlabs.com/newgrouppage9.cfm?objectgroup_id=4&pn=PDA05CF2]

[6.8] Rohde-Schwarz, R&S®RTO1014, Digital oscilloscope 1 GHz, 4 channels, [accessible: https://shop.rohde-schwarz.com/bargain/r-srrto1014-200321-1-1-1.html]

[6.9] J. J. Loferski, P. Rappaport, “Radiation damage in Ge and Si detected by carrier lifetime changes: damage thresholds”, Physical Review, vol. 111, no. 2, pp. 432, 1958

[6.10] E. K. Kowalczuk, C. J. Panagamuwa, R. D. Seager, "Design and operation influences regarding rise and fall time of a photoconductive microwave switch", Loughborough University, 2015

[6.11] California State University Northridge, Gallium Arsenide Semiconductors, [accessible: http://www.csun.edu/~rdconner/630/slides/GaAs.ppt]

[6.12] D. H. Auston, K. P. Cheung, P. R. Smith, "Picosecond photoconducting Hertzian dipoles", Applied physics letters, vol. 45, no. 3, pp.284-286,1984

[6.13] C. H. Lee, "Picosecond optoelectronic switching in GaAs", Applied Physics Letters, vol. 30, no. 2, pp.84-86, 1977

[6.14] M. Tonouchi, "Cutting-edge terahertz technology", Nature photonics, vol. 1, no. 2, pp. 97, 2007

[6.15] VISHAY, TSHG 8200/8400 series, Opto-electronics, Infrared Emitters, [accessible: http://www.vishay.com/docs/84755/tshg8200.pdf]

[6.16] Hewlett Packard, Agilent, 8656B/8657A/8657B, RF Signal Generators, [accessible: http://www.testequipmenthq.com/datasheets/Agilent-8656B-Datasheet.pdf]

CHAPTER 7

7. Conclusion and Future Work

7.1 Conclusion

This research involved working toward the design, characterisation and optimisation of reconfigurable RF circuits based on the interaction of optical illumination and semiconductor. Several simulations and measurement methods were developed for optically-reconfigurable microwave and millimetre wave circuits. The standard implementation process followed was design-simulation-fabrication-measurement-comparison-optimisation. These circuits were mainly designed based on the transmission line, which provides good transmission performance, as well as impedance matching. Much of the previous work on this project has laid the foundations for studying microstrip gaps and the illumination was provided by a laser that required fixed optics. The investigations presented here proposed fibre-coupled laser and LED/IRED optical sources for ease of integration, while still maintaining the optical power requirement. Multiple simulation methodologies and tools were studied and techniques for optimising accuracy were also proposed. Several switching components were fabricated and optimised with good performances achieved in both microwave and millimetre wave regimes.

Chapter 2 contained an explanation of the fundamental physics of semiconductors and the quantum basis that are involved in the interaction between optical illumination and the semiconductor. This interaction was studied from both a classical physics perspective based on Maxwell equations and the modern quantum perspective of wave-particle duality. In more detail, reflection was firstly discussed from the angle of an electromagnetic wave with the introduction of a wave equation and complex refractive index. A section of the electromagnetic wave's absorption and attenuation was followed by an explanation in quantum physics. In this section, the concept of band structure was described as a possible solution to scientists' recent quantum postulation. It was then employed to explain the band transitions in the generation recombination and diffusion of electron-hole excess carriers.

The photoconductivity section contained a detailed explanation and equation derivation of particle behaviour in the generation, recombination, drift and diffusion of excess carriers. Importantly, three recombination mechanisms were introduced, namely, Shockley-Read-Hall, Radiative and the Auger effect. Furthermore, the significant plasma diffusion of high concentrations of electron-hole plasma was analysed with physics equations. Finally, the total carrier concentration, as well as photoconductivity, was quantified for a subsequent analysis. Critical electrical properties were eventually obtained through the derived physics equations along with dielectric permittivity studies, and a solution for simulation was found and later employed to predict the performance of the circuit. Lastly, the comparison and choice of the materials on which the study of GaAs was based in Chapter 6 were discussed.

Chapter 3 mainly consisted of a description of the simulation, measurement and fabrication involved in this research. In terms of simulation, the distributed element model and the full-wave electromagnetic analysis were firstly compared, which highlighted the limitations of the former method. An in-depth comparison was made within the scope of full-wave modelling methodologies, including the FEM, FDTD, FDFD and FIT algorithms, for a detailed explanation. The FDTD-evolved FIT method was finally distinguished as the best method based on its broad band design and computational efficiency, as well as for its time-saving benefit and popularity in modern simulation technologies. With regard to the measurement, a fibre-coupled laser and LED/IRED provided more possibilities and maintained the same required optical power as the free-space VCSEL laser with solid optics. More importantly, the

huge potential of circuit incorporation and integration can be anticipated based on these techniques. These measurement setups also essentially demonstrated flexibility and versatility in the interaction between optical and RF engineering interact. Finally, a detailed fabrication procedure was shared. A standard photolithography process was followed for circuit fabrication and an alternative laser-cutting PCB circuit fabrication, which was hired to improve integration in Chapter 5, was also shown.

Chapter 4 contained a proposal of a superstrate-structure microwave gapline switch and the implementation of a standard characterisation test on this novel device. Optimisation was conducted for a better linearity performance and higher power-handling ability. Chapter 4 began with a review of state-of-the-art optically-controlled microwave switches and this was followed by a list of the improvements targeted in this work. A microstrip gap switch in previous work was selected as the fundamental model and its large transmission loss was analysed with the aid of CST simulation and the modelling created in Chapter 2 in order to identify the reason for this loss. A superstrate microstrip gapline switch model was proposed based on other work on antenna. Simulation software was again employed to implement a sensitivity analysis. A corresponding CST parameter sweep overtook this task and the optimum circuit dimensions were theoretically proposed. Then, the circuit of interest was fabricated and measured and good agreement was achieved between the CST simulated and VNA measured results. An appropriate two-tone non-linearity test with power handling observation was designed and conducted for a full characterisation of the designed switch. The initial results did not demonstrate much competitiveness to other microwave switches, since the superstrate fixture holder had melted during the test and the insertion loss had deteriorated. Several proposed fixtures were fabricated and tested to solve this problem. On the other hand, the contact issue with the suspected reason of non-linearity generation by the Schottky barrier was analysed and confirmed. Several experiments were conducted and better results were found by changing the superstrate materials to reduce the Schottky barrier; however, this caused insertion loss and worse isolation. Finally, a new structure design free of Schottky contact was proposed with a passivation layer included in the superstrate and quartz inserted in the superstrate fixture. This was found to improve both the non-linearity and power-handling ability.

Chapter 5 was concentrated on designing devices at higher frequencies in the millimetre wave region. It began with a literature review of the current millimetre wave switches and a proposal of several aspects that needed to be improved. The chapter was divided into two parts, the first of which contained a proposal for an optically-controlled GCPW switch operating in the millimetre wave region based on a transmission line model. This switch was designed to follow an inverse controlling correlation between the illumination condition and the switch condition; the switch OFF state occurred when optical illumination was provided because the GCPW central conductor was grounded, which significantly reduced the transmission of the device. A full-wave analysis with a multi-layer plasma model was utilised to find the optimum circuit dimension. Detailed circuit fabrication and V connector installation for high frequency were also described and a good agreement was achieved between the measured and simulated results. The results showed considerably good isolation and transmission performances in the millimetre regime.

A millimetre-wave GCPW attenuator controlled by a single IRED was presented in the second part of this chapter. This device was designed on PCB material, Roger 4003C, with compact optical source for better integration with on-board circuits. The proposed device added drilled through-holes on the spacing between the signal and the ground of a straight GCPW transmission line. This effectively increased the interactive region which allowed more utilisation of the optical illumination provided by a high power IRED. Very good attenuation was achieved across the boundary of the microwave and millimetre wave. Furthermore, insertion loss was reduced compared with the device designed in the first part by laser-drilling more vias holes that effectively compressed the spurious surface modes. The employed laser-cutting fabrication technique also demonstrated superiority at a shorter lead time and the benefit of low cost.

Chapter 6 was focused on two superstrate materials, silicon and GaAs, for implementing the switching on the superstrate microwave gapline switch developed in Chapter 4. This switch was used as a mixer in an AM modulation communication system. A pulsed laser system was successfully designed and operated. Importantly, an ad-hoc programmable signal generation system was converted from a baseband signal generator and a modified non-inverting current feedback amplifier. The time taken for the recombination of excess carriers in silicon was

measured using this system and it was found to be relatively long for the requirement of fast switching. Hence, a study of GaAs as superstrate material was proposed. Due to the insufficient photon energy provided from the laser configured in the system designed for silicon, LED/IREDs were selected as new candidates based on more choices of wavelengths and its outstanding promising potential in circuit integration, as discussed earlier in Chapters 3 and 5. Work was done on driving a selected IRED for its high power and high bandwidth. However, it was found that the photoexcitation on a SI-GaAs needed significantly large optical power, not to mention the recognition of a dispersive angle and impedance mismatch in this IRED. Therefore, an investigation was begun of its power requirement with a DC bias test. Theoretical calculations and simulations were conducted and agreed with the measured results from a DC bias test and finally, recommendations were made for the implementation of this designed switching and mixing.

7.2 Future Work

It is considered that several aspects of this project could be improved by further research. Firstly, non-linearity can be a sophisticated problem to analyse, especially when it depends on various parameters. Chapter 4 contained a discussion and characterisation of non-linearity which was mainly indicated by IP_3. Ambient heat condition and structural contacts could be further studied to continue this discussion. Complex problems could be fragmented and addressed in several sub-sections based on the multi-physics modelling tool of COMSOL, which is recommended to deal with such difficult questions. The resistivity across contacts of different layers could be used to identify the source of the non-linearity. The Passive Intermodulation (PIM) measurement could also be hired for a better understanding. Secondly, since the current stepped-impedance GCPW attenuator limits the operating frequency to about $30GHz$, it is proposed that a smaller slow-wave structure in GCPW would work better in millimetre wave frequencies, but it is believed that with a reduced area of illumination, the isolation/attenuation value will be sacrificed from a trade-off between them. Thirdly, to implement a fast switching with GaAs, a rapidly pulsed and powerful laser with a precisely focused optical lens will be needed to provide significant intensity on the photo-conductive region of interest. Alternatively, a two-photon absorption (TPA) method from quantum

technology could be implemented. This second-order process may provide more possibilities, since many powerful pulsed lasers could be considered at longer wavelengths outside the cut-off wavelength boundary.

The work in this research has laid the foundation for the design of optically-reconfigurable microwave and millimetre wave switches by mainly focusing on a circuit for integration and the incorporation of on-board components. Although a significant amount of work is still needed for commercial application, the proposed techniques and designed circuit components are believed to make a certain contribution to future research and implementation.

APPENDIX I

Comparison of Different Switch Technologies

Type of switch	Bandwidth	Insertion loss (dB)	Isolation (dB)	Return loss (dB) @ON	Return loss (dB) @OFF	Switch Time	DC source power/bias	IM_3	1dB Compression	Power Handling	Unit Price
PIN 1 [1]	27-46GHz	1~2.6	12~26	5~10	Unknown	<4ns	100mW	Low	31~36dBm @7.5V	~33dBm (2W)	£30
PIN 2 [2]	DC-50GHz	0.2~0.3	22~46	16~30	Reflective	10ns	50mW	Low	Unknown	23dBm	£5.12

										(~0.2W)	
PIN3 [3]	DC-50GHz	1.2	>30	>20	>10dB	10ns	50mW	Low	Unknown	23dBm (~0.2W)	£9.59
MEMS [4]	DC-26GHz	<1.6	30	2	Reflective	3-5ms	768mW	-110dBc @1.7GHz (2 carriers 20W)	Unknown	1W when hot switching	£223.5
PCS 1 [5]	6.7~30GHz	<2.3	>15	>10	>6.2dB	~10us	mW~ 2.9W	Unknown	Unknown	Unknown	

PCS 2 [6]	DC-65GHz	<2.5	>10 >>20GHz	>7.5	>12.5dB	~10us	mW~2W	Unknown	Unknown	Unknown	
PCS 3 [7]	DC-18GHz	<1.3	>10dB >>6-18GHz	>12	Highly Reflective	~10us	mW~2W	+77dBm	Not Found	>46dBm (40W)	

[1] Triquint, TGS4302 Data Sheet, 2008 (https://www.mouser.co.uk/datasheet/2/412/TGS4302-894344.pdf)

[2] Macom, MA4AGSW1 Data Sheet Rev. V6, 2011 (https://www.mouser.co.uk/datasheet/2/249/MA4AGSW1-476786.pdf)

[3] Macom, MA4AGSW1A Data Sheet Rev. V7, 2011 (https://www.mouser.co.uk/datasheet/2/249/MA4AGSW1A-474765.pdf)

[4] Radiall, R51673310T Data Sheet, 2017 (https://www.mouser.co.uk/datasheet/2/516/R516_Generic_TDS-24-07-17-1149786.pdf)

[5] A. W. Pang, S. Bensmida, C. D. Gamlath, M. J. Cryan, “Non-linear characteristics of an optically reconfigurable microwave switch”, IET Microwaves, Antennas & Propagation, vol. 12, no. 7, pp. 1060-1063, Jan. 2018

[6] A. W. Pang, C. D. Gamlath, M. J. Cryan, “An Optically Controlled Coplanar Waveguide Millimeter-Wave Switch”, IEEE Microwave and Wireless Components Letters, vol. 28, no. 8, pp. 669-71, Aug. 2018

[7] Y. Zhang, A. W. Pang, M. J. Cryan, “Optically Controlled Millimeter-wave Attenuator with Stepped-Impedance Lines”, to be submitted, Oct. 2018